

REPORT DOCUMENTATION PAGE			Form Approved OMB No. 0704-0188	
<small>Public reporting burden for this collection of information is estimated to average 1 hour per response, including the time for reviewing instructions, searching existing data sources, gathering and maintaining the data needed, and completing and reviewing the collection of information. Send comments regarding this burden estimate or any other aspect of this collection of information, including suggestions for reducing this burden, to Washington Headquarters Services, Directorate for Information Operations and Reports, 1215 Jefferson Davis Highway, Suite 1204, Arlington, VA 22202-4302, and to the Office of Management and Budget, Paperwork Reduction Project (0704-0188), Washington, DC 20503.</small>				
1. AGENCY USE ONLY (Leave blank)	2. REPORT DATE 15.Sep.03	3. REPORT TYPE AND DATES COVERED THESIS		
4. TITLE AND SUBTITLE "EFFECT OF RADIATION ON SILICON AND BOROSILICATED GLASS"		5. FUNDING NUMBERS		
6. AUTHOR(S) CAPT ALLRED CLARK L				
7. PERFORMING ORGANIZATION NAME(S) AND ADDRESS(ES) MASSACHUSETTS INSTITUTE OF TECHNOLOGY		8. PERFORMING ORGANIZATION REPORT NUMBER CI02-1279		
9. SPONSORING/MONITORING AGENCY NAME(S) AND ADDRESS(ES) THE DEPARTMENT OF THE AIR FORCE AFIT/CIA, BLDG 125 2950 P STREET WPAFB OH 45433		10. SPONSORING/MONITORING AGENCY REPORT NUMBER		
11. SUPPLEMENTARY NOTES				
12a. DISTRIBUTION AVAILABILITY STATEMENT Unlimited distribution In Accordance With AFI 35-205/AFIT Sup 1 DISTRIBUTION STATEMENT A Approved for Public Release Distribution Unlimited			12b. DISTRIBUTION CODE	
13. ABSTRACT (Maximum 200 words)				
<div style="border: 1px solid black; padding: 10px; display: inline-block;"> 20030923 111 </div>				
14. SUBJECT TERMS			15. NUMBER OF PAGES 255	
			16. PRICE CODE	
17. SECURITY CLASSIFICATION OF REPORT	18. SECURITY CLASSIFICATION OF THIS PAGE	19. SECURITY CLASSIFICATION OF ABSTRACT	20. LIMITATION OF ABSTRACT	

Effect of Radiation on Silicon and Borosilicate Glass

by
Clark L. Allred


Submitted to the Department of Materials Science and Engineering
in partial fulfillment of the requirements for the degree of
Doctor of Philosophy in Materials Science and Engineering
at the


MASSACHUSETTS INSTITUTE OF TECHNOLOGY

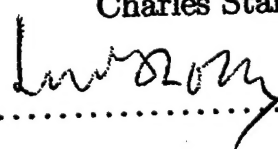
September 2003

© Clark L. Allred, MMIII. All rights reserved.

The author hereby grants to MIT permission to reproduce and
distribute publicly paper and electronic copies of this thesis document
in whole or in part.

Author 
Department of Materials Science and Engineering
August 18, 2003

Certified by 
Jeffrey T. Borenstein
Principal Member of the Technical Staff
Charles Stark Draper Laboratory
Thesis Supervisor

Certified by 
Linn W. Hobbs
Professor of Materials Science and Engineering
and Professor of Nuclear Engineering
Thesis Advisor

Accepted by
Harry L. Tuller
Professor of Ceramics and Electronic Materials
Chair, Departmental Committee on Graduate Students

DISTRIBUTION STATEMENT A
Approved for Public Release
Distribution Unlimited

Effect of Radiation on Silicon and Borosilicate Glass

by

Clark L. Allred

Submitted to the Department of Materials Science and Engineering
on August 18, 2003, in partial fulfillment of the
requirements for the degree of
Doctor of Philosophy in Materials Science and Engineering

Abstract

A study was made that is logically divided into two parts, both involving radiation damage effects. The first is a study of the effects of neutron and gamma radiation on the dimensions of two borosilicate glasses, Pyrex[®] and Hoya SD-2[®]. These two glasses are commonly used as substrates for silicon microelectromechanical (MEMS) devices, and radiation-induced compaction in a substrate can have deleterious effects on device performance. Results are presented for density changes induced in both glasses by neutron irradiation. Pyrex was shown to compact at a rate of (in $\Delta\rho/\rho$ per n/cm²) 8.14×10^{-20} (thermal) and 1.79×10^{-20} (fast). The corresponding results for Hoya SD-2 were 2.21×10^{-21} and 1.71×10^{-21} , respectively. On a displacement per atom (dpa) basis, the compaction of the Pyrex was an order of magnitude greater than that of the Hoya SD-2. Our results are the first reported measurement of irradiation-induced densification in Hoya SD-2. The compaction of Pyrex agreed with a previous study. Our results for gamma irradiations were unexpected. Silicon MEMS strain gauges mounted on glass wafers were gamma-irradiated to hundreds of Mrad. Based on expectations from the literature, the Pyrex was supposed to compact to a level easily measurable by the MEMS strain gauges. Almost no substrate compaction registered in the strain gauges, however. It is hypothesized that the anodic bonding process (by which a silicon wafer was bonded to the glass before etching to create the MEMS strain gauges) was responsible for either 1) changing the bulk radiation response of the glass or 2) creating a layer near the bond interface which somehow prevented the MEMS strain gauges from registering the compaction that was occurring in the glass substrate. While not yet understood, this null result for apparent substrate compaction is of great importance to the problem of mechanically rad-hard MEMS, since it indicates that the response of an anodically bonded Si-glass system to radiation is not simply the sum of the effects on the unbonded materials. To investigate this further, glass samples were prepared in various stages of the anodic bonding process (which involves heating in the presence of an electric field), then irradiated with neutrons. No difference in bulk compaction was noted among the

treated samples or the untreated glass, but this result may have been influenced by the high temperature at which the glass was irradiated; however, temperature alone could not have annealed away all the effects of treatment. We conclude that the unexpected results of the MEMS strain gauge experiment were caused by surface layer phenomena at the bonding interface, though we do not currently understand the exact mechanism for this. The second major topic of this study is the effect of neutron irradiation on the Young's modulus of silicon, the constancy of which is key to the operation of many MEMS devices. The elastic constants of defected and amorphous silicon simulation cells were calculated using EDIP. Simulation cells included some containing randomly generated defect distributions, as well as several that were completely amorphous and one containing a small amorphous region. An extensive and careful characterization of point defects was made. Three important conclusions were drawn from the results of these simulations: 1) defects have independent effects on the elastic constants of silicon up to (at least) a defect concentration of 0.3% 2) the linear effect of Frenkel pairs on the $\langle 110 \rangle$ Young's modulus of silicon is -1653 GPa per defect fraction 3) 17 different point defect types were shown to cause a very similar decrease in the $\langle 110 \rangle$ Young's modulus: $-(0.28 \pm 0.05)\%$ when calculated in isolation using a 1728-atom cell. These three conclusions will be very useful for estimating the effects of radiation damage on the elastic modulus of silicon in cases where point defect content can be estimated, but the exact distribution and species of these defects is unknown. An additional finding is that the effect of a small amorphous region embedded in a crystalline matrix alters the Young's modulus by an amount predictable by its volume fraction, as has been observed in a prior experiment. We summarize our findings for borosilicate glass and silicon by extrapolating from our experimental and simulation results to characterize radiation effects on the operation of a hypothetical resonating silicon beam MEMS device.

Thesis Supervisor: Jeffrey T. Borenstein
Title: Principal Member of the Technical Staff

Thesis Advisor: Linn W. Hobbs
Title: Professor of Materials Science and Engineering
and Professor of Nuclear Engineering

Acknowledgements

I'd like to thank my advisor and Draper supervisor for their support over the last five years. They contributed a great deal to the conception and realization of this thesis. Some specific contributions of collaborators are cited in the text, but the contributions of the following people go beyond what is mentioned (I could not have done this work without them): Dr. Xianglong Yuan (DMSE), Dr. Meri Treska (DMSE), Prof. Martin Bazant (Math Dept), Dr. Gordon Kohse (MIT reactor), and Dr. John Farmer (MURR reactor). There are many others at Draper Lab, MIT, and the various irradiation sites who contributed to this work with ideas and elbow grease. These people include engineers, technicians, scientists, safety personnel, and paper pushers. There are too many of them to name, but their contributions were both valuable and appreciated. I'd also like to thank Prof. Yip for his suggestions which have made this a better thesis.

Most of all, I owe a debt of gratitude to my wife. She has supported and encouraged me throughout this process. For the last five months or so, she has almost functioned as a single parent, but has willingly worked harder than usual herself so that I could put in long hours on writing this thesis. This has truly been a team effort.

I thank the Air Force for supporting me financially during my time at MIT, and Draper Laboratory for letting me participate in the Draper Fellowship program.

The views expressed in this thesis are those of the author and do not reflect the official policy or position of the United States Air Force, Department of Defense, or the U.S. government.

This thesis was prepared at The Charles Stark Draper Laboratory, Inc., under IR&D contract number 03-3-C301-2.

Publication of this thesis does not constitute approval by Draper or the sponsoring agency of the findings or conclusions contained herein. It is published for the exchange and stimulation of ideas.


Clark L. Allred

Contents

1	Introduction	19
1.1	Motivation	19
1.2	Description of borosilicate glasses	22
1.3	Summary of experiments and simulations	25
1.3.1	Irradiations	26
1.3.2	Elastic constant calculations in defected silicon	28
1.3.3	Implications for anodically bonded MEMS	29
2	Radiation effects in borosilicate glasses	31
2.1	Continuous random network model	31
2.2	Damage mechanisms	34
2.2.1	Fast neutrons	34
2.2.2	Thermal neutrons	36
2.2.3	Gamma rays	38
2.3	Previous experiments	38
2.3.1	Silica	38
2.3.2	Borosilicate glasses	40
3	Radiation-induced defects in silicon	49
3.1	Damage mechanisms	49
3.1.1	Neutrons and gamma radiation	49
3.1.2	Point defects and amorphization	50
3.2	Prior study of silicon	52
3.2.1	Dimensional changes	52
3.2.2	Elastic effects	53
3.3	Silicon experiments	54
3.3.1	Irradiation of silicon samples	54
3.3.2	X-ray diffraction measurements	56

3.3.3	Acoustic microscopy measurements	58
4	Borosilicate glass irradiation experiments	61
4.1	Gamma irradiation of pointer beam strain gauges	61
4.1.1	Method	61
4.1.2	Results	70
4.2	TRIM calculations of neutron damage in glass	77
4.2.1	Introduction to TRIM	77
4.2.2	Glass models	78
4.2.3	Fast neutron calculations	80
4.2.4	Thermal neutron calculations	84
4.3	Neutron irradiation of borosilicate glasses	87
4.3.1	Sink/float densitometry method	87
4.3.2	Sink/float apparatus design and execution	90
4.3.3	Unshielded irradiations at the MIT reactor	95
4.3.4	Shielded irradiations at the University of Missouri-Columbia	103
4.4	Discussion	121
5	Simulation of mechanical property effects of defects in silicon	125
5.1	Simulation approaches	125
5.1.1	Choosing EDIP	125
5.1.2	Collision cascades	128
5.1.3	Elastic constants in molecular dynamics	131
5.2	Defect characterization using EDIP	132
5.2.1	Method	132
5.2.2	Results	141
5.3	Comparison with Stillinger-Weber	161
5.4	Discussion	170
5.5	Conclusions	175
6	Implications for MEMS	179
6.1	Overview	179
6.2	Benchmark MEMS scenario	180
6.2.1	Hypothetical MEMS device	180
6.2.2	Radiation environment	183
6.3	Estimation of radiation effects	185

7	Conclusions	191
7.1	Summary	191
7.2	Discussion	197
7.3	Future work	200
A	Pointerbeam Strain Gauge Data	203
B	Sink/Float Data	211
C	Elastic Constant Relations in Diamond Cubic Silicon	217
C.1	Analytic solutions for EDIP elastic constants	217
C.2	Relations among elastic constants	222
C.2.1	Isotropic materials	222
C.2.2	Cubic materials	222
C.2.3	Diamond materials with three-body forces	223
D	Heating analysis for MURR irradiation	225
E	Nuclear activation estimates for glass irradiations	235
F	Nuclear activation measurements	241

List of Figures

1-1	Variation with temperature of the linear coefficient of thermal expansion of silicon,[114] Hoya SD-2,[49] and Pyrex.[33]	23
1-2	Integrated strain due to thermal expansion from 25 C for silicon,[114] Hoya SD-2,[49] and Pyrex.[33]	24
2-1	Schematic diagram of a two-dimensional continuous random network comprised of interconnected polyhedra.	32
2-2	Schematic diagram of network components. The basic unit of SiO_2 is the $[\text{SiO}_4]$ tetrahedron, and that of B_2O_3 is the $[\text{BO}_3]$ triangle.	33
2-3	Schematic representation of a fast neutron collision cascade in borosilicate glass.	36
2-4	Schematic diagram of a thermal neutron capture and (n,α) reaction in borosilicate glass.	37
2-5	Effect of fast neutron irradiation on density of vitreous silica.[99]	39
2-6	Effect of gamma irradiation on density of vitreous silica and Pyrex.[110]	40
2-7	Relative radiation-induced density change in Pyrex with gamma dose from several previous studies.	42
2-8	Relative radiation-induced density change in Pyrex with low gamma dose from several previous studies.	43
2-9	Effects of thermal neutron irradiation on density of Pyrex.[95]	44
2-10	Isothermal annealing of thermal neutron-induced densification in Pyrex.[95] The residual radiation-induced compaction is expressed as a fraction of that prior to annealing.	45
2-11	Isochronal annealing of Pyrex densification from gamma irradiation.[31] Densification of the Pyrex is shown relative to the unirradiated glass density ρ	47
3-1	Triple crystal XRD measurements of lattice parameter changes in neutron-irradiated silicon.[127]	57
3-2	Surface acoustic wave velocity of irradiated silicon samples	59
4-1	Pointer beam MEMS silicon strain gauge, top view. The grey portions are suspended above the glass substrate. The black portions are bonded to the substrate. The top and bottom teeth have $4.5\text{ }\mu\text{m}$ and $5\text{ }\mu\text{m}$ pitch, respectively. The horizontal distance between the inside of the lower black (bonded) portions is 1 mm.	62

4-2	Pointer beam MEMS silicon strain gauge wafer layout. The black squares represent arrays of test fixtures, each one containing a pointer beam strain gauge.	64
4-3	The pointer beam irradiation set up. The Co 60 source is a rectangular plate behind the aluminum window. The wafers sit held loosely by brads attached to a thin aluminum support.	66
4-4	Placement of doimeters on aluminum wafer holder. The dosimetry used the same configuration as shown in Fig. 4-3.	67
4-5	Dosimeter readings and fit curve.	68
4-6	Pointer beam gauge readings from Pyrex wafer.	72
4-7	Pointer beam gauge readings from Hoya SD-2 wafer.	73
4-8	Oxygen recoil cascade in Pyrex, calculated using TRIM. Squares and triangles represent the location in the X-Y plane at which a displacement occurs, for oxygen recoils of 221 and 22 keV, respectively. . . .	85
4-9	The sink/float experiment. Six liquid-filled test tubes are suspended in a water bath. The rear test tubes contains a thermometer probe. A quartz heating element is suspended in the center of the water bath. The large Pyrex container is resting on a magnetic stir plate. . . .	91
4-10	Close-up view of sample pair in test tube. The darker sample on the left has been irradiated.	93
4-11	Diced Pyrex wafer showing sample pair selection.	96
4-12	The effect of neutron irradiation on the density of glass samples. Relative density change is shown versus irradiation time. in the MIT reactor. .	100
4-13	Comparison of MIT reactor results for Pyrex with those of Paymal. .	102
4-14	Schematic representation of the anodic bonding process. The shaded and white portions represent the silicon and glass wafers, respectively. .	104
4-15	Diagram of sample holder during irradiation, in cross section. The inner grey portion is the sample holder. The black inner container is the boron nitride shield. The aluminum container is shown in grey, as is the aluminum slug sitting on top of it. The surrounding black rectangle is the aluminum rabbit, outside which the hashed portion represents water.	108
4-16	High-purity aluminum sample holder shown open at left and closed at center. Two glass samples are shown in the foreground at left. One of the samples has been darkened by irradiation. The boron nitride pillbox thermal neutron shield and its lid are shown at right.	109
4-17	One-dimensional thermal model for shielded irradiation of glass samples at MURR. The origin is at the left. The regions numbered with roman numerals are concentric cylinders. Region I is a Pyrex glass cylinder. and the sample holder. Region III represents the aluminum sample holder inside the boron nitride shield (region V). Regions VII and IX are the aluminum filler and rabbit, respectively. White regions are air gaps between solids regions. Region X is water held at 30 C. .	110

4-18	Relative density change versus irradiation time for Pyrex sink/float samples. The line is fit only to the first two points of the sample A measurements. Each data point is the average of six measurements, and the error bars represent $\sigma/\sqrt{6}$ for these measurements.	116
5-1	C_{11} as a function of point defect fraction. Diamonds indicate interstitials, triangles vacancies, and squares Frenkel pairs. Each point represents the average of three samples. Bars indicate the standard deviation of the three samples. Lines are unweighted least squares fits constrained to match the crystalline value on the Y-axis.	141
5-2	C_{12} as a function of point defect fraction. Symbols are as for Figure 5-1	142
5-3	C_{44} as a function of point defect fraction. Symbols are as for Figure 5-1	142
5-4	Bulk modulus as a function of point defect fraction. Symbols are as for Figure 5-1	143
5-5	Young's modulus as a function of point defect fraction. Points were calculated from the C_{ij} in Figs. 5-1-5-4. Symbols are as in Fig. 5-1. .	143
5-6	Percent volume change as a function of point defect fraction. Symbols are as in Fig. 5-1.	145
5-7	Interstitials generated by random placement and subsequent relaxation using EDIP. The corners of a diamond unit cell are connected by lines, and atoms occupying interstitial positions are darkened. Bonds are drawn between atoms closer than 2.56 Å. H_2 involves two atoms which are extra to the diamond unit cell — all other defects pictured here involve only one extra atom.	150
5-8	Formation energy for $\langle 110 \rangle$ dumbbell calculated in various sized supercells with periodic boundary conditions	151
5-9	Unrelaxed formation energy for an interstitial placed along the unit cell body diagonal in Si, calculated using EDIP. The solid and dashed vertical lines indicate the positions of the hexagonal and tetragonal interstitials, respectively.	152
5-10	The four fold coordinated defect referred to a unit cell. The two displaced atoms are darkened.	153
5-11	Divacancy complexes referred to a unit cell (left to right): V_{2nn} , V_{2a} , and V_{2nnr} . Highlighted and darkened atoms are twofold and threefold coordinated, respectively. At left, two next-nearest neighbors are missing from the upper half of the unit cell. At center, the two-fold coordinated atom (marked with a cross) has broken symmetry and become three-fold coordinated. Annealing V_{2nn} at room temperature yielded the rightmost figure, in which the uppermost atom (black) is five-fold coordinated. This atom is not part of the unit cell shown, but is included to provide context. While V_{2nnr} was generated by annealing V_{2nn} , it actually involves missing nearest neighbors, similar to the simpler V_{2n} (not shown).	155

5-12	Stable EDIP monovacancy configurations. At left is the outward-breathing vacancy (V) observed in all randomly-generated samples. Vacancy neighbors are darkened. The Jahn-Teller distortion with bonding between pairs of vacancy neighbors is shown at center (V_{JT}), and the result upon a room temperature annealing of this defect is shown at right (V_{JT_r}). The cross marks an atom whose position changes significantly between the three configurations shown, as does the circle. V_{JT_r} contains one 5-coordinated atom (circle) and one 3-coordinated atom (back lower left corner).	157
5-13	Unrelaxed formation energy for an interstitial placed along the unit cell body diagonal in Si, calculated using the Stillinger-Weber potential. The vertical lines indicate the positions of the hexagonal (left) and tetragonal (right) interstitials, respectively.	165
5-14	C_{11} as a function of point defect fraction, calculated using Stillinger-Weber. Diamonds indicate interstitials and triangles vacancies. Each point represents the average of three directions in the same sample. Bars indicate the standard deviation among the three directions. Lines are unweighted least squares fits constrained to match the crystalline value on the Y-axis.	166
5-15	C_{12} as a function of point defect fraction, calculated using Stillinger-Weber. Notation is as in Figure 5-14.	167
5-16	C_{44} as a function of point defect fraction, calculated using Stillinger-Weber. Notation is as in Figure 5-14.	167
5-17	Bulk modulus B as a function of point defect fraction, calculated using Stillinger-Weber. Notation is as in Figure 5-14.	168
5-18	Young's modulus $E_{\langle 110 \rangle}$ as a function of point defect fraction, calculated from data shown in Figures 5-14-5-16. Notation is as in Figure 5-14.	168
6-1	MEMS accelerometer from reference [118]. At left, the central square proof mass is suspended above the substrate surface by a beam at each corner. The detail of one of the beam structures at the corner of the central mass is shown at right.	181
6-2	MEMS resonating beam. The silicon beam is suspended above the glass substrate surface, supported at either end by bond pads.	181
D-1	One-dimensional thermal model for shielded irradiation of glass samples at MURR. The origin is at the left. The regions numbered with roman numerals are concentric cylinders. Region I is a Pyrex glass cylinder. and the sample holder. Region III represents the aluminum sample holder inside the boron nitride shield (region V). Regions VII and IX are the aluminum filler and rabbit, respectively. White regions are air gaps between solids regions. Region X is water held at 30°C.	226

List of Tables

1.1	Composition of Pyrex as measured by XPS.	25
1.2	Composition of Hoya SD-2 measured by XPS.	25
3.1	Elastic constants of a silicon layer expressed as a percentage of the crystalline value.[20] Displacements per atom (dpa) were calculated using TRIM.[144]	54
3.2	Irradiation schedule of silicon samples destined for the elastic modulus study. Displacements per atom (dpa) were calculated using TRIM.[144]	55
3.3	Irradiation schedule of silicon samples for XRD lattice parameter measurement. Displacements per atom (dpa) were calculated using TRIM.[144]	55
4.1	Pointer beam strain gauge pre-irradiation positions. Deflection is measured in tooth widths. The initial differential strain between the silicon and glass is residual from the fabrication process.	65
4.2	Gamma dosimeter readings.	69
4.3	Fits to data in Figures 4-6 and 4-7.	71
4.4	Fits to pointer beam data for alternate dosimetry estimate.	71
4.5	Assumed glass compositions for TRIM calculations (atomic percent).	80
4.6	Distribution of primary knock-on atoms input into TRIM.	83
4.7	Summary of TRIM calculations for fast neutrons.	84
4.8	Summary of TRIM calculations for thermal neutrons.	86
4.9	Radiation schedule for glass samples in the MIT reactor.	99
4.10	Scatter of six measurements (averaged across data points).	101
4.11	Results of MIT sink/float measurements.	102
4.12	Physical properties of Carborundum AX05 boron nitride.	107
4.13	Scenarios for glass sample heating during the MURR irradiation. The assumed thermal neutron flux ($n/cm^2/s$) incident on the boron nitride shield and the fraction thereof that is incident on the glass are at left. Air gaps between solid regions of Figure 4-17 are given in meters. ΔT represents the amount by which the glass center (r_0) is above T_o (C).	111
4.14	Results of wax irradiations in the MIT reactor. Waxes were purchased from McMaster-Carr. Nominal melting temperatures are in centigrade.	112

4.15	Planned schedule for irradiation of shielded Pyrex and Hoya SD-2 glass samples at the University of Missouri-Columbia reactor. The calculation assumed that the boron nitride shield would absorb all but 0.4% of the incident thermal neutrons. The ratio of the compaction due to fast neutrons compared to that due to thermal neutrons would be ~ 39 for Hoya SD-2 and ~ 11 for Pyrex (ratios calculated using results from section 4.2). The ΔT figure refers to the predicted difference between irradiated and non-irradiated reference samples in the sink/float experiment.	113
4.16	Results and calculations for the MIT reactor test irradiation of Hoya SD-2 glass. The irradiation was 10 minutes long in a thermal neutron flux of $\sim 4 \times 10^{12}$ n/cm ² /s. The sample was 1 cm \times 1 cm \times 0.078 cm in size. See Appendix E for details on the symbols and equations used for these calculations.	114
4.17	Thermal neutron flux (n/cm ² /s) in the irradiated samples at the Missouri reactor deduced from activation of zinc and antimony. The numbers quoted for each sample type (A, B, C, D, and E) are the mean of the three irradiated sample sets (3, 4, and 5).	117
4.18	Thermal neutron flux (n/cm ² /s) in the irradiated samples at the Missouri reactor deduced from activation of zinc and antimony. The numbers quoted for each sample type (A, B, C, D, and E) are the mean of the three irradiated sample sets (3, 4, and 5).	119
4.19	Interpretation of the results in Figure 4-18 and comparison with the MIT reactor experiment results for Pyrex.	120
4.20	Predictions of the thermal model of section 4.3.4.4 for the likely bounds of the MURR glass irradiation. The assumed thermal neutron flux (n/cm ² /s) incident on the boron nitride shield and the fraction thereof that is incident on the glass are at left. Air gaps between solid regions of Figure 4-17 are given in meters. ΔT represents the amount by which the glass center (r_0) is above T_o (C).	121
5.1	Parameters used in EDIP. The parameters u_1 – u_4 were not adjustable in the fitting process.	128
5.2	Descriptions of amorphous samples. Calculation of numbers of 5-fold and 3-fold coordination defects present used a rounding of the EDIP coordination value Z	135
5.3	Analytical and numerically (energy curve fitting) computed EDIP elastic constants (GPa) and Kleinman's internal strain parameter ζ for the diamond phase. C_{44}^o is the shear modulus when internal relaxation is disallowed. The values published by Justo <i>et al.</i> are provided here for comparison.	139

5.4	Fit slopes to the points in Figs. 5-1– 5-6. Units are per defect fraction, with elastic constants in GPa. “Difference” refers to that between the Frenkel pair result and the sum of the vacancy and interstitial results. The numbers in parentheses are from fits to the data in Clark and Ackland.[27]	144
5.5	Elastic constants (GPa) of EDIP-generated amorphous samples described in the text. Also shown are percent volume change and energy gain per atom with respect to the crystalline values (20.018 \AA^3 atomic volume and -4.6500 eV). Results from experiment (room temperature), tight-binding molecular dynamics (room temperature), and EDIP are shown for comparison. Where published results were not completely consistent with isotropicity, the range of possible derived values is given.	147
5.6	Elastic constants for the crystal, amorphous sample G, and the composite. The Young’s modulus value (E) given for the crystal and the composite sample are the average of the Reuss and Voigt spatial averages.[52] Upper and lower bounds based on Eq. 5.17 are shown for comparison.	149
5.7	Formation energies, volumes, and percent change in elastic constants for a single defect in a 1728-atom supercell, calculated using EDIP. The numbers in parenthesis represent how many of the 90 ‘extra’ atoms randomly inserted into our samples appeared in a particular interstitial type. The number of vacant sites appearing in a particular vacancy complex is also shown in parenthesis, also out of a total of 90.	158
5.8	Coordination and ring statistics changes compared to the percent change in bulk modulus for vacancy defects and the <i>FFCD</i> . Net changes are for isolated defects in a 1728-atom supercell, referred to a similar crystalline supercell. The net change in the number of atoms having a particular coordination is given by N . The numbers under the “rings” heading refer to the net gain or loss of rings of a particular size.	159
5.9	Coordination and ring statistics changes compared to the percent change in bulk modulus for interstitial defects, as in Table 5.8.	160
5.10	Parameters used in the Stillinger-Weber potential. The parameter f is a scaling factor not shown in Equations 5.20 and 5.21 — we have used this factor to multiply both two- and three-body terms in order to obtain a cohesive energy of -4.63 , as described by Balamane <i>et al.</i> [8]	163
5.11	Elastic constants of diamond crystalline silicon in GPa.	163
5.12	Fit slopes to data of Figures 5-14–5-18. Units are GPa per defect fraction. Results from EDIP and Clark and Ackland [27] are provided for comparison.	169
5.13	Formation energies, volumes, and percent change in elastic constants for a single defect in a 1728-atom supercell, calculated using the Stillinger-Weber potential. Energy is in eV, volume in \AA^3 . For comparison, data is reproduced here from Table 5.7 for EDIP and density functional theory calculations from the literature. LDA calculations are designated by (L) and GGA by (G). See Table 5.7 for references.	171

6.1	Estimates of radiation-induced changes in Pyrex, Hoya SD-2, and silicon. A fluence of 1×10^{14} n/cm ² (1 MeV neutrons) and 1 Mrad gamma is assumed.	188
7.1	Results of MIT sink/float measurements.	192
7.2	Summary of TRIM calculations for fast and thermal neutrons.	192
7.3	Estimates of radiation-induced changes in Pyrex, Hoya SD-2, and silicon. A fluence of 1×10^{14} n/cm ² (1 MeV neutrons) and 1 Mrad gamma is assumed. Relative frequency shifts for our hypothetical MEMS silicon resonating beam are shown in parentheses. The frequency shifts for the glass take into account the differential strain relative to that of the silicon in the same column.	197
A.1	Pointerbeam strain gauge readings from Pyrex wafer.	204
A.2	Pointerbeam strain gauge readings from Hoya SD-2 wafer B.	206
A.3	Pointerbeam strain gauge readings from Hoya SD-2 wafer C.	208
B.1	Sink/float temperature data.	211
D.1	Values used for the r_i of Figure D-1.	231
D.2	Experimental values of thermal conductivity κ (W/m-K) and the coefficient of thermal expansion α (K^{-1}).	231
D.3	Scenarios for glass sample heating during the MURR irradiation. The assumed thermal neutron flux (n/cm ² /s) incident on the boron nitride shield and the fraction thereof that is incident on the glass are at left. Air gaps between solid regions of Figure D-1 are given in meters. ΔT represents the amount by which the glass center (r_0) is above T_o ($^{\circ}C$).	234
E.1	Sample activation calculations for isotopes in Hoya SD-2.	240
F.1	Activation of Hoya SD-2 glass. The sample was 1 cm \times 1 cm \times 0.078 cm. The activity (μ Ci) was measured 7 days after a 10 minute irradiation in a thermal neutron flux of about 4×10^{12} n/cm ² /s.	241
F.2	Activation of Hoya SD-2 glass. Fifteen samples were irradiated at the Missouri reactor. Activities are in pCi.	242

Chapter 1

Introduction

1.1 Motivation

What follows concentrates principally on the effects of radiation on the mechanical properties of silicon and two borosilicate glasses, Pyrex[®] and Hoya SD-2[®]. Specifically, we describe the effects of neutron and gamma radiation on the elastic modulus and density of silicon, and on the density of the glasses.

These mechanical properties are important to a common variety of microelectromechanical (MEMS) device, which is composed of a glass substrate wafer bonded to a silicon wafer. The technique for joining the two wafers is known as anodic bonding. After bonding, the silicon is etched to release the structures that are the MEMS devices.

Anodic bonding is accomplished by placing two wafers, one of silicon, and one of glass, in an electric field while maintaining them at an elevated temperature. Alkali ions in the glass are driven away from the interface of the two wafers, creating a

depletion region with a large electric field that presses the two wafers into intimate contact. Silicon atoms can then bond with oxygen atoms at the glass surface, creating a strong bond between the wafers.[35, 86]

After etching the silicon, the MEMS devices are still attached to the glass substrate by "bond pads", structures that suspend the silicon devices above the surface of the substrate. One common suspended silicon structure is a resonating beam, whose natural frequency depends upon such properties as its elastic modulus, its dimensions, its mass, and its state of stress. A change in any of these properties will result in a change in the frequency of the beam oscillations. This change in frequency is the very phenomenon that MEMS devices which use resonating beams are designed to exploit. For example, a chemical sensor may operate by noting the change in beam frequency due to a change in beam mass as material sticks to the surface of the beam. An accelerometer may function by sensing the change in frequency of the beam's oscillations due to stress within the beam that is imposed by acceleration.

In either example, sensor errors would result if radiation damage were to cause a change in the oscillation frequency by altering the mechanical properties of the materials involved. Radiation damage can affect both the elastic constants and the density of silicon and glass. Compaction of the glass substrate, for example, would impose a compressive stress along a resonating beam which was anchored to it. It comes as no surprise that mechanical properties are affected by radiation damage. Until recently, however, the primary interest in the effects of radiation on silicon have been on its electrical properties rather than on its dimensions or elastic properties.

As MEMS devices become ever more sensitive, however, they rely all the more on

the constancy of the mechanical properties of their component materials. In this lies the motivation for the present work. In what follows, we address the problem of radiation damage as it would occur at very low doses, of the type that would accumulate in a space environment over a period of a year. The benchmark environment that we have chosen is comprised of a fluence of 1×10^{14} n/cm² of 1 MeV neutrons and 100 Mrad gamma radiation. Such doses might also be accumulated during shorter times in a reactor environment. At these low doses, recoil collision cascades may be regarded as essentially spatially independent of one another.

In space, it is protons, not neutrons, that are of primary concern. We have, nevertheless, chosen to use neutrons as a reference, since they share a similar mass with protons and have a much longer mean free path in silicon and glass. This allows us to assume a spatially uniform damage distribution, which would not be possible, even on the small scale of MEMS, for protons.

In a reactor environment, thermal neutrons inevitably accompany fast neutrons. For this reason, we also consider the effects of thermal neutrons on Pyrex and Hoya SD-2. Thermal neutrons cause damage in boron-containing materials by means of thermal neutron capture in the form of the (n,α) reaction in ¹⁰B. In a typical reactor environment, the thermal neutron flux will be of the order of, or greater than, the fast neutron flux. For the reactor irradiation experiments that are described in this thesis, the thermal neutron flux ranged from about 7×10^{11} n/cm²/s to 1×10^{14} n/cm²/s.

We have not addressed the issue of how radiation will affect the electrical properties of silicon and glass. The literature on radiation defects in silicon from an electrical property point of view is vast.[79] Changes in the conductivity of silicon will certainly

have significant effects on the operation of a MEMS device. Radiation damage in the glass may lead to local charge buildup at the surface of the glass, which is, in general, in very close proximity (on the order of microns) to the silicon devices. Such charging will be another important consideration in considering the suitability of a particular MEMS device for use in a radiation environment.

1.2 Description of borosilicate glasses

The glasses included in the present study are commonly used for the fabrication of anodically bonded MEMS. Their principal utility is that they possess a coefficient of thermal expansion that closely matches that of silicon over the temperature range of the anodic bonding process. Were this not the case, after cooling to room temperature from the bonding temperature, unacceptably large stresses in the silicon would result. A typical glass wafer thickness is 780 μm .

Figure 1-1 compares the coefficient of thermal expansion of Pyrex and Hoya SD-2 with that of silicon. It can be seen that Hoya SD-2 possesses a coefficient of thermal expansion which more closely follows that of silicon than does Pyrex. The coefficient of thermal expansion of Pyrex, however, does come close to matching the *average* thermal expansion of silicon over the temperature range shown in Figure 1-1. Figure 1-2 shows the integrated strain due to thermal expansion that would accrue with heating from room temperature. For Pyrex, the ideal bonding temperature is shown to be close to 270 °C, since the strain in Pyrex and silicon is identical at that point. Anodic bonding, however, must take place at a higher temperature (350-400 °C). The

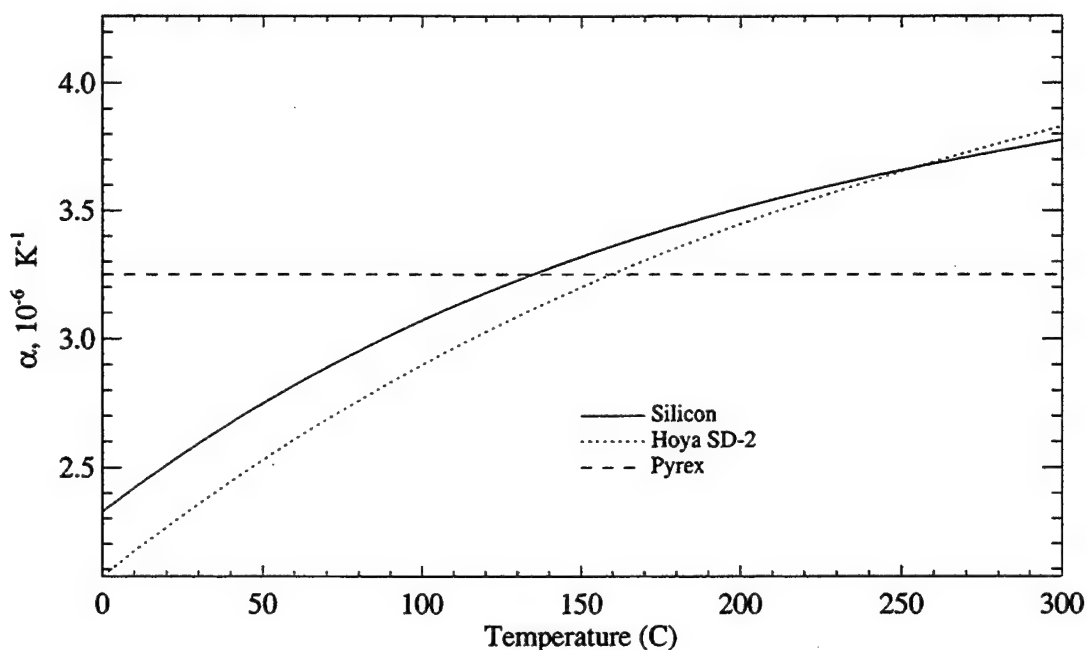


Figure 1-1: Variation with temperature of the linear coefficient of thermal expansion of silicon,[114] Hoya SD-2,[49] and Pyrex.[33]

differential strain with silicon at these higher temperatures is seen to be less for Hoya SD-2 than for Pyrex.

Hoya SD-2, therefore, presents an attractive advantage over Pyrex to MEMS designers. Nothing in the literature describes the effects of radiation on the density of Hoya SD-2, however. The effects of radiation on the density of Pyrex, on the other hand, have been previously studied for both gamma[110, 31, 101, 142] and neutron[96, 95, 97, 98] irradiation. One of the goals of the present work, therefore, is to present results for the effects of radiation on the density of Hoya SD-2 glass, in order to allow MEMS designers to choose between Hoya SD-2 and Pyrex as a substrate for applications involving radiation exposure.

Samples of Pyrex were sent out for examination by X-ray photoelectron spec-

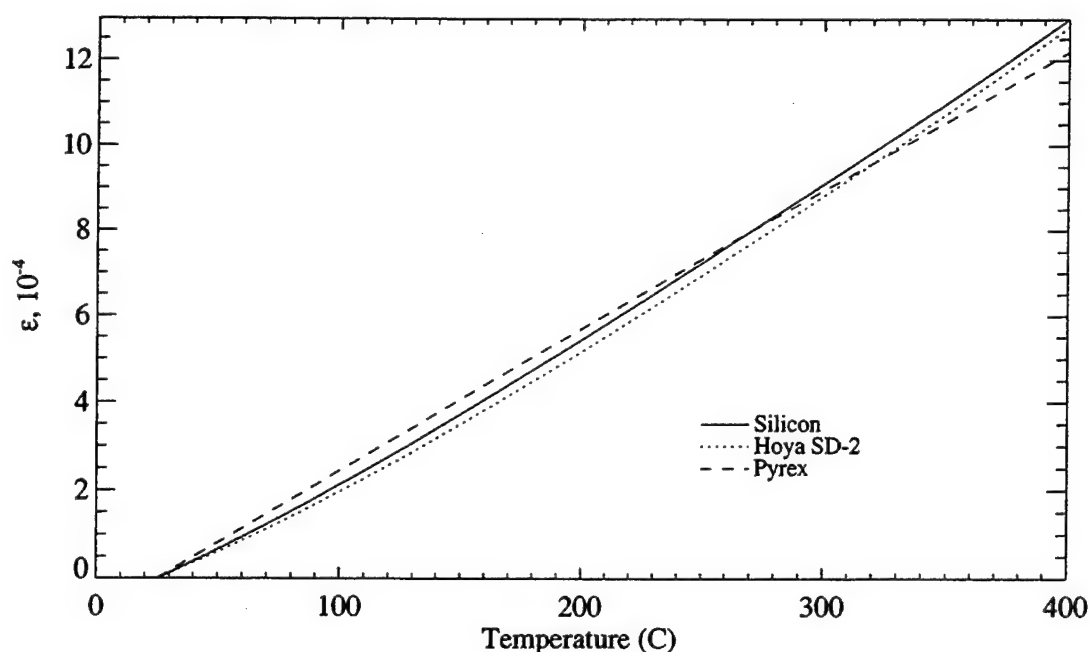


Figure 1-2: Integrated strain due to thermal expansion from 25 C for silicon,[114] Hoya SD-2,[49] and Pyrex.[33]

troscopy (XPS) analysis.[40] Glass wafers were fractured in order to make measurements of the bulk glass at the fracture surface. The fracture surface was ion etched to remove 200 Å from it prior to the measurement. One wafer was of Pyrex fabricated by Corning.[32] The other was of a chemical equivalent of Pyrex produced by Schott.[104] The compositions of the two wafers are displayed in Table 1.1. The density of Pyrex is 2.23 g/cm³.

Two wafers of Hoya SD-2 were examined using XPS as for the Pyrex wafers. The results of these measurements are shown in Table 1.2. It can be seen that the composition variability of Hoya SD-2 is of the same order as that observed between the two Pyrex wafers. Hoya SD-2 contains about a factor of 6 less boron than Pyrex. It also contains about a factor of 11 more aluminum, which is a major component of

Table 1.1: Composition of Pyrex as measured by XPS.

Element	Atom %		
	Borofloat	Pyrex	Mean
C	0.7	1.6	1.2
Na	0.7	1.6	1.2
O	62.8	64.4	63.6
B	6.6	6.2	6.4
Si	27.7	24.9	26.3
Al	1.2	1.0	1.1
K	0.3	0.2	0.3

Table 1.2: Composition of Hoya SD-2 measured by XPS.

Element	Atom %		
	Wafer 1	Wafer 2	Mean
C	0.7	0.5	0.6
Na	0.4	0.6	0.5
O	60.5	61.4	61.0
B	1.2	0.9	1.1
Si	21.6	20.6	21.1
Al	12.5	11.9	12.2
Zn	0.6	0.9	0.8
Mg	2.6	3.3	3.0

this glass. The density of Hoya SD-2 is 2.60 g/cm^3 .

1.3 Summary of experiments and simulations

What follows in this chapter is a synopsis, by way of introduction, of the experiments and calculations that were carried out in the present study. In Chapters 2 and 3, we present a review of the literature relevant to radiation damage in glass and silicon, respectively. In Chapter 4, we describe three experiments in which we subjected glass samples to gamma and neutron irradiation with a view to measuring

radiation-induced compaction. Chapter 5 is an account of our computational work on the modeling of the mechanical properties of defected and amorphous silicon using an empirical interatomic potential. In Chapter 6, we present an application of the findings of the previous chapters (which, taken individually, may appear to have little to do with one another) to the case of a hypothetical resonating beam MEMS device. Chapter 7 contains a summary of our findings and recommendations for future work.

1.3.1 Irradiations

1.3.1.1 Gamma irradiation of pointer beam strain gauges

The compaction of Hoya SD-2 with gamma radiation dose being unknown, we irradiated wafers of Hoya SD-2 and Pyrex (as a control) with gamma radiation at the University of Massachusetts-Lowell. These wafers held silicon MEMS strain gauges that were designed to measure the compaction of the glass. As described in detail in Chapter 4, the strain gauges registered almost no compaction in either glass. This result is particularly surprising for Pyrex, which has been well characterized as compacting with gamma dose. Those previous experiments on Pyrex used the raw glass, whereas we irradiated glass which had been anodically bonded to silicon. It was hypothesized that either 1) anodic bonding had altered the bulk glass radiation response or 2) the anodic bonding depletion layer in the glass and/or interfacial phenomena at the bonding interface were responsible for the null result. This experiment is interesting in that its results raise the possibility that an anodically bonded MEMS device can have a much different response to radiation than might be predicted from

the known response of the individual materials.

1.3.1.2 Neutron irradiation of borosilicate glasses

We conducted two separate neutron irradiations of both of our glasses. After these irradiations, the density change in the glass was measured using the sink/float method described in detail in Chapter 4. The first irradiation was carried out at the MIT reactor. The radiation compaction that we observed in the Pyrex agreed well with previously published results. The compaction of Hoya SD-2 was found to be an order of magnitude less, on a displacement per atom (dpa) basis, than that of Pyrex. In the case of thermal neutrons, the lower boron content of Hoya SD-2 made it even less susceptible than Pyrex to radiation-induced compaction. This is an important result to MEMS designers, for whom the effects of radiation on Hoya SD-2 (a desirable MEMS substrate material) were previously unknown.

The goal of the second round of neutron irradiations was to determine if the anodic bonding process made significant changes in the compaction rate of the bulk glass in response to radiation. The unexplained results of the gamma irradiation experiment suggested this possibility. At the same time, we wished to examine damage caused principally by fast neutrons. To this end, a shield was designed to absorb thermal neutrons, thereby protecting our samples from them. Packaging was designed for the shield in order to dissipate the heat generated within the shielding material by the thermal neutron absorption events. We realized only moderate success in shielding thermal neutrons and dissipating heat. Nevertheless, our results indicate that the anodic bonding process did not make a measurable difference in the response of the

bulk glass density to radiation. The implication of this result is that the anodic bonding interface and glass surface depletion layer are having important effects on the radiation response of bonded MEMS devices.

1.3.2 Elastic constant calculations in defected silicon

At the low radiation doses that are our points of reference, direct measurement of elasticity changes in silicon is not feasible. We therefore turned to the atomistic modeling of defects and their effects on the elasticity of silicon. We used EDIP, an empirical interatomic potential for silicon, to perform these simulations. We prepared 45 simulation cells containing random arrangements of point defects at various concentrations. It was determined that point defects cause Young's modulus to decrease, which was previously unknown. The only previously published result holds that Young's modulus will increase with the presence of point defects. To further support our contradictory claim, we reworked several of our calculations using a second potential (the widely used potential of Stillinger and Weber — "SW").[116] The SW calculations confirmed that defects cause a decrease in Young's modulus. There were some differences between EDIP and SW as to how this reduction occurred, but we explain why these are and why EDIP makes the preferred description of point defects in silicon.

EDIP was also applied to the calculation of the elastic constants of several amorphous silicon simulation cells. These amorphous cells were prepared by quenching from the liquid, and it was determined that the exact details of the cell preparation

process had little effect on the elastic constants of the resulting amorphous silicon. We embedded one of these amorphous cells into a crystalline matrix, and found that our computational models confirmed a published experimental observation that the elastic constants of this composite amorphous/crystalline silicon could be predicted simply by knowing the elastic constants of the two separate phases and their relative volume fraction.

In order to better analyze our results from our randomly generated defected simulation cells, we made an extensive characterization of 17 types of point defects. These point defects either appeared in our randomly generated samples, have been observed by others using different potentials, or have been characterized using *ab initio* methods. This characterization was key to explaining why EDIP was a better choice of interatomic potential than the very popular SW. When working with empirical interatomic potentials, it is important to understand what their strengths and shortcomings are in respect to *ab initio* predictions. The extensive characterization of defect formation energies and volumes, as well as effects of each defect species on the elastic constants, therefore represents a service to the modeling community.

Our calculations involving defected and amorphous silicon simulation cells are described in Chapter 5.

1.3.3 Implications for anodically bonded MEMS

In Chapter 6, we explore what the findings of the glass experiments of Chapter 4 and the computational simulations of Chapter 5 mean for the operation of anodically

bonded MEMS in our assumed radiation environment. We determine that Hoya SD-2 is a better choice of substrate than is Pyrex in terms of resistance to radiation. We also show that, for resonating beam devices bonded at either end to the substrate, the differential silicon-substrate strain that is induced by radiation is of greater importance to device performance than the radiation-induced alteration of the Young's modulus of the resonating silicon beam. The acceptable level of radiation-induced device error will depend on the specifics of the device design and application. For our assumed resonating beam, however, we show that a borosilicate glass substrate is probably inappropriate for high-performance applications in a radiation environment.

Chapter 2

Radiation effects in borosilicate glasses

2.1 Continuous random network model

A glass can be created by quenching from the liquid state. To avoid crystallization, the quenching must be rapid on the time scale of the kinetic processes that arrange atoms into the lowest energy state. For an elemental metal, these processes are quick, and to produce a metallic glass by quenching, a cooling rate $\sim 10^6$ K/s must be achieved. The arrangement topology of an oxide like silica makes greater demands of the crystallization kinetics, and a cooling rate of only $\sim 10^{-4}$ K/s is required for glass formation.

The continuous-random-network model was proposed by Zachariasen.[141] This model describes an oxide glass as being a randomly arranged network of polyhedra, these polyhedra being the basic oxide units of the glass. The continuous random net-

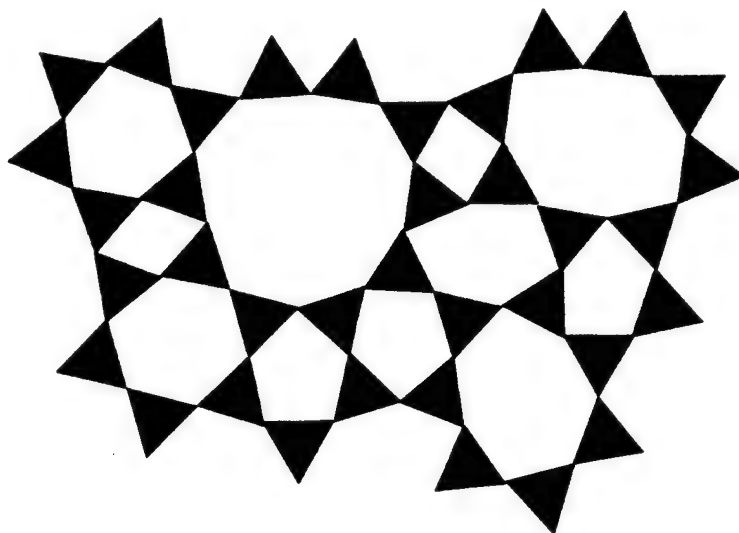


Figure 2-1: Schematic diagram of a two-dimensional continuous random network comprised of interconnected polyhedra.

work and two sample component units are shown in Figures 2-1 and 2-2, respectively.

The connections between polyhedra corners are formed by bridging oxygen atoms. In silica, the Si atoms are fourfold coordinated, whereas the oxygen atoms are only twofold coordinated. As a result, the Si-O-Si bond angles have more flexibility than do the O-Si-O bond angles. This flexibility allows for the formation of polyhedron rings of varied populations. The study of "ring size" is one approach to the characterization of glasses and their response to radiation damage.[54, 55]

When radiation damage processes rupture bonds among tetrahedra, atomic rearrangements with concurrent ring-size changes are among the results. Characterizations in the literature of the relationship between ring size and material density vary. A review of radiation effects in glasses[133] cites topological modeling studies[75] in noting that "larger rings are responsible for the higher density of the denser silica polymorphs because they can fold back on themselves, and the densification of vitreous

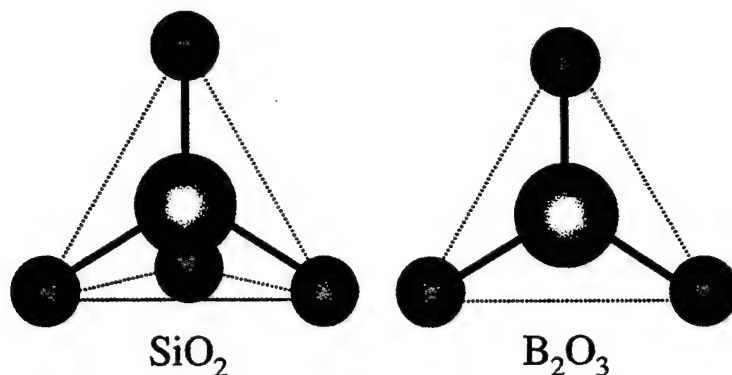


Figure 2-2: Schematic diagram of network components. The basic unit of SiO_2 is the $[\text{SiO}_4]$ tetrahedron, and that of B_2O_3 is the $[\text{BO}_3]$ triangle.

silica by irradiation could arise from opening up of 6-membered rings to larger rings in regional boundaries.” While one might suppose, as some have,[41, 9] that smaller ring result in a denser structure, more recent findings[54] confirm that “whereas it might be supposed that the presence of large rings implies lower density, in fact the opposite is true... As the polymorphs become denser,... the ring size increases and the distribution of ring size widens.” The author goes on to cite the example of crystalline forms of SiO_2 , and indeed finds that average ring size trades monotonically with density.[55]

The physical properties of a silica network can be modified with the addition of alkali atoms. When added to silica, alkali atoms act as “network modifiers.” By providing local charge neutrality for non-bridging oxygen atoms (those atoms not shared by two silica tetrahedra), they allow for the reduction of connectivity in the network.[25] In the case of a borosilicate glass, the addition of alkali atoms can have the opposite effect of increasing the connectivity. When B^{3+} are present, alkali atoms can increase the coordination of the boron atoms by providing local charge neutrality.

Taking sodium as an example, the Na^{1+} combined with the B^{3+} effectively substitute for a fourfold coordinated Si^{4+} . Boron then exists in the basic unit of $[\text{BO}_4]$ tetrahedra, with the sodium ion residing nearby.[25]

Physical properties that change with the addition of alkali atoms to a borosilicate glass include increased fracture toughness[82] and lowered thermal expansivity[39]. With increasing alkali content (as the B/Na ratio falls below one), connectivity is no longer increased and Na^{1+} returns to its role as a network modifier. One can therefore expect the radiation response of a borosilicate glass to depend not only on the concentration of boron, but also on the ratio of this concentration to that of alkali atoms. This special effect of alkali concentration also applies to aluminosilicate glasses, where Al^{3+} can combine with Na^{1+} to substitute for silicon in an $[\text{SiO}_4]$ tetrahedron.[25]

2.2 Damage mechanisms

2.2.1 Fast neutrons

A fast neutron, in the context of this thesis, is taken to be an uncharged nucleon of atomic mass number 1 with a kinetic energy of about 1 MeV. This assumption is made for convenience, since fast neutron dose is commonly cited in terms of the “1 MeV” neutron equivalent fluence. For energies up to 1 MeV, the cross section for kinetic energy transferred (T) to the nucleus by a neutron of energy E_1 can be approximated by[71]

$$\sigma(T, E_1) = \frac{B}{T_m} \quad , \quad (2.1)$$

where B is a constant and

$$0 \leq T \leq T_m \quad , \quad (2.2)$$

with

$$T_m = \frac{4M_1M_2}{(M_1 + M_2)^2} E_1 = \frac{4A}{(1 + A)^2} E_1 \quad . \quad (2.3)$$

In Equation 2.3, T_m is the maximum possible transferred kinetic energy, M_1 and M_2 are the neutron and target mass, respectively, and A is the target atomic mass number. Equation 2.3 is simply the result for a "billiard-ball" elastic collision for a target at rest. Equation 2.1 says that all possible values for transferred energy are equally likely. Equivalently, the scattering in the center-of-mass frame is isotropic. This approximation breaks down at neutron energies substantially higher than 1 MeV.

Neutron collisions with nuclei can result in atoms (primary knock-on atoms, or PKAs) being displaced from their initial positions and then, as energetic ions, colliding with other nuclei and causing further atomic displacements and electronic excitations in the material. This sequence of primary, secondary, and higher-order collisions is called a "collision cascade." Figure 2-3 schematically illustrates a collision cascade resulting from a 1 MeV neutron striking an oxygen atom in Pyrex. The primary knock-on oxygen atom strikes another oxygen, dislodging it from its site, then both atoms continue on through the material, displacing more atoms of various species.

Unlike the incident neutron, the recoil nuclei, being charged, will lose energy to

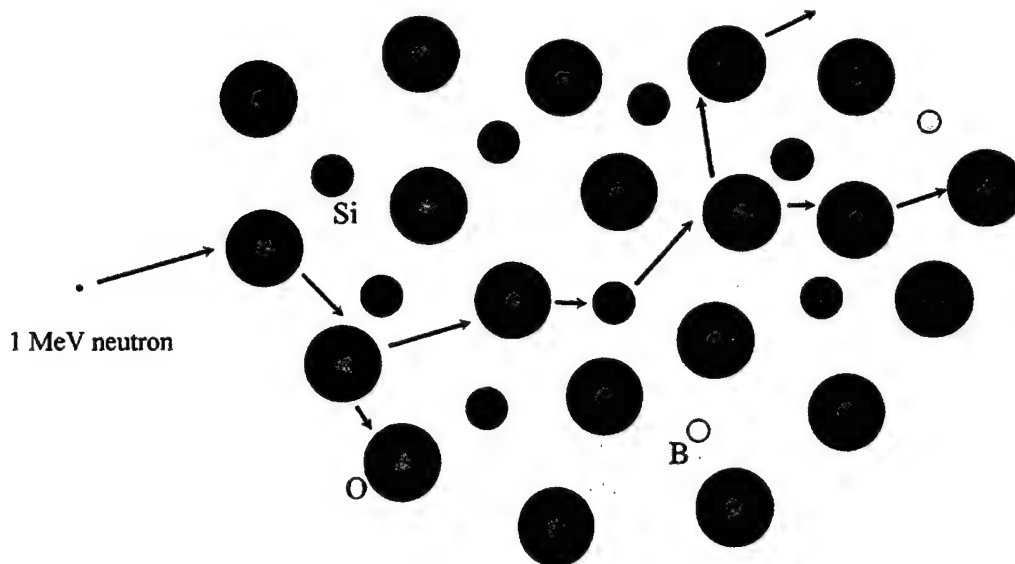
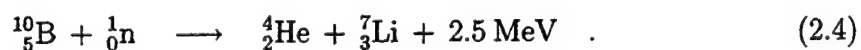


Figure 2-3: Schematic representation of a fast neutron collision cascade in borosilicate glass.

electronic interactions.

2.2.2 Thermal neutrons

Thermal neutrons are those having a Maxwellian energy distribution with a most probable energy of $kT \sim 0.025$ eV. This energy is far below the tens of eV needed to displace an atom from its lattice or network site. We must consider, however, the products of thermal neutron capture reactions. The boron atoms in a borosilicate glass are particularly prone to the absorption of thermal neutrons. The reaction of concern is



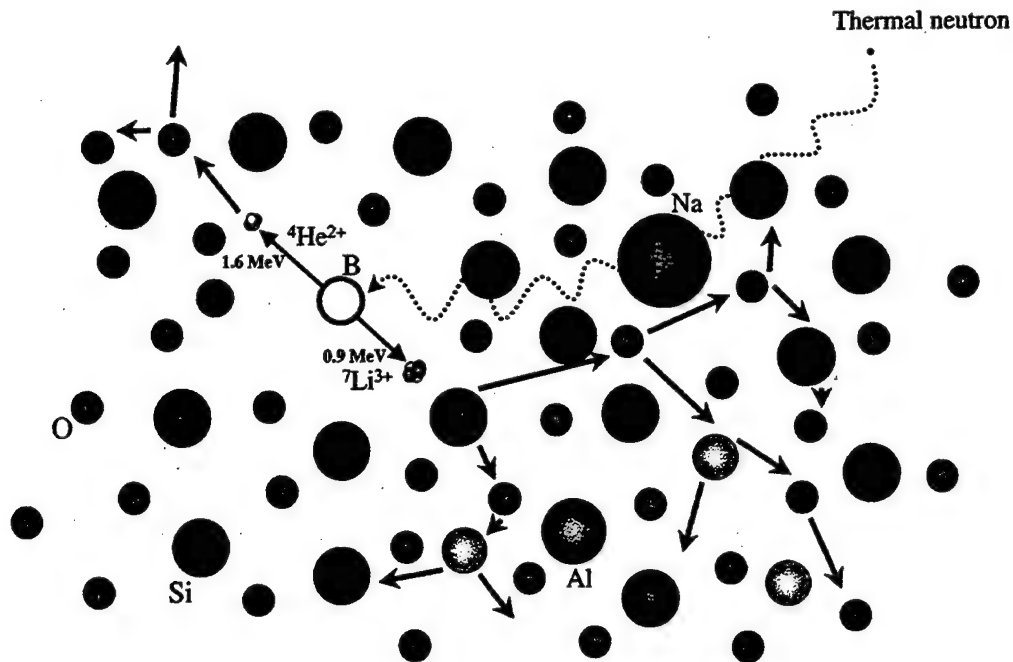


Figure 2-4: Schematic diagram of a thermal neutron capture and (n,α) reaction in borosilicate glass.

The 2.5 MeV energy released in this reaction is apportioned between He and Li recoil ions according to their masses:

$$E_{\text{He}} = \frac{(2.5 \text{ MeV})M_{\text{Li}}}{M_{\text{He}} + M_{\text{Li}}} = 1.59 \text{ MeV}$$

$$E_{\text{Li}} = \frac{(2.5 \text{ MeV})M_{\text{He}}}{M_{\text{He}} + M_{\text{Li}}} = 0.91 \text{ MeV} \quad .$$

Both energetic recoil ions will initiate a collision cascade. A schematic depiction of this is shown in Figure 2-4.

2.2.3 Gamma rays

Gamma rays incident on an oxide glass have two principal means of creating radiation damage. The first is Compton scattering of electrons. Electrons so scattered can then ballistically collide, elastically and inelastically, with atoms in the material. Like all energetic charged particles, the scattered electrons can also leave a trail of electronic excitations in their wake.

The second way in which gamma rays can create radiation damage is more direct — the creation of electronic excitations that lead to bond rearrangements and even atomic displacements. This process is known as radiolysis.[133]

2.3 Previous experiments

2.3.1 Silica

Vitreous silica, as the simplest silicate glass, has been the subject of much early work on radiation damage.[99, 100, 53, 110] Figure 2-5 shows the results of a study by Primak[99] of the densification of silica with fast neutron irradiation. It can be seen that the compaction of vitreous silica attains a maximum, then recovers somewhat as it reaches saturation.

For pure vitreous silica, thermal neutrons have no effect, since neither silicon nor oxygen have a thermal neutron absorption reaction. Gamma rays also cause vitreous silica to compact, as shown in Figure 2-6.

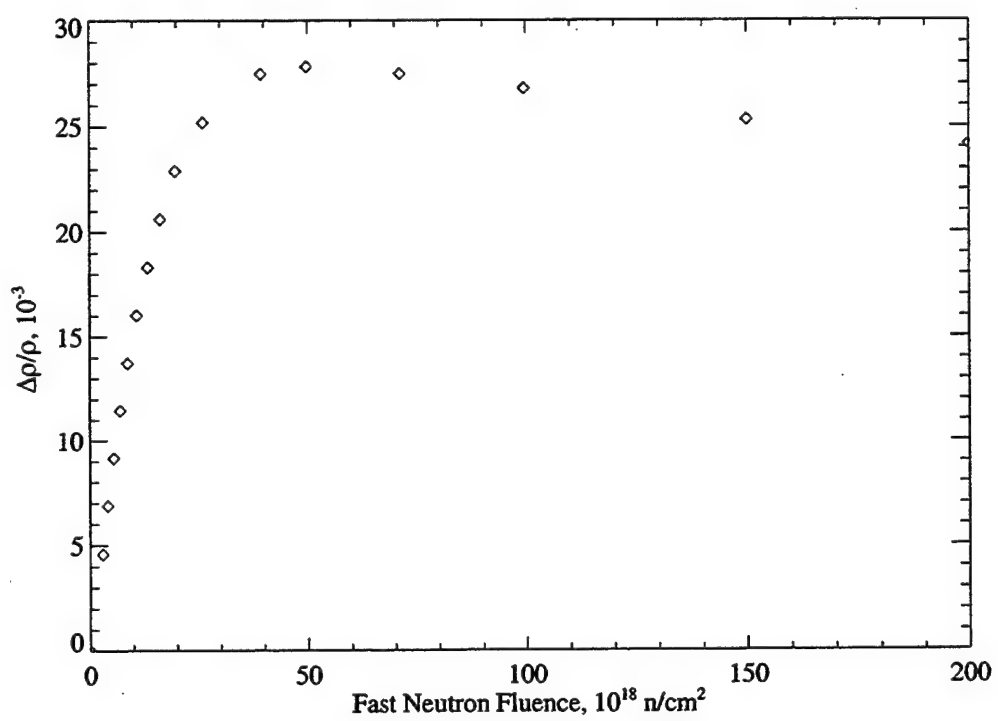


Figure 2-5: Effect of fast neutron irradiation on density of vitreous silica.[99]

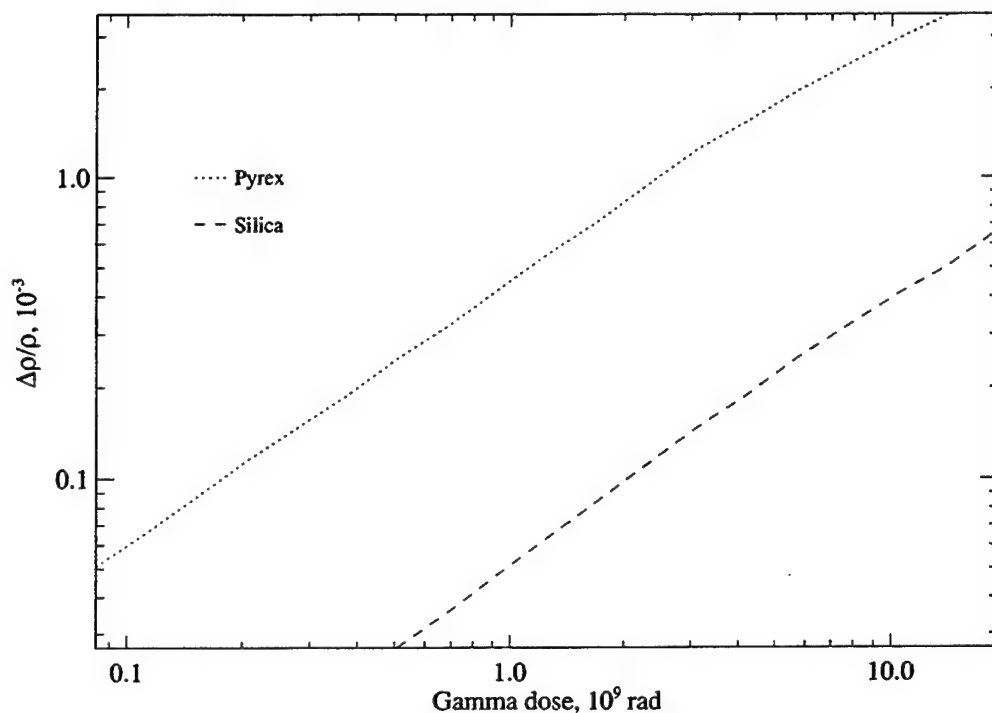


Figure 2-6: Effect of gamma irradiation on density of vitreous silica and Pyrex.[110]

2.3.2 Borosilicate glasses

2.3.2.1 Dimensional changes

Shelby,[110] Connors,[31] Sato,[101] and Zdaniewsky *et al.* [142] have all studied gamma radiation-induced density changes in Pyrex. Figure 2-6 shows a comparison of the compaction with gamma dose of Pyrex with that of vitreous silica. It can be seen that the compaction of Pyrex is about an order of magnitude greater than that of vitreous silica. Shelby's study compared the compaction of several other borosilicate glasses to that of vitreous silica. He concluded that, with increased boron content, increased compaction occurred.

A comparison of the results of Shelby, [110] Connors,[31] Sato,[101] and Zdaniewsky

et al. [142] in Pyrex is shown in Figure 2-7 and (with greater detail at the lower doses) in Figure 2-8. Good agreement is observed among the results of Shelby, Connors, and Sato (although this latter achieved only modest precision in the data). The results of Zdaniewsky *et al.* are in stark disagreement with the three other studies. Since little detail on possible causes of error and uncertainty is furnished by the authors of that study, these data shall be ignored.

It should be noted that the slope of compaction vs. gamma dose (on a log-log plot) for silica varies by as much as a factor of three among studies by Shelby,[110] Higby *et al.*,[53] and Primak.[100] Higby *et al.* attribute this variation to minor differences in impurities or in the degree of phase separation (into alkali-rich and alkali-poor phases). It is not surprising, given these differences in silica results, to see the relatively minor variations in the behavior of different samples of Pyrex shown in Figures 2-7 and 2-8. The difference of 29 % in strain between the results of Shelby and Connors at high doses may be due to differences in glass compositions and/or processing history that may have existed between glass samples.

Paymal[96, 95, 97, 98] carried out an extensive study on the effects of thermal neutron damage on the properties of borosilicate glass. He proposed a theory for his neutron damage observations in which the energy deposited by fast lithium and helium ions in a glass is mostly concentrated in a small end-of-trajectory region, causing a thermal spike. The high-temperature melt is rapidly cooled by the glass matrix, "freezing in" an expanded region. The glass immediately around this expanded region is forced to compact. The relative volume of these expanded/compacted regions would determine the macroscopic density change. His model of competing and inter-

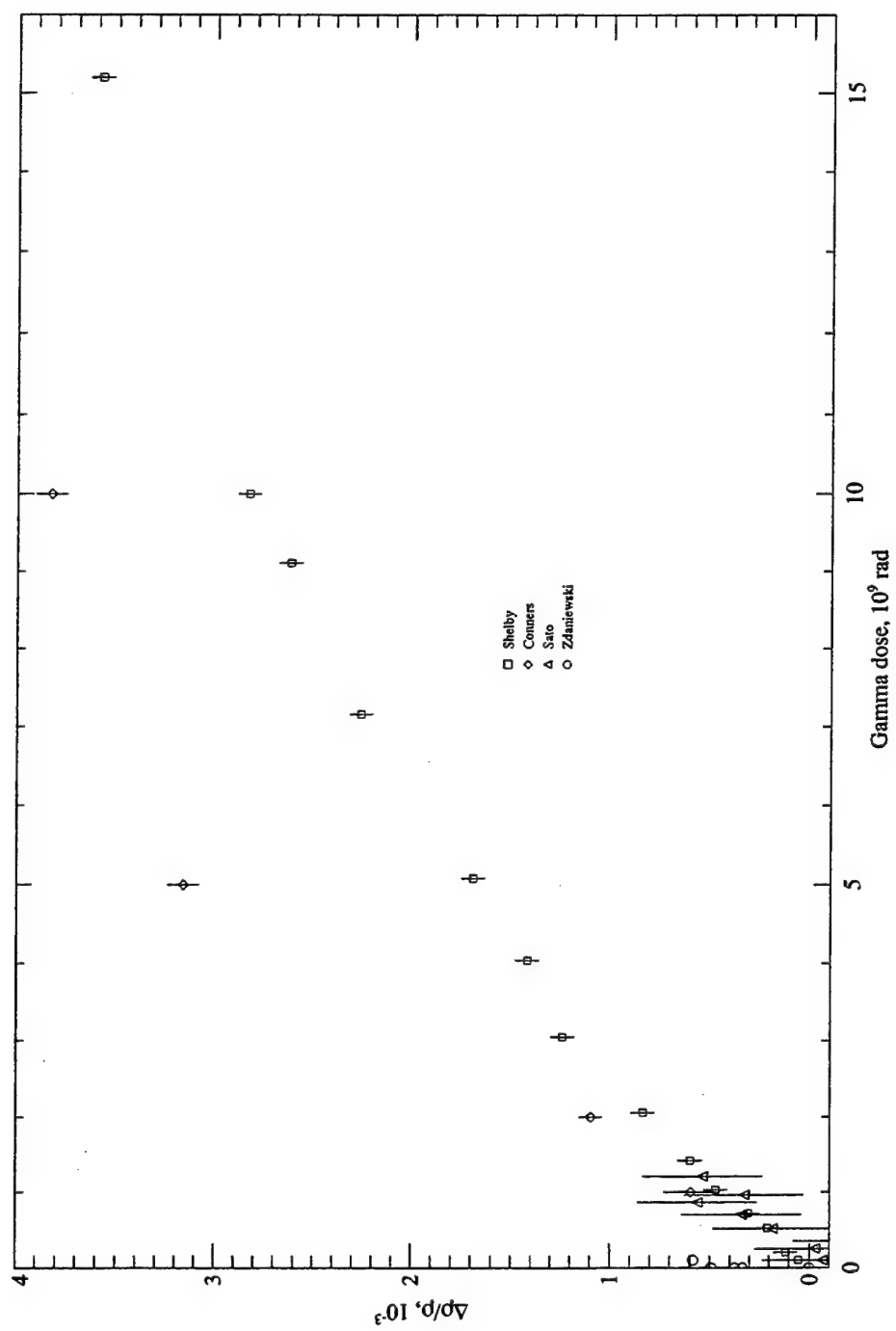


Figure 2-7: Relative radiation-induced density change in Pyrex with gamma dose from several previous studies.

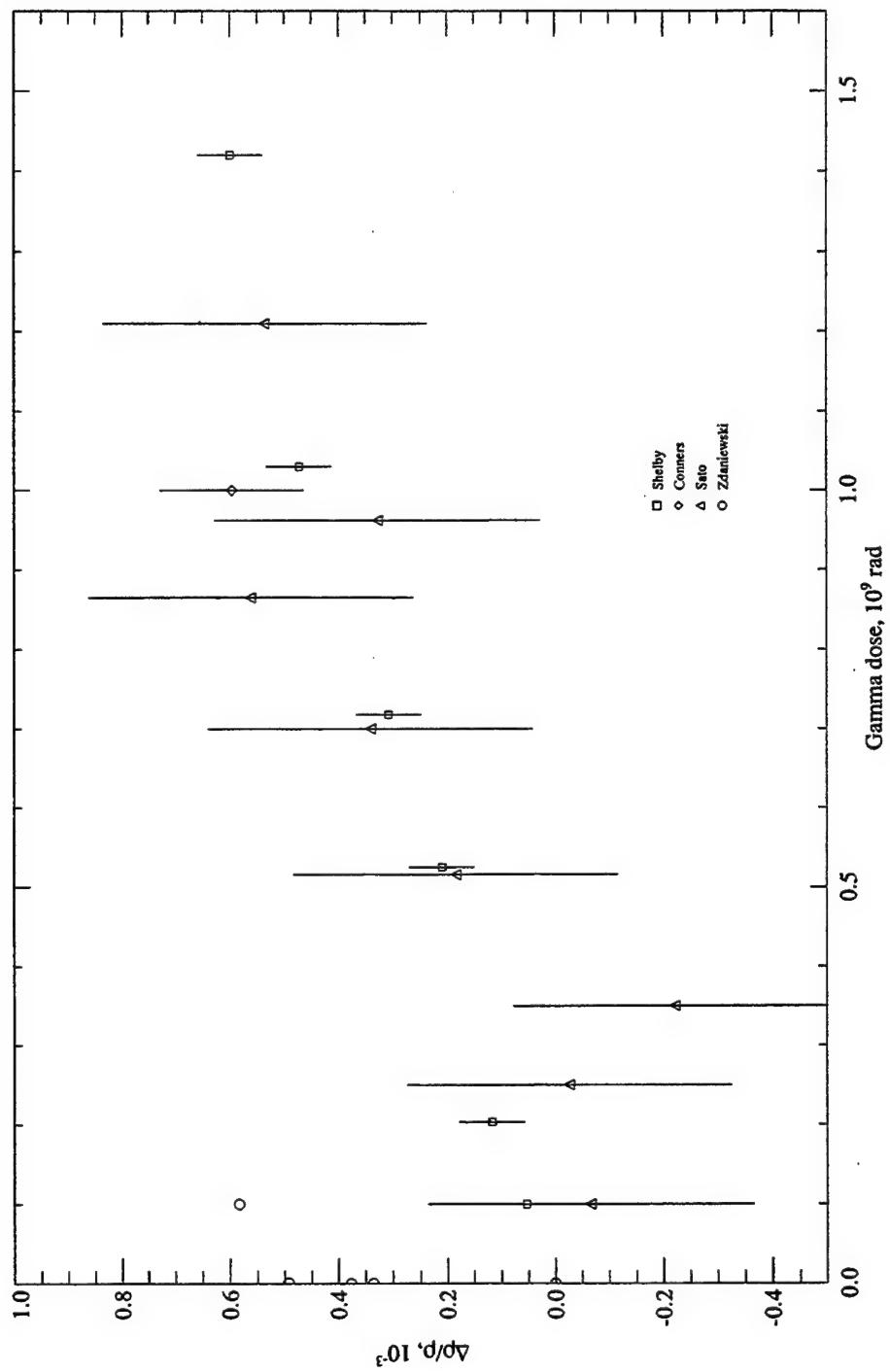


Figure 2-8: Relative radiation-induced density change in Pyrex with low gamma dose from several previous studies.

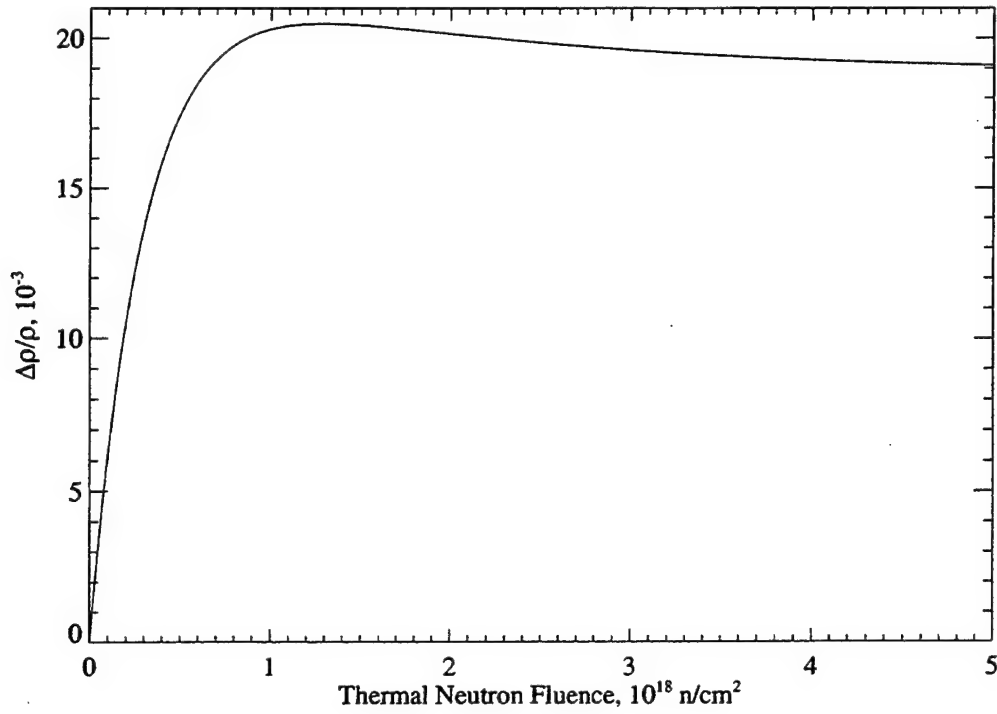


Figure 2-9: Effects of thermal neutron irradiation on density of Pyrex.[95]

dependent regions of compaction and swelling, was fitted to his data for compaction in Pyrex. The resulting empirical relationship is

$$\Delta\rho = 420 - 510e^{-3.28 \times 10^{-18} D} + 90e^{-0.55 \times 10^{-18} D} \quad , \quad (2.5)$$

where ρ is 10^{-4} g/cm^3 and D is n/cm^2 . Equation 2.5 provides a very close fit to the data collected by Paymal. This relationship is shown in Figure 2-9. By comparing the curve for Pyrex in Figure 2-9 with the data in Figure 2-5 for vitreous silica, one can observe that the shape of the densification profile with dose is very similar for both glasses. So, even though Pyrex is known to be more susceptible than vitreous silica

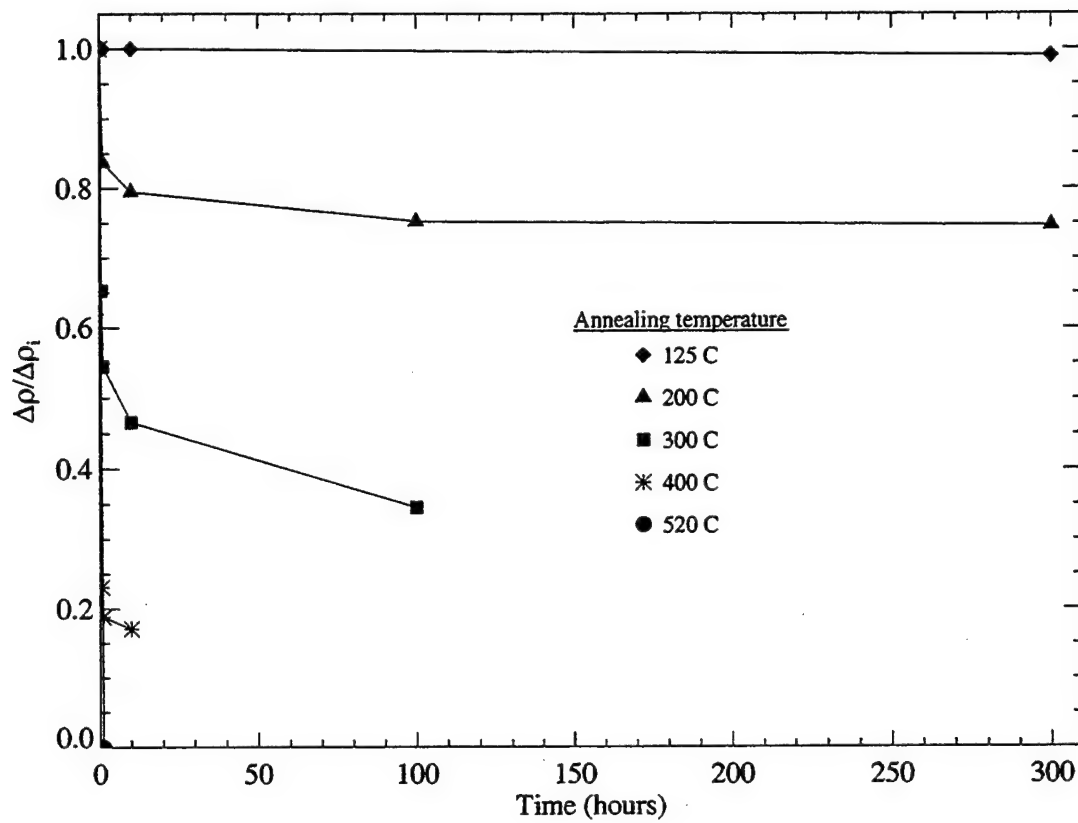


Figure 2-10: Isothermal annealing of thermal neutron-induced densification in Pyrex.[95] The residual radiation-induced compaction is expressed as a fraction of that prior to annealing.

to damage, it is likely that the underlying mechanisms for damage accommodation are the same.

2.3.2.2 Annealing behavior

Elevated temperatures can remove the damage induced by irradiation. Paymal made a study of the annealing behavior of Pyrex that had been irradiated with a thermal neutron fluence of $2.8 \times 10^{17} \text{ n/cm}^2$. [95] He irradiated five samples which were then isothermally annealed. His results are shown in Figure 2-10.

It is interesting to note that the annealing does not simply follow an exponential relation with time and an Arrhenius relation with temperature. If that were the case, above some threshold temperature, all of the irradiation damage could be annealed away, given enough time. The data suggest, however, that at each temperature, only a certain amount of the damage anneals out. Within one hour, almost all of the annealing that can take place at a given temperature has taken place. In fact, for the two samples (at 300 and 400 C) which were measured at the half-hour point, the majority of the annealing has already occurred. It is seen that annealing of the radiation-induced density changes in the glass begins at around 150 C. At 500 C, all of the density change is very quickly gone.

Conners[31] performed isochronal anneals at various temperatures upon Pyrex samples that had been irradiated with gamma to 5×10^9 rad (5×10^7 Gy). Eleven irradiated samples were held at different temperatures for 20 minutes. Her results are presented in Figure 2-11. Interpretation of the data is complicated by the relative imprecision of her density measurements, and also by the fact that, unlike Paymal, she did not measure the pre-anneal density of the irradiated samples. The variation in initial density (pre-irradiation and/or pre-anneal) among her samples was apparently significant. Nevertheless, Conner's data seem to support the assertion that the annealing of radiation damage begins close to 150 C.

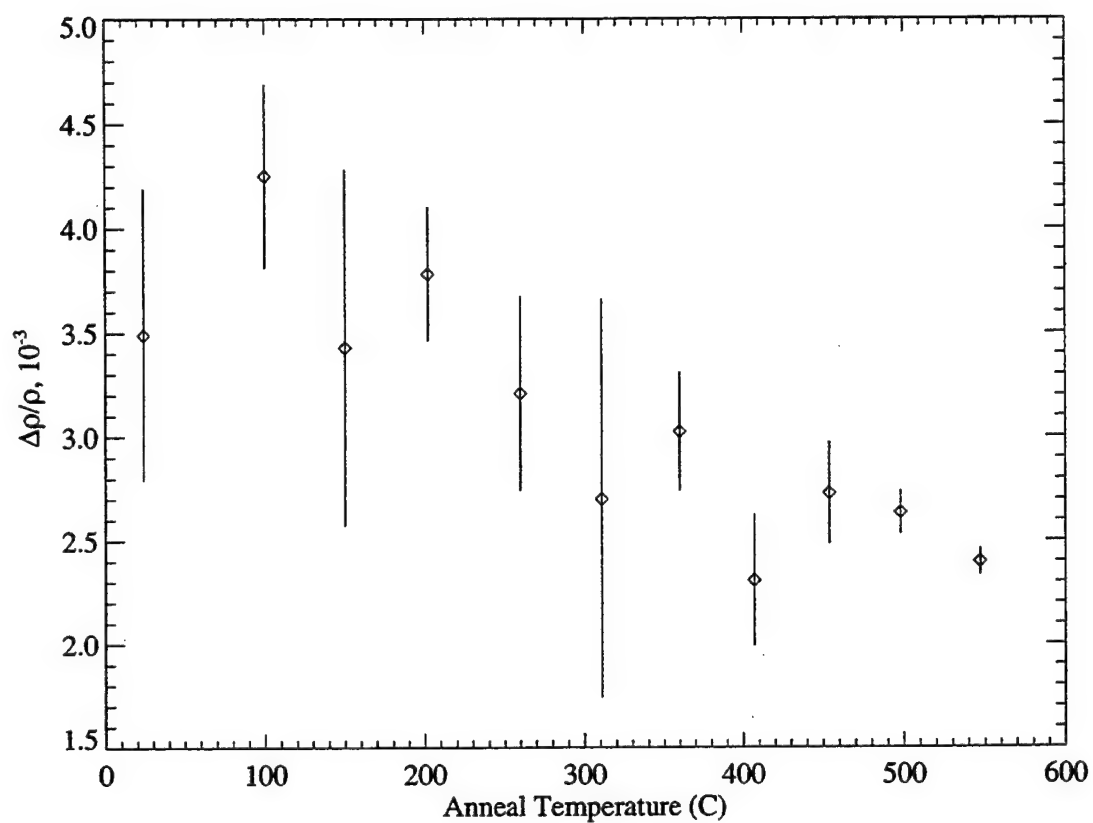


Figure 2-11: Isochronal annealing of Pyrex densification from gamma irradiation.[31]
Densification of the Pyrex is shown relative to the unirradiated glass density ρ .

Chapter 3

Radiation-induced defects in silicon

3.1 Damage mechanisms

3.1.1 Neutrons and gamma radiation

Fast neutrons are the primary cause of radiation damage in silicon for our benchmark radiation environment. A 1 MeV neutron can create primary knock-on atoms (PKA) in Si with a maximum energy of 133 keV, based on the masses of the neutron and the silicon atom, as well as the neutron energy. Approximating the probabilities of all possible recoil energies as equal for this neutron energy yields an average Si PKA of 66.5 keV. Using SRIM2000,[144] an industry-standard ion implantation code, the total number of displacements in a cascade with a 66.5 keV PKA is found to be 973 (SRIM uses a displacement energy of 15 eV for Si). SRIM assumes an amorphous atomic structure, so effects such as channelling are not accounted for.

Where boron doping is present (as in the case of MEMS devices), thermal neu-

trons are a concern due to the n,α reaction. SRIM calculations predict that atomic displacements caused by the energetic He and Li ions leaving the site of a boron thermal neutron capture would total 788. The cascade size is therefore of the same order as that of the fast neutron Si PKA. Thermal neutrons have a longer mean free path in even the most heavily boron-doped silicon (~ 8 cm in 0.33 % B-doped Si) than that of a 1 MeV neutron (~ 4.4 cm), so a given fluence of thermal neutrons will cause less damage than the same fluence of 1 MeV neutrons. Furthermore, our benchmark radiation environment contains only a small thermal neutron component. Compton electrons scattered by gamma rays are not expected to cause much in the way of displacement damage in the material.[84] I will therefore limit the discussion of radiation damage in silicon to that caused by fast neutrons, or, equivalently, that caused by Si recoils.

3.1.2 Point defects and amorphization

Silicon is known to amorphize under ion implantation.[120] How and whether silicon amorphizes with radiation damage depends on temperature as well as on the incident ion flux, mass, and energy. Recent molecular dynamics (MD) simulations suggest that silicon amorphizes through the growth of amorphous zones.[87] In these simulations, growth centers are either directly created as tiny, separated amorphous zones within a subcascade, or nucleate in regions of high defect concentration that are created by the overlap of cascades. The former is considered the most likely, but still requires subsequent cascades in a damaged region in order to cause the amorphous zones to grow.

An MD simulation of a 10 keV recoil in silicon resulted in amorphous zones containing as many as 80 defects, but found the average defect cluster to contain around 15 defects.[91] We should mention that in the aforementioned study, defect content was determined by Wigner-Seitz analysis with respect to crystalline lattice sites. Methods based on topological techniques are more robust for determining defects in cascade damaged regions, where the crystalline lattice can be greatly distorted.[140] Amorphous clusters are expected to recrystallize to some extent around 300 K.[93, 23] The same large surface-to-volume ratio for liquid-like disordered zones that contributes to rapid quenching and the creation of an amorphous zone also contributes to rapid (relative to planar amorphous/crystalline interfaces) recrystallization.[121] Irradiation with electrons during ion bombardment has been shown to prevent the formation of amorphous pockets in silicon,[2] as well as to produce recrystallization in existing amorphous regions.[45] Current models explain this as happening by a bond-breaking model, and do not require thermal activation.[45]

The number of isolated defects compared to the total number of displaced atoms in a cascade is expected to be small.[91, 121] Defects created away from the disordered regions are found to be mostly interstitials.[91] How these point defects interact or how long they take to anneal out is hard to predict: "a number of key parameters such as the diffusivities and thermal equilibrium concentrations of vacancies and self-interstitials, as well as their formation volumes, are far from well established." [123] Indeed, migration energies are reported in a recent survey to be anywhere from 0.45 to 2.8 eV for vacancies, and 0.4 to 4.5 eV for interstitials.[131] Tight-binding atomistic simulations have predicted that an interstitial and a vacancy close to one an-

other can form a metastable complex with a lifetime up to several hours at room temperature.[123] Diffuse scattering experiments have given evidence that Frenkel pairs in silicon separated by 1 nm have a recombination barrier, and may migrate away from each other.[91, 146]

Neutron irradiations have been observed to produce amorphous regions in silicon at 300 K.[24] Another experiment indicates that at 325 K, silicon exposed to fission neutron fluences of up to 5×10^{20} n/cm² does not contain amorphous zones.[119] Defected regions are present, as evidenced by contrast in TEM images generated by strain fields. It may be possible that small amorphous zones were annealed out by the probing electron beam!

3.2 Prior study of silicon

3.2.1 Dimensional changes

Pure silicon has been shown to undergo very small dimensional changes when irradiated. Wittels [134] studied the effect of fast neutrons on germanium and silicon. He found that silicon underwent a 0.017 % expansion in lattice parameter after being irradiated with 4×10^{20} n/cm². Wittels' samples almost certainly experienced significant annealing of damage during irradiation, since an estimate of displacements per atom (dpa) at that fluence of 1 MeV neutrons in a thin silicon sample yields a value of almost 2. Elevated temperatures (though Wittels estimates the temperature during irradiation to be 40 °C) and a low dose rate are likely to have contributed to

the annealing of damage, since this fluence would otherwise amorphize the silicon. Amorphization clearly did not occur, since Wittels made lattice parameter measurements. Wittels' result is therefore not a good candidate for use in an extrapolation to low neutron doses.

Vook [130] subjected silicon to bombardment by 2 MeV electrons. He found no significant lattice expansion or contraction, reporting a relative length expansion of $(4 \pm 19) \times 10^{-26}$ per 2 MeV electron per cm^2 (the uncertainty he reported was greater than the measurement). Moyer and Buschert [84] measured a relative length expansion in pure silicon of 1×10^{-7} after a bombardment of 3×10^{18} 1 MeV electrons per cm^2 . The authors found that dopants helped to stabilize the defects introduced by the electron irradiation, as evidenced by larger lattice parameter changes for doped silicon samples.

3.2.2 Elastic effects

Most of the literature on measurements of the elastic constants of radiation-damaged silicon has concentrated on surface layers, either sputtered or those that have been completely amorphized by ion implantation.[135, 143, 122, 120] One exception is the study by Burnett and Briggs[20] of the effect of ion implantation on the elastic properties of silicon. They irradiated silicon with 180 keV silicon and arsenic ions and used surface acoustic wave spectrometry to measure the change in the implantanted silicon samples' elastic constants. Some of their findings are summarized in Table 3.1.

Table 3.1: Elastic constants of a silicon layer expressed as a percentage of the crystalline value.[20] Displacements per atom (dpa) were calculated using TRIM.[144]

Implanted Ion	Fluence, n/cm ²	C_{11}, C_{44}	Layer thickness, μm	dpa
As	1×10^{14}	92.5	0.011	0.20
As	2×10^{14}	76.6	0.017	0.46
Si	1×10^{14}	97.4	0.024	0.07
Si	2×10^{14}	94.9	0.024	0.14
Si	1×10^{15}	74.0	0.024	0.68

It has been estimated that the crystalline-to-amorphous transition for ion-implanted silicon occurs at a defect concentration of $\sim 7-8\%$.[29] In terms of atomic displacements, the fraction needed to cause amorphization has been estimated as $\sim 15\%$ at room temperature.[26] Judging from the dpa values and the saturation state of $\sim 75\%$ for the elastic constants of Table 3.1, it would appear that amorphization is occurring somewhere around 0.2–0.4 dpa (as calculated by TRIM). In any case, we note that the measurements of Table 3.1 were made of the elastic constants of silicon samples that were either on the brink of amorphization or completely amorphized, with the possible exception of one silicon sample at 0.07 dpa.

3.3 Silicon experiments

3.3.1 Irradiation of silicon samples

Silicon samples were prepared for irradiation at the MIT reactor. Samples for the elastic modulus study were irradiated according to the schedule of Table 3.2. The samples were cut from a $380\ \mu\text{m}$ thick wafer which was uniformly doped with boron

Table 3.2: Irradiation schedule of silicon samples destined for the elastic modulus study. Displacements per atom (dpa) were calculated using TRIM.[144]

Sample	Fast fluence, n/cm ²	Thermal fluence, n/cm ²	dpa (10 ⁻⁶)
A1	1.20×10^{14}	8.00×10^{15}	1
A2	1.65×10^{16}	4.13×10^{16}	83
B2	3.31×10^{16}	8.26×10^{16}	165
C2	6.61×10^{16}	1.65×10^{17}	330
D2	1.32×10^{17}	3.30×10^{17}	660
E2	2.65×10^{17}	6.61×10^{17}	1321

Table 3.3: Irradiation schedule of silicon samples for XRD lattice parameter measurement. Displacements per atom (dpa) were calculated using TRIM.[144]

Sample	Fast fluence, n/cm ²	Thermal fluence, n/cm ²	dpa (10 ⁻⁶)
X1	3.00×10^{12}	2.00×10^{14}	0.5
X2	3.00×10^{13}	2.00×10^{15}	4.6
X3	1.50×10^{13}	1.00×10^{16}	22.9
X4	3.60×10^{14}	2.40×10^{16}	55.1
X5	7.20×10^{14}	4.80×10^{16}	110
X6	1.44×10^{15}	9.60×10^{16}	220
X7	2.88×10^{15}	1.92×10^{17}	440

at a concentration of 100 parts per million (ppm).

Another set of silicon samples (for use in lattice parameter measurements) was irradiated according to the schedule of Table 3.3. These samples were cut from a wafer with a thickness of 435 μm , comprised of a 55 μm epitaxially grown layer on a 380 μm substrate. The substrate was lightly doped (< 1 ppm) with boron, but the epitaxially grown layer was doped with boron to a concentration of 3300 ppm.

3.3.2 X-ray diffraction measurements

Dr. Meri Treska of MIT/Department of Materials Science and Engineering, made measurements of the lattice parameter change in the epitaxially grown layer due to irradiation. Her results are displayed in Figure 3-1. Due to the difference in boron doping between the substrate and the epitaxially grown layer, the expected lattice parameter change in the substrate is negligible at each irradiation dose (the estimated dpa in the substrate is $\sim 1/30$ th of that in the epi-layer).

The bilayer nature of the irradiated sample complicates the interpretation of the lattice parameter measurements. Firstly, the substrate, which will not undergo significant dimensional change, will constrain the lattice parameter change of the epi-layer. Secondly, there are preexisting stresses present in the wafer due to the different doping concentration of the two layers. The irradiation may serve to help relieve some of these stresses at the interface between the layers, even as it causes dimensional change in the epi-layer. This experiment is very useful, however, in terms of predicting dimensional change in silicon as used in MEMS, since MEMS devices are often fabricated from just such a bilayer arrangement.

Examining Figure 3-1, it would appear that in the range of 1–100 ppm dpa, the trend of the expansion of the silicon with dose is undergoing a transition. When performing extrapolations to the very low radiation doses of interest to this thesis, we will therefore only rely on the lowest-dose point.

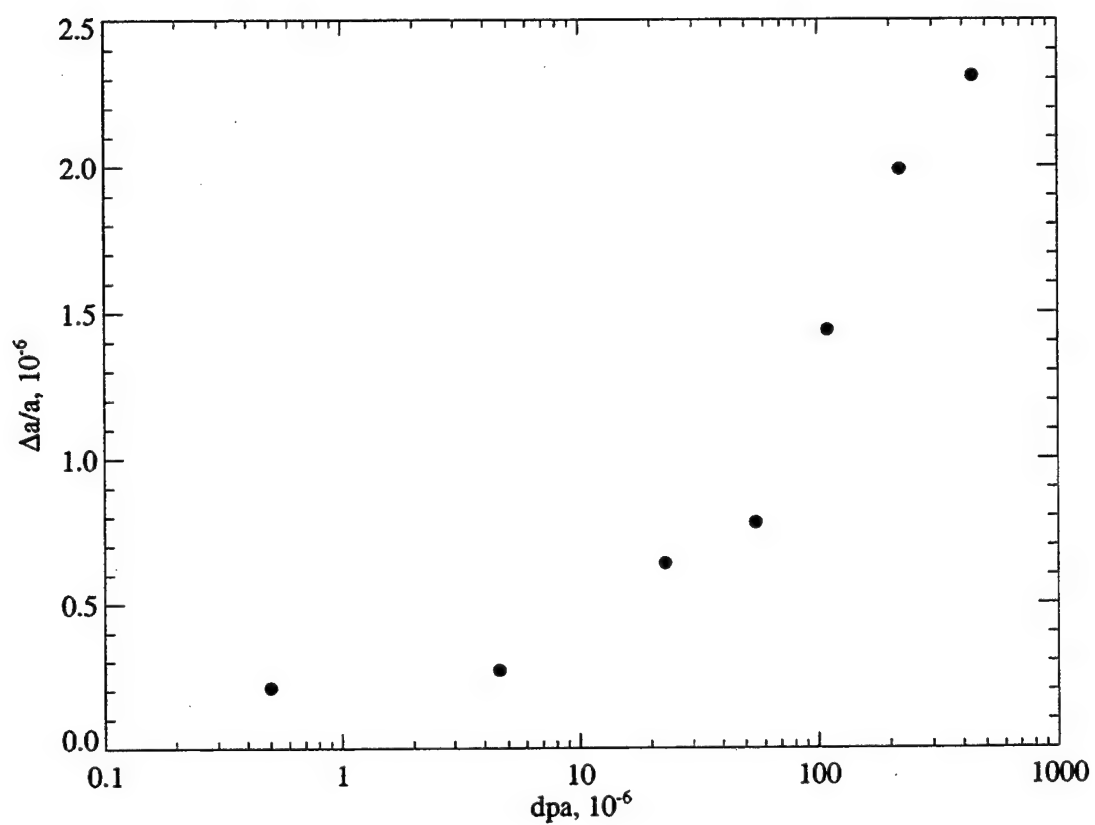


Figure 3-1: Triple crystal XRD measurements of lattice parameter changes in neutron-irradiated silicon.[127]

3.3.3 Acoustic microscopy measurements

The velocity of surface acoustic waves in the irradiated silicon samples were measured at Oxford University by G.A.D. Briggs and colleagues. The method used was surface acoustic wave microscopy.[19] With this method, the velocity of the surface acoustic wave is an indicator of the stiffness of the medium in which it propagates. For an isotropic material, the relationship can be expressed as:

$$v_R = C \sqrt{\frac{E}{2(1 + \nu)\rho}} \quad , \quad (3.1)$$

where v_R is the Rayleigh wave velocity, E is Young's modulus, ν is the Poisson ratio, C is a constant, and ρ is the density.[81] In general, however, deducing the elastic constants from the surface acoustic wave velocity is considerably more involved, and requires foreknowledge of the density.[70, 30] For our purposes here, it suffices to note that as the elastic constants of a material decrease (the expected result of irradiation), so also does the velocity of the surface acoustic wave. The results of the Oxford measurements appear in Figure 3-2.

The results are not what was expected in that there is no clear trend with irradiation dose for the surface acoustic wave velocity. This may be the result of some unforeseen damage to the samples, such as inhomogeneities of the surface in the samples due to treatment at the reactor. Or the results may simply be due to the complex phenomena that are contributing to the transition in the trend of swelling with neutron dose in Figure 3-1.

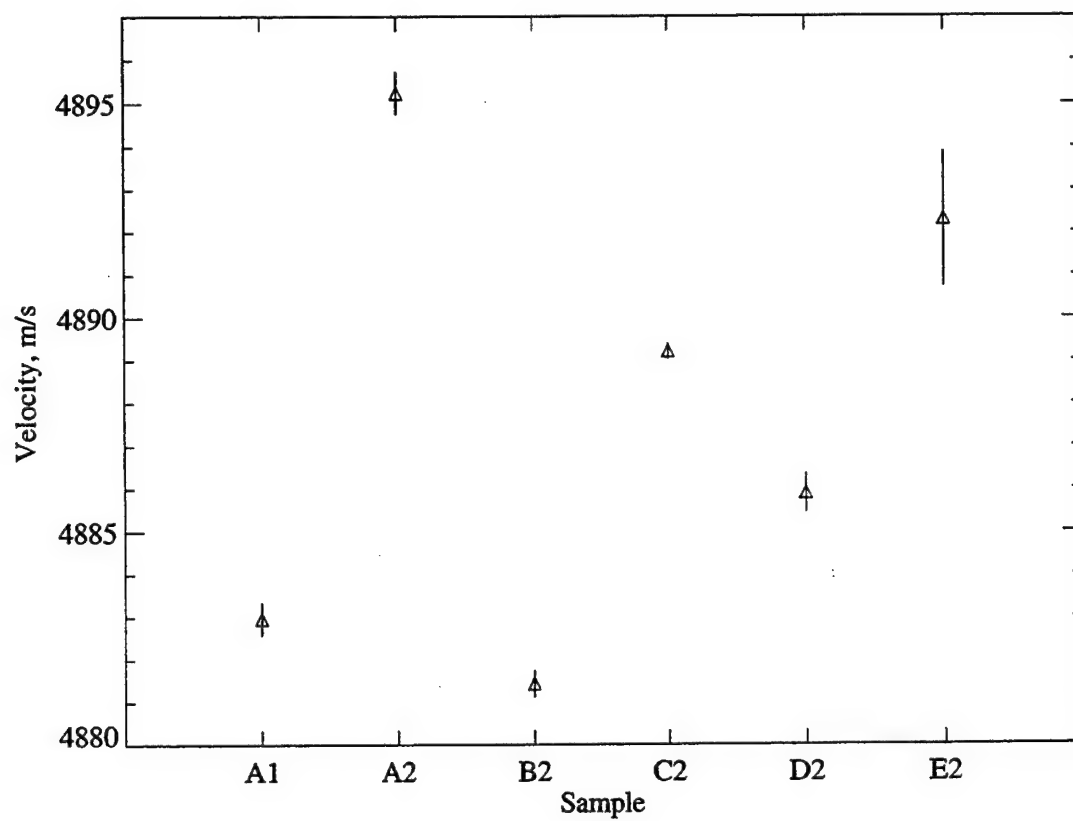


Figure 3-2: Surface acoustic wave velocity of irradiated silicon samples .

Chapter 4

Borosilicate glass irradiation experiments

4.1 Gamma irradiation of pointer beam strain gauges

4.1.1 Method

4.1.1.1 Pointer beam strain gauge

A MEMS pointer beam strain gauge has been developed at Draper Laboratory. Its primary use has been as a monitoring tool for wafer bonding and fabrication processes, as it gives an indication of differential strains present between a glass substrate and the silicon wafer bonded to it. A diagram of the pointer beam device is shown in Figure 4-1.

The key to the operation of the strain gauge lies in the slight offset between the two horizontal supports for the vertical beam. Thus, if the silicon is in compression,

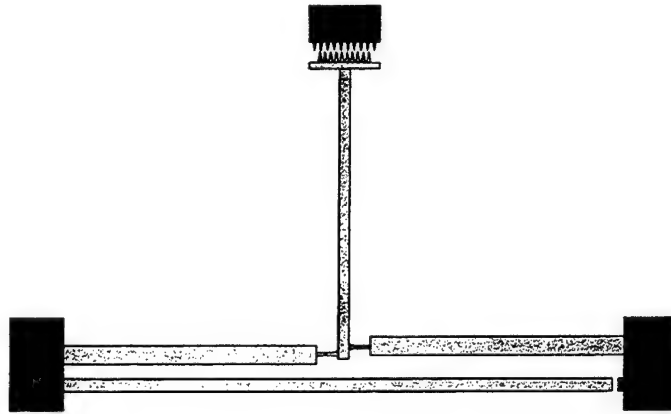


Figure 4-1: Pointer beam MEMS silicon strain gauge, top view. The grey portions are suspended above the glass substrate. The black portions are bonded to the substrate. The top and bottom teeth have $4.5\text{ }\mu\text{m}$ and $5\text{ }\mu\text{m}$ pitch, respectively. The horizontal distance between the inside of the lower black (bonded) portions is 1 mm.

the top of the vertical beam will swing to the left. If the silicon is in tension, it will swing to the right. The row of teeth spaced at $5\text{ }\mu\text{m}$ attached to the vertical beam, when referenced to the row of teeth spaced at $4.5\text{ }\mu\text{m}$ on the bonded silicon block at the top of Figure 4-1 serve as a vernier caliper, allowing one to measure the degree of compression or tension. The beam at the bottom of Figure 4-1 that runs parallel to the offset beams plays no role in the strain measurement: its detached end (on the right) serves to measure strain gradients in the silicon as it curls out of plane.

A finite-element model constructed by Draper engineers gives the relationship of the tip displacement (d) to the relative substrate strain (ϵ in parts per million) as: $d = (0.035\text{ }\mu\text{m})\epsilon$. The pointer displacement can be read under a microscope to 0.1 tooth widths, so the strain (the silicon-substrate differential strain) resolution of the pointer is 1.4×10^{-5} .

The offset of the horizontal beams in Figure 4-1 is critical to this d/ϵ relationship.

To examine the effect of possible fabrication flaws in this offset, we consider a simple geometric construction in which the horizontal beams are attached to the main vertical beam by freely moving hinges. The resulting relationship is:

$$d = \frac{SL_O}{\delta}\epsilon, \quad (4.1)$$

where d and ϵ are as above, S is the length of the vertical beam from tip to midway between the horizontal beam attachment points (the "hinges"), L_O is the initial inner distance between the anodically bonded anchors, and δ is the offset distance between hinges. Taking S to be $535 \mu\text{m}$, L_O to be 1 mm , and δ as its nominal $10 \mu\text{m}$, we get:

$$d = (0.054\mu\text{m})\epsilon \quad (4.2)$$

This geometric model therefore predicts 50% greater sensitivity to strain than does the finite element model. It has not taken flexure bending into account, but is still useful as a model for examining the sensitivity of d/ϵ to the offset δ .

The pointer beam devices used in the gamma irradiations were fabricated at CSDL with a $0.1 \mu\text{m}$ tolerance for in-plane distances. Examining Equation 4.2, we find that a $0.1 \mu\text{m}$ change in δ results in a 1% change in d/ϵ . A 1% variation among pointer beam strain sensitivities would not significantly affect the results we obtained.

Three wafers were made: one Pyrex wafer and two Hoya SD-2 wafers. The devices were arrayed on glass wafers, among other MEMS diagnostic devices, as shown in Figure 4-2. The black squares indicate the locations of test device arrays. At each of

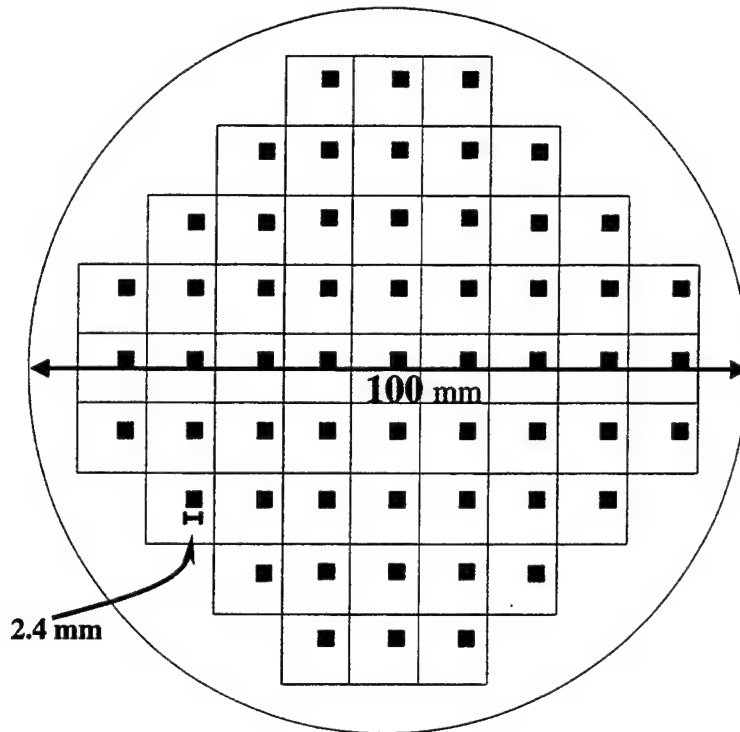


Figure 4-2: Pointer beam MEMS silicon strain gauge wafer layout. The black squares represent arrays of test fixtures, each one containing a pointer beam strain gauge.

these locations, one pointer beam is present, giving a total of 57 pointer beams per wafer. The glass used was about $780\text{ }\mu\text{m}$ thick, and the silicon was $10\text{ }\mu\text{m}$ thick.

To read the strain gauge, one needs a microscope. A reflected-light microscope with a magnification of $1000\times$ was used to make measurements. The as-fabricated beam positions for each numbered device were measured and recorded. The average starting deflection of the pointer beams is shown in Table 4.1 (positive deflection indicates the silicon is in tension).

Due to fabrication non-uniformities, tooth shape and orientation showed considerable variation from one device to the next. As a result, some degree of interpretation was involved in making a deflection reading. In some cases, it was clearly possible

Table 4.1: Pointer beam strain gauge pre-irradiation positions. Deflection is measured in tooth widths. The initial differential strain between the silicon and glass is residual from the fabrication process.

Wafer	Average deflection	Differential strain
Pyrex	+0.34	4.9×10^{-5}
Hoya B	+0.14	2.0×10^{-5}
Hoya C	+0.09	1.3×10^{-5}

to make fractional-tooth readings. When time allowed, multiple measurements of the same pointer beam were made, and the results averaged. One pointer beam on the Pyrex wafer was found to be deflected to 0.85 teeth, which was well outside of the typical deflection range. This pointer beam was discounted as defective, and not used.

4.1.1.2 Gamma irradiation of pointer beam wafers

A ^{60}Co gamma source at the University of Massachusetts at Lowell was used to irradiate the pointer beam samples. The source consisted of a 61 cm \times 61 cm plaque of ^{60}Co strips. The strips were of varying activities. To irradiate the "gamma cave" (the room in which the samples sat), the ^{60}Co plaque would be moved into a holder on an aluminum window that separated the source from the samples. The gamma cave was a very humid environment because the concrete wall with the aluminum window also served, on its other side, as the wall of a large water tank in which the ^{60}Co source was kept. The air inside was sufficiently humid that water was observed to condensed on the aluminum window and sample holder.

An aluminum holder for the samples was fashioned and put into position against

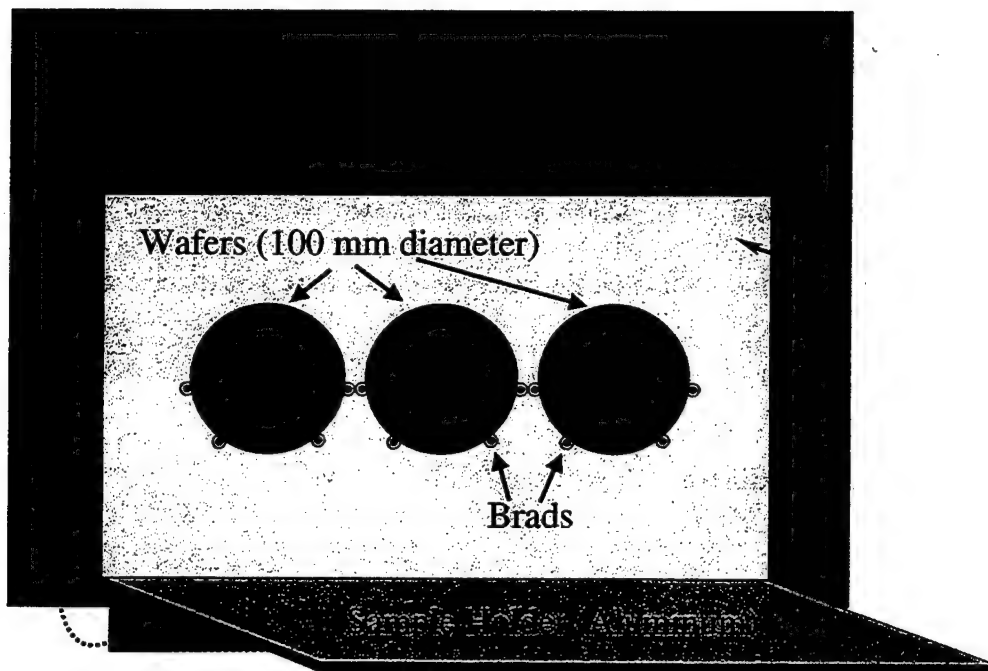


Figure 4-3: The pointer beam irradiation set up. The Co 60 source is a rectangular plate behind the aluminum window. The wafers sit held loosely by brads attached to a thin aluminum support.

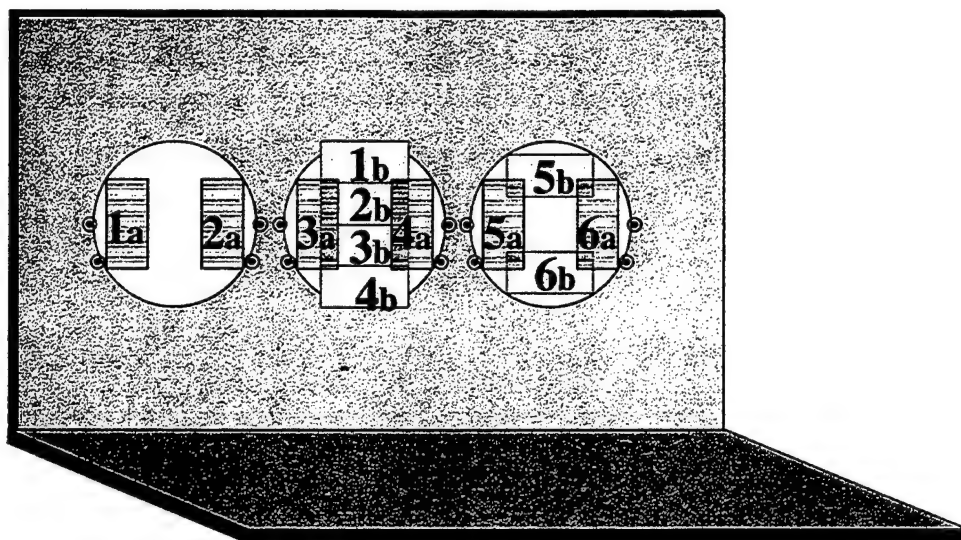


Figure 4-4: Placement of doimeters on aluminum wafer holder. The dosimetry used the same configuration as shown in Fig. 4-3.

the aluminum window as shown in Figure 4-3. An aluminum sheet 1.6 mm thick was bent into an L-shape, then brads were fixed onto it so that the wafers could be slid from the top of the holder down to where they were supported by the brads. Edges on the brads prevented the wafers from tipping off the holder. The MEMS devices faced away from the holder. The wafers, designated "Pyrex," "Hoya B," and "Hoya C," were set into the left, middle, and right holder positions, respectively.

Prior to the irradiation, dosimetry measurements were made by Lowell personnel using FWT-70-40M Optichromic Dosimeters.[43] Six dosimeter packages were placed on the sample holder, as shown in Figure 4-4 by the dark rectangles labeled as series "a." Each dosimeter package held two dosimeters, the readings of which were averaged to give one reading per package. The results are shown in Figure 4-5 with the package centers' horizontal positions measured with respect to the center of the middle wafer.

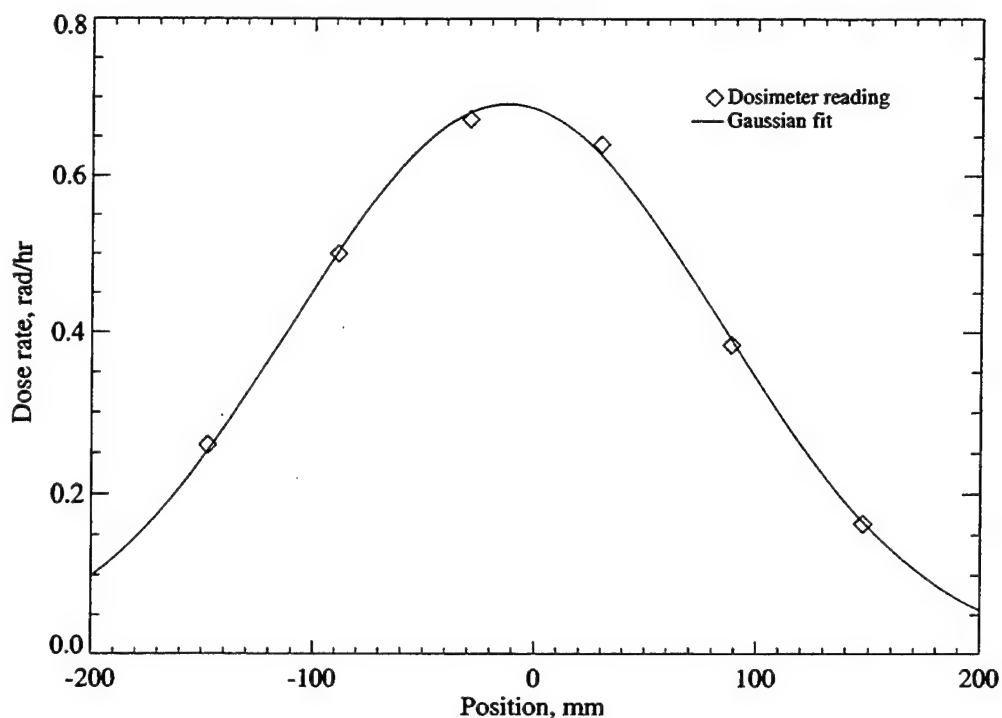


Figure 4-5: Dosimeter readings and fit curve.

The data appear to follow a roughly gaussian trend, and a fitted gaussian curve is shown in Figure 4-5.

A second dosimetry measurement was made at a later date in which four dosimeters were distributed vertically across the center wafer position and two more dosimeters were placed at the top and bottom of the right wafer position. This arrangement is shown in Figure 4-4 by lighter colored rectangles labeled series "b." The measured dose rates were found to be constant to within 5% on the center wafer, and within 10% on the right wafer. The results of both dosimetry measurements are summarized in Table 4.2.

Given the placement of the wafers near the vertical center of the aluminum window

Table 4.2: Gamma dosimeter readings.

Dosimeter	Dose rate, krad	Dosimeter	Dose rate, krad
1a	260	1b	720
2a	500	2b	708
3a	672	3b	744
4a	640	4b	744
5a	384	5b	612
6a	164	6b	564

(near the flat peak of the assumed gaussian vertical variation), doses were determined for individual pointer beams based solely on their horizontal positions and the fitted dose rate curve in Figure 4-5. The average dose rate measured at the right wafer position differed by about 50% in the two measurement series, though the center wafer position measurements remain within 7% of each other. Since the wafer positions are not symmetric about the gaussian in Figure 4-5, it is suspected that in the second dosimetry measurement the ^{60}Co source plaque was placed in its holder with an opposite orientation with respect to the first set of measurements. The ^{60}Co source was removed and replaced several times over the course of the irradiations without verification of the orientation of the source, so a large uncertainty in the radiation dose received for the left and right wafers must be assumed. The effect of this different source placement is considered in the discussion below.

The doses quoted from the dosimeter measurements are water-equivalent doses (the dose that would have been absorbed by water at the dosimeter positions). To find the doses absorbed by Pyrex and Hoya SD-2 glasses for the same gamma flux, a conversion factor was calculated. A ^{60}Co gamma emission spectrum of two lines of

equal intensity, 1.17 MeV and 1.33 MeV, was assumed.[80] Degradation of the emission spectrum upon propagation through the aluminum window and sample holder was accounted for using mass attenuation coefficients from NIST's website.[58] The absorbed dose was calculated using mass energy-absorption coefficients, μ_{en}/ρ , also from NIST.[58] Values for absorbed dose were next calculated for water and the glasses, then compared. Pyrex and Hoya SD-2 absorbed doses were both found to be 0.89 times those measured by the dosimeters for water. It turns out that the thin aluminum windows present have a negligible effect for present purposes on the ^{60}Co emission spectrum, and the conversion factor can simply be taken as the ratio of the μ_{en}/ρ values for the materials involved.

The irradiation of the wafers was often interrupted by the removal of the ^{60}Co source in order to perform other simultaneous experiments in the gamma cave. The wafers were taken to Charles Stark Draper Laboratory for measurement during these interruptions. The pointer beams on all three wafers were all measured after 317, 471, and 630 hours of irradiation. The Hoya C wafer had its pointer beams additionally measured after 184 hours of irradiation.

4.1.2 Results

The results of the pointer beam measurements are summarized in Figure 4-6 and Figure 4-7. Error bars are shown with 1×10^{-5} strain, which is slightly better than the 14 ppm resolution of the vernier on the pointer beams. Lines were fit to the data in Figures 4-6 and 4-7 using least-squares. The results of the fits are shown in Table

Table 4.3: Fits to data in Figures 4-6 and 4-7.

	Strain/rad	Intercept	Reduced χ^2
Pyrex	9.02×10^{-15}	2.13×10^{-6}	0.65
Hoya SD-2	4.34×10^{-14}	-8.51×10^{-7}	0.48

Table 4.4: Fits to pointer beam data for alternate dosimetry estimate.

	Strain/rad	Intercept	Reduced χ^2
Pyrex	1.46×10^{-15}	3.39×10^{-6}	0.66
Hoya SD-2	4.65×10^{-14}	-2.35×10^{-6}	0.49

4.3.

The different dosimetry profile that would result if the ^{60}Co source were inserted into its holder in an orientation inverted about the vertical axis in Figures 4-3 and 4-5 has been considered. Dose values were reassigned to individual pointer beams based on the curve that results from inverting the gaussian curve shown in Figure 4-5 about the ordinate axis. A line was then fitted to both the Pyrex and the Hoya SD-2 data. The results are shown in Table 4.4. These fits represent a 7% and 38% difference for Hoya SD-2 and Pyrex, respectively, from the values in Table 4.3. These values represent the extreme case that the source sat for the entire irradiation duration in the opposite orientation from that previously thought.

While a trend of rising positive strain with increasing dose is clearly seen in only the Hoya SD-2 data, it is statistically shown to be present for both glasses. The very low (and therefore encouraging) reduced chi-squared[16] values for the fits are perhaps not very significant, given how small the measured strains are in comparison to the uncertainty in the measurement. Many other possible fit lines could also

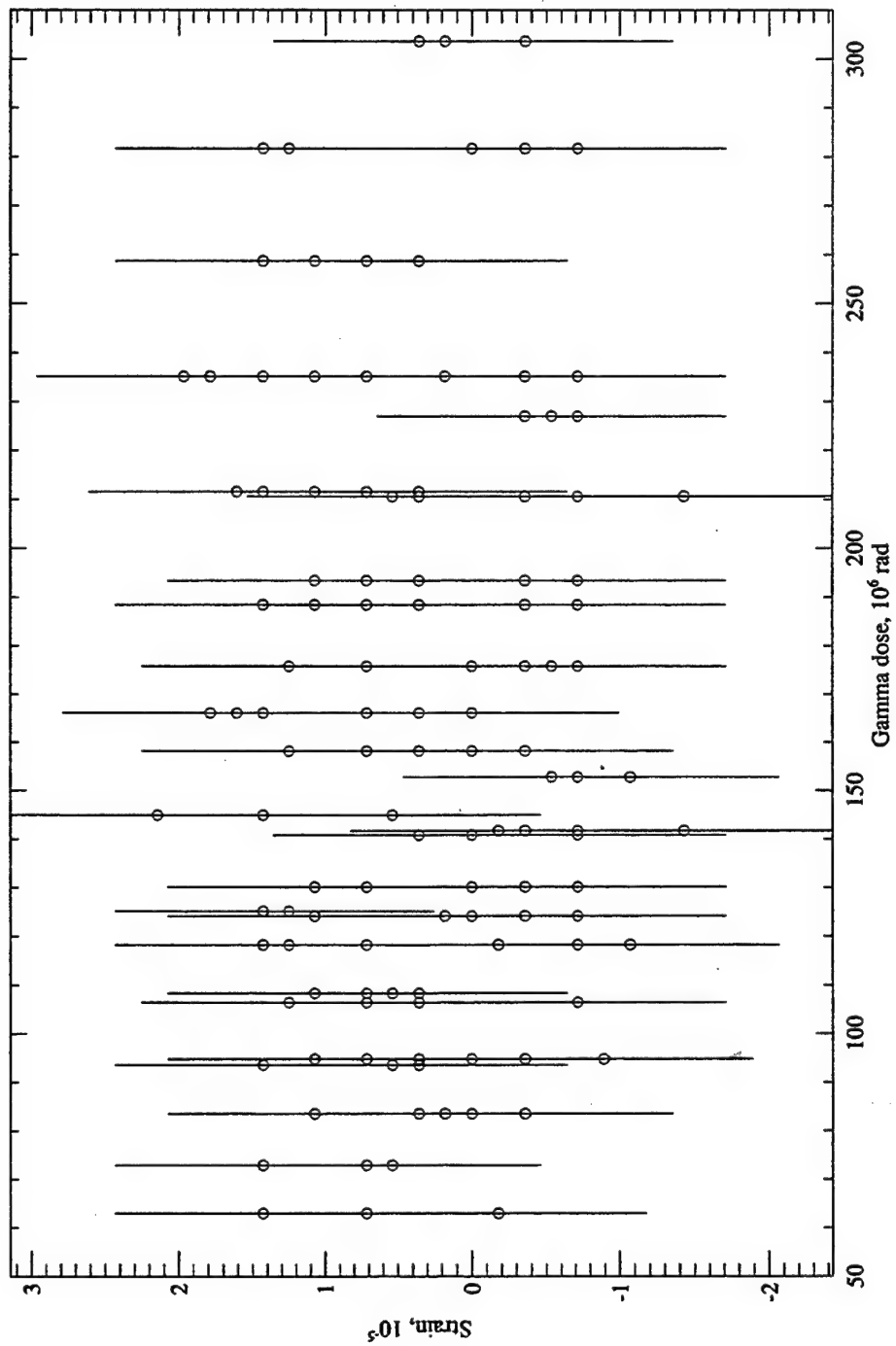


Figure 4-6: Pointer beam gauge readings from Pyrex wafer.

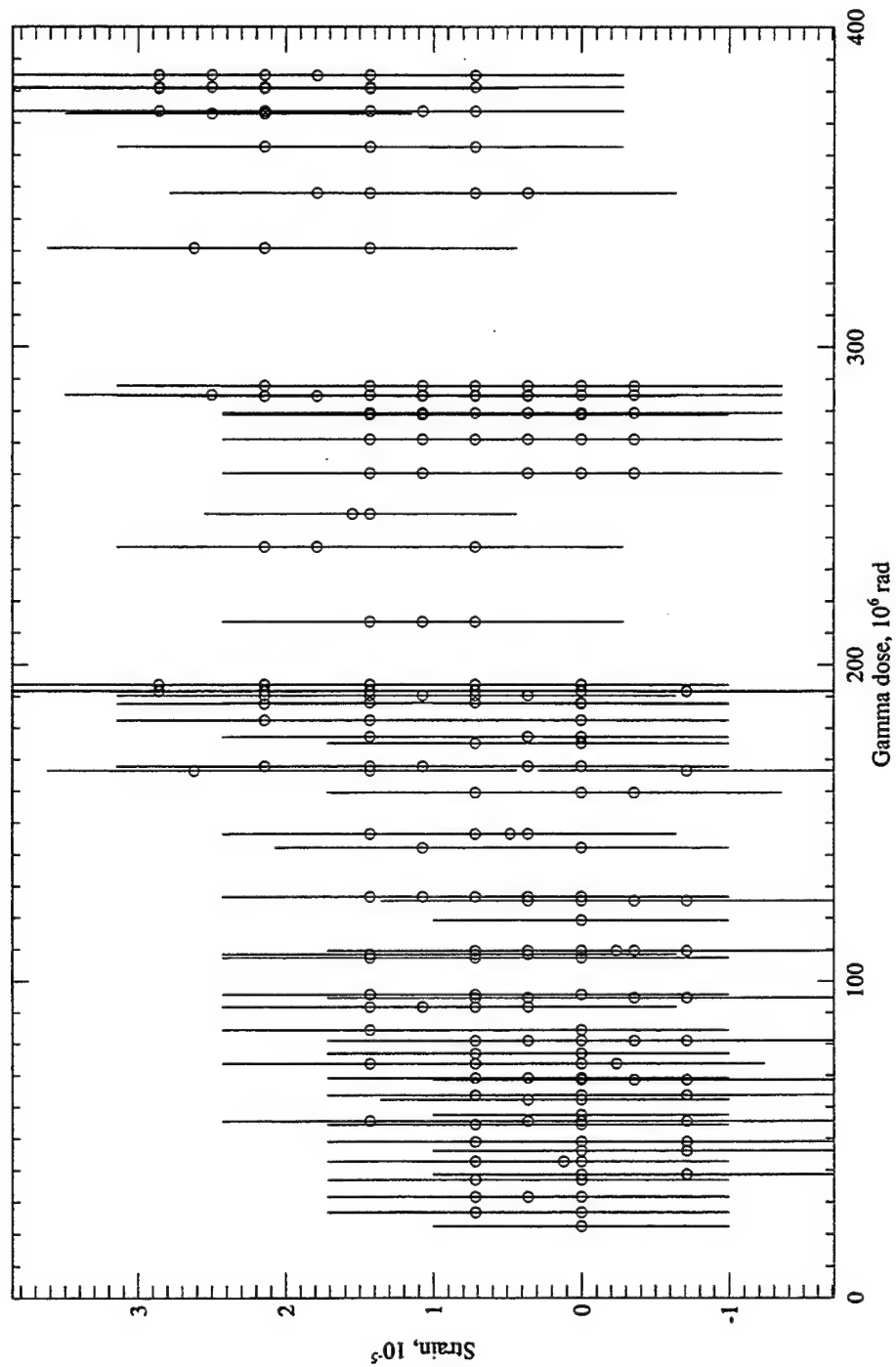


Figure 4-7: Pointer beam gauge readings from Hoya SD-2 wafer.

produce low chi-squared values. Other statistical tests, however, indicate a correlation between dose and strain in the data. One such test that was used was the "Student-t" distribution and the the statistic:

$$t = \frac{r\sqrt{N-2}}{\sqrt{1-r^2}}, \quad (4.3)$$

which follows the Student distribution with $N-2$ degrees of freedom.[115] In Equation 4.3, N is the number of data points and r is the correlation coefficient. The Hoya data was found to have a correlation coefficient of 0.5725, which for the 387 data points collected, represents a probability of 1.0000 that the strain was not random with dose. The data from the Pyrex wafer was less categorical, with a correlation coefficient of only 0.0675. Nevertheless, for the 170 measured data points, even that small correlation means there is a 80 % probability that the data was not of random origin.

It is very clear that the data are not in agreement with those previously collected by Shelby.[110] At 100 Mrad, Shelby shows strain of approximately -20 ppm, whereas the present data show a strain in the Pyrex of about +3 ppm. As Shelby's results have been confirmed by later experiments,[31, 101] there must be some other factor that is acting in the pointer beam experiment to give results so clearly different from Shelby's.

Several explanations for the Pyrex results have been proposed. Firstly, radiation might be compacting the silicon pointer beams along with the glass substrate. In pure silicon, the radiolysis mechanism involving Si-O bonds is absent, and the silicon

is therefore not susceptible to the radiolytic damage caused by gamma rays in glass. Compton scattered atomic electrons with kinetic energy equal to the incoming gamma ray can be produced, however.[71] Bombardment of silicon with 1 MeV electrons shows that expansion in silicon occurs.[84] Not only should this expansion increase the differential strain with respect to a compacting glass substrate, but its magnitude is negligibly small when compared to the expected Pyrex compaction. We can therefore discount the possibility that the silicon is compacting along with the Pyrex.

Secondly, one must consider that the glass being irradiated has been through bonding and microfabrication processes during the construction of the pointer beams. The bonding process, called anodic bonding, is particularly suspect as a cause for changes in material properties. During anodic bonding, the glass is heated to 350-400 °C while in contact with a silicon wafer. Electrodes on either side of the two wafers are set at a potential difference of 500-1000 V. The electric field that results causes sodium ions to drift away from the bonding interface, creating a depletion region with a large electric field. A white powder, containing oxidized sodium, is observed to have appeared on the non-bonded glass surface after anodic bonding. During this process, a layer of SiO_2 forms at the interface of the two wafers.[35, 86] The Vicker's hardness of Pyrex has been observed to increase two-fold after anodic bonding.[35] It is possible that the chemical and microstructural changes induced in Pyrex by the anodic bonding dramatically change the response of the glass to gamma irradiation. This possibility was investigated by performing irradiations of Pyrex and Hoya SD-2 samples that had been processed as for anodic bonding. These experiments are described in section 4.3.4.

Thirdly, the pointer beams may not be performing as designed. To verify the functioning of the pointer beams, a thermal calibration apparatus has been designed and built. An aluminum plate with a thermistor, a temperature controller, and heaters attached to it will heat the glass wafer from underneath while a silicon circumferential ring with a glass wafer resting on it act as an oven for the pointer beams. Heating the pointer beams and the wafer to which they are bonded causes a differential strain to develop between the pointer beams and the glass substrate due to differing coefficients of thermal expansion. By measuring beam deflection and temperature, one can calibrate the beam deflection-to-strain relationship. This experiment has not yet taken place, due to the risk it poses to the expensive objective lens that would be involved. It is judged likely, however, that the pointer beam strain gauges, which have a solid "track record" in the fabrication facility at Draper Laboratory, performed as designed.

Lastly, effects such as radiation-induced creep, interface debonding, and non-densifying deformation may be possible. Experiments involving heavy ion bombardment of silicon, silica, and Pyrex have shown that non-densifying radiation-induced viscous flow can occur.[113, 129] At high enough doses, the dimensional expansion of silica and Pyrex (even in the absence of stress) perpendicular to the irradiating ions can reverse the shrinkage due to saturating compaction that is evident at lower doses.[66, 65] It is unlikely that the deformation present in heavy, high-energy ion bombardment which is due to local melting and quenching of roughly cylindrical ion tracks [15] is present for gamma rays which are producing largely isolated defects.[3] The expected compaction of the glass substrate is providing a stress that may assist

the radiation-induced viscous flow in a thin SiO_2 layer at the anodic bond, thus allowing the pointer beam anchors to slip, removing the strain in the silicon pointer beams. This would not explain the slight tension present in the beams after irradiation, however. Studies of creep in steels [136, 48] indicate that steels will undergo creep at surprisingly low temperatures and stresses while being irradiated. However, even if our glasses shared the same creep behavior as the steels of that study, the low temperature and stress of our experiment would not allow for any significant creep to occur.

4.2 TRIM calculations of neutron damage in glass

4.2.1 Introduction to TRIM

The Transport of Ions in Matter, or TRIM, is a computer code available free of charge from James F. Ziegler as part of the SRIM (Stopping Range of Ions in Matter) software package.[144] SRIM runs on a PC/Windows platform. Widely used in the field of ion implantation, TRIM performs Monte-Carlo simulations of collision cascades for any ion passing through elemental materials as well as compounds. Data provided by TRIM includes the average number of atomic displacements in a cascade, the percentage of energy lost by both incident ions and recoil atoms to ionization and atomic displacement, and the range of incident ions in a material. One can generate a file containing the locations of all collisions within a cascade, along with the corresponding recoil energies.

TRIM (version 2000.38) simulations were carried out for the interaction of fast and thermal neutrons in Pyrex and Hoya SD-2 glasses. The purpose of doing this was two-fold: 1) data were found in the literature[96, 95, 97, 98] for thermal neutron damage in Pyrex, and an equivalence was needed between fast and thermal neutron collision cascades in order to estimate fast neutron damage, and 2) planned experiments on glass would involve exposure to both thermal and fast neutrons, and a way was needed to apportion the observed damage between these two causes.

The key piece of data that TRIM can furnish to help estimate this fast neutron/thermal neutron equivalence is the number of displacements per collision cascade. In the TRIM lexicon, "vacancies" are equivalent to the "displacements" referred to here. In calculating vacancies, TRIM takes into account that an energetic ion that transfers enough energy to a stationary ion to dislodge it from its site may not have enough energy itself after the collision to escape the site. In this case, the incoming ion replaces the ion initially at the site, and no vacancy results. "Displacements" calculated here are this net vacancy result from TRIM, with replacement collisions already taken into account.

4.2.2 Glass models

The stopping power of a material is the amount of energy lost to that material by an effluent charged particle per distance travelled.[112] Quoting Ziegler,[145] "...the stopping [power] of a compound may be estimated by the linear combination of the stopping powers of the individual elements. This [Bragg's] rule is reasonably accurate,

and measured stopping of ions in compounds usually deviates less than 20% from that predicted by Bragg's rule." Furthermore, "the accuracy of Bragg's rule is limited because the energy loss to the electrons in any material depends on the detailed orbital and excitation structure of the matter, and any differences between elemental materials and compounds will cause Bragg's rule to become inaccurate."

TRIM accommodates the simulation of ion transport in compounds like glass using a "cores and bonds" (CAB) model.[112] The "cores" are closed-shell atoms, and the "bonds" are the bonding valence electrons which, depending upon the exact nature of a bond, will contribute differing amounts to the overall stopping power of the material. The TRIM file COMPOUND.DAT contains compositions for many common nuclear materials, and detailed bond information on a subset of these.

Table 4.5 shows the glass compositions used for the TRIM simulations. The Pyrex composition differs slightly from that actually measured by XPS. There are two reasons for this: 1) at the time the Pyrex TRIM calculations were performed, the XPS data were not available and 2) a model for Pyrex was already included in the TRIM database. It was assumed at the time of the calculations that the full CAB model was used, but further inspection of the TRIM COMPOUND.DAT file revealed that no bonding information is present. It is therefore presumed that Bragg's rule alone is being used in the TRIM calculations for both Pyrex (using the default Pyrex model) and Hoya (with manually entered compositions).

Table 4.5: Assumed glass compositions for TRIM calculations (atomic percent).

Element	Pyrex	Hoya SD-2
O	65.0	60.95
Si	25.0	21.1
B	7.0	1.05
Al	1.0	12.2
Na	2.0	0.5
C	—	0.6
Zn	—	0.75
Mg	—	2.95

4.2.3 Fast neutron calculations

The cross section for neutron scattering varies among elements and isotopes. Cross section data for many individual isotopes are available in the literature, as well as data for naturally occurring isotopic averages.[77] Data is often available for the following cross section types: total (σ_{tot}), elastic (σ_{el}), inelastic (σ_{inl}), absorption (σ_{abs}), and nonelastic (σ_{non}), where $\sigma_{tot} = \sigma_{el} + \sigma_{inl} + \sigma_{abs}$, and $\sigma_{non} = \sigma_{inl} + \sigma_{abs}$.

The cross sections for most of the component elements of Pyrex and Hoya SD-2 are almost purely elastic for scattering of 1 MeV neutrons. Exceptions are sodium and zinc, which have nonelastic cross sections that are 13% and 4%, respectively, of their elastic cross sections. The significance of these small nonelastic components to the cross section is further reduced by the relatively minor sodium and zinc concentration in Pyrex and Hoya SD-2. The analysis here therefore makes the simplifying assumption that all primary knock-ons are the result of scattering that is wholly elastic. Furthermore, inspection of the experimental cross section data for the elements in our glass bears out that the approximation isotropic scattering of Equation 2.1

is reasonable for neutron energies below 1 MeV. The analysis therefore assumes a constant value for the cross section, ignoring the relatively minor resonances in the spectra.

The cross section of an individual nuclei (σ) is known as the *microscopic* cross section. The product of this with the number density of atoms, N , is called the *macroscopic* cross section, Σ . [112] The mean free path of a neutron is given by $1/\Sigma$. The probability of a neutron not scattering before travelling a distance x in a material is given by:

$$P_{not}(x) = e^{-\Sigma x}. \quad (4.4)$$

The probability of a neutron scattering before travelling a distance x is therefore:

$$P_{scat}(x) = 1 - e^{-\Sigma x}. \quad (4.5)$$

TRIM can read an input file of individual recoiling nuclei and calculate a collision cascade for each. Since our glasses contain several different elements, one must calculate the relative number of primary knock-on atoms for each constituent atom type. One must also account for range of possible energies for each primary knock-on species, as given by Equation 2.3.

The number density of each element in both glasses was calculated based on the density of the glass and the atomic fraction of the element. Multiplying this number density by the microscopic cross section for elastic neutron scattering from Ref. [77] gives the macroscopic cross section. This then can be used in Equation 4.5 to give

the fraction of incident neutrons that will be scattered by this element. The glass wafer thickness (the distance "x" in Eq. 4.5) used for these calculations was 780 μm , that of a typical MEMS substrate and the precise thickness of the glass used in our experiments.

The most probable scatterer in Pyrex and Hoya SD-2 is oxygen, scattering 2.8% and 2.9%, respectively, of incident 1 MeV neutrons. Silicon is the next largest contributor, scattering around 0.5% of incident neutrons in both glasses, with other elements scattering relatively smaller numbers of neutrons. Multiple scattering of neutrons is therefore ignored when preparing a list of primary knock-on atoms for the TRIM calculation. Each scattering event as predicted by Equation 4.5 is considered to be one involving a 1 MeV neutron, and the total probability for scattering in a glass is assumed to be the sum of the individual scattering probabilities of each element. Furthermore, the neutron flux and energy are assumed to be uniform throughout the glass wafer; *i.e.*, no consideration is given to the fact that the amount of energy deposited by an incident neutron flux will be slightly greater near the entrance side of the wafer than near the exit side due to attenuation of neutron kinetic energy. The numbers of each type of PKA used in TRIM calculations are shown in Table 4.6.

We note that the composition of the input PKAs varies somewhat from the TRIM default Pyrex composition (*e.g.*, the presence of potassium). The composition used to generate the values in Table 4.6 comes from Paymal.[95] Again, the TRIM runs for Pyrex predate the XPS measurements, and it was desirable to leave the native TRIM Pyrex model intact for the target material. The schematic depiction shown earlier in Figure 2-3 for a 1 MeV neutron collision cascade is representative of Pyrex, with

Table 4.6: Distribution of primary knock-on atoms input into TRIM.

Element	Number of PKAs		Energy Range (keV)
	Pyrex	Hoya SD-2	
O	1100	1100	0-221
Si	262	212	0-133
B	23	6	0-310
Al	3	65	0-138
Na	14	3	0-160
C	—	3	0-284
Zn	—	6	0-59
Mg	—	18	0-152
K	3	—	0-97

oxygen, silicon, and boron present in correct proportions and their relative sizes indicating their cross section for scattering the fast neutron (*i.e.*, the relative probability of being the primary knock-on atom).

The motivation for running proportional numbers of PKAs was to reduce computation time. One could have simply run thousands of each type of PKA, then averaged the results together proportionately to the neutron scattering probability of each element, as described above. Instead of doing this, it was judged that ~1400 total PKAs gave acceptable statistical certainty in the averaged result for displacements per PKA, and this total number was shared among the elements according to their importance. The 1100 oxygen PKAs took about 6 hours to calculate on a Pentium 120 MHz computer.

The last column in Table 4.6 shows the range for possible energy transfer from the incident 1 MeV neutron to the PKA (see Eq. 2.3). To simulate the spectrum of possible starting energies of primary knock-on atoms, equally spaced energies for

Table 4.7: Summary of TRIM calculations for fast neutrons.

	Pyrex	Hoya SD-2
Displacements per fast neutron collision	614	644
Probability of fast neutron collision	0.036	0.038
Displacements per incident fast neutron	22	24

PKAs were included in the TRIM input file. For example, 100 of the 1100 oxygen PKAs started with 0 keV, 100 others started with 22.1 keV (being one tenth of $T_m = 221$ keV), and so on up to the last 100 atoms which started with 221 keV. The PKA energies for the other elements were similarly represented by 0, $T_m/10, \dots, T_m$. For elements having n fewer than eleven PKAs, the energy range was simply broken into n intervals. TRIM calculations carried out later revealed that assigning all PKAs an energy of $T_{ave} = T_m/2$ yields very similar results to the above procedure, *i.e.*, the number of displacements in a collision cascade varies fairly linearly with initial PKA energy in these energy ranges. Figure 4-8 shows the locations in the X-Y plane of displacements calculated by TRIM for two oxygen recoil collision cascades. One is for the case of maximum energy transfer of 221 keV, the other for one-tenth of that.

Table 4.7 summarizes the results of the TRIM calculations for fast neutron collision cascades in Pyrex and Hoya SD-2. The numbers given here assume a $780 \mu\text{m}$ thickness for the glass.

4.2.4 Thermal neutron calculations

Calculating collision cascades for the thermal neutron damage case was simpler than for fast neutrons. The recoil ions (Li^{3+} and He^{2+}) are monoenergetic, as explained

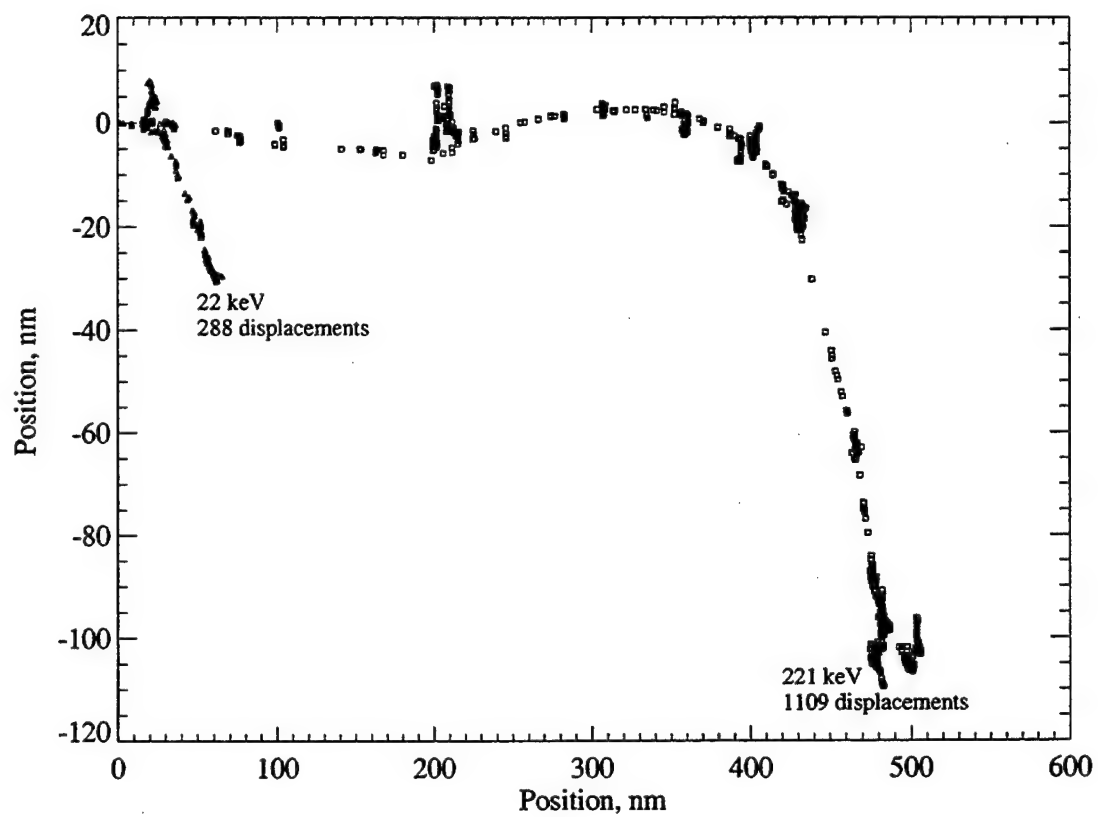


Figure 4-8: Oxygen recoil cascade in Pyrex, calculated using TRIM. Squares and triangles represent the location in the X-Y plane at which a displacement occurs, for oxygen recoils of 221 and 22 keV, respectively.

Table 4.8: Summary of TRIM calculations for thermal neutrons.

	Pyrex	Hoya SD-2
Displacements per thermal neutron absorption	578	664
Probability of thermal neutron absorption	0.173	0.047
Displacements per incident thermal neutron	100	31

in Equation 2.4. The cases of incident helium and lithium particles were calculated separately with TRIM. The sum of the average vacancies per collision cascade gives the effect of a boron neutron absorption. Because manually created files can allow TRIM to simulate ions originating within a material (as would be the case for neutron absorption), both helium and lithium ion trajectories originating from inside the glass were considered case. The results were the same for incident ions and for ions starting from inside the glass (*i.e.*, the surface binding energy information included in the TRIM calculation had negligible effects on the results). Overnight runs were carried out, accumulating $\sim 17,000$ lithium ions and $\sim 38,000$ helium ions (the statistics are stable long before this many ions are treated).

As with the fast neutron case, one must determine how many of the incident thermal neutrons will be absorbed in the glass. The cross section for thermal neutron absorption for ^{10}B is 3837 barns ($1 \text{ barn} = 1 \times 10^{-24} \text{ cm}^2$), and that of naturally occurring boron is 767 barns.[85] Using this cross section, the number density of boron in Pyrex ($3.2 \times 10^{21} \text{ boron/cm}^3$) and Hoya SD-2 ($8.0 \times 10^{20} \text{ boron/cm}^3$), and a glass thickness of $780 \mu\text{m}$ in Equation 4.5 yields probabilities for thermal neutron of absorption of 17.3% and 4.7% in Pyrex and Hoya SD-2, respectively. The results of the TRIM calculations are summarized in Table 4.8.

To calculate displacements per atom for the values in Table 4.7 and Table 4.8, one may use the atom number densities (based on composition and mass density) of $6.90 \times 10^{22}/\text{cm}^3$ for Pyrex and $7.65 \times 10^{22}/\text{cm}^3$ for Hoya SD-2.

4.3 Neutron irradiation of borosilicate glasses

4.3.1 Sink/float densitometry method

Compaction of borosilicate glasses with neutron dose was studied by irradiating glass samples and then measuring the change in their density by means of the sink/float technique. Knight[68] was the first to employ this method, developed as a way to monitor density uniformity between glass production lots. This technique has since been used for sensitive studies of subtle compaction in glass by Paymal,[96, 95, 97, 98] Shelby,[109, 110] Sato,[101] and Zdaniewsky *et al.*[142] Not all experimenters had equal success in obtaining sensitivity using this method, as evidenced by the strange results of Zdaniewsky *et al.* and the large uncertainty reported by Sato, shown in Figures 2-7 and 2-8.

A couple of other methods used in the literature were considered. The column-gradient method involves the preparation of a glass column which has been carefully filled with two liquids of differing densities in such a way that there remains a density gradient over the height of the column. Standards of known density are then floated in the column, and the density of any other floated object can then be determined from the height at which it rests in the column. Higby *et al.*[53] employed this technique,

obtaining $\Delta\rho/\rho$ sensitivity of about 36 ppm. Another method involved floating a bob with the experimental sample in a dense liquid whose density was adjusted by varying its temperature. The bob was attached to an analytical balance. When the experimental sample just floated, then the reading of the balance could be converted to a density. $\Delta\rho/\rho$ sensitivity of about 50 ppm was obtained with this method.[99]

By comparison, the sensitivities obtained using the sink/float technique have been from 50 ppm $\Delta\rho/\rho$ for Shelby to 90 ppm for Connors and 300 ppm for Sato. While perhaps not as consistently sensitive as the other techniques, the sink/float technique appeared simpler to implement than the bob technique and much less expensive than the column gradient method.

To perform a sink/float measurement, a pair of glass samples (whose densities we wish to compare) are placed in a test tube containing a heavy liquid in which they just float. The liquid is then heated by means of a water bath. If the starting density of the liquid is sufficiently close to that of the glass, raising the temperature of the liquid by a few degrees will cause the liquid density to become smaller than that of the densest glass sample (the coefficient of thermal expansion of the glass is much smaller than that of the liquid). This glass sample will now sink. By recording the temperature at which this occurs and then by continuing to heat the liquid until the less dense sample sinks, one can calculate the relative difference in the densities of the two samples using the coefficient of thermal expansion of the liquid.

An approximate formula that relates a difference in sinking temperature to a

density difference can be derived as

$$\frac{\Delta\rho}{\rho} = \frac{3\Delta T(\alpha_G - \alpha_L)}{1 - 3\Delta T\alpha_G} \quad , \quad (4.6)$$

where ΔT is the difference in sinking temperature between the irradiated and unirradiated glass samples, α_G is the linear coefficient of thermal expansion of the glass, α_L is the linear coefficient of thermal expansion of the liquid (a third of the volumetric coefficient of thermal expansion), and ρ is the glass density. In Equation 4.6, we have neglected the possibility that the coefficient of thermal expansion is different between the glass samples. Since the thermal expansion of the glass is $\sim 10^{-6}$ and that of the liquid is $\sim 10^{-4}$, even a large relative difference in α_G would not have much of an effect. In fact, α_G can be assumed to be effectively zero, and a decent approximation can be made simply by

$$\frac{\Delta\rho}{\rho} = 3\Delta T\alpha_L \quad . \quad (4.7)$$

Assuming small density differences, an uncertainty of 0.01 °C in each temperature reading, and taking the uncertainty in the coefficient of thermal expansion for the liquid to be about 1%, one obtains a predicted uncertainty in $\Delta\rho/\rho$ of about 50 ppm. As the density difference between the two glass samples becomes greater, however, the uncertainty in measurement rises.

4.3.2 Sink/float apparatus design and execution

A picture of the constructed sink/float apparatus is shown in Figure 4-9. Shown are six 38 mm o.d. \times 200 mm Pyrex test tubes, suspended by O-rings from holes in a plexiglass lid that are cut in a regular circular pattern. The tubes are filled with dense liquid, and stoppered with Neoprene[®] rubber, a material resistant to degradation through contact with vapor from the organic liquids in the test tube (Conners[31] had reported that her stopper material was degrading and dropping bits into her liquids – this was not a problem with the Neoprene). The lid rests on a cylindrical 25 cm o.d. \times 25 cm Pyrex jar. A 2.5 cm o.d. \times 25 cm (only the bottom 12.5 cm are actively heated) 500 watt immersion heater is suspended from a hole in the center of the lid. The heater is attached to a Variac[®] transformer. The jar is filled with water to above the fluid level in the test tubes, and a 7.6 cm stir bar is at the bottom of the jar, for use with a heavy-duty stir plate. A horizontal line is drawn on the exterior of each test tube about 5 cm up from the test tube bottoms.

A platinum resistance temperature detector probe was inserted through a rubber stopper and immersed as shown in the liquid of one of the test tubes (the rearmost test tube in Figure 4-9). The probe was attached to a precision thermometer with 0.01 °C readout and 0.05 °C accuracy at the temperatures of interest. The heavy liquids used were tetrabromoethane (also known as acetylene tetrabromide) and bromonaphthalene. The first was suspected of being quite hazardous,[1, 57] so all work was performed in a vent hood while wearing goggles, a respirator with organic vapor filter cartridges, and Viton[®] gloves. The tetrabromoethane has a density of 2.96 g/cm³,

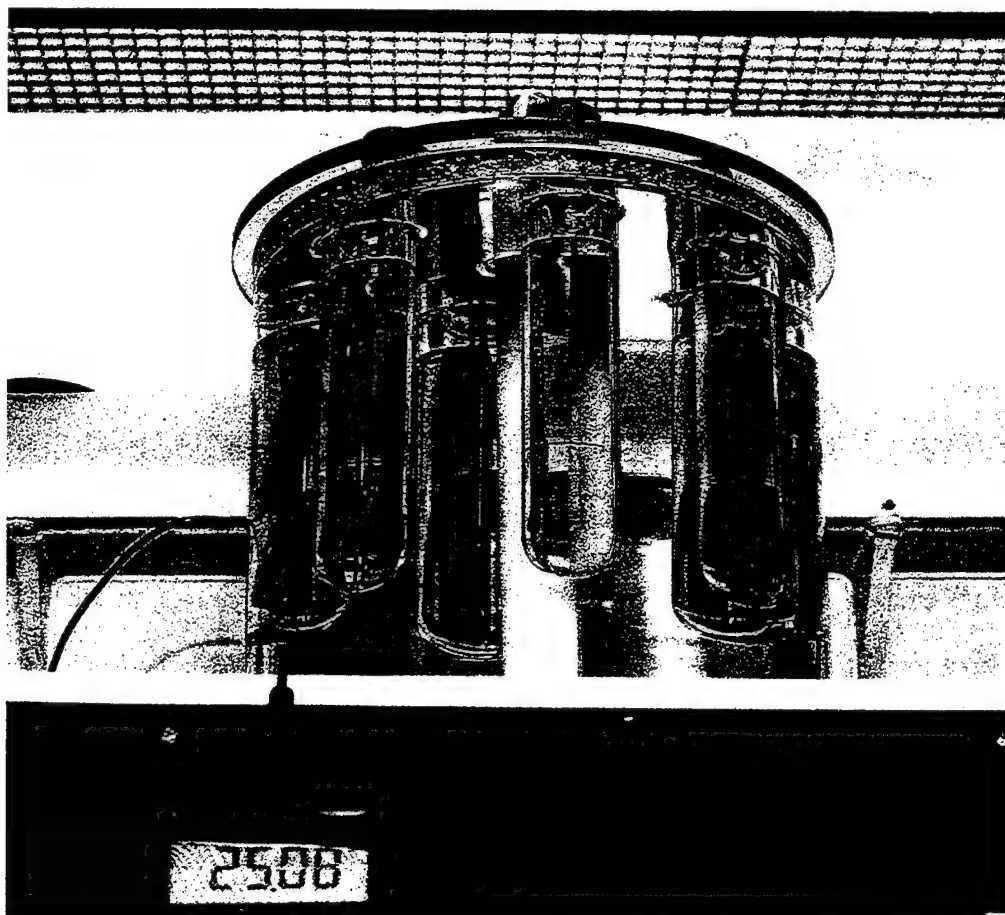


Figure 4-9: The sink/float experiment. Six liquid-filled test tubes are suspended in a water bath. The rear test tubes contains a thermometer probe. A quartz heating element is suspended in the center of the water bath. The large Pyrex container is resting on a magnetic stir plate.

and the bromonaphthalene has a density of 1.48 g/cm^3 . Mixtures of these liquids were made in a 1 L beaker. Initial liquid proportions were based on the manufacturers' densities cited here for the liquids and the glasses ($\rho_{\text{Pyrex}} = 2.23 \text{ g/cm}^3$, $\rho_{\text{HoyaSD-2}} = 2.60 \text{ g/cm}^3$). All of the sample pairs were individually dropped in the mixture to verify that they all floated, and the liquid was adjusted by adding milliliter quantities of the lighter or denser liquid. The densest sample was identified and then just made to float. Measurement runs were first performed on Pyrex. This gave a 0.11 ± 0.04 C per minute liquid heating rate. In most cases, the liquid temperature rose steadily and predictably — a given $0.01 \text{ }^\circ\text{C}$ increment is traversed in about 6 seconds. The system showed a response time of about 10 minutes to a change in heater power, which was used to speed up the heating during multiple runs with the same sample set where the approximate temperature gaps between critical temperatures for sample sinking were already known. A high stir setting was used, with the presence of the tubes preventing a vortex from forming (with the tubes removed at this setting, the vortex extended to the very bottom of the jar).

The line drawn on each test tube served as the official point at which each sample had "sunk." The use of this line was necessary, since the samples tended to stick to the surface of the liquid (and, less often, to each other), and only very vigorous shaking freed them up. Samples took several minutes to sink once they had left the surface, sometimes hovering at a fixed depth before resuming the fall. The sinking of the samples followed a predictable pattern. During initial heating from at least a couple of degrees below the sinking temperature of the first sample, the samples were located near the edges of the test tube. As its sinking temperature would approach,



Figure 4-10: Close-up view of sample pair in test tube. The darker sample on the left has been irradiated.

a sample would move toward the center of the tube when the tube was vigorously jostled. Soon afterward, a jostling of the tube would break the sample free from the surface of the liquid, where it would assume a stationary position several millimeters below the liquid surface, still centered in the tube. After resting in this position (sometimes for minutes), the sample would proceed to steadily sink. After crossing the demarkation line, a sample would continue on to the bottom of the tube, move to the side and then begin to rise along the wall of the tube, sometimes to two-thirds of the liquid height, whereupon the sample would redescend (this time near the tube wall) until it came to final rest on the tube bottom. A pair of samples is shown floating on the surface of the liquid in Figure 4-10.

The observed pattern is clear evidence of a strong convective current in the test tube. The liquid near the wall of the tube, being heated by the water bath, is rising, while the current in the center of the tube is falling. Near the top surface of the liquid there appeared to be a separate convective cell that kept the samples

caught in a holding position (perhaps this position was near the interface of the top and bottom convective cells) after they broke free from the liquid surface. The convective current was washing the samples up the tube wall after their first descent, keeping them suspended until the liquid density was sufficiently low that the samples could sink despite the upward flow. These convective influences clearly had a great impact on the collected data; however, since both the irradiated samples and reference samples appeared to very consistently follow the same currents, it is believed that the difference in their density was reliably recorded by the experiment. The test tubes were periodically shaken to break the samples free from the tube wall or liquid surface, but this shaking was never seen to have any observable effect on the flow of the lower convective cell. Viewing of the samples was clear and easy. This was greatly helped by the magnifying effect of the water-filled cylindrical jar and the heavy liquid-filled test tubes.

On subsequent runs, the water bath was emptied by siphoning then refilled with tap water to rapidly cool the liquid in the tubes and bring the samples back to floating. Care was taken for each run to start at a temperature several degrees below the sinking temperature of the first sample to sink, so that the system would be at steady state before any sinking occurred.

Runs were attempted in which the starting temperature was high and all samples were firmly at the bottom of the test tubes at the start. By stirring the water bath without heating, the liquid in the tubes was cooled. The cooling rate obtained this way was impractically low, so cool water was added. This process was not well controlled, and yielded results that do not at all agree with the heating runs. This

approach was therefore abandoned.

4.3.3 Unshielded irradiations at the MIT reactor

4.3.3.1 Sample preparation

Pyrex and Hoya SD-2 wafers approximately 0.78 mm thick were diced using a diamond saw. Squares approximately 3 mm \times 3 mm were cut for use in the sink/float apparatus. The sink/float technique compares the density of one material sample to that of another. Accordingly, samples were needed both to be irradiated and to be left unirradiated for comparison purposes. For each planned exposure level, samples were prepared in pairs, with one to be irradiated and one not. Since the sink/float method assumes the use of two pieces of glass of initially identical density, it was necessary to minimize the probability of the glass pieces within a sample pair having an initial density difference due to local inhomogeneities in a glass wafer. Care was therefore taken to take sample pairs from the same wafer, and even to take adjacent pieces of glass as pairs. Figure 4-11 shows an example of how the pairs were selected from a diced Pyrex wafer.

For the first set of sink/float measurements, involving the MIT reactor-irradiated samples, it was not known beforehand how easily the irradiated and unirradiated glass samples could be distinguished. Reference samples were therefore prepared with a corner cut from each square wafer, the cut connecting the midpoint of two sides.

All samples came back tinted a brown color, evidence of trapped electronic defects. The color of the Pyrex samples varied continuously and conspicuously from light to

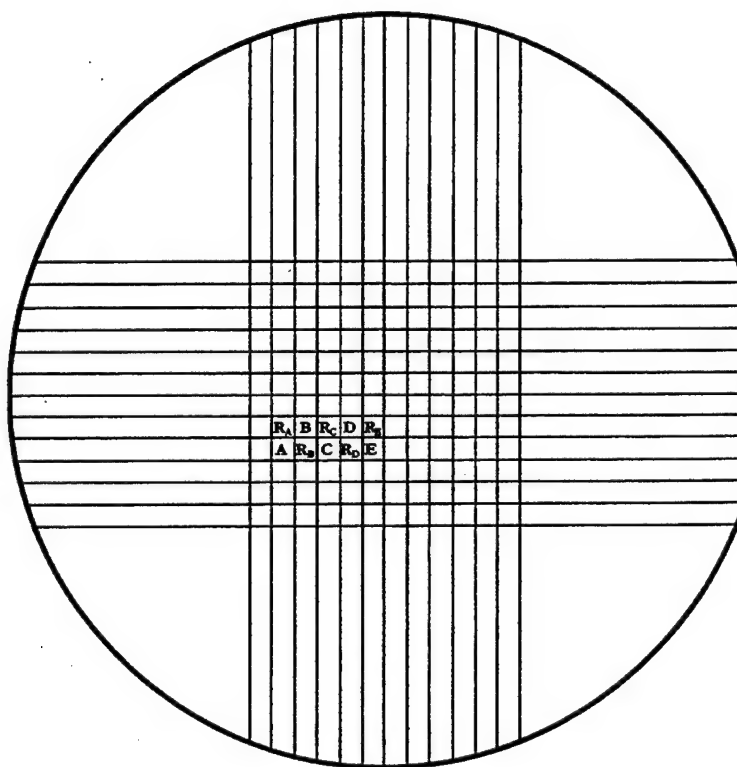


Figure 4-11: Diced Pyrex wafer showing sample pair selection.

medium brown as the sample exposure rose. In the case of the Hoya SD-2, the coloration seemed to be quite equal among the three samples receiving the highest doses, which points to a possible saturation of the electronic defects. The Hoya SD-2 glass was not as darkly colored as the Pyrex. These observations are just cursory impressions, however, and no quantification of this effect was made using optical absorption spectrometry or other techniques.

Samples were cleaned by rinsing them with acetone. During the cleaning of the Hoya SD-2 samples, problems with air currents in the vent hood led to a complete mix-up of the samples. Their activities had been individually measured upon their arrival at CSDL, and monotonically rose with exposure time, so it was possible to relabel them (we assume correctly).

4.3.3.2 Reactor environment

Samples were irradiated by MIT nuclear reactor personnel in a pneumatic tube, designated as 1PH1, inserted into the core of the MIT reactor. Estimates furnished by MIT personnel of the fast and thermal neutron fluxes for samples within 1PH1 are 1×10^{11} n/cm²/s fast and 6.7×10^{11} n/cm²/s thermal. Samples were held within plastic tubes ("rabbits") that are 2.5 cm in diameter and about 6.1 cm long. These rabbits are used to shuttle samples to various proximities to the reactor core in pneumatic tubes. The samples were sealed in polystyrene wrapping, then buried in silica sand within the rabbit. The silica sand served as a heat sink for the heat that was generated within the samples by the irradiation. Of particular concern for heating was the large boron cross section for thermal neutron absorption, as shown in Equation

2.4. The temperature of the samples during irradiation was not monitored, but did not exceed the softening point (~ 90 C) of the polystyrene wrap.

An irradiation schedule was decided for the glass samples based on work by Paymal[96] and the TRIM calculations discussed in section 4.2. Based upon the experiment design, it was determined that a strain in compaction of 1×10^{-3} was the greatest that would be practical to measure. Paymal's data for Pyrex compaction was for thermal neutrons only, and predictions made based on the low-fluence linear portion of his strain-to-fluence curve show that a 6000 second exposure would result in approximately this 1×10^{-3} strain value. Due to the comparatively low fast neutron flux and the similarity of thermal and fast neutron displacement rates (100 displacements per incident thermal neutron, 22 for a fast neutron), the effects of fast neutrons were expected to be very small. Based on the TRIM-predicted displacement numbers, the damage attributed to fast neutrons in the MIT irradiation would only be 0.3% and 1% of the the damage from thermal neutrons for Pyrex and Hoya SD-2, respectively. At the estimated 10 Mrad/hr gamma dose rate, the compaction due to gamma damage was expected to be completely negligible.

It was our desire to also irradiate a sample set that would be shielded by cadmium against thermal neutrons, in order to isolate the fast neutron effects. This proved difficult, however, due to the large amount of heat that a cadmium shield produced in test irradiations which threatened to melt the plastic rabbits.

No radiation effects data were available for Hoya SD-2 glass, so it was decided that it would be exposed to the same fluences as the Pyrex. While its lower boron content should result in fewer displacements due to thermal neutron absorption, no

Table 4.9: Radiation schedule for glass samples in the MIT reactor.

Pyrex	Hoya	Time, s	Thermal $\frac{n}{\text{cm}^2}$	Fast $\frac{n}{\text{cm}^2}$
PU1A	HU1A	30	2.0×10^{14}	3.0×10^{12}
PU1B	HU1B	60	4.0×10^{14}	6.0×10^{12}
PU1C	HU1C	600	4.0×10^{15}	6.0×10^{13}
PU1D	HU1D	1800	1.2×10^{16}	1.8×10^{14}
PU1E	HU1E	6000	4.0×10^{16}	6.0×10^{14}

predictions could be made as to how much strain would result. The radiation schedule for the glass samples is shown in Table 4.9.

4.3.3.3 Sink/float measurements

Of particular note during this round of sink/float measurements was the fact that the Hoya SD-2 glass showed markedly less attraction for the surface of the liquid than did the Pyrex. This led to improved precision of the measurement as evidenced by less scatter in the data collected for Hoya SD-2 than that of the Pyrex samples. There was some concern that the corners cut from the reference samples for both cases would alter their falling times. No significant difference in the hydrodynamics of the reference samples was noted. They, like the square samples, typically fell edge-on.

4.3.3.4 Results

The results for six measurements each of Pyrex and Hoya SD-2 are shown in Figure 4-12. The error bars shown represent the standard deviation of the six measurements divided by the square root of six. This is the uncertainty for the mean value of the six measurements.[16] It is important to distinguish between this scatter, which

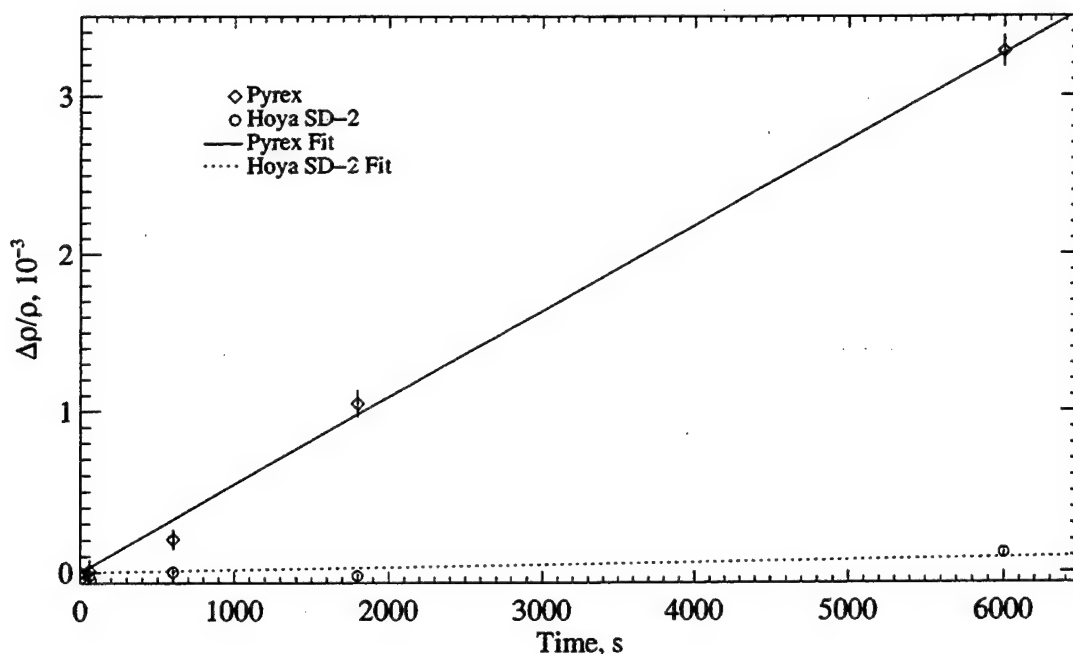


Figure 4-12: The effect of neutron irradiation on the density of glass samples. Relative density change is shown versus irradiation time. in the MIT reactor.

is indicative of the repeatability and precision of the sink/float method, and the accuracy of the conversion of a measured ΔT to a strain. An inaccuracy in the thermal expansivity of the heavy liquids used will add to the inaccuracy of the strain values, but will not contribute to scatter. Scatter in the points is due solely to uncertainty in temperature readings, convective currents, and delays in sinking due to liquid surface attraction. In the ideal situation (no current-induced inaccuracies, no surface-sticking), with our 0.01 °C temperature control, we expect 6 ppm scatter in the data. Table 4.10 summarizes the observed scatter. It can be seen that our experiment achieved sensitivity on par with the very best [110] of other published sink/float results. The raw data for these measurements are listed in Appendix B.

Additional uncertainty (but not scatter) is introduced by the uncertainty of the

Table 4.10: Scatter of six measurements (averaged across data points).

	Pyrex, 10^{-6}	Hoya SD-2, 10^{-6}
σ	55	16
$\frac{\sigma}{\sqrt{6}}$	22	6

thermal expansivity of the liquid. The data analysis here has been done using a value measured by Connors.[31] Connors used the sink/float technique to detect gamma-induced density changes in glasses with densities from 2.13 g/cm³ to 2.52 g/cm³. Her liquid mixtures were all composed of the same two chemicals used here, tetrabromoethane and bromonaphthalene. She observed that the volumetric thermal expansion for all of her liquids averaged to 840 ppm/C, with a standard deviation of 8 ppm/C, and this was the value she then applied to all of her data analysis. A 1% uncertainty in the value for the thermal expansivity of the liquid introduces a 1% uncertainty into the level of strain being measured.

Linear fits constrained to pass through the origin were made to the data from Figure 4-12. Since the data are plotted vs. time, this is not very easy to interpret. So the TRIM estimates of the displacements caused by fast or thermal neutrons (Tables 4.7 and 4.8) were combined with the known fluxes of the MIT reactor to produce the numbers shown in Table 4.11. These numbers relate the relative density change in both glasses to the fluence of neutrons through them, and are valid for a thin target (such as our samples). We have assumed that damage from fast neutron recoil cascades and that from the Li³⁺ and He²⁺ are comparable purely by the number of displacements they cause.

Table 4.11: Results of MIT sink/float measurements.

	Pyrex	Hoya SD-2
$\frac{\Delta\rho/\rho}{n/\text{cm}^2}$, thermal	8.14×10^{-20}	2.21×10^{-21}
$\frac{\Delta\rho/\rho}{n/\text{cm}^2}$, fast	1.79×10^{-20}	1.71×10^{-21}

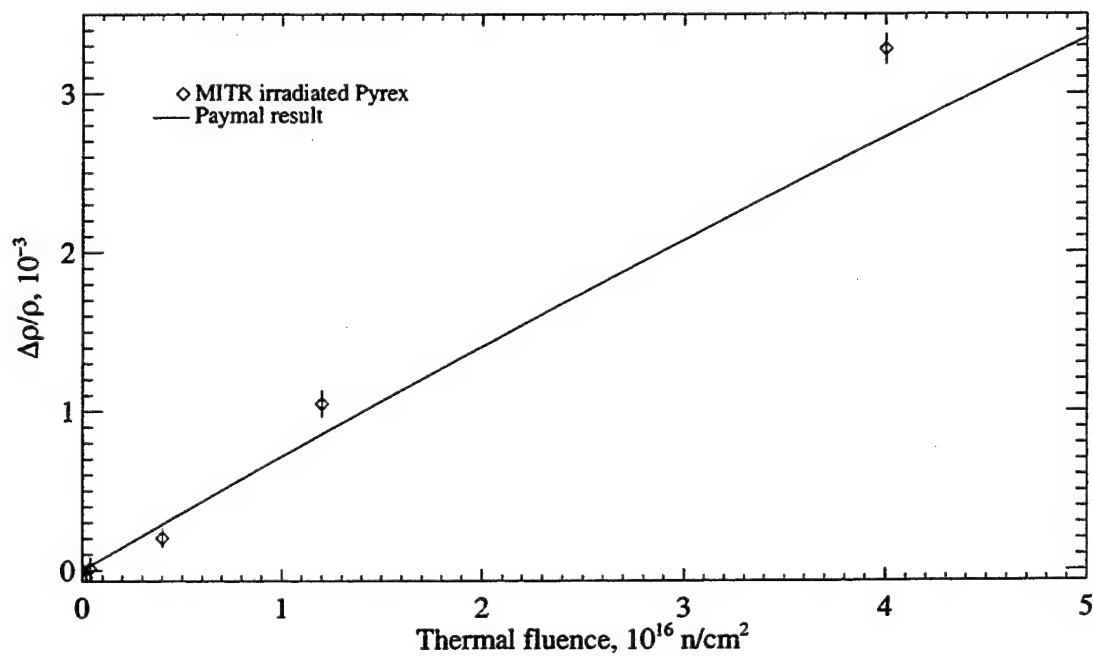


Figure 4-13: Comparison of MIT reactor results for Pyrex with those of Paymal.

A comparison of our results for Pyrex with those previously obtained by Paymal[96, 95, 97, 98] is shown in Figure 4-13. There is good agreement between our results and Paymal's. The small deviations between the two curves can be due to a number of reasons. Among these are differences in samples size, differences in the reactor environment, and small differences in composition. Paymal appears to have used 5 mm cubes of Pyrex, which would have somewhat more self-shielding than our samples. The fast neutron and gamma environments almost certainly were somewhat different for Paymal's irradiations. Overall, the agreement that we observe between our results for Pyrex and Paymal's gives us confidence in our experimental procedure.

4.3.4 Shielded irradiations at the University of Missouri-Columbia

4.3.4.1 Motivation

The results of the MIT reactor irradiations of Pyrex and Hoya SD-2 glass made it clear that the Hoya SD-2 glass is more resistant to radiation compaction than is Pyrex. But even with an order of magnitude less compaction than Pyrex for a given displacement dose, the results of the pointer beam strain gauge gamma irradiations (section 4.1) are left unexplained. To examine what, if any, effects the anodic bonding process had on the radiation compaction of the two glasses, it was decided to prepare samples in various states of the bonding process and then to irradiate them.

An additional motivation was to attempt to isolate, in as much as this would be possible, fast neutron damage in the glasses. The damage for the MIT irradiations was dominated by that from thermal neutrons, and it was hoped that the assumptions

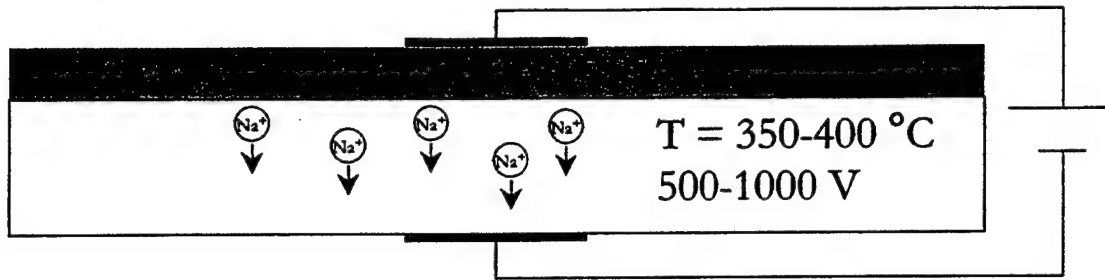


Figure 4-14: Schematic representation of the anodic bonding process. The shaded and white portions represent the silicon and glass wafers, respectively.

we've made about relating thermal neutron to fast neutron damage based on TRIM simulations could be tested.

4.3.4.2 Sample preparation

Anodic bonding is accomplished by placing a silicon wafer in close contact with a glass wafer, then subjecting the pair of wafers to elevated temperatures while they sit in an electric field. In the case of our samples, we followed a standard procedure used in the fabrication of silicon MEMS devices. The wafers were heated to 350 C and then allowed to sit at this temperature for about one hour. During this time, 1000 V were applied across the wafers as shown in Figure 4-14.

At the elevated temperature, sodium ions in the glass become mobile, and move away from the interface. The resulting depletion region gives rise to a large electric field at the interface of the two wafers. This brings the wafers into intimate contact, and oxygen-silicon bonds are formed between the wafers. After cooling back down to room temperature, a white powder on the side of the glass away from the interlayer interface was observed to have appeared on the footprint of the cathode. X-ray

analysis confirmed that this powder was largely composed of sodium oxide.[127]

The sample set is composed of five different glass types, which we label A through E. The first (A) is the as-delivered glass wafer. The second (B) is a wafer that has been heated to 350 C, following the temperature schedule of a standard anodic bonding cycle. The third type (C) is the same as type B, except that a voltage has been applied across the wafer during the heating cycle. This type was run through the full bonding process, but with the silicon wafer missing. The fourth type (D) was anodically bonded to a silicon wafer. The silicon wafer was then etched away in a KOH bath. The fifth type (E) was like type D, but was additionally dipped into a HF bath to ensure that the interface bonding layer would be completely removed.

The wafers were then diced with a diamond saw as for the samples in section 4.3.3 into 3 mm \times 3 mm pieces. Thickness of the wafers was either 780 μ m or slightly less for those that had been etched. Five sample pairs were selected for sink/float measurement from each wafer, again selecting neighboring glass squares for the irradiated/reference pairs as in Figure 4-11. With full sample sets for both Pyrex and Hoya SD-2, there was a total of 50 samples for irradiation and 50 paired reference samples.

4.3.4.3 Reactor environment

The glass samples were irradiated at the University of Missouri-Columbia 10 MW research reactor (MURR). Similar to the MIT reactor, the MURR uses "rabbits" in tubes to shuttle samples in and out of the radiation environment. A key difference for our experiment was that the MURR rabbits are made of aluminum, not plastic. They

run inside of tubes through which water flows at a constant 30 C. Thus there is the possibility of removing heat from the samples and their packaging during irradiation.

The fast flux of location of our samples was estimated, based on the characterization furnished by MURR personnel, to be $\sim 6 \times 10^{12}$ n/cm²/s. The thermal flux was cited as being $\sim 3 \times 10^{13}$ n/cm²/s. We were warned (only in the aftermath of the experiment while trying to make sense of the results, unfortunately), however, that this measurement is relatively old, and that shielding in the reactor had degraded significantly. A recent estimate of thermal flux predicted an absolute upper limit of 1×10^{14} n/cm²/s. The gamma dose rate for our samples was on the order of 10 Mrad/hr, similar to the MIT reactor. Based on the gamma-induced compaction in previous studies of Pyrex and silica, the gamma doses accrued in our samples during the MURR irradiation were of negligible effect on density.

4.3.4.4 Shield design

Given the large thermal neutron component to the neutron flux environment at MURR, it was necessary to shield the samples against them in order to see the effects of fast neutrons. Following the recommendation of MURR personnel (who discouraged the use of cadmium), a shield design was made using boron nitride. We used high-purity AX05 grade boron nitride[21] in order to avoid nuclear activation of impurities. Table 4.12 shows various properties of AX05. Of particular note for our application are its softness (making it easy to machine) and good thermal conductivity.

It was (somewhat arbitrarily) decided that a fast/thermal neutron flux ratio of 50

Table 4.12: Physical properties of Carborundum AX05 boron nitride.

Density, g/cm ³	1.9
Specific heat at 700 C (J/g/C)	1.5
Maximum use temperature in	
Oxidizing atmosphere	850 C
Inert atmosphere	1800 C
Hardness-Knoop (kg/mm ²)	3.42-4.91
Thermal Conductivity (W/m/K) at 25 C:	
Parallel to pressing direction	73.3
Perpendicular to pressing direction	121.2
Thermal Expansion Coefficient 25-1500 C (10 ⁻⁶ /C)	
Parallel to pressing direction	0.57
Perpendicular to pressing direction	-0.46
Open porosity	14.2%

was desirable for this experiment. Using the density of AX05, the atomic weight of boron and nitrogen, and the average thermal neutron capture cross section for boron of 767 barns, it was calculated that a shield thickness of 1.6 mm would be sufficient to shield out all but 0.4 % of the incident thermal neutrons, thereby achieving the desired flux ratio. Reactor personnel told us, however, that in practice only 90-99 % of the thermal neutrons could be effectively shielded. This is due to the thermalizing effect thick shielding has on epi-thermal and fast neutrons. We kept the 1.6 mm thickness, however, since this was about as thin a boron nitride shield as could be comfortably machined and handled.

The rapid absorption of thermal neutrons by the shield was expected to create a substantial amount of heat. Calculations predicted that in a thermal flux of $\sim 3 \times 10^{13}$ n/cm²/s, the shield would rise in temperature at an initial rate of about 14 C/s. Because of the need to keep the glass samples below 100 C to avoid annealing of ra-

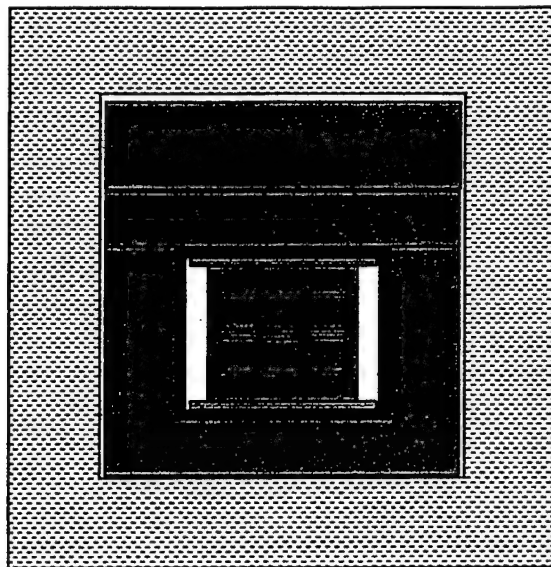


Figure 4-15: Diagram of sample holder during irradiation, in cross section. The inner grey portion is the sample holder. The black inner container is the boron nitride shield. The aluminum container is shown in grey, as is the aluminum slug sitting on top of it. The surrounding black rectangle is the aluminum rabbit, outside which the hashed portion represents water.

diation damage, this heat needed to be evacuated. The concept for sample packaging was therefore as shown in Figure 4-15. An aluminum sample holder would sit inside the cylindrical boron nitride shield inside the aluminum rabbit. The space between the BN shield and the rabbit wall needed to be filled with a solid aluminum casing so that the heat generated within the shield would have a highly conductive path to the rabbit wall, which was in contact with water at 30 C.

The rabbit, casing, slug, and sample holder were machined using 1100 Aluminum, which is high purity and approved for MURR use. The sample holder contained six hollows on each face in which samples were snugly held, with a sliding door that kept them secure. The pinching down of bendable flanges (1100 aluminum is very soft) allowed the door to be secured. Figure 4-16 contains a photo of the sample holder.

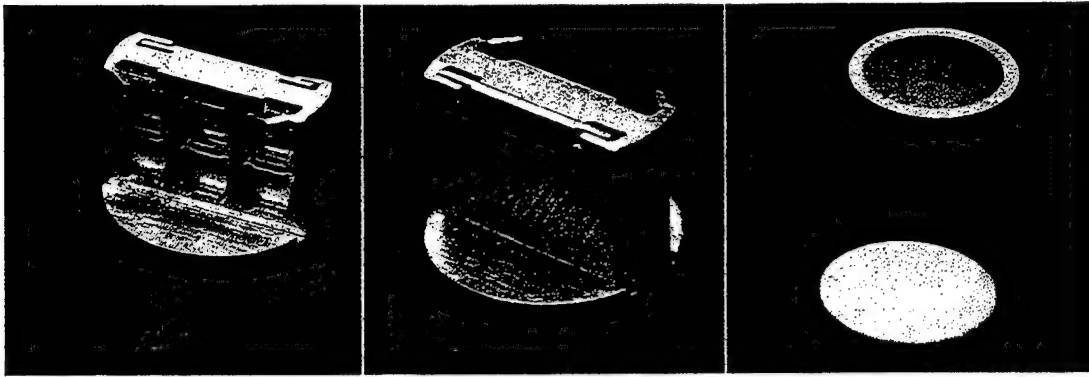


Figure 4-16: High-purity aluminum sample holder shown open at left and closed at center. Two glass samples are shown in the foreground at left. One of the samples has been darkened by irradiation. The boron nitride pillbox thermal neutron shield and its lid are shown at right.

The boron nitride shield was press fit into the aluminum casing, after which the casing was press fit into the rabbit, which had been sent from the reactor. The BN lid was placed on the BN pillbox, and the aluminum lid was placed on top of the BN lid. The Al lid was made to be of a slightly smaller diameter (~ 0.1 mm) than the inner diameter of the rabbit, so press fitting was not necessary. This loose fit was done to allow for later extraction of the samples. An aluminum slug was pressed into the rabbit on top of the Al lid, then the rabbit lid was welded into place. The slug was put into place by MURR personnel because they needed to inspect the contents of the rabbit prior to irradiation. They cut the slugs (which were originally about 6 cm in height — the amount needed to fill all the empty space in the rabbits that were shipped to us) and the rabbits down in height from the top in order to reduce the mass at risk for activation.

In view of the terrible heating problem posed by the boron nitride shield, a rough thermal analysis was made of the experimental geometry. The analysis is summarized

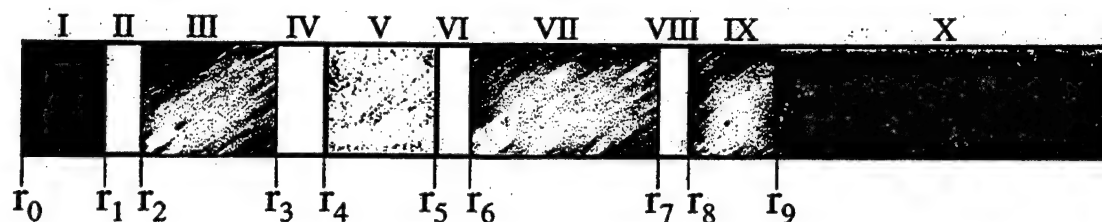


Figure 4-17: One-dimensional thermal model for shielded irradiation of glass samples at MURR. The origin is at the left. The regions numbered with roman numerals are concentric cylinders. Region I is a Pyrex glass cylinder, and the sample holder. Region III represents the aluminum sample holder inside the boron nitride shield (region V). Regions VII and IX are the aluminum filler and rabbit, respectively. White regions are air gaps between solids regions. Region X is water held at 30 C.

here — the details comprise Appendix D. We assumed an infinite concentric cylindrical geometry in which the layers included the glass samples, the aluminum sample holder, the BN shield, the aluminum casing, and the rabbit wall. This arrangement is shown in Figure 4-17. Solving the heat equation for this model, we obtained the results of Table 4.13. The estimation of effective air gaps is explained in Appendix D. It can be seen that for the larger thermal neutron flux and a shield that is less than ideally efficient, the heating facilitated by even a 1 mil gap between layers V and VII will result in a large temperature rise in the glass samples.

Based on prior studies of the annealing of radiation damage in borosilicate glass (see section 2.3.2.2, we wished to keep the temperature of the samples below 150 C in order to avoid thermally annealing the radiation damage as it was created. The thermal analysis showed that it was possible to keep temperatures at these levels, but that variables over which we had little control could make temperatures exceed the desired level. We therefore wished to include some type of temperature monitor. We decided upon including some waxes of known melting temperature, the idea being

Table 4.13: Scenarios for glass sample heating during the MURR irradiation. The assumed thermal neutron flux ($\text{n/cm}^2/\text{s}$) incident on the boron nitride shield and the fraction thereof that is incident on the glass are at left. Air gaps between solid regions of Figure 4-17 are given in meters. ΔT represents the amount by which the glass center (r_0) is above T_o (C).

Flux	Fraction	I-III (Glass-Al)	III-V (Al-BN)	V-VII (BN-Al)	VII-IX (Al-Al)	ΔT
3×10^{13}	0.01	0.00	0.00	0.00	0.00	1.44
		1.00×10^{-4}	0.00	0.00	0.00	1.96
		0.00	1.00×10^{-3}	0.00	0.00	2.14
		0.00	0.00	2.54×10^{-5}	0.00	48.35
1×10^{14}	0.10	0.00	0.00	0.00	0.00	7.32
		1.00×10^{-4}	0.00	0.00	0.00	24.93
		0.00	1.00×10^{-3}	0.00	0.00	30.62
		0.00	0.00	2.54×10^{-5}	0.00	178.04

that if we shaped pointy bits of wax, we would be able to tell if they had melted during the experiment. Two important questions were raised regarding the wax. The first was if irradiation would change the baseline melting temperature. This might happen due to bond breaking and crosslinking of the polymers that make up the wax. The second issue was the risk of activation of impurities in the wax.

Several waxes of various nominal melting points were irradiated at the MIT reactor to fluences on the order of those expected for the glass experiments at the University of Missouri-Columbia. It was believed that the ambient temperature of the irradiation tube (2PH1) would be under 50 C. After three days of irradiation, for a total fast neutron flux of $\sim 4 \times 10^{17} \text{ n/cm}^2$, the results were as shown in Table 4.14.

The two samples described as "melted" were very much changed from their original state. They no longer resembled wax, but were brittle. That they had melted was evident by the the fact that they had run into the shape of their container. The

Table 4.14: Results of wax irradiations in the MIT reactor. Waxes were purchased from McMaster-Carr. Nominal melting temperatures are in centigrade.

Sample	Type	Color	Nominal T_m	Change
S3	Hi-Temp	Tan	137.8	None
S4	Machinable	Purple	114.4	None
S2	Super-Flex	Dark Brown	83.3	Melted
S1	EZ-Sculpt	Red	66.7	Melted
S5	Parrafin	White	54.4	Vaporized

pure parrafin wax had apparently disappeared from its container. The two non-melted waxes looked somewhat shriveled and discolored. It is very possible that these changes were due, in part, to the large gamma dose they would have recieved during their three day irradiation. The fast dose at the Missouri reactor could be accumulated with much less gamma dose, so this may not have been a problem for the glass irradiations.

The waxes, however, could not be used for the Missouri experiment since they had activated significantly during this irradiation. Though the boron nitride shielding would significantly reduce this activation, MURR personnel denied us permission to include the waxes in our experiment. We therefore irradiated the glass samples without temperature monitoring capability.

4.3.4.5 Irradiation schedule of sink/float samples

The five sample sets for each glass type were sent to the University of Missouri-Columbia research reactor (MURR) for irradiation according to the schedule of Table 4.15. We used the results from the previous experiment for the raw glass to estimate

Table 4.15: Planned schedule for irradiation of shielded Pyrex and Hoya SD-2 glass samples at the University of Missouri-Columbia reactor. The calculation assumed that the boron nitride shield would absorb all but 0.4% of the incident thermal neutrons. The ratio of the compaction due to fast neutrons compared to that due to thermal neutrons would be ~ 39 for Hoya SD-2 and ~ 11 for Pyrex (ratios calculated using results from section 4.2). The ΔT figure refers to the predicted difference between irradiated and non-irradiated reference samples in the sink/float experiment.

Set	Time h	Fast Fluence n/cm^2	$\Delta\rho/\rho$ (raw glass)		$\Delta T, C$	
			Hoya SD-2	Pyrex	Hoya SD-2	Pyrex
1	18.3	3.95×10^{17}	9.60×10^{-4}	7.86×10^{-3}	1.14	9.36
2	14.6	3.16×10^{17}	7.68×10^{-4}	6.29×10^{-3}	0.91	7.48
3	11.0	2.37×10^{17}	5.76×10^{-4}	4.72×10^{-3}	0.67	5.61
4	7.3	1.58×10^{17}	3.84×10^{-4}	3.14×10^{-3}	0.46	3.74
5	3.7	7.91×10^{16}	1.92×10^{-4}	1.57×10^{-3}	0.23	1.87

the amount of compaction for a given neutron dose. Irradiations had to be planned while taking into account the limitations of the sink/float measurement technique. If ΔT were too small, it might be beyond sensitivity of our measurements. If ΔT were too large, the time required for the measurement might become impractical, or worse, require the heating of the heavy liquids to dangerous temperatures.

Our irradiation schedule was optimistic in that we counted on the boron nitride shield to increase the fast/thermal neutron ratio to 50:1. We expected, however, that thermalization by the BN shield and the other packaging materials of our experiment of higher-energy neutrons would reduce this ratio somewhat.

A critical limitation for planning purposes was activation of the glass samples and their packaging. The packaging materials we selected were of high purity (the AX05 grade boron nitride and the 1100 aluminum). The activation of these materials was unpredictable, but less critical than that of the glass samples. The samples could

Table 4.16: Results and calculations for the MIT reactor test irradiation of Hoya SD-2 glass. The irradiation was 10 minutes long in a thermal neutron flux of $\sim 4 \times 10^{12}$ n/cm²/s. The sample was 1 cm \times 1 cm \times 0.078 cm in size. See Appendix E for details on the symbols and equations used for these calculations.

Element	Sb		Zn
Active isotope	122	124	65
Data			
Activity, μCi , $t = 7 \text{ days}$	1.40	0.132	0.226
Parent isotope	121	123	64
Abundance of parent (%)	57.3	42.7	48.9
σ	5.90×10^{-24}	4.15×10^{-24}	7.60×10^{-25}
$t_{1/2}$, days	2.72	60.3	265
Calculations			
Activity, μCi , $t = 0$	8.33	0.143	0.230
n_o , cm ⁻³	9.09×10^{19}	4.92×10^{19}	1.90×10^{21}
Atom % of element	0.207	0.151	5.07
Average atom %	0.179		5.07

always be removed in a hot cell were the packaging activation a problem. We had to make sure that the glass samples would remain below the 5 mrem/hr limit imposed by Draper Laboratory regulations.

We made detailed calculations of likely activation based on the chemical composition of the glasses, as measured by XPS (see section 1.2). The method for doing these calculations is discussed in detail in Appendix E. These calculations predicted that even for a thermal flux of 3×10^{12} n/cm²/s, activation would not be of major concern.

To verify these calculations, a test irradiation of two (one of each of Pyrex and Hoya SD-2) 1 cm \times 1 cm glass samples was carried out at the MIT reactor. The results of counting the activity of the samples after the irradiation are shown in Table 4.16. Only the Hoya SD-2 glass experienced significant activation.

Antimony was not detected in Hoya SD-2 by the original XPS measurements (see section 1.2). Furthermore, the zinc concentration deduced from the activity of Zn-65 was over a factor of five more than was detected by XPS. We chose to use the concentration of antimony that was deduced from the activation experiment and the XPS value for zinc for planning purposes for the Missouri reactor irradiation experiments.

4.3.4.6 Sink/float experiment

The sink/float experiment involved only the Pyrex samples. The irradiated samples were sufficiently darkened to be easily distinguished from the non-irradiated reference samples. It was therefore not necessary to cut a corner from the latter as for the first set of sink/float measurements. The experiment took place within a hood that was very brightly lit, and although an effort was made to cover the experiment with aluminum foil when not in use, darkening of the heavy liquid solution was noticed over a period of two months. Bromated compounds are known to break down with light. The experiments were accomplished with a few weeks after the solutions were first mixed and exposed to the light, and we did not notice any change in the behavior of the liquids during this period.

4.3.4.7 Results

After irradiation at the Missouri reactor, the glass samples underwent a two month cooling period. Upon receiving the glass samples from the Missouri reactor, it was determined that the Hoya SD-2 samples had activated much more than had been

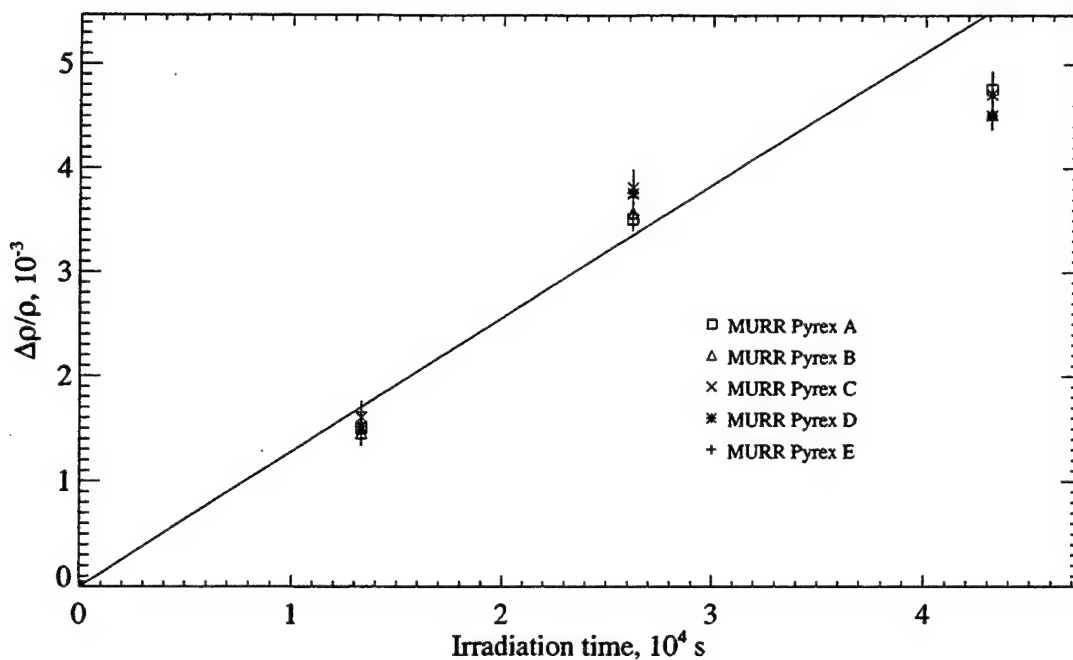


Figure 4-18: Relative density change versus irradiation time for Pyrex sink/float samples. The line is fit only to the first two points of the sample A measurements. Each data point is the average of six measurements, and the error bars represent $\sigma/\sqrt{6}$ for these measurements.

anticipated. The principal problem isotope was Sb-124. The activity of these samples well exceeded the permissible limit for bringing them into Draper Laboratory. Therefore, results for density change in the Hoya SD-2 glass samples could not be obtained. Furthermore, since the activity of the Hoya SD-2 samples was unacceptable, personnel at the Missouri reactor declined to irradiate sample sets one and two.

The Pyrex samples manifested very low activity, however, and it was possible to make sink/float measurements of their density change. A plot of density change versus irradiation time is given in Figure 4-18.

Looking at Figure 4-18, it is immediately clear that the various treatments to which the glass samples were subjected made no detectable difference to the bulk

Table 4.17: Thermal neutron flux ($n/cm^2/s$) in the irradiated samples at the Missouri reactor deduced from activation of zinc and antimony. The numbers quoted for each sample type (A, B, C, D, and E) are the mean of the three irradiated sample sets (3, 4, and 5).

Assumes 0.18 % Sb and 0.75 % Zn.

Type	Sb-124	Zn-65	Ratio
A	3.32×10^{13}	1.41×10^{13}	0.42
B	3.43×10^{13}	1.49×10^{13}	0.43
C	3.40×10^{13}	1.44×10^{13}	0.42
D	3.28×10^{13}	1.34×10^{13}	0.41
E	2.51×10^{13}	1.07×10^{13}	0.43

glass irradiation-induced densification. All the densification measurements at each irradiation time are within the measurement uncertainty of each other, and we noticed no systematic ordering of measurements for the five glass types.

In order to compare these results with those of the previously irradiated raw glass, it is necessary to analyze the data in terms of densification caused by fast and thermal neutron damage. In order to estimate the thermal neutron flux to which the samples were subjected, we examined the measured activities of the Hoya SD-2 glass samples. The activity measurements are catalogued in Appendix F. The activity of the irradiated Pyrex samples was low enough that it was not possible to identify the activated species. Using the activities of isotopes Zn-65 and Sb-124 and taking the concentrations of antimony and zinc to be 0.18 % and 0.75 % (from the MIT test irradiation and the original XPS measurements, respectively), we obtain the results shown in Table 4.17.

The thermal neutron flux incident on our glass samples deduced from the Sb-124

activity is troubling, since this is slightly above the nominal incident thermal neutron flux of 3×10^{13} n/cm²/s that was originally quoted to us by MURR personnel. Also of concern is that the predictions for flux made using the activity of Zn-65 is less than half those made using the activity of Sb-124. It was hypothesized that the composition of the Hoya SD-2 we irradiated may have been substantially different than that of the samples used in the XPS measurements.

New XPS measurements were therefore made on a sample of the Hoya SD-2 glass taken from the wafer that supplied the irradiated samples of type A (untreated glass).[127] The result was an atomic concentration of 0.925 % Zn and 0.72 % Sb. The results of a recalculation of the thermal neutron flux based on these new values are given in Table 4.18. The flux according to the Zn and the Sb activation are closer to each other using the new values for atomic composition, both in absolute and relative terms. There is obviously some residual error in the relative proportion of zinc to antimony. For the analysis that follows, we assume the thermal flux incident on our samples was the average of the values in Table 4.18 for glass types A, B, and C. This value is $F_{th} = 1.01 \times 10^{13}$ n/cm²/s.

The samples of type E clearly had less activity than the other wafers. This is not surprising, since sample E had been etched in both KOH and HF to remove the silicon layer to which it had been bonded. There is therefore less mass in an E sample than in samples of other types. Similarly, type D is missing a smaller amount of mass due to etching in KOH.

We now compare the results of Figure 4-18 to those of MIT reactor irradiation of Pyrex glass (Table 4.11). As before, we use the TRIM predictions for displacements

Table 4.18: Thermal neutron flux ($\text{n/cm}^2/\text{s}$) in the irradiated samples at the Missouri reactor deduced from activation of zinc and antimony. The numbers quoted for each sample type (A, B, C, D, and E) are the mean of the three irradiated sample sets (3, 4, and 5).

Assumes 0.72 % Sb and 0.925 % Zn.

Type	Sb-124	Zn-65	Ratio
A	8.26×10^{12}	1.14×10^{13}	1.38
B	8.52×10^{12}	1.21×10^{13}	1.41
C	8.46×10^{12}	1.17×10^{13}	1.38
D	8.14×10^{12}	1.09×10^{13}	1.34
E	6.23×10^{12}	8.65×10^{13}	1.39

in fast and thermal neutron collision cascades (Tables 4.7 and 4.8) to apportion densification between fast and thermal neutron damage. Using the reported fast neutron flux of $6 \times 10^{12} \text{ n/cm}^2/\text{s}$ and the activation-deduced thermal neutron flux of $1.01 \times 10^{13} \text{ n/cm}^2/\text{s}$, we obtained the results of Table 4.19. Linear fits were made to the data in Figure 4-18 using only the two lowest-dose points and constraining the fit to pass through the origin. At the highest irradiation time, the trend of the data makes it appear as though the data is departing from the linear relation that we have assumed to be present at the lower doses. This is probably due to saturation of the densification due to radiation damage.

Since the Pyrex densification in the MIT reactor irradiation agreed well with the previous work by Paymal, we will assume that this should also be the result for the samples of type A (the untreated glass). In this case, it would appear that the present results for the untreated glass are over a factor of seven off the mark. The obvious culprit for this error is the probable elevated temperature.

Table 4.19: Interpretation of the results in Figure 4-18 and comparison with the MIT reactor experiment results for Pyrex.

Type	$\frac{\Delta\rho/\rho}{n/cm^2}$, thermal	$\frac{\Delta\rho/\rho}{n/cm^2}$, fast
A	1.12×10^{-20}	2.46×10^{-21}
B	1.18×10^{-20}	2.59×10^{-21}
C	1.22×10^{-20}	2.69×10^{-21}
D	1.15×10^{-20}	2.54×10^{-21}
E	1.21×10^{-20}	2.66×10^{-21}
Pyrex (MIT)	8.14×10^{-20}	1.79×10^{-20}

With the range of possible unshielded thermal neutron flux values being from 3×10^{13} n/cm²/s to 1×10^{14} n/cm²/s, it would appear that our thermal neutron shield operated far less efficiently than we had hoped. The shield effectively removed 66–90 % of the incident thermal neutrons. The thickness of the shield was calculated to absorb 99.6 % of the incident thermal neutron flux. It doubtless did just this. However, as mentioned above, the shielding materials around our samples will have thermalized higher-energy neutrons, and we had no estimate of just how many extra thermal neutrons this would produce inside the boron nitride shield.

Table 4.20 contains the predictions of the thermal model described in section 4.3.4.4 for the two scenarios that bound the likely experimental situation. The second scenario seems the more plausible since, as related to us by personnel at both the MIT and Missouri reactors, 10 % is a typical value for the saturation level for a thermal neutron shield in the reactor environment. Furthermore, the temperature of the first scenario of Table 4.20 is close to the temperature at which the annealing of radiation damage begins. Given the large annealing effects present in our data, the higher temperature appears more likely.

Table 4.20: Predictions of the thermal model of section 4.3.4.4 for the likely bounds of the MURR glass irradiation. The assumed thermal neutron flux ($n/cm^2/s$) incident on the boron nitride shield and the fraction thereof that is incident on the glass are at left. Air gaps between solid regions of Figure 4-17 are given in meters. ΔT represents the amount by which the glass center (r_0) is above T_o (C).

Flux	Fraction	I-III (Glass-Al)	III-V (Al-BN)	V-VII (BN-Al)	VII-IX (Al-Al)	ΔT	T (C)
3×10^{13}	0.34	1.00×10^{-4}	1.00×10^{-3}	2.54×10^{-5}	0.00	109	139
1×10^{14}	0.10	1.00×10^{-4}	1.00×10^{-3}	2.54×10^{-5}	0.00	219	249

4.4 Discussion

Perhaps the only completely unambiguous result produced by our experiments is the characterization of the neutron-induced densification of Hoya SD-2, which was seen to be an order of magnitude more radiation-resistant than Pyrex. Our execution of the sink/float technique was quite successful, as evidenced by the agreement of our Pyrex data with previous results and the relatively low scatter in our data.

The results of the pointer beam strain gauge experiment remain unexplained. Complex interfacial phenomena of the anodic bond between the silicon beam and the glass substrate may be to blame for the unexpected results. The irradiation of treated glasses seems to indicate that anodic bonding has no effect on the radiation response of the bulk glass. Though the temperature of the irradiations at the Missouri reactor certainly affected our results, all of the treated glasses compacted to the same degree. One may wonder if the any "rad hardness" that had been imparted to the glass by the anodic bonding process had not simply been annealed away by the elevated temperatures during the irradiation. A measurable fraction of the radiation-

induced compaction remained despite the high temperatures, and it seems unlikely that the differences between our glass samples would be able to dramatically affect their radiation response and yet anneal out at lower temperatures than did some of the radiation damage.

Furthermore, there are changes that anodic bonding caused in the glass that elevated temperature alone could not remove. The sodium oxide that was observed to crystallize on the backside (away from the bonding interface) of the glass came from within the glass. Sodium was thereby permanently removed from the glass. The electric field that moved the sodium through the glass (and perhaps had other effects as well) during anodic bonding was not present during irradiation. It is therefore impossible that the elevated irradiation temperature could have completely annealed away all of the anodic bonding-induced alterations in the glass.

Had bulk radiation response in the glass been significantly altered, we would therefore expect to see some residual differences in the radiation compaction of our treated and untreated glass samples. We did not observe these differences, and therefore surmise that the bonding interface and/or the depletion layer in the glass was (were) responsible for relieving stresses and differential strains between the silicon MEMS and the glass substrate in our gamma irradiation experiment. The mechanism for this process is not understood, and will require further study.

Other sources of uncertainty in our results include the not-very-well-defined fluxes of thermal and fast neutrons for our experiments and the apparently variable and unpredictable composition variations in our glasses. The reactor calibrations for neutron flux at the specific locations of our irradiations were not recent measurements, and

may be significantly different than the numbers we assumed. We have attempted to estimate the thermal flux of the irradiations, at least, by using the activation of antimony and zinc in the Hoya SD-2 glass. The large relative variability in the concentration of these minor component (bordering on being only a trace in the case of antimony) elements in Hoya SD-2 limits the precision of these calculations, however.

We are nevertheless able to conclude that in its raw form, Hoya SD-2 is significantly more radiation resistant than Pyrex. It will be important to now verify the result of the pointer beam strain gauge gamma irradiation, which indicates that the anodically bonded device does not follow the predictions of irradiation-induced silicon-substrate strain that are made based on the radiation compaction/swelling of the individual materials.

Chapter 5

Simulation of mechanical property effects of defects in silicon

5.1 Simulation approaches

5.1.1 Choosing EDIP

5.1.1.1 Empirical silicon potentials

Atomistic modeling is ideally done using *ab initio* quantum-mechanical calculations. For systems with many atoms, however, this is not always possible, or, given limited computer resources, possible. Empirical potentials permit the simulation of larger systems for longer times than *ab initio* methods. Unfortunately, these potentials sacrifice accuracy in the effort to simplify calculations. Typically having a simple functional form with parameters fit to experimental and *ab initio* data, these potentials are often limited in their transferability to problems other than the specific ones they

were designed and fit for.

The most popular potential to date for silicon has been the one by Stillinger and Weber.[116] This potential would be quite attractive for studying the elastic properties of silicon, since it makes a good description of elastic constants in the crystal. An extensive review and comparison of the most used and characterized empirical interatomic potentials for silicon found that none of the potentials was generally superior to the rest, however.[8]

For our purpose of modeling the effect of defects on the elastic constants of silicon, we need a potential that not only describes the elasticity of the crystalline state, but has transferability to defected silicon (up to and including the amorphous state). It is for this reason that we chose to use the environment-dependent interatomic potential (EDIP).[12, 13, 61] This potential incorporates an explicit coordination dependence. This is in the spirit of the embedded atom method used in metals,[38] and is a feature that Stillinger-Weber lacks. EDIP has been shown to make a good description of point defects, dislocation cores, and amorphous silicon.[61] Stillinger-Weber, however, does handle dislocations well, but only makes a good description of amorphous silicon with specially fit parameters.[128]

5.1.1.2 Description of EDIP

EDIP describes the energy of each atom in terms of separate two-body and three-body potentials:

$$E_i = \sum_{j \neq i} V_2(R_{ij}, Z_i) + \sum_{j \neq i} \sum_{k \neq i, k > j} V_3(\vec{R}_{ij}, \vec{R}_{ik}, Z_i) \quad , \quad (5.1)$$

where R_{ij} and R_{ik} are the neighbor distances, and Z_i is the coordination of the central atom. The coordination is given by

$$Z_i = \sum_{m \neq i} f(R_{im}) \quad , \quad (5.2)$$

with f being the contribution that each atom m makes to the coordination of the central atom i as a function of their separation distance r :

$$f(r) = \begin{cases} 1 & \text{if } r < c \text{ ,} \\ e^{\frac{a}{1 - (\frac{a-c}{r-c})^3}} & \text{if } c < r < a \text{ ,} \\ 0 & \text{if } r > a \text{ .} \end{cases} \quad (5.3)$$

The two-body term is

$$V_2(r, Z) = A \left[\left(\frac{B}{r} \right)^p - e^{-\beta Z^2} \right] e^{\frac{a}{r-a}} \quad . \quad (5.4)$$

The three-body interaction is given by

$$V_3(\vec{R}_{ij}, \vec{R}_{ik}, Z_i) = g(R_{ij})g(R_{ik})h(l_{ijk}, Z_i) \quad , \quad (5.5)$$

where $l_{ijk} = \cos \theta_{ijk}$,

$$g(r) = e^{\frac{\gamma}{r-a}} \quad , \quad (5.6)$$

Table 5.1: Parameters used in EDIP. The parameters u_1 – u_4 were not adjustable in the fitting process.

$a = 3.1213820 \text{ \AA}$	$c = 2.5609104 \text{ \AA}$	$Q_o = 312.1341346$	$B = 1.5075463 \text{ \AA}$
$\sigma = 0.5774108 \text{ \AA}$	$A = 7.9821730 \text{ eV}$	$\lambda = 1.4533108 \text{ eV}$	$\alpha = 3.1083847$
$\rho = 1.2085196$	$\beta = 0.0070975$	$\gamma = 1.1247945 \text{ \AA}$	$\eta = 0.2523244$
$\mu = 0.6966326$			
$u_1 = -0.165799$	$u_2 = 32.557$	$u_3 = 0.286198$	$u_4 = 0.66$

and

$$h(l, Z) = \lambda \left[\left(1 - e^{-Q(Z)(l+\tau(Z))^2} \right) + \eta Q(Z)(l + \tau(Z))^2 \right] . \quad (5.7)$$

The function τ is defined with four non-adjustable parameters:

$$\tau(Z) = u_1 + u_2(u_3 e^{-u_4 Z} - e^{-2u_4 Z}) . \quad (5.8)$$

The parameters used by EDIP are shown in Table 5.1.

5.1.2 Collision cascades

Modeling of collision cascades poses several challenges. The number of atoms in the volume across which a 10 keV-order collision cascade develops is considerable, and recent simulations have involved on the order of 10^5 atoms. Supercomputing facilities have been used for the cascade simulations, following the evolution of the cascade for 8-20 picoseconds.[91, 121] Some attempts at following the annealing of cascade damage have been made, using molecular dynamics[121] and Monte-Carlo[14] calculations. An annealing study of cascade-damaged silicon[121] followed the cascade

for 8 ps at an ambient temperature of 80 K, then annealed the system for 1 ns at 1300 K (only six defects survived the 800-atom disordered region). Presumably, the annealing was done at that elevated temperature so as to produce changes in a computationally accessible time. In all of these studies, only a few cascades were simulated, giving damage profiles with little statistical significance.

One approach to the problem of statistics has been to break down the keV-order collision cascade into its component parts - lower energy subcascades. The threshold for subcascade formation in silicon is estimated at 1 keV.[91] A study[87] was made in which secondary recoils resulting from a 500 keV Si atom are found using the MDRANGE[88] code (a SRIM-like ion range code which includes crystallographic information), then these smaller cascades are studied with MD simulations. Enough of these smaller cascades were sent through a simulation cell to completely amorphize it. This method seems valid, given the linear dependence of defect production on recoil energy above 200 eV.[124] One possible inaccuracy of this method is that it ignores the occasional large defect cluster that can be produced by higher-energy recoils (e.g., the 80-defect cluster caused by the 10 keV recoil mentioned above). This study also simplified things by ignoring small-energy recoils. The cutoff energy for this was tried at two different values (15 eV and 3 eV), and not found to be important to the final amorphized state. The choice of this parameter did, however, have great impact on the rate of amorphization, which slowed down considerably with the 3 eV threshold.

In addition to the computational burden of large simulation cells and the many time steps needed to consider annealing of cascade damage, finding an appropri-

ate potential also presents a challenge. Molecular dynamics (MD) simulations for cascades in silicon have been based mainly on the Stillinger-Weber (SW)[116] and Tersoff[126] potentials. Recently, the Environment-Dependent Interatomic Potential (EDIP)[12, 13, 61] has been used in radiation-induced amorphization studies.[87] While much may be learned from simulations using both potentials (e.g., how tetrahedral bonding affects cascade evolution compared to FCC metals), there are significant shortcomings for both. The SW potential heavily penalizes coordinations other than tetrahedral, and the Tersoff potential has an overly high melting point of 2400 K. This could lead to an overestimation of recrystallization of disordered zones on one hand, and an initial resistance to the creation of liquid-like zones during a cascade on the other. The melting point for EDIP was determined to be 1550 ± 50 K (the experimental value is 1685 K),[87] and its functional form contains coordination dependence, making it a good candidate for use in a collision cascade, in which localized melting and sudden quenching into disordered states play an important role.

A problem with any of these potentials when simulating collision cascades is that they have all been fit to equilibrium crystal properties such as point defect formation energies, cohesive energy, and elastic constants. They are not designed for the high-energy close approaches between atoms that occur in a collision.[23] A solution to this is to spline a repulsive function to the two-body part of one of the above empirical potentials. This is the approach taken in some studies[91, 23] but seemingly (and oddly, given the common authors among these papers) not in others.[87, 121] Studies have been published that treat the effect of the shape of the repulsive potential used on the resultant cascade profile.[63, 92] The Biersack-Ziegler-Littmark (ZBL) potential is

compared to an *ab initio* characterization of the repulsive interaction of silicon atoms at small distances, and it is concluded that the exact shape of the repulsive potential has little effect on the vacancy production of a collision cascade. Empirical potentials also lack the ability to account for the electronic slowing-down of a recoil. This has been handled by the inclusion of a frictional force based on experimental stopping powers[91, 89] or by the use of a Lindhard electronic stopping power model.[23] In at least one case, authors have intentionally neglected it, stating that for 5 keV self-ions in silicon, it is of little importance to cascade evolution.[90]

5.1.3 Elastic constants in molecular dynamics

The effect of defects on the elastic constants of silicon has been studied previously. De Sandre et al. used semi-empirical tight-binding MD to calculate elastic constants for defected silicon.[46] De Sandre *et al.* modeled defect concentrations ranging from 9.3% to 27.8%. In light of work by Colombo and Maric[29] which concludes that the host crystal stops behaving "like a distorted diamond lattice" at defect concentrations of about 7-8%, it is perhaps best to interpret Colombo's work as being on various states of amorphous silicon. Clark and Ackland[27] reported 0 K "dynamical matrix" calculations which used an empirical interatomic potential. These calculations required the inversion of 1539 x 1539 matrices, and employed a supercomputing facility. Their results are somewhat difficult to interpret, however, since they observed a "characteristic defect stiffening" effect, whereas one of their references[103] for this "characteristic" effect reported a softening due to defects!

Both molecular dynamics (MD) and Monte-Carlo (MC) methods have been applied to the calculation of elastic constants in silicon. In both cases, fluctuation formulas are used to yield elastic constants. Two ensembles which have been used include the HtN (isoenthalpic, isotension) and EhN (microcanonical) ensembles.[62, 67] The fastest-converging results are obtained using EhN calculations, but this requires knowledge (and calculation) of second derivatives of the potential being used - this can be "nontrivial for potentials that have terms beyond pair interactions." [62] HtN methods converge slowly, so precision would likely suffer were this method to be used. Changes on the order of 1% in elastic constants would likely go unnoticed.

Zero temperature relaxations using an empirical potential, however, could give very precise results, with considerably less effort than with MD or MC. Since the elastic constants of silicon vary only slightly with temperature[78] ($(1/C_{ij})(\Delta C_{ij}/\Delta T)$ $10^{-4}/\text{K}$), 0 K calculations should closely approximate the behavior at finite temperature.

5.2 Defect characterization using EDIP

5.2.1 Method

5.2.1.1 Sample creation

5.2.1.1.1 Defected samples Defected samples were created by inserting vacancies and interstitials into 1728-atom supercells ($6 \times 6 \times 6$ unit cells), using periodic boundary conditions. Randomly selected atoms were removed to produce vacancies

and random positions were chosen to insert extra atoms. Three types of sample were produced: one containing only vacancies, one having only interstitials, and one containing Frenkel pairs. Fifteen samples were produced of each sample type, consisting of three sets of supercells containing 1,2,3,4, and 5 defects, for a grand total of 45 sample supercells.

Upon insertion of defects, the supercells were relaxed at 0 K by relaxing atomic positions while iterating over cell dimension changes. Isotropic expansion and cell-length changes along individual axes were iteratively explored following a simple energy gradient algorithm. The supercells were then annealed at 300 K for 500 ps using the DL_POLY [44] NPT ensemble with Berendsen thermostat and barostat. After annealing, the supercells were again relaxed at 0 K.

It was hoped that this procedure would yield samples representing several different defect types in random geometries, as might result in regions of a collision cascade rich in point defects. Some samples were thrown out and regenerated, since sometimes a randomly chosen vacancy and a randomly placed extra atom annihilated either immediately or upon annealing. Other times, a randomly chosen position for an extra atom was too close to a crystalline position in the supercell, and mayhem resulted upon relaxation due to the large forces present. Samples were visually inspected to ensure that the desired scattered defects were present and discernably distinct. In most cases, only isolated defects were present. Exceptions included a two-interstitial agglomerate (H_2), and divacancy complexes involving missing nearest neighbors (V_{2n}) and missing next nearest neighbors (V_{2nn}). A breaking of symmetry in the (V_{2nn}) complex yielded another divacancy type (V_{2a}).

In addition to these 45 defected samples, 17 additional 1728-atom supercells were prepared in order to characterize the formation energy (E_f), volume (V_f), and effects on elastic constants of various interstitial and vacancy configurations. These samples were created by intentionally arranging atomic positions within the supercell then relaxing at 0 K, as above. E_f , V_f , and elastic constants for each sample were calculated before annealing the sample at 300 K for 500 ps, as above. Calculations were then repeated on the annealed samples.

5.2.1.1.2 Amorphous samples The preparation of three 216-atom amorphous samples (A-C) and one 64-atom sample (G) used here is described in detail in a separate paper.[11] Brief descriptions of the samples are given in Table 5.2. Of particular note is sample C, which was cooled from 1100 K at constant enlarged volume to create a void. Sample D resulted from a liquid quench at constant pressure. These amorphous samples were prepared by Prof. Martin Bazant of MIT/Department of Mathematics.

Two 1728-atom amorphous samples were prepared by Dr. Xianglong Yuan of MIT/Department of Materials Science and Engineering by quenching from high temperature at constant pressure. Sample E was prepared by heating a crystalline sample to 3000 K, equilibrating for 300 ps, then cooling to 10 K at 1 K/ps. Sample F started with random atomic positions at 5000 K, then was cooled to 10 K, also at 1 K/ps. All amorphous samples used here were annealed at 300 K for 500 ps, then relaxed at 0 K as for the defected samples above.

Table 5.2: Descriptions of amorphous samples. Calculation of numbers of 5-fold and 3-fold coordination defects present used a rounding of the EDIP coordination value Z .

Sample	Size	5-fold	3-fold	Other
A	216	6	0	
B	216	5	1	
C	216	13	3	Void present
D	216	10	0	
E	1728	116	2	
F	1728	112	2	
G	64	0	0	

5.2.1.1.3 Composite sample A composite sample was prepared by embedding sample G into a crystalline matrix. This was done by first cutting out a $2 \times 2 \times 2$ unit cell cube from a $6 \times 6 \times 6$ unit cell supercell. The crystalline supercell was then homogeneously and anisotropically expanded to accomodate the relaxed sample G. The composite was then relaxed at 0 K as above, then annealed as above at 300 K and relaxed again at 0 K.

5.2.1.2 Elastic constant calculation

5.2.1.2.1 Approach Strain can be defined as:[94]

$$\epsilon_{ij} = \frac{1}{2} (e_{ij} + e_{ji}), \quad (5.9)$$

where

$$e_{ij} = \frac{\partial u_i}{\partial x_j}, \quad (5.10)$$

with u being displacement and x being position. The work needed to impose a strain ϵ is (switching to Voigt notation)

$$\frac{\Delta E}{V} = \frac{1}{2} C_{ij} \epsilon_i \epsilon_j, \quad (5.11)$$

where C_{ij} are the elastic constants and V is the volume. For a cubic system like silicon, only three independent constants exist. We make the approximation for our defected samples that this symmetry remains intact.

Computationally convenient strains to impose on an orthorhombic supercell aligned with the diamond unit cell axes are suggested by Eq. 5.11. The tensor strain notation shown in Eq. 5.12 is used in Eqs. 5.13–5.15, with non-specified strains all equal to zero:

$$\epsilon = \begin{bmatrix} \epsilon_1 & \frac{1}{2}\epsilon_6 & \frac{1}{2}\epsilon_5 \\ \frac{1}{2}\epsilon_6 & \epsilon_2 & \frac{1}{2}\epsilon_4 \\ \frac{1}{2}\epsilon_5 & \frac{1}{2}\epsilon_4 & \epsilon_3 \end{bmatrix}, \quad (5.12)$$

$$C_{11} = \frac{1}{V} \frac{\partial^2 E}{\partial \epsilon_1^2}, \quad (5.13)$$

$$C_{11} + C_{12} = \frac{1}{2V} \frac{\partial^2 E}{\partial \epsilon^2}, \quad \epsilon = \epsilon_1 = \epsilon_2, \quad (5.14)$$

$$C_{44} = \frac{1}{V} \frac{\partial^2 E}{\partial \epsilon_4^2}. \quad (5.15)$$

By imposing isotropic strains ($\epsilon_1 = \epsilon_2 = \epsilon_3$), we can also obtain the bulk modulus:

$$B = V \frac{\partial^2 E}{\partial V^2}. \quad (5.16)$$

Other useful relations involving elastic constants of isotropic and cubic materials are given in Appendix C.2.

5.2.1.2.2 Defected samples Elastic constants were calculated by fitting polynomials to plots of energy vs. strain. Excellent results were obtained for a wide range of energy sampling intervals in strain for the crystal and for samples containing only point defects, but the amorphous samples were found to be apt to change bonding structure with large imposed strains. By trial-and-error, it was determined that a step size in strain of 1×10^{-5} was sufficiently small to not cause bonding rearrangements in the amorphous samples, yet produced large enough energy differences to numerically extract second derivatives from fit polynomials.

The number of points to fit was also decided by experimentation. The second derivative of the energy was of primary concern here. A greater number of points would help to recognize and account for higher-order effects, but a large number of points at large strains would also allow higher-order effects to dominate the fit. A total of 21 points in the strain interval $\pm 1 \times 10^{-4}$ was calculated for each sample discussed here, but it was found that fitting only the nine middle points yielded the most consistent results.

Starting from the relaxed structure, strains were sequentially imposed in steps of

1×10^{-5} . Atomic positions were relaxed at each strain step. Starting again from zero strain, negative strain was then incrementally imposed. Fourth and fifth order fits to the resultant curves were found to give essentially identical results, with lower-order fits giving slightly different results, and higher-order fits being numerically unreliable. All results reported here are based on fourth-order least-squares fits.

To help minimize the error in our assumption that cubic symmetry holds for the defected samples, all C_{ij} were independently calculated for all three orthogonal directions, then averaged. The variation of C_{44} among the three directions was greatest, and rose to $\sim 1\%$ for a few of the samples, but was typically similar to that of C_{11} and C_{12} , namely $\lesssim 0.1\%$. The lesser precision of C_{44} is to be expected, given the sample preparation method described in section 5.2.1.1, which guarantees that the relaxed sample will occupy an energy minimum with respect to the isotropic and monoaxial expansions used to obtain energy curves for B and C_{11} , but will not guarantee this for the shear applied to calculate C_{44} .

As a validation of our numerical approach, we compared values found for the crystal with those previously published for EDIP. [61] When discrepancies were observed, we calculated analytical values[10] for the EDIP diamond lattice elastic constants, and found that our numerically calculated values agreed to within about four significant figures. The results for these values are shown in Table 5.3. It can be seen that the values of Justo *et al.*, calculated using a deformation/energy method, much like our results in the "numerical" column of Table 5.3, were not accurate to the number of places published. They should be disregarded. Details on calculating the analytical elastic constants from the potential are given in Appendix C.1.

Table 5.3: Analytical and numerically (energy curve fitting) computed EDIP elastic constants (GPa) and Kleinman's internal strain parameter ζ for the diamond phase. C_{44}^o is the shear modulus when internal relaxation is disallowed. The values published by Justo *et al.* are provided here for comparison.

	Analytical	Numerical	Justo <i>et al.</i> [61]	Expt.[50, 34]
C_{11}	171.99	172.00	175	167.54
C_{12}	64.72	64.71	62	64.92
C_{44}	72.75	72.75	71	80.24
C_{44}^o	112.39	112.39	112	111 ^a
B	100.47	100.47	99	99.13
ζ	0.51727	0.51727 ^b	0.497 ^c	0.72
$E_{(100)}^d$	136.60	136.62	143	131.28
$E_{(110)}^d$	164.05	164.05	164	170.63

^aNot experimentally accessible. Calculated using *ab initio* (LDA) methods in Ref. [13].

^bCalculated computationally by shearing a supercell and measuring atomic relaxation.

^cCalculated from C_{ij} using Eq. C.18.

^dCalculated from C_{ij} using Eqs. C.23 and C.24.

5.2.1.2.3 Amorphous samples In the case of a truly amorphous material, the elastic properties will be isotropic, and only two independent elastic constants will exist. The finite size and periodic boundary conditions imposed on the samples of our study prohibit this isotropic ideal. We nevertheless calculated the C_{ij} for our amorphous Si samples as above, averaging over results from three independent directions.

An additional step we applied to the amorphous sample elastic constant results was to distill the set of four elastic constants to a self-consistent set by means of an iterative process. The bulk modulus, being direction-independent, was left alone. By pairing each of the three C_{ij} with B , a prediction of the other two C_{ij} 's was made. At each iteration, the original C_{ij} was averaged with the two predicted values until a self-consistent set was achieved. For the largest samples, the change in the C_{ij} 's due

to this process was $\lesssim 0.1\%$ for C_{11} and C_{12} , and about 0.5% for C_{44} . For the smallest samples, these changes were $\sim 1\%$ and $\sim 10\%$, respectively. The small adjustments necessary to achieve self-consistency of the large (1728 atoms) samples demonstrates their close approximation to the isotropic ideal.

5.2.1.2.4 Composite sample One of the goals of our work was to see what effect amorphous regions embedded in a crystalline matrix (as might be residual from a collision cascade) would have on the overall elastic modulus. As for the defected samples, cubic symmetry doesn't strictly apply for the composite sample studied here, nor is the composite sample isotropic. We wish nevertheless to compare the elastic modulus of the composite with that of the component parts (crystalline and amorphous). We therefore calculated the C_{ij} 's of the composite as for the defected samples. We then reduced the crystalline and composite C_{ij} 's to an effective isotropic Young's modulus E by using the mean of the Reuss and Voigt spatial-average limits.[52]

For isotropic materials, upper and lower bounds on the Young's modulus of a two-phase composite (E_c) are given by: [17, 7]

$$\left[\frac{V_1}{E_1} + \frac{(1 - V_1)}{E_2} \right]^{-1} < E_c < V_1 E_1 + (1 - V_1) E_2, \quad (5.17)$$

where V_1 and E_1 are, respectively, the volume fraction and Young's modulus of the embedded material, and E_2 is the Young's modulus of the matrix. Clearly, the crystalline matrix we had here is not isotropic, but the Reuss and Voigt limits for polycrystalline aggregates provide a convenient way to test the applicability of the Eq. 5.17 to our

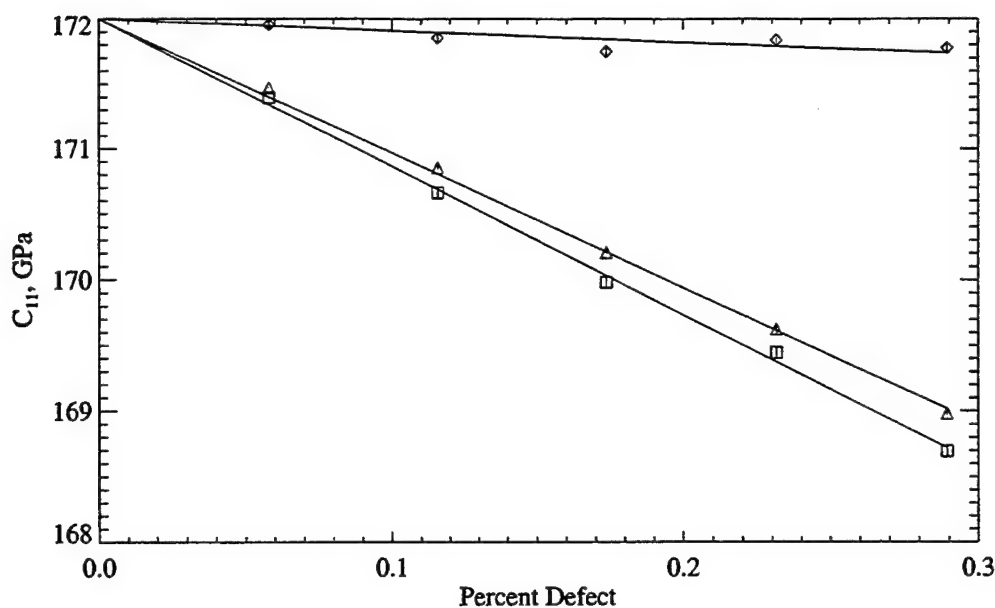


Figure 5-1: C_{11} as a function of point defect fraction. Diamonds indicate interstitials, triangles vacancies, and squares Frenkel pairs. Each point represents the average of three samples. Bars indicate the standard deviation of the three samples. Lines are unweighted least squares fits constrained to match the crystalline value on the Y-axis.

embedded amorphous Si sample.

5.2.2 Results

5.2.2.1 Defected samples

The results of the elastic constant calculations for the samples generated by random placement of vacancies and interstitials are summarized in Figs. 5-1-5-4 and 5-5.

It can be seen that the trend of the elastic constants with defect content is approximately linear. An unweighted fit was used, since the small standard deviation of the single defect samples, as well as the small number of samples, made weighted fitting difficult to interpret. The fit slopes are summarized in Table 5.4.

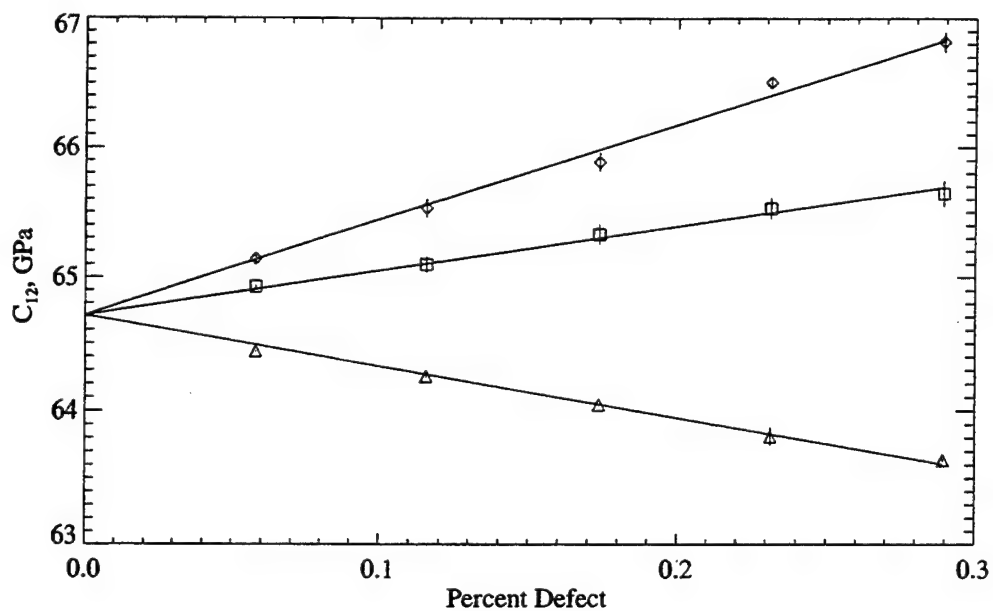


Figure 5-2: C_{12} as a function of point defect fraction. Symbols are as for Figure 5-1

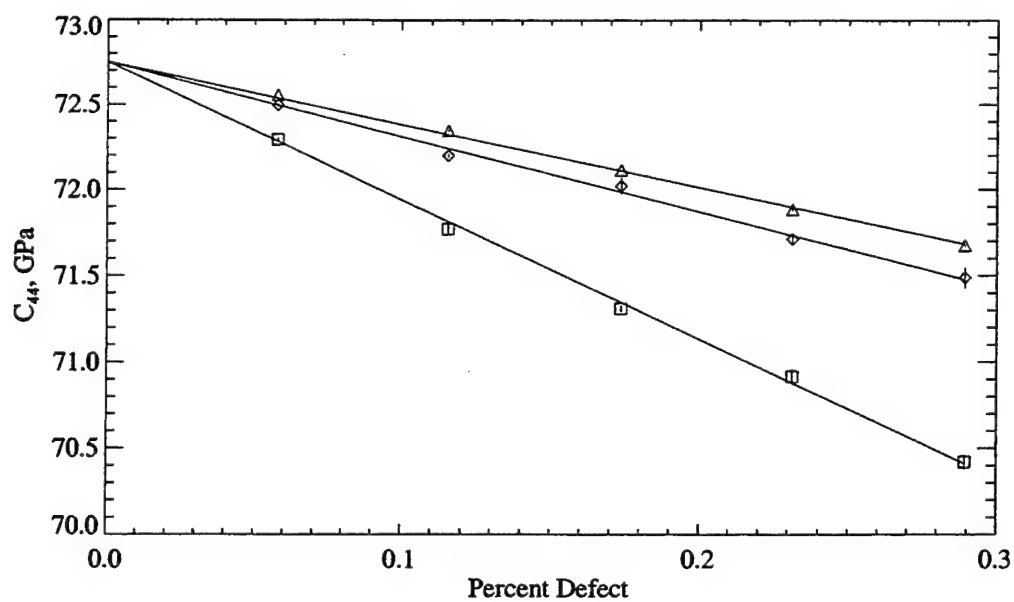


Figure 5-3: C_{44} as a function of point defect fraction. Symbols are as for Figure 5-1

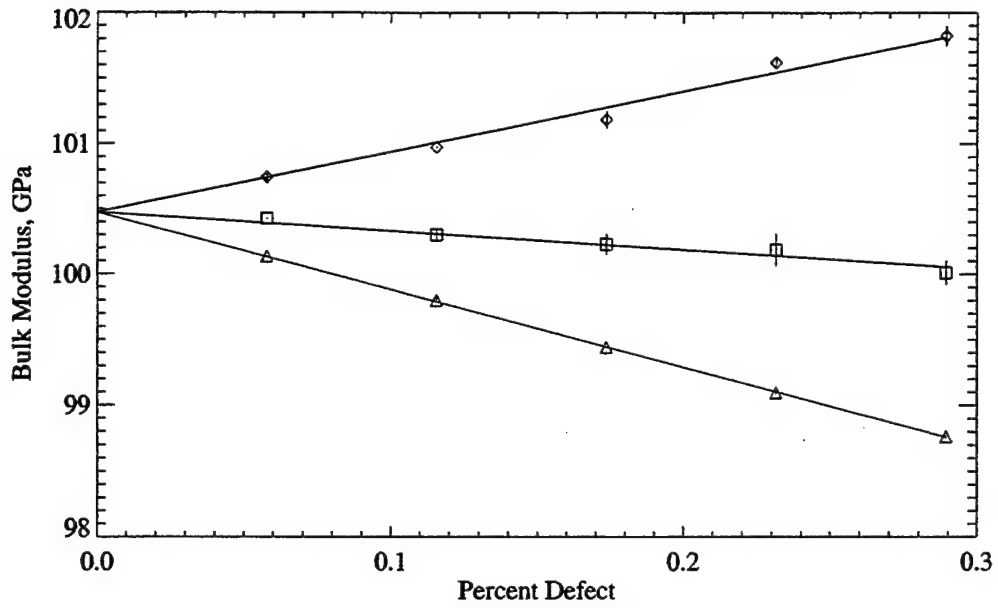


Figure 5-4: Bulk modulus as a function of point defect fraction. Symbols are as for Figure 5-1

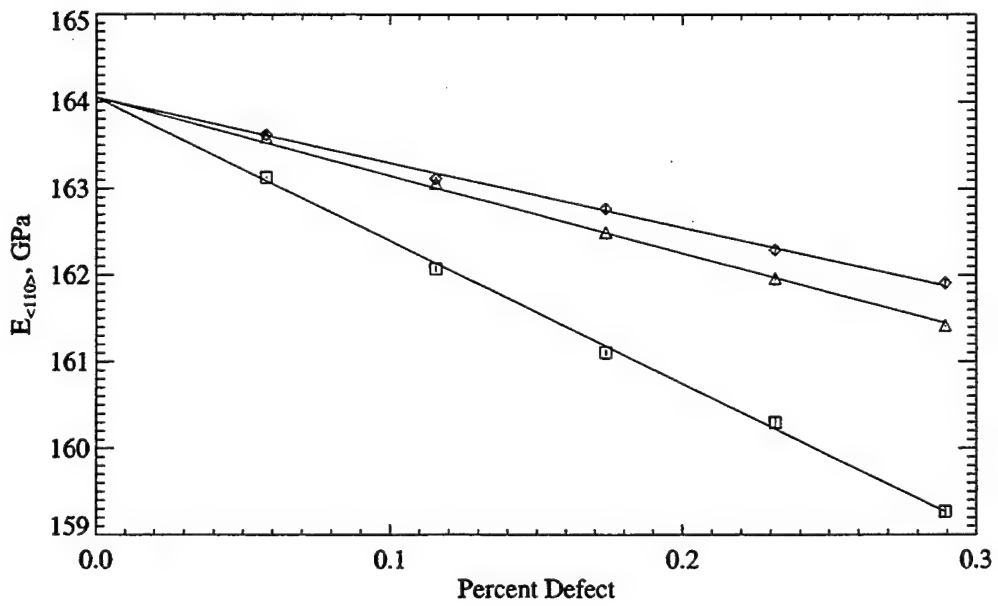


Figure 5-5: Young's modulus as a function of point defect fraction. Points were calculated from the C_{ij} in Figs. 5-1-5-4. Symbols are as in Fig. 5-1.

Table 5.4: Fit slopes to the points in Figs. 5-1- 5-6. Units are per defect fraction, with elastic constants in GPa. "Difference" refers to that between the Frenkel pair result and the sum of the vacancy and interstitial results. The numbers in parentheses are from fits to the data in Clark and Ackland.[27]

	C_{11}	C_{12}	C_{44}	B	$E_{(110)}$	$\Delta V/V$
Vacancies	-1030. (821.)	-381. (565.)	-369. (-8.7)	-593. (648.)	-899. (217)	0.42
Interstitials	-89.2 (715.)	733. (443.)	-440. (-57.9)	462. (531.)	-751. (161)	1.35
Frenkel pairs	-1133.	339.	-809.	-145	-1653.	1.78
Vac.+Int.	-1119.	352.	-810.	-130	-1651.	1.77
% Difference	-1.2	3.6	0.1	-10.3	-0.2	-0.9

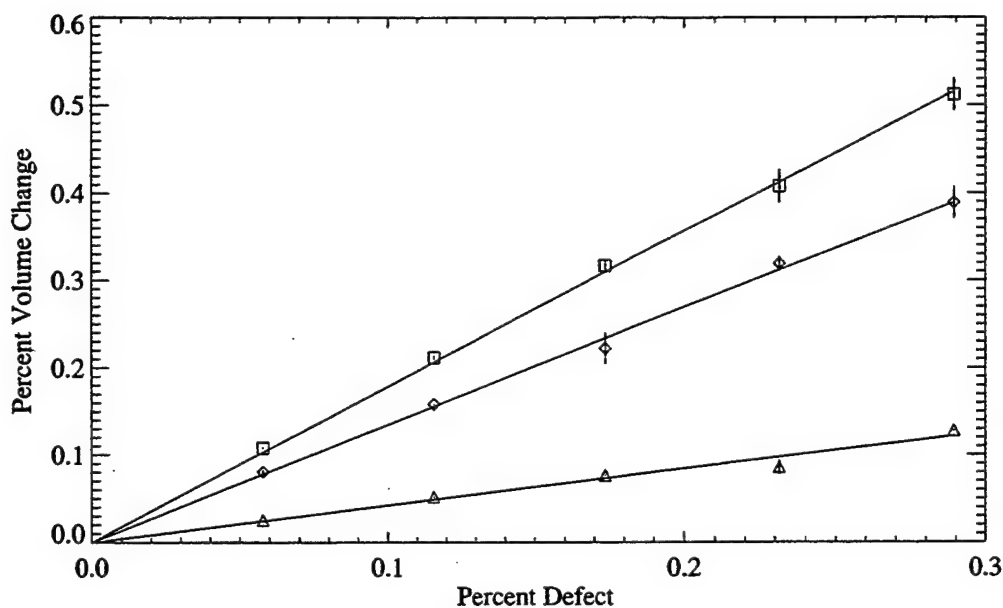


Figure 5-6: Percent volume change as a function of point defect fraction. Symbols are as in Fig. 5-1.

The isolated defects appear to be having largely independent effects on the elastic constants and volume, as evidenced by the linear trends in Figs. 5-1–5-4 and 5-6, as well as by the close agreement between the slope of the Frenkel pair plots and the sum of the vacancy and interstitial slopes as shown in Table 5.4. Both interstitials and vacancies are shown to cause volume expansion in Fig. 5-6, vacancies to a lesser degree than interstitials. The general softening of the elastic constants with rising defect concentration (with the exception of interstitials for C_{12} and the bulk modulus, and Frenkel pairs for C_{12}) does not agree with the previous finding that both interstitials and vacancies in silicon stiffen the crystal. Vacancies are found here to soften each of the elastic constants considered, the opposite being true for all but C_{44} according to Clark and Ackland.[27] Points of agreement between that study and the present one include the softening of C_{44} by both vacancies and interstitials (though the effect is an

order of magnitude greater here), and the stiffening of both B and C_{12} by interstitials.

5.2.2.2 Amorphous samples

Elastic constants of our amorphous samples are shown in Table 5.5, along with experimental[36, 46, 122, 108, 60, 147, 120, 143] and calculated[46, 128, 87] data for comparison. It can be seen that the differences among samples is slight, with the exception of sample C, which contained a void. The elastic constants for our amorphous samples appear to be fairly insensitive to the coordination defects described in Table 5.2. None of elastic constants of sample G, which has perfect 4-coordination throughout, is an outlier when compared to the other samples. Not surprisingly, sample G is the lowest energy configuration. It is interesting to note, however, that the volume change of sample G is the greatest of all EDIP samples reported in Table 5.5 (with the exception, of course, of sample C).

We note that despite close agreement of our large amorphous samples with the amorphous sample of Vink *et al.*[128] for the values of C_{11} and C_{12} , our value for C_{44} is about a factor of two different. As mentioned above, our large (1728 atoms) amorphous samples came very close to satisfying the isotropic ideal represented by:

$$C_{44} = \frac{1}{2} (C_{11} - C_{12}). \quad (5.18)$$

Since even our smallest (64 atoms) samples came within 10 % of satisfying Eq. 5.18, with all larger samples being even closer than this (even sample C with its void), one would expect the 1000 atom sample of Vink *et al.* to exhibit fairly isotropic

Table 5.5: Elastic constants (GPa) of EDIP-generated amorphous samples described in the text. Also shown are percent volume change and energy gain per atom with respect to the crystalline values (20.018 Å³ atomic volume and -4.6500 eV). Results from experiment (room temperature), tight-binding molecular dynamics (room temperature), and EDIP are shown for comparison. Where published results were not completely consistent with isotropicity, the range of possible derived values is given.

	C_{11}	C_{12}	C_{44}	B	E	% ΔV	ΔE , eV
A	131.3	80.4	25.5	97.4	70.3	3.8	0.1885
B	130.2	82.9	23.6	98.7	65.7	4.4	0.1999
C (Void)	98.7	57.9	20.4	71.5	55.9	10.9	0.2432
D	134.7	82.7	26.0	100.0	71.7	3.3	0.1868
E	133.0	81.9	25.5	99.0	70.5	3.1	0.2059
F	132.9	81.1	25.9	98.4	71.4	3.3	0.2064
G (Defect Free)	131.0	81.4	24.8	97.9	68.6	5.2	0.1815
EDIP (Ref. [128])	130	81	25 ^a	97	67-145	2	0.199
EDIP quench (Ref. [87])						3.5	0.25
EDIP irradiated (Ref. [87])						2.2-3.6	0.19-0.40
Expt. (Ref. [46]) ^b	156	58.4	48.8	90.9	124		
Expt. (Ref. [120])	156	57.8	49.2	90.6	125	1.3	
Expt. (Ref. [143])	138	42	48	74	118		
TBMD (Ref. [46])	149	46.9	55.4	75-84	127-136		
Expt. (Ref. [36])						1.8	

^aThe published value was actually 56. This is over a factor of two greater than predicted by Equation 5.18, so is obviously a mistake. The value shown here was calculated with Equation 5.18 from the published C_{11} and C_{12} .

^bThe values for C_{ij} here are based on the measured Young's modulus of Tan *et al.*[122] combined with a Raleigh wave measurement discussed in De Sandre *et al.* [108, 46, 60, 147]

properties. We suggest that a factor of two error might have been introduced when calculating C_{44} , which would mean that the actual C_{44} of the Vink *et al.* amorphous sample should be 28 GPa.

Despite the fact that amorphous samples, both real and computational, have properties that vary according to the method of preparation,[87] it seems likely from the results in Table 5.5 that EDIP errs systematically in predicting the elastic constants of amorphous silicon. All of the experimental studies cited here agree well on the value of C_{44} , and using EDIP to generate and calculate the elastic constants of amorphous samples yields a result consistently about a factor of two below this value.

5.2.2.3 Composite sample

The elastic constants of our composite sample are shown (along with those of the component parts) in Table 5.6. It can be seen that the Young's modulus of the composite is within the upper and lower bounds predicted by Eq. 5.17. This was true, in fact, for all of several different methods we used for applying Eq. 5.17, including using the Young's modulus for $\langle 100 \rangle$ and $\langle 110 \rangle$ directions (as opposed to using spatially averaged values).

Predictions based on Eq. 5.17 did not hold, however, for elastic constants calculated using a similarly prepared composite sample that skipped the annealing step. The crystalline-amorphous interface, when only relaxed at 0 K, seems the likely reason for this.

Table 5.6: Elastic constants for the crystal, amorphous sample G, and the composite. The Young's modulus value (E) given for the crystal and the composite sample are the average of the Reuss and Voigt spatial averages.[52] Upper and lower bounds based on Eq. 5.17 are shown for comparison.

	C_{11}	C_{12}	C_{44}	E
Crystal	172.	64.7	72.8	159.
Amorphous G	131.	81.4	24.8	68.6
Composite	169.	65.4	69.9	154.
Upper Bound				156.
Lower Bound				151.

5.2.2.4 Isolated defects

The interstitial defects that resulted from the random-placement generation process described in section 5.2.1.1 are illustrated in Fig. 5-7. It can be seen that the defects $DB_1, DB_2,$ and DB_3 are minor variations on the $\langle 110 \rangle$ dumbbell defect, DB . In each case, the atom positions are very similar, but sufficiently different to cause the bonding geometry to change. All of these configurations relaxed to the $\langle 110 \rangle$ dumbbell configuration upon annealing the isolated defect at room temperature. We infer that these defects were stabilized by other defects.

The DB_4 defect complex is also a variation on the $\langle 110 \rangle$ dumbbell in which two neighbors of the atom that is 'split' to form the dumbbell are moved together to bond. While the other dumbbell variations may simply be EDIP artifacts, this defect has been seen before with the Tersoff 3 potential.[76]

The formation energy of 3.38 eV calculated for the $\langle 110 \rangle$ dumbbell defect does not precisely agree with one (3.35 eV) previously published.[61] This is perhaps partly due to our independent relaxation of all three cell dimensions in addition to atomic

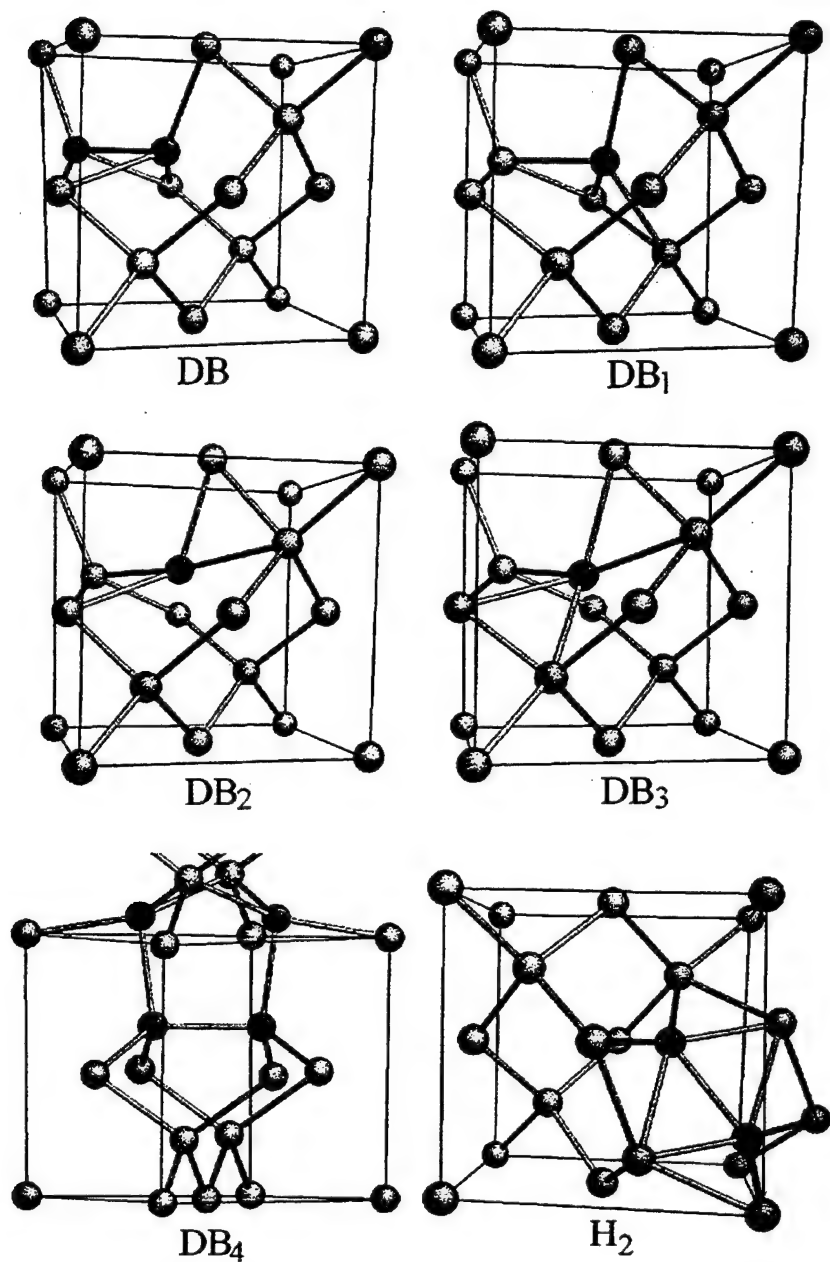


Figure 5-7: Interstitials generated by random placement and subsequent relaxation using EDIP. The corners of a diamond unit cell are connected by lines, and atoms occupying interstitial positions are darkened. Bonds are drawn between atoms closer than 2.56 Å. H_2 involves two atoms which are extra to the diamond unit cell — all other defects pictured here involve only one extra atom.

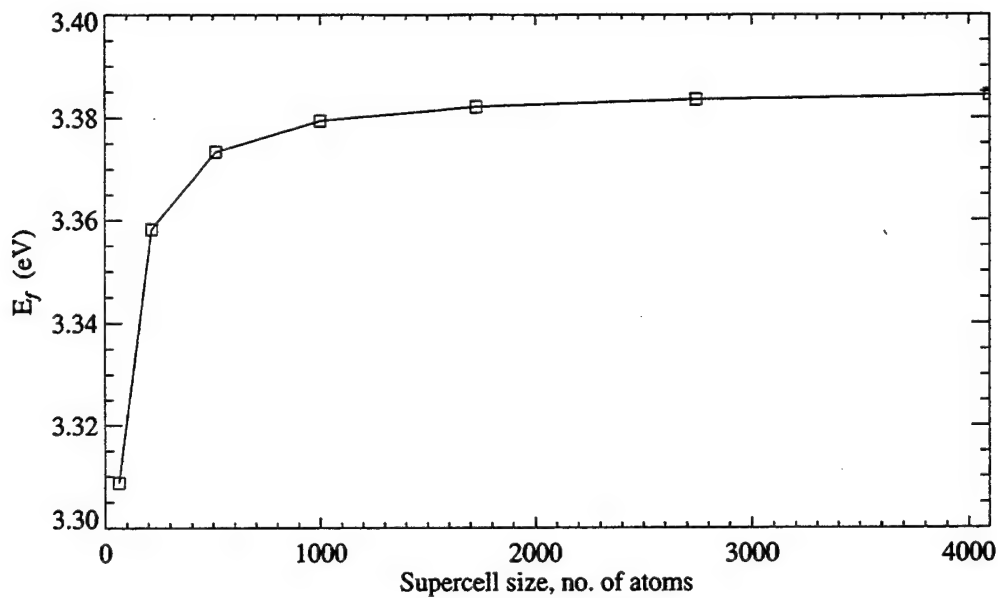


Figure 5-8: Formation energy for $\langle 110 \rangle$ dumbbell calculated in various sized supercells with periodic boundary conditions

coordinates, as well as to size effects with periodic boundary conditions, as suggested by Fig. 5-8. Effects of an overlapping strain field due to periodic boundary conditions don't appear to be of concern (at least to the level of precision discussed here) for our 1728 atom samples. While we did not verify this for each of the many samples discussed in the present work, we take confidence in the leveling off of the curve in Fig. 5-8.

We calculated the unrelaxed formation energies of the tetragonal and hexagonal interstitials for EDIP, and obtained 10.58 eV and 6.85 eV, respectively, in agreement with Justo *et al.* We noted, however, that these two interstitial positions are not stable in EDIP, as shown in Fig. 5-9. An interstitial will shift away from these positions upon relaxation. In fact, even at 0 K, numerical error generated during the relaxation of atomic positions provided sufficient asymmetry to cause the hexagonal

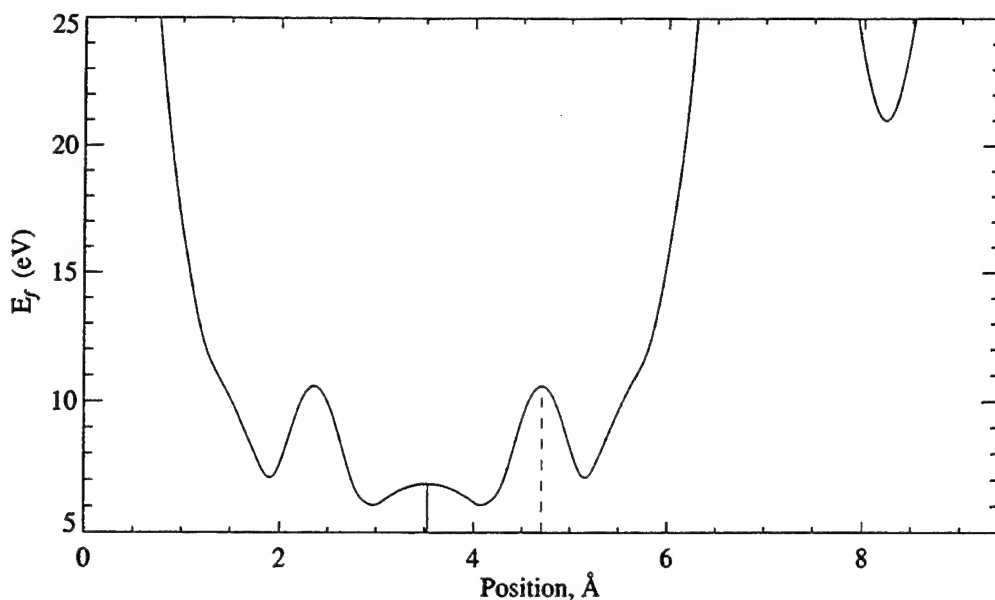


Figure 5-9: Unrelaxed formation energy for an interstitial placed along the unit cell body diagonal in Si, calculated using EDIP. The solid and dashed vertical lines indicate the positions of the hexagonal and tetragonal interstitials, respectively.

interstitial to relax into an off-center position (Hex_A). This asymmetric position remains six-fold coordinated. To obtain a relaxed formation energy for the hexagonal interstitial, therefore, the interstitial position had to be artificially maintained. After room-temperature annealing, both hexagonal and tetragonal interstitials relaxed into a $\langle 110 \rangle$ dumbbell. This instability of the tetrahedral interstitial agrees with LDA predictions.[72] The result that the unrelaxed hexagonal interstitial is unstable, but that relaxing the system while constraining symmetry among its neighbors yields a metastable defect, also agrees with the *ab initio* result.[28]

We also note in passing that a bond defect involving no coordination defects is stable using EDIP, the relaxed formation energy and formation volume of which are 2.38 eV and $+1.1 \text{ \AA}^3$, respectively. This defect has been studied numerous times

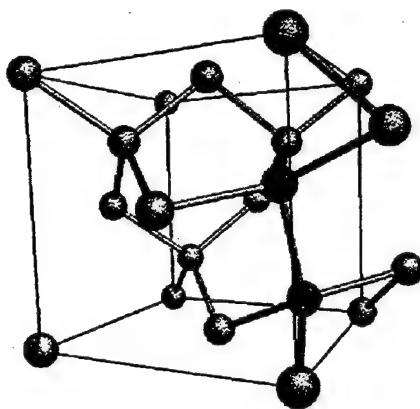


Figure 5-10: The four fold coordinated defect referred to a unit cell. The two displaced atoms are darkened.

under various names. We adopt the latest nomenclature for this defect: the fourfold coordinated defect (*FFCD*).[47] The *FFCD* is pictured in Fig. 5-10. The earliest (to our knowledge) descriptions of this defect were by Stillinger and Weber,[116] and by Wooten, Winer, and Weaire,[137] who used it to generate samples of amorphous Si. Later, Motooka[83] described how a divacancy/di-interstitial complex results in an equivalent configuration. Tang *et al.*[123] later rediscovered this arrangement as the result of the close approach of a vacancy-interstitial pair, and made a tight-binding calculation of the formation energy (3.51 eV). Stock *et al.*[117] identified the Stillinger and Weber bond defect, the WWW bond-switching mechanism, and the Tang “I-V complex” as one and the same. Cargoni *et al.*[22] examined the bond defect with tight-binding molecular dynamics (TBMD) and *ab initio* Hartree-Fock calculations, reporting a formation energy of 3.26 eV. Marques *et al.*[76] used the Tersoff 3 (T3) potential[126] to calculate a formation energy of 3.01 eV. Recently, Goedecker *et al.*[47] used density functional theory (DFT) to calculate the formation energy of this

defect. The local density approximation (LDA) predicted 2.34 eV, and the general gradient approximation (GGA) predicted 2.42 eV. These latest *ab initio* calculations are in remarkable agreement with EDIP.

It is interesting to note that while the formation energy of this defect is dramatically lower than that of the other defects present in our samples, it does not occur in any of them. This is perhaps due to the orchestrated movement of atoms that is required to produce it, which decreases the likelihood of it naturally occurring.

Three types of divacancies cropped up in the samples with random vacancy placement. One involved missing nearest neighbors (V_{2n}) with symmetric outward breathing. Another involved missing next-nearest neighbors (V_{2nn}). The third also consisted of missing next-nearest neighbors, but differed in that the common neighbor to the two vacant sites shifted to become threefold coordinated (V_{2a}). When isolated in a supercell, V_{2a} survived annealing, but V_{2nn} relaxed into a fourth configuration, V_{2nnr} , involving missing nearest neighbors that differed from V_{2n} in that instead of involving six threefold coordinated atoms, it had only three threefold coordinated atoms accompanied by a single fivefold coordinated atom. These vacancy configurations are illustrated in Fig. 5-11. Though one case of the divacancy V_{2nn} had survived the annealing step in one of the random-placement samples, it was not in isolation in the supercell, and the strain fields of the other defects present may have served to stabilize it to some degree.

The relaxed monovacancy and divacancy energies show good qualitative agreement with DFT/LDA calculations, which predict 3.29 eV, 4.63 eV, and 5.90 eV for V , V_{2n} , and V_{2nn} , respectively.[107] The binding energy for the divacancy is therefore 1.60 eV

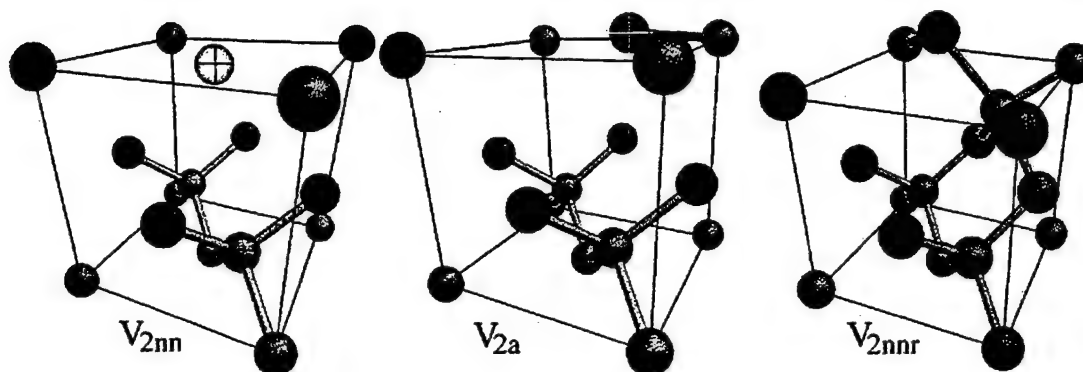


Figure 5-11: Divacancy complexes referred to a unit cell (left to right): V_{2nn} , V_{2a} , and V_{2nnr} . Highlighted and darkened atoms are twofold and threefold coordinated, respectively. At left, two next-nearest neighbors are missing from the upper half of the unit cell. At center, the two-fold coordinated atom (marked with a cross) has broken symmetry and become three-fold coordinated. Annealing V_{2nn} at room temperature yielded the rightmost figure, in which the uppermost atom (black) is five-fold coordinated. This atom is not part of the unit cell shown, but is included to provide context. While V_{2nnr} was generated by annealing V_{2nn} , it actually involves missing nearest neighbors, similar to the simpler V_{2n} (not shown).

and 1.95 eV according to EDIP and DFT/LDA, respectively. We note that while the monovacancy, “simple” divacancy, and “split” divacancy of Seong *et al.*[107] have the same unrelaxed structures as V , V_{2n} , and V_{2nn} , respectively, the energies we cite here are for the relaxed structures, on which DFT/LDA and EDIP differ. In the case of V , for example, Seong *et al.* report a monovacancy structure that is somewhere between the symmetric V favored by EDIP and the distorted V_{JT} .

The formation volume for an isolated vacancy was found to be $+28.8 \text{ \AA}^3$. The EDIP monovacancy is therefore outward-breathing (the atomic volume of the EDIP crystal is 20.0 \AA^3), in agreement with early *ab initio* calculations.[102, 74] Later calculations have predicted an inward-breathing vacancy,[64, 5, 107] and a recent DFT/LDA calculation study showed that the relaxation around a neutral monova-

cancy has a formation volume of -1.7 \AA^3 . [6] The negative formation volume accompanied a Jahn-Teller distortion in which the neighbors of the vacant site bond pairwise across $\langle 110 \rangle$ directions. While we found that such a defect is stable using EDIP (and it did indeed have a negative formation volume of -14.5 \AA^3), its formation energy was higher than that of the monovacancy: 4.06 eV. When comparing formation volumes of various defects, it is helpful to remember that the unrelaxed vacancy has a formation volume of $+20 \text{ \AA}^3$, whereas that of an unrelaxed mono-interstitial configuration is -20 \AA^3 . A negative formation volume, therefore, is not as surprising for an interstitial as for a vacancy, where relaxation must be very significant to pack atoms more efficiently than the crystal.

The defect (V_{JT}) disappeared upon annealing at 300 K for 500 ps in three samples we tested, evolving each time into a defect (V_{JT_r}) involving one 3-coordinated and one 5-coordinated atom and having a formation energy and volume of 3.65 eV and -6.7 \AA^3 , respectively. We calculated the effect of both V_{JT} and V_{JT_r} on the elastic constants at 0 K. Whereas the monovacancy V is seen to cause a reduction in every elastic constant, the other two monovacancy types show behavior similar to the FFCD in that they actually stiffen C_{12} and the bulk modulus. In each case, however, the Young's modulus is observed to lessen. The three monovacancy configurations are illustrated in Fig. 5-12. The comparison of V_{JT_r} with V_{2nnr} reveals a common structure: each has a fivefold coordinated atom with four bonds almost being co-planar, and the fifth bond pointing in the general direction of the threefold coordinated atoms (this is not particularly evident in Figs. 5-11 and 5-12 — only two of the almost co-planar bonds are shown in each case).

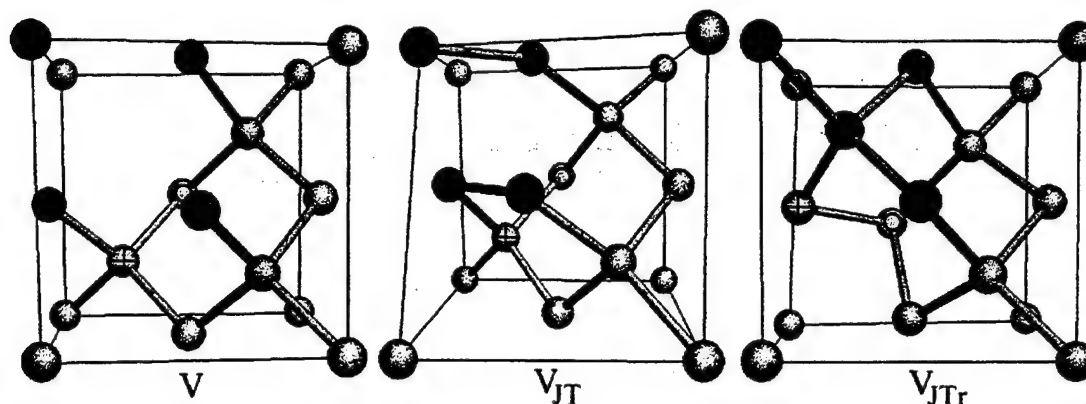


Figure 5-12: Stable EDIP monovacancy configurations. At left is the outward-breathing vacancy (V) observed in all randomly-generated samples. Vacancy neighbors are darkened. The Jahn-Teller distortion with bonding between pairs of vacancy neighbors is shown at center (V_{JT}), and the result upon a room temperature annealing of this defect is shown at right (V_{JT_r}). The cross marks an atom whose position changes significantly between the three configurations shown, as does the circle. V_{JT_r} contains one 5-coordinated atom (circle) and one 3-coordinated atom (back lower left corner).

The results for formation energy, formation volume, and effects on elastic constants of the isolated defect samples are summarized in Table 5.7. While the sign on the deviation from crystalline elastic constants varied between vacancies and interstitials in some cases (C_{12} and B), all defects were observed to reduce Young's modulus. When taken on a per-atom basis, the effect on the $\langle 100 \rangle$ Young's modulus is quite similar among all defect types presented in Table 5.7, being bracketed between -0.25 % and -0.45 % (aside from the tetrahedral interstitial, which is locally unstable according to both EDIP and LDA calculations).

While one might expect that greater formation volume magnitude would be accompanied by a larger formation energy (due to larger strain fields), we found that the relationship between formation volume and and formation energy among defects

Table 5.7: Formation energies, volumes, and percent change in elastic constants for a single defect in a 1728-atom supercell, calculated using EDIP. The numbers in parenthesis represent how many of the 90 'extra' atoms randomly inserted into our samples appeared in a particular interstitial type. The number of vacant sites appearing in a particular vacancy complex is also shown in parenthesis, also out of a total of 90.

	E_f , eV			$V_f \text{\AA}^3$							
	EDIP	LDA	GGA	EDIP	LDA	C_{11}	C_{12}	C_{44}	B	$E_{(100)}$	$E_{(110)}$
DB	3.38 (67)	2.88 ^a	3.31 ^a	8.7	-2.0 ^b	-0.02	0.72	-0.32	0.29	-0.35	-0.25
DB_1	3.55 (4)			7.0		-0.04	0.64	-0.35	0.25	-0.28	-0.27
DB_2	3.55 (4)			6.7		-0.10	0.59	-0.38	0.20	-0.41	-0.31
DB_3	3.53 (6)			6.2		-0.03	0.54	-0.40	0.22	-0.35	-0.28
DB_4	3.50 (1)			-0.6		-0.03	0.56	-0.36	0.22	-0.29	-0.26
Tet	4.10 (0)	3.43 ^c	4.07 ^c	19.6		0.12	0.81	-0.43	0.41	-0.18	-0.24
Hex	4.19 (0)	2.87 ^a	3.31 ^a	8.3		-0.11	0.50	-0.45	0.16	-0.38	-0.35
Hex_A	3.95 (0)			7.4		-0.10	0.63	-0.50	0.21	-0.42	-0.38
$FFCD$	2.38 (0)	2.34 ^a	2.42 ^a	1.1	5.9 ^b	-0.12	0.18	-0.31	0.01	-0.26	-0.25
H_2	4.81 (8)			-4.0		-0.09	1.00	-0.42	0.43	-0.58	-0.36
V	3.22 (84)	3.29 ^d		28.8	12.8 ^d	-0.31	-0.42	-0.27	-0.34	-0.26	-0.28
V_{JT}	4.06 (0)	3.49 ^e		-14.5	-1.7 ^e	-0.21	0.32	-0.44	0.03	-0.45	-0.38
V_{JT_r}	3.65 (0)			-6.7		-0.18	0.24	-0.32	0.01	-0.37	-0.29
V_{2n}	4.84 (2)	4.63 ^d		53.4	16.3 ^d	-0.54	-0.61	-0.46	-0.55	-0.50	-0.49
V_{2nn}	6.77 (2)	5.90 ^d		51.3	14.1 ^d	-0.67	-0.81	-0.57	-0.72	-0.61	-0.60
V_{2nnr}	5.23 (0)			16.2		-0.38	0.05	-0.50	-0.18	-0.57	-0.48
V_{2a}	5.84 (2)			47.6		-0.61	-0.75	-0.58	-0.65	-0.54	-0.58

^aFrom Ref. [47]

^bFrom Ref. [123]

^cFrom Ref. [72]

^dFrom Ref. [107]

^eFrom Ref. [6]

Table 5.8: Coordination and ring statistics changes compared to the percent change in bulk modulus for vacancy defects and the *FFCD*. Net changes are for isolated defects in a 1728-atom supercell, referred to a similar crystalline supercell. The net change in the number of atoms having a particular coordination is given by N. The numbers under the "rings" heading refer to the net gain or loss of rings of a particular size.

Defect	N			Rings							$\Delta B, \%$
	2	3	5	5	6	7	9	11	12	14	
V_{JT}	0	0	0	4	-12	0	4	0	0	0	0.03
<i>FFCD</i>	0	0	0	4	-12	8	0	0	0	0	0.01
V_{JT_r}	0	1	1	4	-10	0	2	0	0	0	0.01
V_{2nnr}	0	3	1	4	-16	0	0	2	0	0	-0.18
V	0	4	0	0	-12	0	0	0	4	0	-0.34
V_{2n}	0	6	0	0	-18	0	0	0	2	9	-0.55
V_{2a}	0	6	0	2	-22	0	0	0	7	0	-0.65
V_{2nn}	1	6	0	0	-22	0	0	0	8	0	-0.72

was not completely rigid. The two defects with the lowest formation energies, H_2 and the *FFCD*, did indeed have low formation volume magnitudes. The relationship between V_{2n} and V_{2nnr} , however, is the opposite of what one would expect, as is the large formation volume that accompanies the most stable monovacancy V .

We examined the changes in ring structure that accompanied the defects of Table 5.7 in an attempt to relate ring statistics and coordination numbers to the observed changes in elastic constants. The interstitial defects which involved extra atoms did not present any obvious pattern in this regard, but the vacancy defects did. Table 5.8 shows the ring and coordination figures for the vacancy and *FFCD* defects. A ring is defined here as a closed path which is a series of sequentially bonded atoms without overlap, and a primitive ring is a ring which cannot be decomposed into two smaller rings.[139, 75] Dr. Xianglong Yuan of MIT/Department of Materials Science

Table 5.9: Coordination and ring statistics changes compared to the percent change in bulk modulus for interstitial defects, as in Table 5.8.

Defect	N		Rings					$\Delta B, \%$
	5	6	3	4	5	6	7	
H_2	8	0	6	0	2	-2	0	0.43
Tet	4	0	0	6	0	0	0	0.41
DB	2	0	2	0	0	0	2	0.29
DB_1	2	0	2	0	1	-4	4	0.25
DB_4	2	0	0	1	8	-12	8	0.22
DB_3	4	0	3	1	0	-2	3	0.22
Hex_A	6	1	6	0	0	5	0	0.21
DB_2	2	0	2	0	1	-4	3	0.20
Hex	6	1	6	0	0	5	0	0.16

and Engineering determined these primitive ring statistics using a recent effective ring search algorithm of his own invention.[139]

It can be seen that with increased numbers of undercoordinated atoms, the bulk modulus is lessened. Concurrent with this trend are the softening effects of the loss of 6-rings and the gain of larger rings. Offsetting factors include the gain of overcoordinated atoms and rings of size less than six. The relationship between coordination, ring size population, and bulk modulus was more complicated for many of the defects not shown in Table 5.8, but the greatest stiffening of the bulk modulus did coincide with the H_2 and Tet defects, which were characterized by overcoordinated atoms and small rings. The numbers for these other defects are shown in Table 5.9. The Hex and Hex_A defects would appear to be likely to raise the bulk modulus more than other defects above them in Table 5.9, given their 3-rings and their lack of large rings, but perhaps their peculiar planar geometry partially nullifies these stiffening

characteristics.

It is interesting to note that while EDIP may have erred in predicting a locally unstable hexagonal interstitial, Hex_A (which is locally stable under EDIP) is quite similar to Hex in its effects on the supercell elastic constants. The ordering of the formation energies of the tetrahedral and the Hex_A interstitials agrees with LDA calculations,[72] while this was not the case with the symmetric hexagonal interstitial.

Finally, we used the numbers in Table 5.7 to predict the results for the samples (summarized in Figs. 5-1-5-4) generated by random defect placement. We compared the elastic constant changes in these samples to the sum of the individual contributions listed in Table 5.7 for the defects involved. This sum usually overestimated the change in elastic constants, making the worst approximation for the samples containing the highest defect concentration. The error was in some cases as high as 33 %, but averaged only 10 %. The accumulation of elastic constant changes was therefore nearly linear with increasing defect content, as was shown in Figs. 5-1-5-4, though some saturation effects are understandably present at such high defect concentrations.

5.3 Comparison with Stillinger-Weber

Despite our opinion that EDIP was the best choice of potential for modeling the effects of defects on the elastic constants of silicon, we recognize that no empirical potential makes an appropriate description of every physical situation. We therefore chose to carry out several of the calculations presented above using another potential, in order to provide a comparison for our major conclusion that point defects of any species

universally reduce Young's modulus in silicon. The obvious choice for a comparison potential was that of Stillinger and Weber (SW), [116] for it has been "by far the most widely used." [8]

The SW potential, like EDIP, is comprised of a two-body term and a three-body term:

$$E = \frac{1}{2} \sum_i \sum_{j \neq i} V_2(r_{ij}) + \sum_i \sum_{j \neq i} \sum_{k \neq i, k > j} V_3(\vec{r}_{ij}, \vec{r}_{ik}) \quad , \quad (5.19)$$

where r is the interatomic spacing. The two-body term V_2 is given by

$$V_2 = \epsilon A \left[B \left(\frac{\sigma}{r_{ij}} \right)^p - 1 \right] \exp \left(\frac{1}{\frac{r_{ij}}{\sigma} - a} \right) \quad , \quad (5.20)$$

and the three body term V_3 is

$$V_3 = \epsilon \lambda \exp \left(\frac{\gamma}{\frac{r_{ij}}{\sigma} - a} \right) \exp \left(\frac{\gamma}{\frac{r_{ik}}{\sigma} - a} \right) \left(\cos \theta_{jik} + \frac{1}{3} \right)^2 \quad . \quad (5.21)$$

The angle in the cosine of Equation 5.21 is that with atom i at the vertex and subtended by \vec{r}_{ij} and \vec{r}_{ik} . The parameters of Equations 5.20 and 5.21 are summarized in Table 5.10. The SW uses a sharp cutoff radius for r_{ij} of $\sigma a = 3.77118 \text{ \AA}$.

The SW crystalline elastic constants are compared to those of EDIP and experiment in Table 5.11. Also included are the crystalline elastic constants of the potential used by Clark and Ackland [27] for their calculations of the effects of monovacancies and two interstitial types on the elastic constants of silicon. Both the SW and EDIP potentials appear to make a reasonable description of the crystalline elastic constants,

Table 5.10: Parameters used in the Stillinger-Weber potential. The parameter f is a scaling factor not shown in Equations 5.20 and 5.21 — we have used this factor to multiply both two- and three-body terms in order to obtain a cohesive energy of -4.63, as described by Balamane *et al.* [8]

$\epsilon = 2.16826$ eV	$A = 7.049556277$	$B = 0.6022245584$
$\sigma = 2.0951$ Å	$p = 4$	$a = 1.80$
$\lambda = 21.0$	$\gamma = 1.20$	$f = 1.066989$

Table 5.11: Elastic constants of diamond crystalline silicon in GPa.

	SW	Clark and Ackland [27]	EDIP	Expt.[50, 34]
C_{11}	161.67	149.82	171.99	167.54
C_{12}	81.59	123.69	64.72	64.92
C_{44}	60.27	26.13	72.75	80.24
B	108.28	132.40	100.47	99.13
$E_{\langle 100 \rangle}$	106.94	37.95	136.60	131.28
$E_{\langle 110 \rangle}$	137.83	59.58	164.05	170.63

with EDIP coming very close indeed to the experimental values. Looking at $E_{\langle 100 \rangle}$ and $E_{\langle 110 \rangle}$, it is obvious that the Clark and Ackland potential is unacceptably far from experiment.

Using the SW potential, 10 simulation cells were prepared with random defect populations. The cells were prepared as for the EDIP cells described previously: random positions were chosen for vacancies or interstitials in a 1728-atom crystalline cell. Atomic positions and all three cell dimensions were then relaxed at 0 K. The result was annealed at 300 K for 500 ps, then again relaxed at 0 K. In this manner, cells containing 1–5 vacancies and (separately) 1–5 interstitials were created.

The visualization of the annealed defects using AtomEye[73] made it readily appar-

ent that the interstitial defects produced in this random process were quite different than those of EDIP. While they were almost all variations on the $\langle 110 \rangle$ dumbbell, much as the configurations DB_{1-4} shown in Figure 5-7, they preferred undercoordination to overcoordination. For example, two of ten randomly generated interstitials resembled the DB_4 geometry, except that bonds between the two uppermost pairs of atoms (see Figure 5-7) were missing, making the topmost pair 2-fold coordinated and the lower pair 3-fold coordinated (using a cutoff of 2.56 Å for determining coordination). Several of the pre-annealing random configurations contained tetragonal interstitials. This can be understood by considering the unrelaxed formation energy of an interstitial along the body diagonal of the silicon unit cell. This formation energy is plotted for the SW potential in Figure 5-13. Unlike EDIP (compare with Figure 5-9), SW predicts a stable tetrahedral interstitial, in contradiction of *ab initio* calculations.[72]

As for the EDIP-prepared cells above, we carried out deformations of the cells in order to produce energy-strain curves from which to calculate the elastic constants C_{11}, C_{12}, C_{44} , and B . The results of these elastic constant calculations are shown in Figures 5-14-5-18. The slopes fit to the data in these figures are given in Table 5.12. Examining Table 5.12, we see that the Stillinger-Weber potential makes a very different description of the effects of vacancies on the elastic constants. With the SW potential, C_{11} , C_{12} , C_{44} , and B are all predicted to rise with increasing vacancy content. It is interesting to note, however, that despite this description very different from that made by EDIP, the Young's modulus is nevertheless predicted to *decrease*.

It is highly unlikely that cascade damaged regions will contain vacancies without the presence of interstitials. Indeed, Caturla *et al.* [23] observed that for boron and

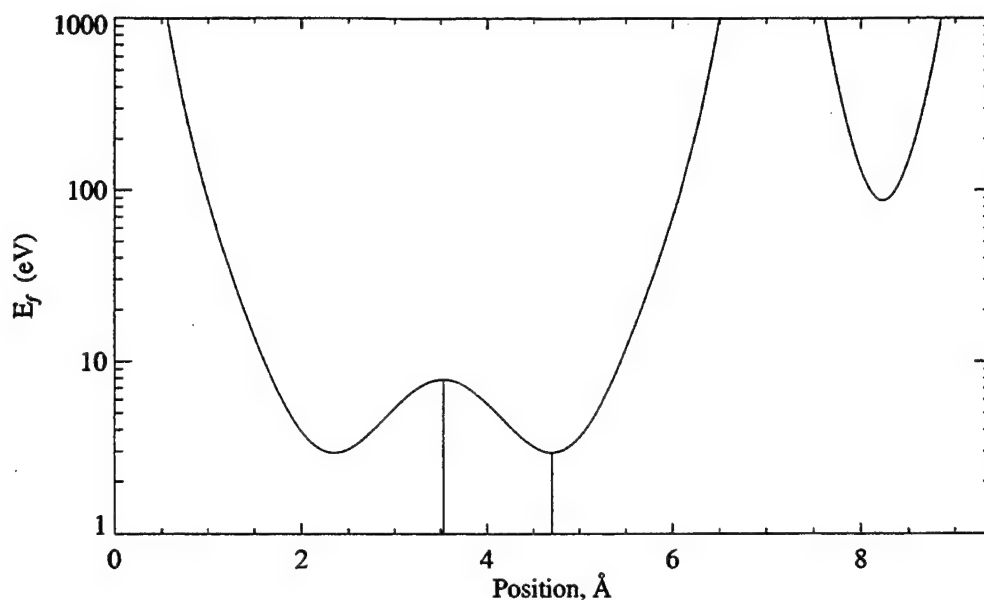


Figure 5-13: Unrelaxed formation energy for an interstitial placed along the unit cell body diagonal in Si, calculated using the Stillinger-Weber potential. The vertical lines indicate the positions of the hexagonal (left) and tetragonal (right) interstitials, respectively.

arsenic collision cascades in silicon, the numbers of isolated vacancies and interstitials left in the wake of the cascades were roughly equal. This being the case, the real issue at hand is what effects Frenkel pairs will have on the elastic constants. With the EDIP simulations above, we observed that at the high concentrations simulated, the defects were fairly independent of each other in their effects on the elastic constants. It is clear, despite the large scatter in the interstitial calculations of Figures 5-14-5-18 (this being due to the smaller numbers of SW simulation cells and the wide variability of interstitial species), that this conclusion also holds for the SW results. In the case of SW vacancies (of which there was only one type in our samples), the linear trend is unmistakable. Since the individual defect effects are fairly independent of each other, the effects of equal numbers of interstitials and vacancies (Frenkel pairs) can

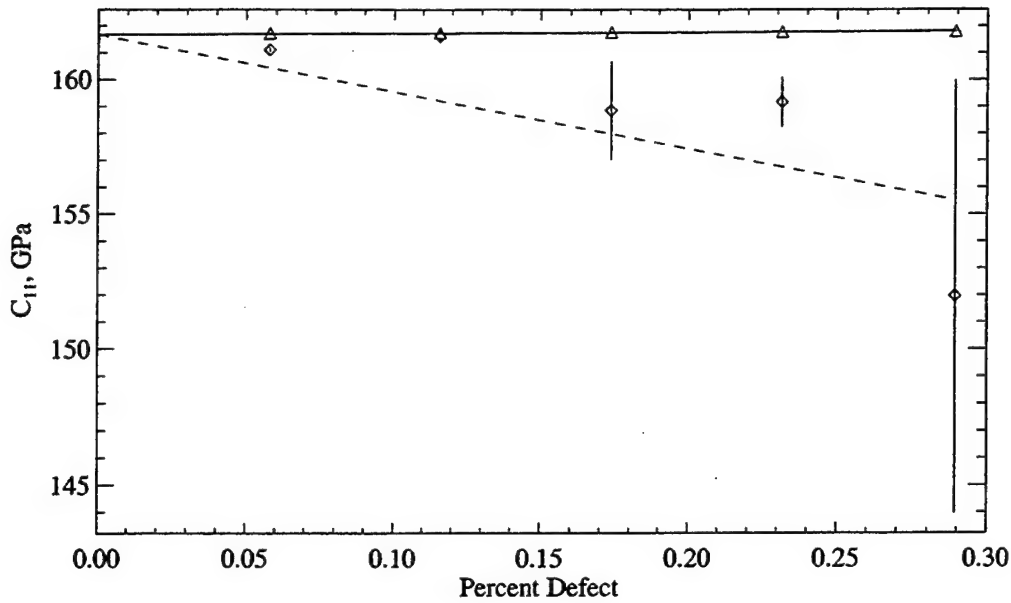


Figure 5-14: C_{11} as a function of point defect fraction, calculated using Stillinger-Weber. Diamonds indicate interstitials and triangles vacancies. Each point represents the average of three directions in the same sample. Bars indicate the standard deviation among the three directions. Lines are unweighted least squares fits constrained to match the crystalline value on the Y-axis.

be estimated by simply adding the slopes of Table 5.12, as shown in the rightmost column. EDIP and SW predictions for Young's modulus are of the same order, and stand in stark contrast to the prediction of the potential of Clark and Ackland.

Despite the good agreement between EDIP and SW on the issue of Young's modulus, the large difference in the description made by the two of vacancy effects warrants investigation. To this end, we carried out calculations using isolated point defects in 1728-atoms simulations cells. We examined three defects: the monovacancy V , the tetrahedral interstitial Tet , and the lowest-energy $\langle 110 \rangle$ dumbbell (DB) interstitial variant that we observed (there were several variants, with only slight differences atomic positions and formation energy, and no differences in the bonding topology).

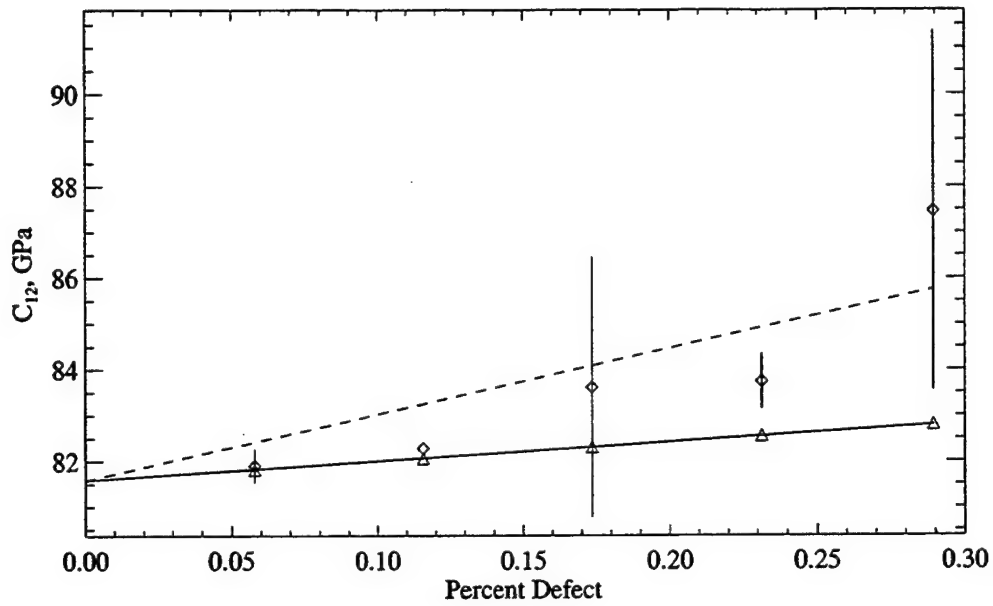


Figure 5-15: C_{12} as a function of point defect fraction, calculated using Stillinger-Weber. Notation is as in Figure 5-14.

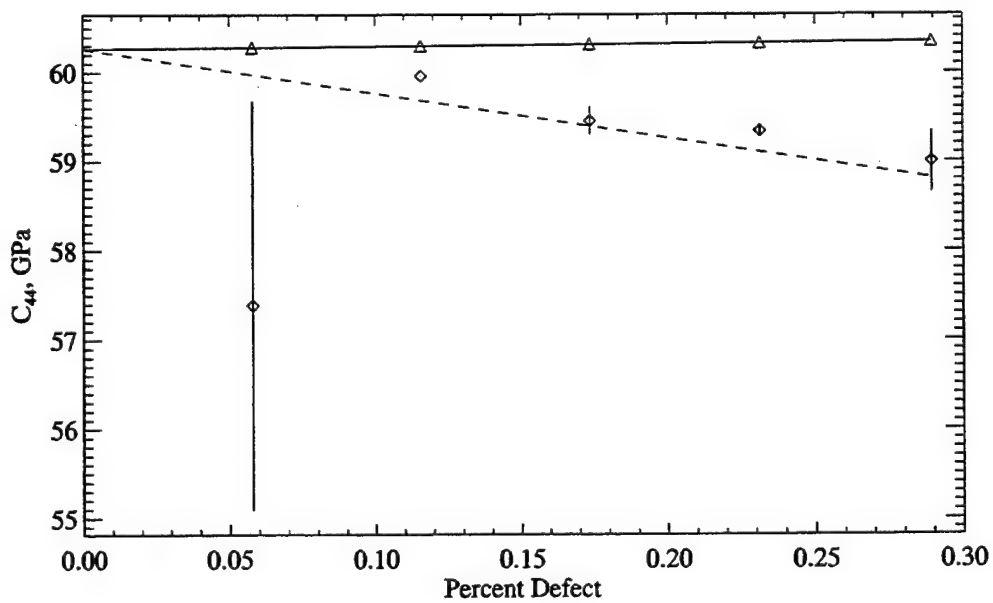


Figure 5-16: C_{44} as a function of point defect fraction, calculated using Stillinger-Weber. Notation is as in Figure 5-14.

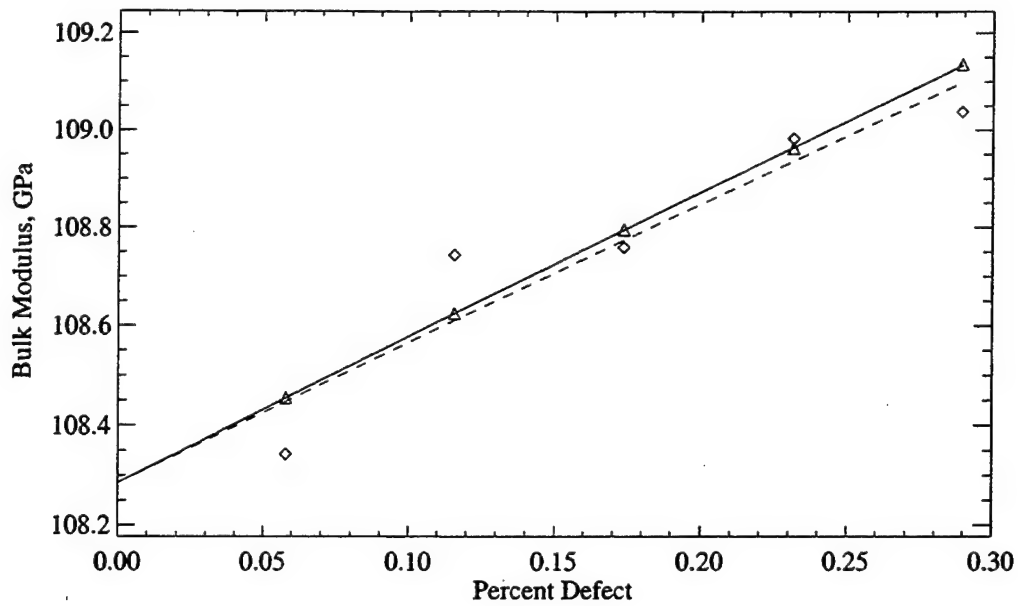


Figure 5-17: Bulk modulus B as a function of point defect fraction, calculated using Stillinger-Weber. Notation is as in Figure 5-14.

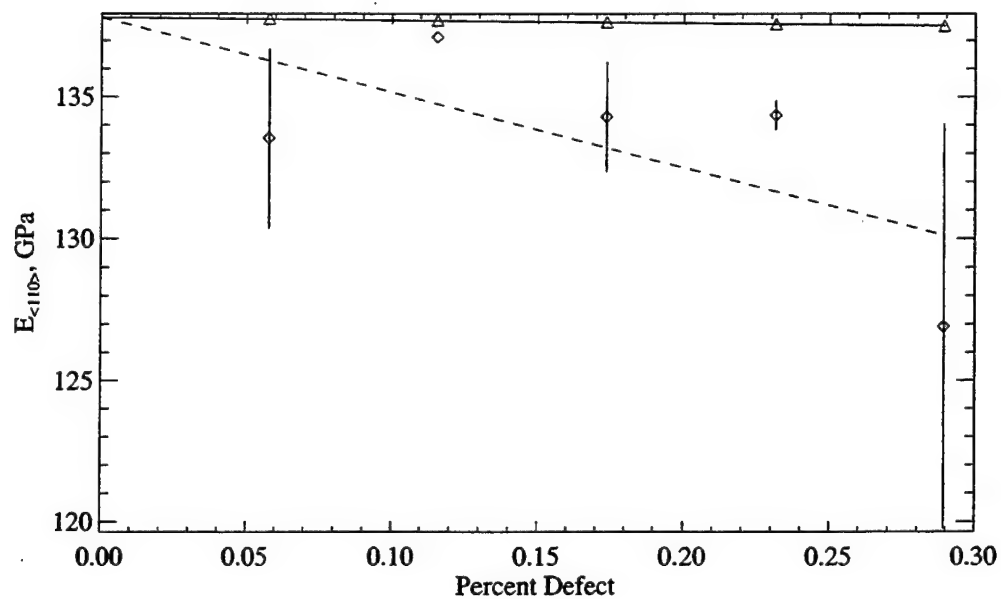


Figure 5-18: Young's modulus $E_{(110)}$ as a function of point defect fraction, calculated from data shown in Figures 5-14–5-16. Notation is as in Figure 5-14.

Table 5.12: Fit slopes to data of Figures 5-14–5-18. Units are GPa per defect fraction. Results from EDIP and Clark and Ackland [27] are provided for comparison.

	Potential	Interstitials	Vacancies	Vac+Int
C_{11}	SW	-2129	45	-2084
	EDIP	-89	-1030	-1119
	C&A	715	821	1536
C_{12}	SW	1437	417	1864
	EDIP	733	-381	352
	C&A	443	565	1008
C_{44}	SW	-504	26	-478
	EDIP	-440	-369	-809
	C&A	-58	-9	-67
B	SW	281	293	674
	EDIP	462	-593	-131
	C&A	531	648	1179
$E_{\langle 110 \rangle}$	SW	-2666	-99	-2765
	EDIP	-751	-899	-1650
	C&A	161	217	378

The formation energies and volumes, as well as effects on elastic constants are shown in Table 5.13 for these three defects.

It is readily seen in Table 5.13 that EDIP makes a description of these defects that is superior to that made by SW. This is true in terms of both formation energy and formation volume, for all three defects. Additionally, in the case of the tetrahedral interstitial, EDIP was shown in Figure 5-9 to predict an unstable defect for the unrelaxed configuration, in agreement with *ab initio* calculations, whereas SW predicts the opposite. For the vacancy, SW predicts a *negative* formation volume and very low energy. This means that SW silicon actually *densifies* with the introduction of monovacancies. This was a surprising result in the case of the Jahn-Teller vacancy V_{JT} discussed in section 5.2.2.4, but was somewhat explainable in terms of the purely

four-fold coordination that resulted in that case. The SW monovacancy, however, had 4 3-fold coordinated atoms (the vacancy neighbors). It is not surprising, therefore, that the SW vacancy gives significantly different results in terms of elasticity effects than does EDIP.

One also may wonder at the large difference between EDIP and SW seen for interstitials for C_{11} in Table 5.12. Most of the SW interstitials in the randomly generated defected simulation cells were minor variations on the lowest-energy *DB* of Table 5.13. Like for the vacancy, the prediction made by EDIP is much closer to the *ab initio* formation energy and volume. Of perhaps equal importance for elastic constant effects, however, is the difference in bonding topology for this defect between EDIP and SW. Referring to the EDIP *DB* configuration shown in Figure 5-7, we see that the left and rear face-centered atoms are 5-fold coordinated. The EDIP distance from the five-fold atoms to the interstitial dumbbell atoms (darkened) is 2.48 Å. This interatomic distance is 2.70 Å for SW, and using a generous 2.56 Å as a “bond” cutoff, this results in the interstitial dumbbell atoms being 2-fold coordinated. Furthermore, the EDIP 5-fold coordinated atoms become 3-fold coordinated with SW. The EDIP bond topology of the dumbbell defect agrees with *ab initio* calculations, whereas the SW description does not.[72]

5.4 Discussion

We have used a well tested, well characterized potential to study the effects of defects on the elastic constants of silicon. That our new results contradict those of

Table 5.13: Formation energies, volumes, and percent change in elastic constants for a single defect in a 1728-atom supercell, calculated using the Stillinger-Weber potential. Energy is in eV, volume in \AA^3 . For comparison, data is reproduced here from Table 5.7 for EDIP and density functional theory calculations from the literature. LDA calculations are designated by (L) and GGA by (G). See Table 5.7 for references.

	<i>DB</i>			<i>Tet</i>			<i>V</i>		
	SW	EDIP	DFT	SW	EDIP	DFT	SW	EDIP	DFT
E_f	4.70	3.38	3.31(G)	5.25	4.10	4.07(G)	2.82	3.22	3.29(L)
V_f	14.23	8.7	-2.0(L)	23.15	19.6		-13.46	28.8	12.8(L)
C_{11}	-0.24	-0.02		-0.03	0.12		0.03	-0.31	
C_{12}	0.32	0.72		0.25	0.81		0.28	-0.42	
C_{44}	-0.54	-0.32		-1.01	-0.43		0.03	-0.27	
B	0.05	0.29		0.11	0.41		0.16	-0.34	
$E_{\langle 100 \rangle}$	-0.72	-0.35		-0.27	-0.18		-0.18	-0.26	
$E_{\langle 110 \rangle}$	-0.54	-0.25		-0.65	-0.24		-0.03	-0.28	

Clark and Ackland[27] is not surprising, in view of the untested potential they used. The elastic constants of the potential of Clark and Ackland are significantly different from experiment, perhaps even more so than the authors realized. They appear to have mistakenly used the experimental constants of Si at 1477 K as a reference for their calculations at 0 K.[27, 67] The elastic constants of the Clark and Ackland potential differ from experiment[50] by 11 %, 91 % and 67 %, for C_{11} , C_{12} , and C_{44} , respectively. The disagreement in results is perhaps best summarized by considering Young's modulus, which is commonly of importance in practical situations. We observed that all defect types, whether isolated or in random arrangements, caused a lessening of Young's modulus, whereas the results of Clark and Ackland imply that the presence of vacancies or interstitials causes Young's modulus to increase.

The SW calculations of section 5.3 give results that are different in many ways from those made using EDIP. The end result for the decrease in Young's modulus due

to Frenkel pairs is very similar. A particularly startling result is that even though SW makes a poor description of the monovacancy, and therefore predicts, in contradiction to EDIP, that C_{11} , C_{12} , C_{44} , and B are increased by the presence of vacancies, the effect on Young's modulus is nevertheless to decrease it. This may indicate the importance of having a potential that at least makes a decent description of the relative magnitudes of C_{11} , C_{12} , and C_{44} . With these values far from experiment, and not even in proper proportion to each other (Table 5.11), the potential of Clark and Ackland produces a Young's modulus about 1/3 the experimental value. The problems SW demonstrated with describing the individual defects were somewhat mitigated by the fact that it, at least, made a reasonable description of the relative proportions of the crystalline elastic constants.

The only other study of the effects of defects on elastic constants that we were able to find in the literature was that of De Sandre *et al.*[46] It is difficult to compare our findings with regard to point defects with those of that study given that the lowest concentration considered there was 9.3 %, at which point the crystal-to-amorphous transition has begun.[29]

Since it would appear from Table 5.4 that, even at the high defect concentrations studied here, point defects have an effect on the elastic constants that is fairly independent of one another, the details of coordination within each defect as it relates to connectivity in the lattice appears to be important. As shown in Table 5.7, a vacancy will have different effects on the elastic constants depending on its relaxed bonding configuration. While EDIP does (by design) produce elastic constants for silicon close to those of experiment, the configurations of relaxed point defects it

produces do not correspond precisely with those predicted by *ab initio* calculations. The volume expansion shown in Fig. 5-6 is likely not in good agreement with reality, since the samples involved contained mostly monovacancies, which were shown here to be outward-breathing in EDIP. As mentioned above, recent *ab initio* calculations indicate that the monovacancy may relax inward, with its neighbors bonding pairwise to produce only 4-fold coordination. The result would be a (slightly) negative formation volume, which would correspond to a densification with increasing monovacancy content. Therefore, even though we have demonstrated (by comparison with the Stillinger-Weber potential) that the description of defects made by EDIP is quite good, we must therefore be cautious as to which results presented here we expect to correspond to reality.

This word of caution does not preclude two generalizations of practical interest, however. We reiterate that the general trend of Young's modulus is consistently downward with increasing defect content. This effect varies within a very narrow range for the defect configurations considered here. It should therefore be possible to make reasonable predictions of the shift in the Young's modulus of a radiation-damaged silicon sample in which isolated point defects dominate, even if the exact geometry of each point defect is not well known. The calculation presented here of the crystalline/amorphous composite sample is also encouraging. It would appear that a reasonable prediction of changes in Young's modulus can also be made for radiation-damaged samples in which amorphous regions are important, based simply on the volume fraction of amorphous material, according to Eq. 5.17.

We have been unable to locate experimental studies in the literature with which

to compare our major result of the decrease of Young's modulus with defect concentration. A related study by Burnett and Briggs [20] measured the elastic constants of a surface layer of silicon after bombardment with arsenic and silicon ions. TRIM modeling of their implantation fluences indicate that they irradiated the surface layer to a dose of 0.07 to 1.95 dpa. If we assume that every TRIM displacement results in a Frenkel pair, then the lowest defect content of this study is close to the amorphization threshold.[29] We cannot, therefore, quantitatively compare our results at much lower defect concentrations to the experimental values for the elastic constants of silicon, except to note that for all ion doses in the experiments of Burnett and Briggs, both C_{11} and C_{44} were observed to decrease with irradiation. This agrees qualitatively with our EDIP-based predictions.

Lacking directly comparable experimental studies involving silicon, we looked into the literature on metals. There exists a considerable body of work studying radiation cascades in BCC and FCC metals.[59, 37] These appear to be fundamental studies in support of a related body of literature concerned with the mechanical properties of steels.[69, 4] The mechanical properties of most interest appear to be the yield strength and hardness, and studies of the effects of radiation on these properties often refer to "radiation hardening" and "radiation embrittlement." [106, 42] Unfortunately, these experiments involve a very different situation than the one we have computationally modeled. Radiation hardening involves defects clusters and precipitates that occur as a result of radiation damage.[106] These defects impeded the motion of the dislocations, by which crystalline materials plastically deform. Thus, irradiated metals are "hardened." Hardness and yield strength are related properties,[7] but it is

quite possible for these to increase independently of the Young's modulus. Indeed, in the only study we located that reported the effect of radiation on Young's modulus, it was found that although the yield strength rose with radiation dose, the Young's modulus decreased. A 0.5 % decrease was observed for a neutron fluence of 1.1×10^{16} n/cm². The energy of the incident fast neutrons is not described, but by assuming this fluence to be the 1 MeV equivalent, we can make a prediction of what effect such a fluence would have had on the elastic constants of silicon. Assuming a thin sample (dimensions for the steel were not given) and using the TRIM-2003 value of 1077 displacements per recoil, we estimate a Frenkel pair fraction of 5×10^{-5} . Using the EDIP predicted value of -1653 GPa per defect fraction, we obtain a 0.05% decrease in Young's modulus. It is interesting to note that this prediction for silicon is within an order of magnitude of that measured in the austenitic (FCC) steel. Too many variables are unaccounted for, however, to make the comparison very meaningful (neutron energy, differences in cascade formation in steel versus silicon, grain boundary and dislocation effects in the steel, and others). At the very least, however, it boosts our confidence in our assertion that defects reduce Young's modulus.

5.5 Conclusions

We have characterized the structure of various point defects according to EDIP and calculated their individual effects on elastic constants. We have shown that elastic constants of silicon vary with defect concentration in a roughly linear fashion at defect concentrations up to 0.3 %. The repetition of several calculations in section

5.3 using the Stillinger-Weber potential supported the conclusions made based on the EDIP-based simulations. The SW result for the Young's modulus decrease caused by Frenkel pairs was found to be (see Table 5.12) -2765 GPa per defect fraction. The EDIP result was -1653 GPa per defect fraction (see Table 5.4), and is the preferred result. The discrepancy between the two results is explainable in terms of the incorrect description made by SW of the $\langle 110 \rangle$ dumbell interstitial and the monovacancy. In any case, the previously published result of 378 GPa per defect fraction, based on a little known potential used by Clark and Ackland [27] is clearly to be discounted.

We have demonstrated the effects of an amorphous region embedded in a crystalline supercell to be well described by a simple equation involving the volume fraction of amorphous material. We have also produced and found elastic constants for several amorphous samples, and concluded that EDIP consistently underestimates C_{44} for amorphous Si when compared to experimental results. This discrepancy may be due to the limitations of the potential, but it may also be due to the fact that the experimentally measured samples consisted of thin layers amorphized by ion bombardment, whereas the computational simulation samples were quenched from the melt.

We predict that both interstitial and vacancy defects, singly and in random combination, lessen the Young's modulus of silicon, contrary to the findings of a previous study.[27] We feel that difference is likely due to the superior description made by EDIP of the elastic constants of silicon, as well as EDIP's superior description of defects in terms of formation energy, volume, and bond topology. We also conclude that the individual contributions of various defect types to changes in Young's modulus

are confined to a surprisingly small range. Specifically, for a 1728-atom simulation cell, individual point defects of 17 varieties, whether vacancies or interstitials, reduced Young's modulus in the $\langle 110 \rangle$ direction by 0.28 %, with a standard deviation of ± 0.05 %.

Chapter 6

Implications for MEMS

6.1 Overview

It is well known that environmental factors such as temperature can adversely impact the performance of MEMS devices. In this chapter, we will demonstrate that radiation is also a potential source of performance degradation for sensitive devices through the alteration of mechanical properties of common MEMS materials. Space-based electronic devices are notoriously susceptible to degradation due to radiation, since the electrical properties of materials can be dramatically altered by relatively low radiation doses. Mechanical properties such as density and elasticity can also be altered by radiation damage. While these changes are slight, they can be of critical importance to a MEMS device operating in space or in a reactor environment.

6.2 Benchmark MEMS scenario

6.2.1 Hypothetical MEMS device

In order to illustrate the possible impact of radiation-induced dimensional and elasticity changes in glass and silicon on a MEMS device, we will consider a silicon MEMS resonant beam anodically bonded to a glass substrate. In order to choose typical dimensions, we draw inspiration from a real MEMS accelerometer developed by engineers in Korea.[118] An illustration of the device is shown in Figure 6-1. In this design, a central mass is suspended above the substrate surface by silicon beams. These beams are driven in oscillation at their natural frequency. When the device undergoes an acceleration, the stress in these oscillating beams changes, thus changing the natural frequency of the oscillation. A feedback loop allows the device to measure the change in frequency, from which the acceleration is deduced. A MEMS chemical or biological agent sensor might also operate in a similar fashion with a resonating beam, measuring the frequency shift as the mass of the beam changes due to accumulation of material on its surface.

In what follows, we will consider the effects of radiation damage on a simple resonating beam which is anodically bonded to a borosilicate glass substrate. The arrangement is shown in Figure 6-2. The dimensions of the beam are estimates of those of the beams in reference [118]. These dimensions are a height h of 40 μm , a width w of 10 μm , and length L of 800 μm .

The natural frequency of oscillation of a beam fixed at both ends and subjected

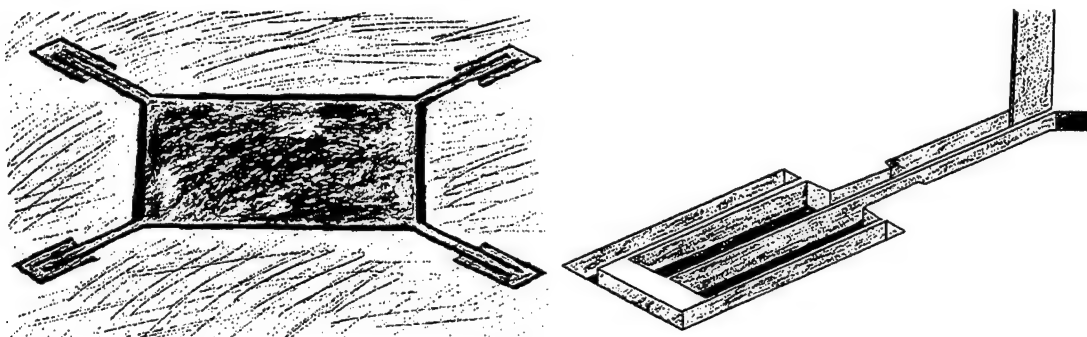


Figure 6-1: MEMS accelerometer from reference [118]. At left, the central square proof mass is suspended above the substrate surface by a beam at each corner. The detail of one of the beam structures at the corner of the central mass is shown at right.

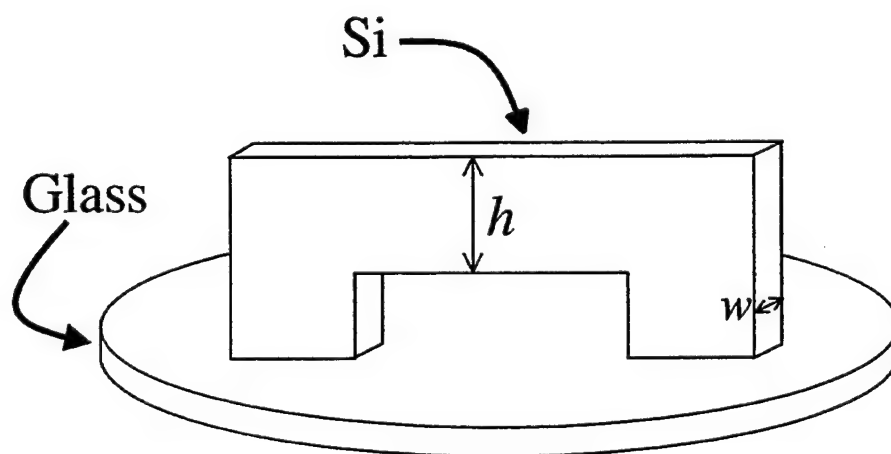


Figure 6-2: MEMS resonating beam. The silicon beam is suspended above the glass substrate surface, supported at either end by bond pads.

to uniform axial loading is given by

$$f = \frac{1}{2\pi} \sqrt{\frac{192EI}{M_{eff}L^3} + \frac{24F}{5M_{eff}L}} \quad , \quad (6.1)$$

where E is the Young's modulus of the beam, M_{eff} is the effective mass of the beam, I is the area moment of inertia of the beam $wh^3/12$, and the axial force $F = EA\epsilon$ is a function of the applied strain. In order to determine the effective mass of the beam, we use

$$f = \frac{1}{2\pi} \sqrt{\frac{EI\lambda^4}{ML^3}} \quad , \quad (6.2)$$

where M is the beam mass and $\lambda = 4.73004074$. [18] Equating Equations 6.1 and 6.2 for $F = 0$, we obtain $M_{eff} = M/2.607$. The mass M is assumed to be $whL\rho$ ($\rho_{Si} = 2.33 \text{ g/cm}^3$).

The overall shift in frequency will be

$$\Delta f = \frac{\partial f}{\partial E} \Delta E + \frac{\partial f}{\partial F} \Delta F + \frac{\partial f}{\partial I} \Delta I + \frac{\partial f}{\partial L} \Delta L \quad . \quad (6.3)$$

Since we are considering the special case of $F = 0$ (no initial tension in the beam), we have $\Delta F = EA\epsilon$. The differential strain between glass substrate and silicon beam is $\epsilon = \epsilon_{glass} - \epsilon_{Si}$ and $A = wh$. We assume $\Delta L = (\epsilon + \epsilon_{Si})L$, that is, the silicon length change is only dependent on the compaction of the glass substrate. Finally, we have

$$\Delta I = \frac{w^3}{12} \Delta h + \frac{hw^2}{4} \Delta w \quad , \quad (6.4)$$

where

$$\Delta h = (\epsilon_{Si} - \nu_{001}\epsilon)h \quad (6.5)$$

$$\Delta w = (\epsilon_{Si} - \nu_{110}\epsilon)w \quad (6.6)$$

We assume that the Poisson ratios are $\nu_{001} = 0.36$ and $\nu_{110} = 0.06$.[138]

Substituting into and then solving Equation 6.3, we get

$$\frac{\Delta f}{f} = 958\epsilon + \frac{1}{2}\epsilon_{Si} + \frac{1}{2}\frac{\Delta E}{E} \quad (6.7)$$

6.2.2 Radiation environment

We assume a reactor environment involving fast (1 MeV equivalent) and thermal neutron fluxes, as well as gamma flux. Gamma radiation will be present in space, but protons, rather than neutrons, will be of primary concern in terms of ballistic collision displacement damage. It is convenient for the present analysis to examine the neutron case, since the mean free path of a 1 MeV neutron in Si is about 4.5 cm. This is a long mean free path on the MEMS scale, and will result in recoil ions that are uniformly distributed in silicon MEMS components. By contrast, a 1 MeV proton was shown in a SRIM-2003 [144] simulation to penetrate to only about 17 μm , which would complicate the analysis of elastic effects in MEMS parts due to the sharp gradient in damage with depth from the surface. With neutrons, we will also not have to account for the electronic stopping that is so important for protons. Proton fluences (1 MeV equivalent) accumulated in space would be about 1×10^{14}

n/cm² over one year. We will take, for the reasons discussed above, a benchmark dose of neutrons to be the same. Typical gamma dose for a year in space is 1 MRad.

Fast neutrons cause damage by displacing atoms from their lattice sites through collisions with atomic nuclei. A 1 MeV neutron has an elastic scattering cross-section in silicon of about 4.5 barns (10^{-24} cm²), with no non-elastic cross section of any importance to our analysis. The energy spectrum of Si recoils that scatter such neutrons is approximately flat.[71] The maximum recoil energy for an Si atom is given by Equation 2.3. We therefore assume equal probability for recoil atoms in Si to have energies from 0 eV to $T_m = 133$ keV. Calculations were made using SRIM-2003 of such a recoil spectrum in Si, and it was determined that on average, a primary knock-on atom (PKA) creates about 1077 vacant lattice sites through its collisions and the ensuing sub-cascades. To calculate the probability of an effluent neutron creating a PKA within a Si thickness x , one can use Equation 4.5, $P_{scat}(x) = 1 - e^{-\sigma Nx}$, with $\sigma = 4.5$ barns and N being the number density [125] of Si (4.99×10^{22} n/cm³).

For a given neutron fluence and a thin piece of silicon, then, we can estimate the number of initial displacements in the silicon. How these displacements translate into damage will depend on temperature, dose rate, and total dose.[132, 91, 90] Damage can be categorized into isolated defects and amorphous “pockets.” At high temperatures, more of the vacancy-interstitial pairs will anneal out shortly after forming. At high dose rates, amorphization becomes more probable, since regions of high defect concentration are more likely to get hit by another cascade before annealing has had a chance to happen.

Since computational studies of damage cascades are limited in the time scales they

can address, the actual damage profile is hard to specify for low neutron fluences. We therefore take the approach of characterizing the effects of such damage by examining the two extreme cases: 1) the displaced atoms are all in amorphous pockets and 2) the displaced atoms all form isolated defects.

6.3 Estimation of radiation effects

We can bracket the changes to overall elastic modulus E_C in terms of the volume fraction of amorphous material V_1 and the elastic moduli of the matrix E_2 and the embedded amorphous regions by using (see Equation 5.17)

$$\left[\frac{V_1}{E_1} + \frac{(1 - V_1)}{E_2} \right]^{-1} < E_c < V_1 E_1 + (1 - V_1) E_2 \quad , \quad (6.8)$$

where V_1 and E_1 are, respectively, the volume fraction and Young's modulus of the embedded material, and E_2 is the Young's modulus of the matrix.

Estimating the volume fraction of amorphous material is somewhat tricky, partly due to the lack of an easy definition of an 'amorphous' atom. Molecular dynamics simulations [23] have shown that heavy ions (As) will cause defects that occur mostly in disordered (amorphous) zones in Si, and that light ions (B) will cause damage wherein isolated defects predominate. Comparing to the SRIM results for these simulations and interpolating to the Si mass, we determine that the total number of defects (vacancies + interstitials) for a recoil in the MD simulations is a constant factor of that predicted by SRIM for a given recoil mass. Interpolating between the

masses of As and B to obtain such factor for Si, we estimate that MD simulations such as these would predict about 660 atoms occupying amorphous zones for an average PKA recoiling from a 1 MeV neutron collision.

Another complicating factor is the survival rate of the initially generated defects. The molecular dynamics simulations of Caturla *et al.*[23] included an annealing simulation that showed relative stability for the damage caused by a 5 keV As ion at room temperature. With an annealing time of only 0.5 ns, however, one cannot be too confident that this damage would survive a real-life annealing. However, the authors do cite some experimental evidence [105] that gives some idea of what to expect in terms of defect survival. It was observed that for heavy implanted ions such as Sb, the number of surviving defects in silicon is greater than that predicted by TRIM, while for a light ion such as B, the number of surviving defects is less than the TRIM estimate. For Ga (near the midpoint in mass between Si and Sb), the TRIM displacements underestimate the surviving defects at low energy, but overestimate the defects at 1 MeV. It appears that, both in terms of mass and in energy, our ~ 67 keV Si PKAs lie in the region where the TRIM displacement estimates may be a fair approximation of reality. We will therefore make no adjustments to our initial displacement estimates to account for annealing.

The benchmark neutron fluence will cause 2.24×10^{13} PKA/cm³, each of which will cause about 1785 point defects (vacancies + interstitials), per the SRIM/Caturla *et al.* analysis described above. Using the slopes from Figure 2, we predict that the relative shift of Young's modulus would be about -5×10^{-6} for the case of 1785 isolated defects per cascade, where we have used the slope of the line in Figure 5-5 describing

the dependence of Young's modulus on the Frenkel pair concentration. For the other extreme case of the 660 atoms in amorphous zones per cascade, Equation 6.8 brackets the relative shift in Young's modulus to be between -1.45×10^{-7} and -2.80×10^{-7} , where we have used the results of Table 5.5 for computational amorphous sample A.

Borosilicate glass such as Pyrex is susceptible to compaction from cascade damage (protons and neutrons) and from gamma exposure, whereas silicon is very resistant to ionizing radiation such as gamma and electrons.[84] The Pyrex compaction from neutron the neutron fluence considered here would be around -6×10^{-7} strain. Extrapolations from experiment to this neutron fluence predict that silicon would expand by about 2.5×10^{-8} (strain) with this same neutron fluence (see Figure 3-1).[56] Such differential compaction would put the hypothetical beam under compression, causing even more dramatic changes to its frequency. Additionally, extrapolation predicts that a gamma dose of 1 MRad will cause an additional -4.70×10^{-7} compaction of the Pyrex.[31, 110] Hoya SD-2 was observed to compact with neutron fluence at a rate about 10.5 times less than did Pyrex (Figure 4-12). Since the pointer beam experiment had unexplained results, we apply this multiplying factor to the known gamma compaction of Pyrex to predict that of Hoya SD-2. A summary of these predictions is found in Table 6.1.

We can now substitute values from Table 6.1 into Equation 6.7. The large multiplier in front of the substrate-beam differential strain makes the device very sensitive to compaction in the glass. In fact, the glass compaction completely dominates the change in frequency, producing 0.1% $\Delta f/f$ for the Pyrex-mounted device in our assumed environment. By contrast, were the silicon beam to be mounted on a silicon

Table 6.1: Estimates of radiation-induced changes in Pyrex, Hoya SD-2, and silicon. A fluence of 1×10^{14} n/cm² (1 MeV neutrons) and 1 Mrad gamma is assumed.

	Neutron		Gamma
	$\Delta l/l$	$\Delta E/E$	$\Delta l/l$
Si	2.5×10^{-8}	$-0.15-5 \times 10^{-6}$	~ 0
Pyrex	-6.0×10^{-7}	—	-4.7×10^{-7}
Hoya SD-2	-5.7×10^{-8}	—	-4.5×10^{-8}

substrate (so as to have zero differential strain), $\Delta f/f$ would be between -6.3×10^{-8} and -2.5×10^{-6} .

Clearly, borosilicate glass is the weak link for radiation hardness for MEMS. The boron contained within the glass makes it even more vulnerable to compaction. We did not consider thermal neutron damage explicitly, having no estimate of the thermal neutron fluence in space. For a reactor environment (in which thermal neutrons are plentiful), one could estimate the effect of thermal neutrons by comparing the values of “displacements per incident neutron” in Tables 4.8 and 4.7. By using as multipliers the ratio of these numbers for fast and thermal neutrons and the ratio of the thermal fluence with the fast fluence of 1×10^{14} n/cm² from our example, one may translate the results of Table 6.1 into equivalent effects for thermal neutron damage. The outlook for a Pyrex-based device subjected to thermal neutrons is not encouraging — an incident thermal neutron causes almost 5 times more displacements in Pyrex than does a fast neutron.

On the other hand, our pointer beam strain gauge experiment, which involved the irradiation of actual MEMS devices, did not agree at all with the prediction made here on the basis of the known effects of radiation on the the mechanical properties of the

individual materials. Specifically, the greatest problem cited here is the differential substrate-beam strain, with its large coefficient in Equation 6.7. This differential strain was almost immeasurably absent in the irradiated MEMS strain gauges. It may be, that when this surprising result is understood, that anodically bonded devices may actually present certain advantages for use in a radiation environment.

Chapter 7

Conclusions

7.1 Summary

We have considered the effects of neutron and gamma irradiation on the pertinent mechanical properties of three materials commonly used in MEMS fabrication: silicon and two borosilicate glasses, Pyrex and Hoya SD-2. What follows is a brief summary of the experiments and calculation we have carried out.

Neutron irradiation of borosilicate glasses at the MIT reactor. We irradiated glass samples at the MIT reactor with thermal and fast neutrons. We measured the densification of the glasses using a sink/float technique. The observed densification was principally due to thermal neutrons, but the TRIM-deduced equivalences summarized below allow us to, nevertheless, present the findings of Table 7.1. The results for Pyrex agree with those of previous experiments. These are no previously published results for Hoya SD-2.

Table 7.1: Results of MIT sink/float measurements.

	Pyrex	Hoya SD-2
$\frac{\Delta\rho/\rho}{n/\text{cm}^2}$, thermal	8.14×10^{-20}	2.21×10^{-21}
$\frac{\Delta\rho/\rho}{n/\text{cm}^2}$, fast	1.79×10^{-20}	1.71×10^{-21}

Table 7.2: Summary of TRIM calculations for fast and thermal neutrons.

	Pyrex	Hoya SD-2
Displacements per fast neutron collision	614	644
Probability of fast neutron collision	0.036	0.038
Displacements per incident fast neutron	22	24
Displacements per thermal neutron absorption	578	664
Probability of thermal neutron absorption	0.173	0.047
Displacements per incident thermal neutron	100	31

TRIM calculations. We made estimates of the number of atomic displacements caused in our glasses by fast (1 MeV) and thermal neutrons using the computer code TRIM.[144] These calculations were made in order to allow us to apportion the radiation damage (which was observed in our experiments as changes in the density of our glasses) between the two primary causes in our experiments — fast and thermal neutrons. Table 7.2 contains the principal findings of these calculations.

Gamma irradiation of MEMS pointer beam strain gauges We irradiated MEMS pointer beam strain gauges on glass wafers with gamma radiation at the University of Massachusetts, Lowell. The goal of this experiment was to characterize the densification of Hoya SD-2, the response of Pyrex to gamma irradiation (sizeable compaction) already being well known from the literature. The pointer beam strain gauges were designed to measure differential strain between the silicon of the pointer

beams themselves and the glass wafers to which they were bonded. From the literature, we expect the gamma radiation to have a negligible effect on the silicon pointer beams. Thus, we hoped to directly measure the compaction of the glass. It was surprising to see, therefore, that almost no induced substrate-beam differential strain was observed after irradiation. Furthermore, the slight differential strain that was observed was in the wrong direction, making it appear that the glass had expanded. It was hypothesized that the anodic bonding process used in MEMS fabrication had either changed the radiation response of the bulk glass or that surface layer effects at the bonding interface between silicon and glass were responsible for relieving the stresses of the differential strain induced by radiation.

Neutron irradiation of borosilicate glasses at the University of Missouri-Columbia. In order to test the theory that the anodic bonding process could change the bulk glass response to radiation, further neutron irradiations were performed on Pyrex and Hoya SD-2 at the University of Missouri-Columbia. Another goal of these irradiations was to produce damage in our glasses that had fast neutrons as its principal source. To this end, we designed a boron nitride shield for our samples that would absorb most of the incident thermal neutrons during irradiation. In absorbing these neutrons, a large amount of heat would be produced within the shield. The water cooled irradiation tubes of the Missouri reactor offered the possibility of protecting our samples from this heat. We irradiated Pyrex and Hoya SD-2 glass samples that were prepared in five different varieties, corresponding to various stages of the anodic bonding process: 1) raw glass, 2) heat treated, 3) heat and electric field treated, 4)

bonded to silicon, then etched in KOH to remove the silicon, and 5) bonded to silicon, then etched in KOH and HF to remove the silicon and a bit of glass. After irradiation, the Hoya SD-2 had activated to dangerous levels due to a higher-than-previously measured antimony content. We were thus not able to make sink/float measurements of the Hoya SD-2. The Pyrex sink/float measurements revealed that the five different preparations had no effect on the bulk glass radiation response. It was also evident from the measurements that the samples had been subjected to higher-than-desired temperatures during irradiation, since the compaction of the Pyrex was uniformly less than that measured previously in the samples of the MIT reactor experiments.

The elevated irradiation temperatures may have annealed out some of the anodic bonding-induced changes in the glasses. It is not possible, however, that all the changes made by anodic bonding were removed by annealing during irradiation, since sodium was permanently removed from the glasses during anodic bonding. Furthermore, the electric field that was present during anodic bonding was not present during irradiation. Since no measurable differences in the radiation-induced compaction of our treated and untreated glasses were found, we conclude that the glass substrates of the strain-gauge gamma irradiation experiment were compacting as expected. The MEMS strain gauges did not register this compaction, however. The answer to the mystery may lie in understanding the behavior of the silicon/glass bonded interface during irradiation. The alkali-depleted region in the glass at the bonded interface may also play a role in the process of relieving stresses between the glass and the silicon MEMS parts.

Simulation of mechanical property effects of defects in silicon We performed atomistic computer simulations of defected silicon systems using EDIP, a fairly recently developed interatomic potential. Having a coordination dependence, it is particularly capable of modeling defects. We calculated the elastic constants of simulation cells containing point defects of various species at various concentrations. It was determined that, for randomly generated defect arrangements, the effect of Frenkel pairs on the $\langle 110 \rangle$ Young's modulus of silicon is -1653 GPa per defect fraction. This contradicts the only previously published study,[27] which concluded that Young's modulus would increase with both vacancy and interstitial content. In order to confirm our result, we carried out some of the same calculations using the Stillinger-Weber (SW) potential, which is, historically, the most widely used silicon potential. The SW result for the reduction of $\langle 110 \rangle$ Young's modulus due to Frenkel pairs was of the same order as that of EDIP. We have provided evidence that EDIP makes a better description of point defects than does SW.

An important (and surprising) result of the simulation of random point defect arrangements is that their effects on elastic constants remain essentially independent of each other to the high defect concentration of 0.3%. At such a high concentration, the strain fields around the defects are overlapping. One might expect that, even at lower concentrations, the trend of the elastic constants with defect concentration would depart from linearity. The curves we have generated for 45 randomly generated samples, however, are clearly linear.

Using EDIP, we calculated the elastic constants of several amorphous simulation cells, prepared by quenching from the liquid. We determined that the exact details of

the quenching process do not significantly alter the elastic constants of the resulting amorphous silicon. Additionally, we modeled an amorphous region embedded in a crystalline matrix. We confirmed the previously published experimental observation that the elastic modulus of the composite amorphous/crystalline material can be predicted simply by the amorphous volume fraction and the elastic moduli of the crystal and the amorphous region.

We made an extensive characterization of 17 types of point defects, as described by EDIP. We calculated formation energies and volumes for these defects, as well as their effects on the elastic constants. It was determined that an individual vacancy or interstitial reduced the $\langle 110 \rangle$ Young's modulus of a 1728-atom simulation cell by $-(0.28 \pm 0.05)\%$. This is a surprisingly narrow range of variation. This is a conveniently useful result, since it implies that one need not know the defect type in order to predict its effects on elastic constants.

Estimation of radiation effects on MEMS By extrapolating from our experiments, our calculations, and the values from the literature, we have considered the impact of our benchmark radiation environment (1×10^{14} n/cm² of 1 MeV neutrons and 100 Mrad gamma) on the operation of a hypothetical anodically bonded MEMS silicon resonating beam. A beam suspended above the glass substrate by bond pads at both ends will have its resonant frequency changed by the differential silicon/substrate strain, alterations in the silicon beam dimensions, and by shifts in the silicon Young's modulus. All three of these causes for frequency shifts occur in our benchmark radiation environment, as shown in Table 7.3. The accompanying relative frequency shifts

Table 7.3: Estimates of radiation-induced changes in Pyrex, Hoya SD-2, and silicon. A fluence of 1×10^{14} n/cm² (1 MeV neutrons) and 1 Mrad gamma is assumed. Relative frequency shifts for our hypothetical MEMS silicon resonating beam are shown in parentheses. The frequency shifts for the glass take into account the differential strain relative to that of the silicon in the same column.

	Neutron		Gamma
	$\Delta l/l$	$\Delta E/E$	$\Delta l/l$
Si	2.5×10^{-8} (1.3×10^{-8})	$-0.15-5 \times 10^{-6}$ ($-0.08-2.5 \times 10^{-6}$)	~ 0
Pyrex	-6.0×10^{-7} (-6.0×10^{-4})	—	-4.7×10^{-7} (-4.5×10^{-4})
Hoya SD-2	-5.7×10^{-8} (-7.9×10^{-5})	—	-4.5×10^{-8} (-4.3×10^{-5})

for a beam of dimensions $800\mu\text{m} \times 40\mu\text{m} \times 10\mu\text{m}$ are also shown.

It can be seen that glass-related frequency shifts are orders of magnitude above those of silicon alone. Hoya SD-2 is a better choice for a substrate than is Pyrex, having effects on beam frequency that are about an order of magnitude smaller than those of Pyrex. A silicon beam mounted on silicon, or a silicon device mounted at a single point to the glass, would alleviate the differential beam/substrate strain that is the primary cause of frequency shifts.

7.2 Discussion

Experimentally, we have succeeded in characterizing the radiation-induced compaction of Hoya SD-2, and found it to be more resistant than Pyrex. This is a useful finding, especially for the field of MEMS. Of greater importance, however, is the result that anodically bonded silicon-borosilicate MEMS do not react to irradiation as one expects when one considers the unbonded and untreated materials. It is perhaps

good news for MEMS designers that the radiation-induced differential strain between substrate and silicon device is surprisingly low, but this phenomenon bears further investigation. The interaction of the alkali-depleted region near the bond interface with other possible layers in the glass, as well as possible radiation-assisted creep at the bond interface may be responsible for the observed behaviour.

Our conclusion that point defects in silicon have effects on the elastic modulus that are independent of their concentration and species is of fundamental importance. Much remains to be understood of the spatial distribution of defects that are left in the wake of a collision cascade in silicon, especially one caused by a silicon recoil. Previously published studies of collision cascades in silicon either did not examine room-temperature annealing[121] or used recoil ions of significantly different mass.[23] Furthermore, no current MD calculation can realistically simulate macroscopic annealing times. If one can estimate the average point defect concentration, however, our results demonstrate that one need not know either their spatial distribution or species in order to estimate their effect on the elastic modulus. We have shown that this remains true to very high defect concentrations. We have also confirmed the experimental observation that the effect on the elastic modulus of a small amorphous region is well described by a simple formula based on volume fraction. Combining this fact with our conclusions regarding point defects enables one to predict the likely effects of a collision cascade on the elastic modulus of silicon, given the amorphous fraction and the point defect concentration.

With rapid progress these days in the development of quantum-mechanical computational techniques, one may wonder if an empirical potential such as EDIP is of

much utility. The present study is an example of a computational study still out of reach for *ab initio* methods using most computer resources. The precise calculation of the elastic constants of our randomly defect-populated simulation cells required about 11,000 static energy calculations in cells of 1728 atoms, not counting the sometimes hundreds of computational steps between each of these which were necessary for the realistic relaxation of imposed strains. The preparation and annealing of our amorphous and defected simulation cells required tens of millions of MD time steps. The number of simulation cells and defect configurations that we examined was needed to provide data regarding trends in the elastic modulus. These trends have application beyond EDIP simulations. It is likely that EDIP inaccurately describes particular aspects of certain defects; however, by calculating the elastic constants of cells containing many defect types, existing in many different arrangements and at different concentrations, with under- and over-coordinated atoms, we have been able to find trends that *ab initio* studies, for practical reasons at this time, cannot.

Furthermore, it is not always the case that *ab initio* calculations are "more correct." For example, we've shown that it was necessary to use a 1728-atom cell to obtain three significant figures of precision for point defect formation energies (see Figure 5-8). Recent *ab initio* calculations of point defect energies used only 216 atoms.[47] It may be that what these calculations gained by using more physically accurate models was mitigated somewhat by the effects of overlapping strain fields. It should also be borne in mind that quantum-mechanical methods are not really completely "*ab initio*", or from first principles. They require the use of pseudo-potentials for core electrons and simplifying assumptions like the Local Density Approximation

(LDA) of density functional theory. Doubtlessly, as computers grow more efficient, so will *ab initio* methods grow in scale. But so, too, will the scale of problems that can be addressed by empirical potentials like EDIP.

Empirical potentials are most useful when well characterized. Simply examining the limitations of a potential's functional form and the database used for parameter fitting does not allow one to confidently predict which applications are appropriate for a potential. A large body of literature in which a potential is applied to a wide variety of situations allows one to evaluate results from one's own use of the same potential. From this point of view, the extensive characterization of the elastic properties of defects using EDIP represents a useful point of reference to the scientific community. The systematic, careful approach and broad scope of the present study also helped, as a collateral benefit, to discover and correct several errors in past characterizations of EDIP, including the C_{44} of amorphous silicon[128] and the originally published crystalline elastic constants.[61]

7.3 Future work

There is much that we would have liked to not have to include in this section. The expense and long time scale of reactor experiments presented obstacles that were sometimes quite vexing. Given sufficient funds and the time for preparation and cooling, we would like to perform neutron irradiation experiments on the pointer beam MEMS strain gauges. The main obstacles to doing this are the problems of heat, handling, and activation cooling. The MEMS devices are not sealed (they must

be read under a powerful microscope), and the side of the wafer containing the MEMS must never be touched. Given the large amount of glass supporting several of these gauges, nuclear activation would be considerable. A large amount of borosilicate glass also means either 1) a heat problem from thermal neutron absorption in the glass (and no way to touch one side of glass to help remove heat) or 2) a heat problem in the shield that's absorbing the thermal neutrons in place of the glass.

An experiment to verify the functioning of the pointer beam strain gauges has been built. A specially designed heating plate and oven cover for the delicate MEMS devices has been constructed with the intention of using heat to generate differential strain between the pointer beams and the glass substrate. This experiment awaits the availability of an expensive and delicate objective lens for use in an experiment that will subject said lens to high heat. In short, we must purchase such a lens, since the risk to it is considerable.

Expense will be a likely obstacle to future experiments. We attempted to plan a gamma irradiation of the glasses which would attain the doses necessary for producing densification measurable by the sink/float technique. A large DOE nuclear facility in Idaho wanted upwards of \$50,000 to perform such irradiations (this was similar to the price estimated by the MIT reactor for in-core thermally controlled experiments).

There is much that could yet be accomplished by computational work. Neutron recoil cascade simulations using EDIP should be performed. The results of such cascades should be studied for the annealing of defects and elastic properties. Dr. Xianglong Yuan's methods for the identification of amorphous zones and point defects should be tested and used on these cascades.

Finally, the anodic bond interface should be further studied in an attempt to explain the baffling results of our pointer beam strain gauge gamma irradiation experiment. The chemical and mechanical properties of the depletion region may hold the key to a better understanding of the effects of radiation on anodically bonded devices.

Appendix A

Pointerbeam Strain Gauge Data

The following tables contain the raw data from pointerbeam strain gauge measurements. All measurements were made under a microscope. In Tables A.1-A.3, "No" refers to the strain gauge number and "Pos" refers to the horizontal position (in mm) of the strain gauge on the experimental configuration. This horizontal position is important in determining the gamma dose received (see Figure 4-5). the "Read" columns refer to multiple readings of the pointerbeams. All readings are in tooth-widths as read from the vernier gauge. The readings are grouped by their irradiation duration, indicated at the top of the columns by a number of hours.

Table A.1: Pointerbeam strain gauge readings from Pyrex wafer.

		Unirradiated																
		317 Hours								471 Hours				630 hours				
No	Pos	Read1	Read2	Read3	Read4	Mean	Read1	Read2	Mean	Shift	Read1	Read2	Mean	Shift	Read1	Read2	Mean	Shift
1	-126.4	0.35	0.30	0.30	0.30	0.313	0.25		0.250	-0.063								
2	-116.8	0.85	0.80	0.85	0.80	0.825	0.85		0.850	0.025	0.80	0.80	0.80	-0.025	0.90	0.90	0.900	0.075
3	-107.2	0.40	0.30	0.30	0.30	0.325	0.25		0.250	-0.075	0.30	0.30	0.30	-0.025	0.40	0.40	0.400	0.075
4	-136.0	0.30			0.25	0.275	0.25	0.25	0.250	-0.025	0.25	0.25	0.25	-0.025	0.30	0.30	0.300	0.025
5	-126.4	0.40			0.35	0.375	0.35	0.35	0.350	-0.025	0.30	0.35	0.35	-0.050	0.45	0.40	0.425	0.050
6	-116.8	0.40			0.35	0.375	0.30	0.35	0.325	-0.050	0.35	0.35	0.35	-0.025	0.45	0.50	0.475	0.100
7	-107.2	0.40	0.35	0.35	0.35	0.363	0.35	0.35	0.350	-0.013	0.35	0.35	0.30	-0.038	0.35	0.40	0.375	0.013
8	-97.6	0.30			0.25	0.275	0.20	0.25	0.225	-0.050	0.25	0.25	0.20	-0.050	0.35	0.35	0.350	0.075
9	-145.6	0.30	0.25	0.25	0.25	0.263	0.30	0.30	0.300	0.038	0.30	0.30	0.30	0.038	0.30	0.30	0.300	0.038
10	-136.0	0.40	0.40	0.40	0.35	0.388	0.40	0.40	0.400	0.013	0.40	0.40	0.40	0.013	0.50	0.50	0.500	0.113
11	-126.4	0.40			0.35	0.375	0.35	0.35	0.350	-0.025	0.40	0.35	0.35	0.38	0.40	0.40	0.400	0.025
12	-116.8	0.40			0.30	0.350	0.40	0.40	0.400	0.050	0.35	0.35	0.35	0.35	0.40	0.40	0.400	0.050
13	-107.2	0.40			0.30	0.350	0.40	0.40	0.400	0.050	0.35	0.35	0.35	0.35	0.40	0.40	0.400	0.050
14	-97.6	0.40	0.30	0.30	0.30	0.325	0.40	0.40	0.400	0.075	0.40	0.40	0.40	0.075	0.45	0.40	0.425	0.100
15	-88.0	0.35	0.30	0.30	0.30	0.313	0.30	0.30	0.300	-0.013	0.30	0.40	0.35	0.38	0.40	0.40	0.400	0.088
16	-155.2	0.30	0.25	0.25	0.25	0.263	0.25	0.25	0.250	-0.013	0.30	0.30	0.30	0.30	0.35	0.35	0.350	0.088
17	-145.6	0.45			0.45	0.450	0.55	0.55	0.550	0.100	0.50	0.50	0.50	0.050	0.60	0.60	0.600	0.150
18	-136.0	0.40			0.35	0.375	0.35	0.35	0.350	-0.025	0.35	0.35	0.35	-0.025	0.40	0.45	0.425	0.050
19	-126.4	0.45			0.40	0.425	0.50	0.50	0.500	0.075	0.45	0.45	0.45	0.025	0.50	0.50	0.500	0.075
20	-116.8	0.40			0.30	0.350	0.40	0.40	0.400	0.050	0.35	0.35	0.35	0.35	0.40	0.45	0.425	0.075
21	-107.2	0.40			0.30	0.350	0.30	0.30	0.300	-0.050	0.30	0.30	0.30	-0.050	0.35	0.30	0.325	-0.025
22	-97.6	0.30			0.30	0.300	0.35	0.35	0.350	0.050	0.35	0.35	0.35	0.050	0.40	0.40	0.400	0.100
23	-88.0	0.40			0.40	0.400	0.30	0.30	0.300	-0.100	0.30	0.30	0.30	-0.100	0.35	0.35	0.350	-0.050
24	-78.4	0.20	0.20	0.20	0.20	0.200	0.15	0.15	0.150	-0.050	0.20	0.15	0.15	-0.025	0.25	0.20	0.225	0.025
25	-155.2	0.30	0.30	0.30	0.30	0.300	0.40	0.40	0.400	0.100	0.30	0.35	0.33	0.025	0.40	0.40	0.400	0.100
26	-145.6	0.30			0.30	0.300	0.40	0.40	0.400	0.100	0.40	0.35	0.35	0.38	0.40	0.40	0.400	0.100
27	-136.0	0.35			0.30	0.325	0.40	0.40	0.400	0.075	0.40	0.40	0.40	0.075	0.45	0.45	0.450	0.125

Table A.1, continued

No	Pos	Unirradiated				317 Hours			471 Hours			630 hours		
		Read1	Read2	Read3	Read4	Mean	Read1	Read2	Shift	Mean	Read1	Read2	Mean	Shift
28	-126.4	0.40			0.40	0.400	0.40	0.40	0.025	0.45	0.40	0.45	0.50	0.100
29	-116.8	0.00	0.00	0.00	0.00	0.000	0.05	0.05	0.050	0.00	0.00	0.00	0.05	0.050
30	-107.2	0.30			0.30	0.300	0.35	0.35	0.050	0.35	0.35	0.35	0.40	0.100
31	-97.6	0.30			0.30	0.300	0.25	0.25	-0.050	0.25	0.25	0.25	0.35	0.050
32	-88.0	0.40			0.40	0.400	0.35	0.40	0.375	0.45	0.45	0.40	0.50	0.100
33	-78.4	0.30	0.25	0.30	0.30	0.288	0.25	0.25	-0.038	0.25	0.25	0.25	0.30	0.013
34	-155.2	0.20	0.20	0.20	0.20	0.200	0.25	0.25	0.050	0.30	0.30	0.30	0.30	0.100
35	-145.6	0.30			0.30	0.300	0.35	0.35	0.050	0.40	0.35	0.38	0.40	0.100
36	-136.0	0.45			0.45	0.450	0.45	0.45	0.000	0.40	0.40	0.40	0.45	0.000
37	-126.4	0.40	0.20	0.20	0.40	0.400	0.40	0.40	0.000	0.40	0.40	0.40	0.35	0.050
38	-116.8	0.25			0.20	0.213	0.30	0.30	0.088	0.30	0.30	0.30	0.35	0.113
39	-107.2	0.25			0.25	0.250	0.35	0.35	0.100	0.30	0.30	0.30	0.40	0.125
40	-97.6	0.30			0.30	0.300	0.30	0.30	0.000	0.25	0.30	0.28	0.35	0.025
41	-88.0	0.35	0.20	0.20	0.35	0.350	0.30	0.30	-0.050	0.30	0.30	0.30	0.35	0.025
42	-78.4	0.25	0.20	0.20	0.25	0.225	0.15	0.15	-0.075	0.15	0.20	0.18	0.20	0.025
43	-145.6	0.30			0.30	0.300	0.40	0.40	0.100	0.35	0.35	0.33	0.40	0.100
44	-136.0	0.40	0.35	0.35	0.40	0.375	0.40	0.40	0.025	0.45	0.45	0.45	0.50	0.100
45	-126.4	0.40			0.40	0.400	0.45	0.45	0.050	0.45	0.40	0.43	0.50	0.100
46	-116.8	0.35			0.35	0.350	0.40	0.40	0.050	0.40	0.40	0.40	0.40	0.050
47	-107.2	0.25	0.20	0.20	0.20	0.213	0.30	0.30	0.088	0.30	0.30	0.30	0.35	0.138
48	-97.6	0.30			0.30	0.300	0.25	0.25	-0.050	0.35	0.30	0.33	0.40	0.100
49	-88.0	0.30			0.30	0.300	0.20	0.30	-0.100	0.30	0.25	0.28	0.30	0.000
50	-136.0	0.35			0.35	0.350	0.35	0.35	0.000	0.35	0.35	0.35	0.40	0.050
51	-126.4	0.40			0.40	0.400	0.45	0.40	0.425	0.40	0.45	0.43	0.50	0.100
52	-116.8	0.35			0.35	0.350	0.40	0.35	0.375	0.40	0.35	0.38	0.45	0.100
53	-107.2	0.30			0.30	0.300	0.20	0.25	-0.075	0.25	0.25	0.25	0.25	0.050
54	-97.6	0.30			0.30	0.300	0.25	0.30	0.275	0.25	0.30	0.28	0.35	0.050
55	-126.4	0.40	0.40	0.40	0.40	0.400	0.40	0.40	0.000	0.45	0.40	0.43	0.40	0.025

Table A.1, continued

		Unirradiated										317 Hours					471 Hours					630 hours				
No	Pos	Read1	Read2	Read3	Read4	Mean	Read1	Read2	Mean	Shift	Read1	Read2	Mean	Shift	Read1	Read2	Mean	Shift	Read1	Read2	Mean	Shift				
56-	116.8	0.40	0.40	0.40	0.40	0.400	0.35		0.350	-0.050	0.40	0.35	0.38	-0.025	0.40	0.45	0.425	0.025								
57-	107.2	0.30	0.30	0.30	0.30	0.300	0.25		0.250	-0.050	0.30	0.25	0.28	-0.025	0.40	0.40	0.400	0.100								

Table A.2: Pointerbeam strain gauge readings from Hoya SD-2 wafer B.

		Unirradiated			317 Hours			471 Hours			630 hours				
No	Pos	Read1	Read2	Read3	Mean	Read1	Shift	Read1	Read2	Mean	Shift	Read1	Read2	Mean	Shift
1	-8.4	0.15	0.15	0.15	0.150	0.30	0.150	0.20	0.25	0.225	0.075	0.25	0.25	0.250	0.100
2	1.2	0.20	0.20	0.20	0.200	0.40	0.200	0.40	0.35	0.375	0.175	0.40	0.40	0.400	0.200
3	10.8	0.20	0.20	0.20	0.200	0.20	0.000	0.15	0.20	0.175	-0.025	0.35	0.35	0.350	0.150
4	-18.0	0.20			0.200	0.35	0.150	0.30	0.30	0.300	0.100	0.35	0.35	0.350	0.150
5	-8.4	0.20			0.200	0.40	0.200	0.35	0.35	0.350	0.150	0.40	0.40	0.400	0.200
6	1.2	0.20			0.200	0.20	0.000	0.25	0.30	0.275	0.075	0.30	0.30	0.300	0.100
7	10.8	0.10			0.100	0.10	0.000	0.20	0.15	0.175	0.075	0.20	0.20	0.200	0.100
8	20.4	0.10			0.100	0.20	0.100	0.15	0.20	0.175	0.075	0.20	0.20	0.200	0.100
9	-27.6	0.10			0.100	0.20	0.100	0.15	0.10	0.125	0.025	0.20	0.20	0.200	0.100
10	-18.0	0.15	0.15	0.15	0.150	0.15	0.000	0.25	0.25	0.250	0.100	0.30	0.30	0.300	0.150
11	-8.4	0.15	0.15	0.15	0.150	0.20	0.050	0.20	0.15	0.175	0.025	0.20	0.20	0.200	0.050
12	1.2	0.25			0.250	0.30	0.050	0.25	0.25	0.250	0.000	0.30	0.30	0.300	0.050
13	10.8	0.10			0.100	0.15	0.050	0.10	0.15	0.125	0.025	0.20	0.15	0.175	0.075
14	20.4	0.00			0.000	0.00	0.000	0.00	0.00	0.000	0.000	0.05	0.05	0.050	0.050
15	30.0	0.20			0.200	0.20	0.000	0.30	0.25	0.275	0.075	0.30	0.30	0.300	0.100
16	-37.2	0.20	0.20	0.20	0.200	0.20	0.000	0.30	0.30	0.300	0.100	0.35	0.35	0.350	0.150
17	-27.6	0.15			0.150	0.15	0.000	0.20	0.20	0.200	0.050	0.30	0.30	0.300	0.150
18	-18.0	0.10			0.100	0.15	0.050	0.10	0.05	0.075	-0.025	0.20	0.20	0.200	0.100
19	-8.4	0.10			0.100	0.15	0.050	0.10	0.10	0.100	0.000	0.20	0.20	0.200	0.100
20	1.2	0.10			0.100	0.15	0.050	0.15	0.10	0.125	0.025	0.20	0.20	0.200	0.100
21	10.8	0.10	0.10	0.10	0.100	0.10	0.000	0.10	0.10	0.100	0.000	0.15	0.15	0.150	0.050

Table A.2, continued

		Unirradiated			317 Hours			471 Hours			630 hours				
No	Pos	Read1	Read2	Read3	Mean	Read1	Shift	Read1	Read2	Mean	Shift	Read1	Read2	Mean	Shift
22	20.4	0.10	0.10	0.10	0.100	0.10	0.000	0.10	0.05	0.075	-0.025	0.15	0.15	0.150	0.050
23	30.0	0.10			0.100	0.10	0.000	0.10	0.05	0.075	-0.025	0.15	0.15	0.150	0.050
24	39.6	0.20	0.20	0.20	0.200	0.15	-0.050	0.30	0.30	0.300	0.100	0.30	0.30	0.300	0.100
25	37.2	0.25	0.25	0.25	0.250	0.25	0.000	0.25	0.25	0.250	0.000	0.40	0.40	0.400	0.150
26	27.6	0.30			0.300	0.45	0.150	0.45	0.45	0.450	0.150	0.50	0.50	0.500	0.200
27	18.0	0.05			0.050	0.10	0.050	0.10	0.05	0.075	0.025	0.10	0.10	0.100	0.050
28	8.4	0.10			0.100	0.15	0.050	0.15	0.10	0.125	0.025	0.20	0.20	0.200	0.100
29	1.2	0.00			0.000	0.05	0.050	0.05	0.05	0.050	0.050	0.10	0.10	0.100	0.100
30	10.8	0.05			0.050	0.05	0.000	0.05	0.00	0.025	-0.025	0.10	0.10	0.100	0.050
31	20.4	0.10			0.100	0.10	0.000	0.10	0.05	0.075	-0.025	0.20	0.20	0.200	0.100
32	30.0	0.10			0.100	0.15	0.050	0.10	0.10	0.100	0.000	0.15	0.10	0.125	0.025
33	39.6	0.15	0.15		0.150	0.25	0.100	0.25	0.25	0.250	0.100	0.30	0.30	0.300	0.150
34	37.2	0.25	0.25	0.25	0.250	0.40	0.150	0.30	0.35	0.325	0.075	0.45	0.40	0.425	0.175
35	27.6	0.20			0.200	0.15	-0.050	0.30	0.25	0.275	0.075	0.35	0.35	0.350	0.150
36	18.0	0.00	0.00	0.00	0.000	0.00	0.000	0.05	0.05	0.050	0.050	0.15	0.10	0.125	0.125
37	8.4	0.10	0.10	0.10	0.100	0.20	0.100	0.20	0.20	0.200	0.100	0.25	0.25	0.250	0.150
38	1.2	-0.05	-0.05	-0.05	-0.050	-0.10	-0.050	-0.05	-0.10	-0.075	-0.025	0.00	0.00	0.000	0.050
39	10.8	0.05			0.050	0.15	0.100	0.10	0.10	0.100	0.050	0.20	0.20	0.200	0.150
40	20.4	0.15			0.150	0.15	0.000	0.20	0.15	0.175	0.025	0.20	0.20	0.200	0.050
41	30.0	0.10			0.100	0.15	0.050	0.15	0.10	0.125	0.025	0.20	0.20	0.200	0.100
42	39.6	0.10	0.15	0.10	0.117	0.30	0.183	0.25	0.20	0.225	0.108	0.30	0.30	0.300	0.183
43	27.6	0.10			0.100	0.30	0.200	0.25	0.20	0.225	0.125	0.30	0.30	0.300	0.200
44	18.0	0.10			0.100	0.25	0.150	0.20	0.20	0.200	0.100	0.30	0.30	0.300	0.200
45	8.4	0.10			0.100	0.10	0.000	0.20	0.15	0.175	0.075	0.25	0.30	0.275	0.175
46	1.2	0.15			0.150	0.15	0.000	0.25	0.25	0.250	0.100	0.35	0.35	0.350	0.200
47	10.8	0.10	0.10	0.10	0.100	0.10	0.000	0.20	0.20	0.200	0.100	0.30	0.30	0.300	0.200
48	20.4	0.10	0.10	0.10	0.100	0.10	0.000	0.15	0.15	0.150	0.050	0.20	0.20	0.200	0.100
49	30.0	0.10			0.100	0.10	0.000	0.20	0.20	0.200	0.100	0.25	0.20	0.225	0.125

Table A.2, continued															
		Unirradiated			317 Hours			471 Hours			630 hours				
No	Pos	Read1	Read2	Read3	Mean	Read1	Shift	Read1	Read2	Mean	Shift	Read1	Read2	Mean	Shift
50	-18.0	0.10			0.100	0.20	0.100	0.15	0.15	0.150	0.050	0.20	0.20	0.200	0.100
51	-8.4	0.20			0.200	0.20	0.000	0.25	0.25	0.250	0.050	0.30	0.30	0.300	0.100
52	1.2	0.20			0.200	0.15	-0.050	0.30	0.25	0.275	0.075	0.40	0.35	0.375	0.175
53	10.8	0.15			0.150	0.20	0.050	0.20	0.20	0.200	0.050	0.30	0.30	0.300	0.150
54	20.4	0.20			0.200	0.35	0.150	0.30	0.30	0.300	0.100	0.35	0.35	0.350	0.150
55	-8.4	0.20	0.20	0.20	0.200	0.30	0.100	0.30	0.30	0.300	0.100	0.35	0.35	0.350	0.150
56	1.2	0.25	0.25	0.25	0.250	0.35	0.100	0.30	0.30	0.300	0.050	0.40	0.40	0.400	0.150
57	10.8	0.20	0.20	0.20	0.200	0.25	0.050	0.25	0.25	0.250	0.050	0.30	0.30	0.300	0.100

Table A.3: Pointerbeam strain gauge readings from Hoya SD-2 wafer C.

		Unirradiated			184 Hours			317 Hours			471 Hours			630 hours					
No	Pos	Read1	Read2	Read3	Mean	Read1	Read2	Mean	Shift	Read1	Read2	Mean	Shift	Read1	Read2	Mean	Shift		
1	109.6	0.10			0.100	0.15	0.15	0.150	0.050	0.10	0.000	0.15	0.15	0.125	0.025	0.20	0.200	0.100	
2	119.2	0.15	0.15	0.20	0.167	0.20	0.15	0.175	0.008	0.15	-0.017	0.15	0.15	0.150	-0.017	0.20	0.200	0.033	
3	128.8	0.10			0.100	0.15	0.15	0.150	0.050	0.10	0.000	0.15	0.10	0.125	0.025	0.20	0.200	0.100	
4	100.0	0.10			0.100	0.15	0.10	0.125	0.025	0.10	0.000	0.20	0.15	0.175	0.075	0.25	0.250	0.150	
5	109.6	0.05			0.050	0.10	0.10	0.100	0.050	0.05	0.000	0.05	0.05	0.050	0.000	0.20	0.200	0.150	
6	119.2	0.10			0.100	0.15	0.15	0.150	0.050	0.20	0.100	0.15	0.15	0.150	0.050	0.20	0.200	0.100	
7	128.8	0.10			0.100	0.15	0.15	0.150	0.050	0.15	0.050	0.10	0.15	0.125	0.025	0.20	0.200	0.100	
8	138.4	0.10			0.100	0.10	0.15	0.125	0.025	0.10	0.000	0.10	0.10	0.100	0.000	0.20	0.200	0.100	
9	90.4	0.15			0.150	0.15	0.15	0.150	0.000	0.15	0.000	0.15	0.15	0.150	0.000	0.20	0.200	0.050	
10	100.0	0.10			0.100	0.10	0.10	0.100	0.000	0.10	0.000	0.10	0.10	0.100	0.000	0.20	0.200	0.100	
11	109.6	0.10			0.100	0.10	0.10	0.100	0.000	0.10	0.000	0.05	0.05	0.050	-0.050	0.10	0.100	0.000	
12	119.2	0.10	0.10	0.10	0.100	0.10	0.10	0.100	0.000	0.10	0.000	0.05	0.05	0.050	-0.050	0.15	0.10	0.125	0.025
13	128.8	0.10			0.100	0.10	0.10	0.100	0.000	0.05	-0.050	0.10	0.05	0.075	-0.025	0.20	0.15	0.175	0.075
14	138.4	0.10			0.100	0.15	0.15	0.150	0.050	0.10	0.000	0.10	0.10	0.100	0.000	0.20	0.20	0.200	0.100
15	148.0	0.15			0.150	0.15	0.15	0.150	0.000	0.10	-0.050	0.10	0.10	0.100	-0.050	0.20	0.20	0.200	0.050

Table A.3, continued

Table A.3, continued																	
Unirradiated			184 Hours			317 Hours			471 Hours			630 hours					
No	Pos	Read1	Read2	Read3	Mean	Read1	Read2	Mean	Shift	Read1	Read2	Mean	Shift	Read1	Read2	Mean	Shift
16	80.8	0.15			0.150	0.20	0.15	0.175	0.025	0.15	0.000	0.20	0.15	0.175	0.025	0.20	0.200
17	90.4	0.10			0.100	0.15	0.10	0.125	0.025	0.10	0.000	0.15	0.15	0.150	0.050	0.20	0.200
18	100.0	0.10			0.100	0.10	0.10	0.100	0.000	0.15	0.050	0.10	0.10	0.100	0.000	0.15	0.150
19	109.6	0.05			0.050	0.10	0.10	0.100	0.050	0.15	0.100	0.10	0.05	0.075	0.025	0.15	0.125
20	119.2	0.05			0.050	0.05	0.05	0.050	0.000	0.05	0.000	0.05	0.00	0.025	-0.025	0.10	0.100
21	128.8	0.10			0.100	0.10	0.10	0.100	0.000	0.10	0.000	0.05	0.05	0.050	-0.050	0.10	0.100
22	138.4	0.00			0.000	0.00	0.05	0.025	0.025	0.00	0.000	0.05	0.00	0.025	0.025	0.10	0.100
23	148.0	0.10			0.100	0.10	0.10	0.100	0.000	0.05	-0.050	0.05	0.10	0.075	-0.025	0.20	0.200
24	157.6	0.15			0.150	0.15	0.15	0.150	0.000	0.10	-0.050	0.15	0.15	0.150	0.000	0.20	0.200
25	80.8	0.15	0.15	0.15	0.150	0.20	0.20	0.200	0.050	0.15	0.000	0.15	0.15	0.150	0.000	0.30	0.300
26	90.4	0.10			0.100	0.10	0.10	0.100	0.000	0.15	0.050	0.10	0.05	0.075	-0.025	0.15	0.20
27	100.0	0.10	0.10	0.10	0.100	0.05	0.05	0.050	-0.050	0.15	0.050	0.10	0.10	0.100	0.000	0.10	0.15
28	109.6	0.20			0.200	0.15	0.15	0.150	-0.050	0.20	0.000	0.20	0.15	0.175	-0.025	0.20	0.200
29	119.2	-0.30	-0.30	-0.30	-0.300	-0.25	-0.25	-0.250	0.050	-0.25	0.050	-0.25	-0.30	-0.275	0.025	-0.20	-0.20
30	128.8	0.10			0.100	0.10	0.10	0.100	0.000	0.10	0.000	0.05	0.10	0.075	-0.025	0.10	0.100
31	138.4	0.05	0.05	0.05	0.050	0.10	0.10	0.100	0.050	0.10	0.050	0.10	0.10	0.100	0.050	0.10	0.100
32	148.0	0.00			0.000	0.05	0.05	0.050	0.050	0.00	0.000	0.00	0.00	0.000	0.000	0.05	0.10
33	157.6	0.20	0.20	0.20	0.200	0.20	0.20	0.200	0.000	0.20	0.000	0.20	0.20	0.200	0.000	0.25	0.250
34	80.8	0.10			0.100	0.10	0.10	0.100	0.000	0.10	0.000	0.20	0.20	0.200	0.100	0.25	0.20
35	90.4	-0.10			-0.100	-0.10	-0.10	-0.100	0.000	-0.05	0.050	-0.10	-0.10	-0.100	0.000	0.00	0.000
36	100.0	0.10			0.100	0.10	0.10	0.100	0.000	0.15	0.050	0.10	0.10	0.100	0.000	0.15	0.150
37	109.6	0.00			0.000	0.05	0.05	0.050	0.050	0.10	0.100	0.00	0.05	0.025	0.025	0.10	0.100
38	119.2	0.05			0.050	0.05	0.05	0.050	0.000	0.05	0.000	0.05	0.05	0.050	0.000	0.10	0.100
39	128.8	0.10			0.100	0.10	0.10	0.100	0.000	0.15	0.050	0.15	0.10	0.125	0.025	0.15	0.150
40	138.4	0.10			0.100	-0.30	-0.30	-0.300	-0.400	-0.25	-0.350	-0.30	-0.30	-0.300	-0.400	-0.25	-0.25
41	148.0	0.10			0.100	0.10	0.10	0.100	0.000	0.05	-0.050	0.10	0.10	0.100	0.000	0.10	0.15
42	157.6	0.20			0.200	0.20	0.20	0.200	0.000	0.20	0.000	0.20	0.20	0.200	0.000	0.20	0.200
43	90.4	0.10			0.100	0.15	0.10	0.125	0.025	0.20	0.100	0.10	0.05	0.075	-0.025	0.20	0.200

Table A.3, continued																		
No	Pos	Unirradiated			184 Hours			317 Hours			471 Hours			630 hours			Shift	Mean
		Read1	Read2	Read3	Mean	Read1	Read2	Mean	Shift	Read1	Read2	Mean	Shift	Read1	Read2	Mean		
44	100.0	0.10			0.100	0.10	0.10	0.100	0.000	0.000	0.10	0.10	0.100	0.15	0.20	0.175	0.075	
45	109.6	0.00			0.000	0.00	0.00	0.000	0.000									
46	119.2	0.05	0.05	0.05	0.050	0.05	0.05	0.050	0.10	0.050	0.05	0.05	0.050	0.10	0.10	0.100	0.050	
47	128.8	0.10			0.100	0.15	0.15	0.150	0.050	0.15	0.15	0.150	0.050	0.20	0.20	0.200	0.100	
48	138.4	0.10			0.100	0.10	0.15	0.125	0.025	0.10	0.000	0.10	0.075	0.15	0.10	0.125	0.025	
49	148.0	0.10			0.100	0.15	0.15	0.150	0.050	0.10	0.000	0.10	0.100	0.20	0.15	0.175	0.075	
50	100.0	0.05			0.050	0.15	0.15	0.150	0.100	0.15	0.100	0.15	0.125	0.20	0.20	0.200	0.150	
51	109.6	0.10			0.100	0.10	0.10	0.100	0.000	0.10	0.000	0.05	0.10	0.15	0.125	0.025		
52	119.2	0.20			0.200	0.25	0.25	0.250	0.050									
53	128.8	0.10			0.100	0.10	0.10	0.100	0.000	0.10	0.000	0.05	0.050	0.15	0.10	0.125	0.025	
54	138.4	0.10			0.100	0.10	0.10	0.100	0.000	0.10	0.000	0.05	0.050	0.20	0.20	0.200	0.100	
55	109.6	0.20			0.200	0.20	0.20	0.200	0.000	0.20	0.000	0.15	0.20	0.30	0.30	0.300	0.100	
56	119.2	0.20	0.20	0.20	0.200	0.20	0.20	0.200	0.000	0.00	-0.200							
57	128.8	0.20			0.200	0.20	0.20	0.200	0.000	0.20	0.000	0.15	0.20	0.20	0.20	0.200	0.000	

Appendix B

Sink/Float Data

The following table contains the data from the sink/float density measurements. "Time" is the approximate time of irradiation of each sample. "Sink temperature" refers to the point at which the irradiated sample of each pair sank past the reference line. "Reference" is the corresponding temperature for the reference sample. All temperatures are in Celsius. Sample names with four characters are from the MIT reactor irradiation, and those with three are from the University of Missouri - Columbia reactor irradiation. Samples with names containing a "P" were Pyrex and those with an "H" were Hoya SD-2.

Table B.1: Sink/float temperature data.

Sample	Time	Sink Temperature	Reference	Difference
PU1A	30 s	32.34	32.29	-0.05
		32.24	32.19	-0.05
		32.29	32.31	0.02
		32.43	32.31	-0.12
		32.27	32.28	0.01
		32.24	32.12	-0.12
PU1B	60 s	32.32	32.29	-0.03

Table B.1, <i>continued</i>				
Sample	Time	Sink Temperature	Reference	Difference
		32.18	32.53	0.35
		32.24	32.24	-0.00
		32.24	32.36	0.12
		32.25	32.02	-0.23
		32.30	32.17	-0.13
PU1C	600 s	31.72	32.26	0.54
		31.87	32.04	0.17
		32.02	32.39	0.37
		31.89	31.98	0.09
		31.74	31.94	0.20
		31.86	31.95	0.09
PU1D	1800 s	31.13	32.39	1.26
		30.84	32.35	1.51
		30.94	32.36	1.42
		31.00	32.40	1.40
		30.93	31.89	0.96
		31.03	31.96	0.93
PU1E	6000 s	28.33	32.19	3.86
		28.14	31.96	3.82
		28.49	32.35	3.86
		28.65	32.12	3.47
		28.26	32.36	4.10
		28.15	32.46	4.31
HU1A	30 s	22.87	22.87	-0.00
		22.77	22.79	0.02
		22.81	22.72	-0.09
		22.71	22.74	0.03
		22.77	22.77	-0.00
		22.71	22.70	-0.01
HU1B	60 s	22.78	22.88	0.10
		22.80	22.77	-0.03
		22.91	22.81	-0.10
		22.66	22.68	0.02
		22.78	22.73	-0.05
		22.68	22.60	-0.08
HU1C	600 s	22.66	22.76	0.10
		22.80	22.77	-0.03
		22.85	22.88	0.03
		22.71	22.69	-0.02
		22.85	22.82	-0.03
		22.83	22.80	-0.03
HU1D	1800 s	22.78	22.69	-0.09
		22.69	22.74	0.05
		22.80	22.75	-0.05

Table B.1, <i>continued</i>				
Sample	Time	Sink Temperature	Reference	Difference
		22.74	22.69	-0.05
		22.74	22.72	-0.02
		22.68	22.68	-0.00
HU1E	6000 s	22.53	22.79	0.26
		22.52	22.66	0.14
		22.69	22.81	0.12
		22.56	22.66	0.10
		22.61	22.76	0.15
		22.61	22.68	0.07
3PA	11.98 h	29.87	35.24	5.37
		29.60	35.30	5.70
		29.52	35.30	5.78
		29.47	35.17	5.70
		29.70	35.39	5.69
		29.48	35.24	5.76
4PA	7.28 h	31.92	36.00	4.08
		32.03	36.13	4.10
		31.92	36.13	4.21
		31.68	36.10	4.42
		32.10	36.16	4.06
		32.06	36.26	4.20
5PA	3.70 h	34.19	35.89	1.70
		34.27	35.99	1.72
		34.23	36.19	1.96
		34.28	36.13	1.85
		34.53	36.21	1.68
		34.25	36.07	1.82
3PB	11.98 h	30.67	35.86	5.19
		30.70	35.97	5.27
		30.60	36.13	5.53
		30.44	36.06	5.62
		30.67	36.00	5.33
		30.71	36.07	5.36
4PB	7.28 h	31.10	35.27	4.17
		31.02	35.22	4.20
		31.02	35.39	4.37
		30.75	35.05	4.30
		30.99	35.24	4.25
		31.04	35.23	4.19
5PB	3.70 h	34.19	36.07	1.88
		34.26	36.01	1.75
		34.18	35.83	1.65
		34.07	35.84	1.77
		34.33	35.82	1.49

Table B.1, <i>continued</i>				
Sample	Time	Sink Temperature	Reference	Difference
		34.17	36.02	1.85
3PC	11.98 h	29.51	34.69	5.18
		29.35	34.91	5.56
		29.24	35.04	5.80
		29.25	34.84	5.59
		29.27	34.82	5.55
		29.16	35.13	5.97
4PC	7.28 h	30.60	35.06	4.46
		30.33	35.03	4.70
		30.60	34.89	4.29
		30.41	34.92	4.51
		30.18	34.59	4.41
		30.25	35.11	4.86
5PC	3.70 h	33.14	35.02	1.88
		32.78	35.00	2.22
		33.00	34.74	1.74
		32.75	34.73	1.98
		32.97	34.66	1.69
		33.13	35.07	1.94
3PD	11.98 h	30.26	35.58	5.32
		30.19	35.72	5.53
		30.03	35.54	5.51
		30.21	35.59	5.38
		30.30	35.58	5.28
		30.24	35.43	5.19
4PD	7.28 h	31.88	36.39	4.51
		31.85	36.45	4.60
		31.98	36.32	4.34
		31.80	36.35	4.55
		31.90	36.39	4.49
		31.99	36.32	4.33
5PD	3.70 h	34.44	36.33	1.89
		34.49	36.27	1.78
		34.48	36.20	1.72
		34.41	36.30	1.89
		34.51	36.28	1.77
		34.68	36.45	1.77
3PE	11.98 h	31.10	36.29	5.19
		30.81	36.15	5.34
		31.17	36.38	5.21
		30.66	36.31	5.65
		30.77	36.31	5.54
		30.88	36.27	5.39
4PE	7.28 h	31.87	36.27	4.40

Table B.1, <i>continued</i>				
Sample	Time	Sink Temperature	Reference	Difference
		31.94	36.31	4.37
		31.91	36.28	4.37
		31.93	36.30	4.37
		31.84	36.41	4.57
		31.81	36.34	4.53
5PE	3.70 h	34.32	36.28	1.96
		34.33	36.28	1.95
		34.49	36.33	1.84
		34.19	36.30	2.11
		34.34	36.32	1.98
		34.26	36.26	2.00

Appendix C

Elastic Constant Relations in Diamond Cubic Silicon

C.1 Analytic solutions for EDIP elastic constants

The following is taken largely from the PhD thesis of Prof. Martin Bazant of MIT/Department of Mathematics, [10] and is reproduced here with minor alterations and additions. In order to explain the differences between my computational results for the elastic constants of the perfect crystal and those originally published for the EDIP potential, I had to recalculate the analytical values, starting from scratch (since the published ones supposedly were the analytical values). The algebra necessary for doing this is what follows.

EDIP (like the Stillinger-Weber potential)[116] is a three-body cluster potential

of the form:

$$E = \sum_{i,j} \phi(R_{ij}) + \sum_{i,j} \sum_{k>j} \psi(R_{ij}, R_{ik}) h(l_{ijk}), \quad (\text{C.1})$$

where ϕ , ψ and h are differentiable, R_{ij} is the separation between a pair of atoms, and l_{ijk} is the cosine of the angle of two radial bonds for a central atom. From Eq. C.1, we (1) change the notation to refer to a central atom so that $r_i = R_{0i}$ and $l_{ij} = l_{0ij}$, (2) perform Taylor expansions of ϕ , ψ , and h , then (3) discard terms involving products of infinitesimals above second order (the discarded terms have no effect on the second derivatives that are the elastic constants). We obtain:

$$\begin{aligned} \Delta E = & \sum_i \left(\phi' \Delta r_i + \frac{1}{2} \phi'' \Delta r_i^2 \right) \\ & + \sum_i \sum_{j>i} \left\{ h \left[\phi_1 (\Delta r_i + \Delta r_j) + \frac{1}{2} \psi_{11} (\Delta r_i^2 + \Delta r_j^2) \right. \right. \\ & + \left. \psi_{12} \Delta r_i \Delta r_j \right] + h' \Delta l_{ij} \left[\psi + \psi_1 (\Delta r_i + \Delta r_j) \right] \\ & + \left. \frac{1}{2} h'' \psi \Delta l_{ij}^2 \right\}, \end{aligned} \quad (\text{C.2})$$

where subscripts on ψ refer to partial derivatives with respect to first and second arguments, and ψ is assumed to be symmetric under the exchange of atoms (which implies that $\psi_1 = \psi_2$ and $\psi_{11} = \psi_{22}$). We highlight that ϕ , ψ , and h , as well as their derivatives, are to be evaluated for a given reference structure (diamond, in the case considered here).

Both EDIP and SW have been designed to have zero angular energy at the tetrahedral angle. For diamond, therefore, $h = 0$. This is not the case for graphite, where h remains zero for EDIP, but $h > 0$ for SW. By imposing equilibrium, we obtain

that $h' = \phi' = 0$. Both EDIP and SW have cutoffs just short of the second neighbor distance for the diamond structure. If the cutoff is extended so that ϕ includes second neighbor forces, ϕ' is not generally zero at the first neighbor distance. The complications arising in this situation have been considered elsewhere.[10] Numerically solving $\phi' = 0$ for R gives 2.3514745 Å as the EDIP equilibrium nearest neighbor distance in diamond.

For EDIP or SW in the diamond structure, given the above conditions, Eq. C.2 reduces to:

$$\Delta E = \frac{1}{2}\phi'' \sum_i \Delta r_i^2 + \frac{1}{2}h''\psi \sum_i \sum_{j>i} \Delta l_{ij}^2. \quad (\text{C.3})$$

Using Eq. 5.11, we assume the only possible non-zero strains from Eq. 5.12 are ϵ_1 , ϵ_2 , and ϵ_6 . The result is

$$\frac{\Delta E}{V} = \frac{1}{2}C_{11}(\epsilon_1^2 + \epsilon_2^2) + C_{12}\epsilon_1\epsilon_2 + \frac{1}{2}C_{44}\epsilon_6^2, \quad (\text{C.4})$$

where we have used cubic symmetry to combine terms (*i.e.*, $C_{11}=C_{22}$, $C_{12}=C_{21}$, and $C_{44}=C_{66}$). One must merely differentiate Eq. C.4 to show that:

$$C_{11} = \frac{1}{V} \frac{\partial^2 \Delta E}{\partial \epsilon_1^2}, \quad (\text{C.5})$$

$$C_{12} = \frac{1}{V} \frac{\partial^2 \Delta E}{\partial \epsilon_1 \partial \epsilon_2}, \quad (\text{C.6})$$

$$\text{and } C_{44} = \frac{1}{V} \frac{\partial^2 \Delta E}{\partial \epsilon_6^2}. \quad (\text{C.7})$$

We must now evaluate the terms Δr_i^2 and Δl_{ij}^2 in Eq. C.3. We start with the positions of four neighbors relative to the central atom. In units of $\frac{a}{4}$, where a is the

lattice constant, the neighbor positions are

$$\begin{aligned}
\tilde{r}_1 &= (1 + \epsilon_1 + \frac{\epsilon_6}{2})\hat{i} + (1 + \epsilon_2 + \frac{\epsilon_6}{2})\hat{j} + (1 - \epsilon_6\zeta)\hat{k} \\
\tilde{r}_2 &= (-1 - \epsilon_1 - \frac{\epsilon_6}{2})\hat{i} + (-1 - \epsilon_2 - \frac{\epsilon_6}{2})\hat{j} + (1 - \epsilon_6\zeta)\hat{k} \\
\tilde{r}_3 &= (-1 - \epsilon_1 + \frac{\epsilon_6}{2})\hat{i} + (1 + \epsilon_2 - \frac{\epsilon_6}{2})\hat{j} + (-1 - \epsilon_6\zeta)\hat{k} \\
\tilde{r}_4 &= (1 + \epsilon_1 - \frac{\epsilon_6}{2})\hat{i} + (-1 - \epsilon_2 + \frac{\epsilon_6}{2})\hat{j} + (-1 - \epsilon_6\zeta)\hat{k} \quad , \quad (C.8)
\end{aligned}$$

where ζ is the Kleinman relaxation parameter, defined in terms of the distance z moved by a relaxing central atom under shear strain as $\frac{4z}{a\epsilon_6}$.

We now compute the changes in bond lengths and angles using Eq. C.8, then Taylor expand the results. Since we will only be taking second derivatives, we can discard any terms higher than second order without losing exactitude. We can also discard mixed terms involving ϵ_6 since Eqs. C.5–C.7 involve no such mixed partial derivatives. The distortions in bond lengths and angles, minus the irrelevant terms, are

$$\frac{\Delta r_i}{r} = \frac{1}{3}(\epsilon_1 + \epsilon_2) + \frac{1}{9}(\epsilon_1^2 + \epsilon_2^2 - \epsilon_1\epsilon_2) \pm \frac{1}{3}(1 - \zeta)\epsilon_6 + \frac{1}{36}(2\zeta + 1)^2\epsilon_6^2 \quad (C.9)$$

$$\begin{aligned}
\Delta l_{12,34} &= -\frac{4}{9}(\epsilon_1 + \epsilon_2) + \frac{2}{27}(\epsilon_1^2 + \epsilon_2^2 + 8\epsilon_1\epsilon_2) \mp \frac{4}{9}(2\zeta + 1)\epsilon_6 \\
&\quad - \frac{1}{27}(2\zeta + 1)(2\zeta - 5)\epsilon_6^2 \quad (C.10)
\end{aligned}$$

$$\Delta l_{13,24} = -\frac{4}{9}(\epsilon_1 - 2\epsilon_2) + \frac{2}{27}(\epsilon_1^2 - 2\epsilon_2^2 - 4\epsilon_1\epsilon_2) + \frac{1}{54}(2\zeta + 1)(10\zeta - 1)\epsilon_6^2 \quad (C.11)$$

$$\Delta l_{14,23} = \frac{4}{9}(2\epsilon_1 - \epsilon_2) - \frac{2}{27}(2\epsilon_1^2 - \epsilon_2^2 + 4\epsilon_1\epsilon_2) + \frac{1}{54}(2\zeta + 1)(10\zeta - 1)\epsilon_6^2, \quad (C.12)$$

where the upper sign in Eq. C.9 refers to $i = 1, 2$ and the lower sign refers to $i = 3, 4$. Similarly, in Eq. C.11, the upper sign applies to atoms 1 and 2 and the lower sign to atoms 3 and 4.

Eqs. C.9–C.12 suffice for calculation of all sums appearing in Eq. C.2, but only the two appearing in Eq. C.3 are required for EDIP:

$$\sum_{i=1}^4 \left(\frac{\Delta r_i}{r} \right)^2 = \frac{4}{9} [(\epsilon_1 + \epsilon_2)^2 + (1 - \zeta)^2 \epsilon_6^2] \quad (\text{C.13})$$

$$\sum_{i=1}^3 \sum_{j=i+1}^4 \Delta l_{ij}^2 = \frac{64}{27} (\epsilon_1^2 + \epsilon_2^2 - \epsilon_1 \epsilon_2) + \frac{32}{81} (1 + 2\zeta)^2 \epsilon_6^2, \quad (\text{C.14})$$

where we have once again discarded terms of order greater than two.

We now have all the required pieces to evaluate Eqs. C.5–C.7, which simplify to:

$$C_{11} = \frac{2}{3a^3} \left[a^2 \phi'' + \frac{256}{9} h'' \psi \right] \quad (\text{C.15})$$

$$C_{12} = \frac{2}{3a^3} \left[a^2 \phi'' - \frac{128}{9} h'' \psi \right] \quad (\text{C.16})$$

$$C_{44} = \frac{2}{3a^3} \left[a^2 \phi'' (1 - \zeta)^2 + \frac{128}{27} h'' \psi (1 + 2\zeta)^2 \right], \quad (\text{C.17})$$

where a is again the lattice constant for the diamond unit cell. The unrelaxed elastic constant C_{44}^0 is obtained by setting $\zeta = 0$ in Eq. C.17. We note that atomic relaxation will reduce the shear elastic constant to a minimum. We therefore set $\partial C_{44} / \partial \zeta = 0$, and solve for ζ , which is found to be

$$\zeta = \frac{27a^2 \phi'' - 256h'' \psi}{27a^2 \phi'' + 512h'' \psi}. \quad (\text{C.18})$$

It should be possible to follow the above procedure of Taylor expanding the potential as well as bond length and angle distortions in terms of strain for other crystal structures and potentials. In particular, Eqs. C.15–C.18 apply to Stillinger-Weber as well as to EDIP.

C.2 Relations among elastic constants

The following equations are provided for convenience. E represents Young's modulus, B represents bulk modulus, and Voigt notation is used for the elastic constants C_{ij} .

C.2.1 Isotropic materials

$$C_{44} = \frac{1}{2}(C_{11} - C_{12}) \quad (\text{C.19})$$

$$E = \frac{C_{11}^2 + C_{11}C_{12} - 2C_{12}^2}{C_{11} + C_{12}} \quad (\text{C.20})$$

$$B = C_{11} - \frac{4}{3}C_{44} \quad (\text{C.21})$$

C.2.2 Cubic materials

$$B = \frac{C_{11} + 2C_{12}}{3} \quad (\text{C.22})$$

$$E_{\langle 100 \rangle} = \frac{C_{11}^2 + C_{11}C_{12} - 2C_{12}^2}{C_{11} + C_{12}} \quad (\text{C.23})$$

$$E_{\langle 110 \rangle} = \frac{4C_{44}(C_{11}^2 + C_{11}C_{12} - 2C_{12}^2)}{C_{11}^2 + C_{11}C_{12} - 2C_{12}^2 + 2C_{11}C_{44}} \quad (\text{C.24})$$

C.2.3 Diamond materials with three-body forces

For the diamond structure, if a three body cluster potential (Eq. C.1) has only first-neighbor interactions and has an angular function with a minimum of zero at the tetrahedral angle ($h = h' = 0, h'' > 0$) then the following relation is implied:[51, 13]

$$(7C_{11} + 2C_{12})C_{44} = 3(C_{11} + 2C_{12})(C_{11} - C_{12}). \quad (C.25)$$

Using the experimental data from Table 5.3, this equation is not too well satisfied: the ratio of the two sides is 1.14.

For these same conditions, another relation, involving the unrelaxed shear modulus C_{44}^o , has been reported by Bazant *et al.*: [13]

$$4C_{11} + 5C_{12} = 9C_{44}^o. \quad (C.26)$$

This relation is satisfied to within 0.4 % using the experimental and *ab initio* data from Table 5.3. This extraordinarily good agreement, when contrasted with the results of Eq. C.25, implies that a three-body cluster potential like EDIP or SW is well suited to diamond, except that internal relaxation under shear (which will involve shifts in electronic states) is not well described. This is a very subtle form of environment dependence not accounted for in EDIP.

Combining Eqs. C.25 and C.26, we find a relation that describes the effect of

internal relaxation on the shear modulus:

$$C_{44}^o - C_{44} = \frac{(C_{11} + 8C_{12})^2}{9(7C_{11} + 2C_{12})}. \quad (\text{C.27})$$

Using the experimental values in Table 5.3 for C_{11} and C_{12} to predict C_{44} according to Eqs. C.26 and C.27, we obtain a value only 12 % smaller than experiment.

Finally, we can recast Eq. C.18 in terms of C_{11} and C_{12} , using Eqs. C.15 and C.16:

$$\zeta = \frac{C_{11} + 8C_{12}}{7C_{11} + 2C_{12}}. \quad (\text{C.28})$$

Appendix D

Heating analysis for MURR irradiation

What follows is a rough analysis of the heating that occurs during irradiation of glass samples inside a boron nitride thermal neutron shield at the University of Missouri-Columbia reactor. The simplifying assumptions make this only a first-order approximation, but it serves as a model for examining the relative importance of different variables.

A pictorial representation of the physical model used is shown in Figure D-1. We use a one-dimensional model of infinite concentric cylinders. The innermost region contains the glass samples. These sit in an aluminum sample holder, which in turn sits in the boron nitride shield. The BN shield is press fit into an aluminum space-filler, which is press fit into the aluminum rabbit. The exterior of the rabbit is kept at a constant 30 °C by circulating water.

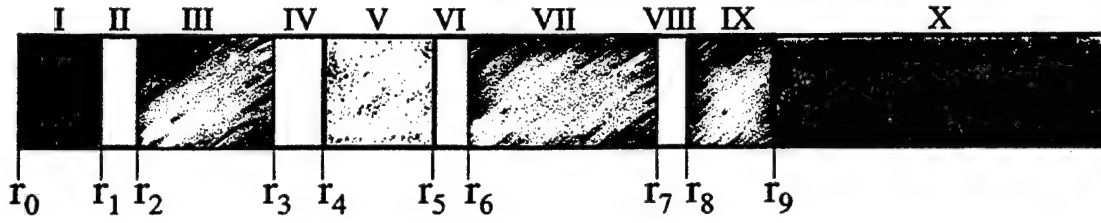


Figure D-1: One-dimensional thermal model for shielded irradiation of glass samples at MURR. The origin is at the left. The regions numbered with roman numerals are concentric cylinders. Region I is a Pyrex glass cylinder, and the sample holder. Region III represents the aluminum sample holder inside the boron nitride shield (region V). Regions VII and IX are the aluminum filler and rabbit, respectively. White regions are air gaps between solids regions. Region X is water held at 30°C.

At steady state, the heat equation is:

$$\nabla^2 T + \frac{q'''}{\kappa} = 0 \quad , \quad (\text{D.1})$$

where T is temperature (K), q''' is internally generated heat (W/m^3), and κ is thermal conductivity ($\text{W}/\text{m}\cdot\text{K}$). In cylindrical coordinates, with only radial temperature dependence, Equation D.1 becomes

$$\frac{\partial^2 T}{\partial r^2} + \frac{1}{r} \frac{\partial T}{\partial r} + \frac{q'''}{\kappa} = 0 \quad . \quad (\text{D.2})$$

The solution to Equation D.2 is:

$$T = -\frac{1}{4} \frac{q'''}{\kappa} r^2 + C_1 \ln r + C_2 \quad , \quad (\text{D.3})$$

where C_1 and C_2 are constants to be determined by boundary conditions.

For the one-dimensional model shown in Figure D-1, we apply Equation D.3 to

each region individually. Heat generation from the thermal neutron capture of boron is present in the glass and boron nitride shield (regions I and V, respectively). All other regions have $q''' = 0$. The temperature for each region is therefore given by:

$$T_I = -\frac{1}{4} \frac{q_I'''}{\kappa_I} r^2 + C_{I1} \ln r + C_{I2} \quad (D.4)$$

$$T_{II} = C_{II1} \ln r + C_{II2} \quad (D.5)$$

$$T_{III} = C_{III1} \ln r + C_{III2} \quad (D.6)$$

$$T_{IV} = C_{IV1} \ln r + C_{IV2} \quad (D.7)$$

$$T_V = -\frac{1}{4} \frac{q_V'''}{\kappa_V} r^2 + C_{V1} \ln r + C_{V2} \quad (D.8)$$

$$T_{VI} = C_{VI1} \ln r + C_{VI2} \quad (D.9)$$

$$T_{VII} = C_{VII1} \ln r + C_{VII2} \quad (D.10)$$

$$T_{VIII} = C_{VIII1} \ln r + C_{VIII2} \quad (D.11)$$

$$T_{IX} = C_{IX1} \ln r + C_{IX2} \quad , \quad (D.12)$$

where roman numerals are used to denote the region to which a particular constant belongs.

At each interface between regions, we have the boundary condition that equates the heat flux q (W/m²) across the boundary. For the interface r_1 between regions I and II, this is expressed as

$$q_I|_{r_1} = -\kappa_I \left. \frac{\partial T_I}{\partial r} \right|_{r_1} = -\kappa_{II} \left. \frac{\partial T_{II}}{\partial r} \right|_{r_1} = q_{II}|_{r_1} \quad , \quad (D.13)$$

and from it we obtain

$$C_{III} = -\frac{1}{2} \frac{q_1'''}{\kappa_{II}} r_1^2 + \frac{\kappa_I}{\kappa_{II}} C_{II} \quad (D.14)$$

An alternate way to obtain C_{III} is to consider that, at steady state, the heat leaving region I must be equal to the heat Q_I (W) generated within region I. Expressing this in equation form, we have

$$Q_I = A_1 q_{II} = -2\pi r_1 L \kappa_{II} \left. \frac{\partial T_{II}}{\partial r} \right|_{r_1} = q_1''' \pi r_1 L \quad (D.15)$$

Using the derivative of Equation D.5, we obtain

$$C_{III} = -\frac{1}{2} \frac{q_1'''}{\kappa_{II}} r_1^2 \quad (D.16)$$

Comparing this result with that of Equation D.14, we see that C_{II} must be zero. This is fortunate, for otherwise the $\ln r$ term in Equation D.4 would cause a problem at $r = 0$.

Applying a boundary condition of the continuity of heat flow across interfaces (as in Equation D.13) to the other interfaces in the model, we obtain

$$C_{III} = -\frac{1}{2} \frac{q_1'''}{\kappa_{III}} r_1^2 \quad (D.17)$$

$$C_{IV} = -\frac{1}{2} \frac{q_1'''}{\kappa_{IV}} r_1^2 \quad (D.18)$$

$$C_{VI} = -\frac{1}{2\kappa_V} (q_1''' r_1^2 - q_V''' r_4^2) \quad (D.19)$$

$$C_{VII} = -\frac{1}{2\kappa_{VI}} [q_1''' r_1^2 + q_V''' (r_5^2 - r_4^2)] \quad (D.20)$$

$$C_{VII} = -\frac{1}{2\kappa_{VII}}[q_I'''r_1^2 + q_V'''(r_5^2 - r_4^2)] \quad (D.21)$$

$$C_{VIII} = -\frac{1}{2\kappa_{VIII}}[q_I'''r_1^2 + q_V'''(r_5^2 - r_4^2)] \quad (D.22)$$

$$C_{IX} = -\frac{1}{2\kappa_{IX}}[q_I'''r_1^2 + q_V'''(r_5^2 - r_4^2)] \quad (D.23)$$

Another boundary condition requires temperatures for two regions to be equal at the interface. For example, at r_1 we have

$$T_I|_{r_1} = T_{II}|_{r_1} \quad (D.24)$$

Using this second boundary condition and Equations D.4-D.12 provides solutions for the other unknown constants:

$$C_{I2} = \frac{1}{4} \frac{q_I'''}{\kappa_I} r_1^2 + C_{III} \ln r_1 + C_{II2} \quad (D.25)$$

$$C_{II2} = (C_{III1} - C_{III}) \ln r_2 + C_{III2} \quad (D.26)$$

$$C_{III1} = (C_{IV1} - C_{III1}) \ln r_3 + C_{IV2} \quad (D.27)$$

$$C_{IV2} = (C_{V1} - C_{IV1}) \ln r_4 + C_{V2} - \frac{1}{4} \frac{q_V'''}{\kappa_V} r_4^2 \quad (D.28)$$

$$C_{V2} = (C_{VI1} - C_{V1}) \ln r_5 + C_{VI2} + \frac{1}{4} \frac{q_V'''}{\kappa_V} r_4^2 \quad (D.29)$$

$$C_{VI2} = (C_{VII1} - C_{VI1}) \ln r_6 + C_{VII2} \quad (D.30)$$

$$C_{VII2} = (C_{VIII1} - C_{VII1}) \ln r_7 + C_{VIII2} \quad (D.31)$$

$$C_{VIII2} = (C_{IX1} - C_{VIII1}) \ln r_8 + C_{IX2} \quad (D.32)$$

$$C_{IX2} = T_o - C_{IX1} \ln r_9 \quad , \quad (D.33)$$

where T_o is the water temperature in region X.

This model uses cylindrical shells of infinite length to represent the various regions. Obviously, the real cylindrical shells are finite. Additionally, the glass and aluminum of regions I and III are not at all cylindrical. The glass samples are square wafers and the aluminum is of a complex shape (see Figure 4-16). To facilitate our estimates, therefore, a cylinder of equivalent volume to our five Pyrex samples (more important to this model than Hoya SD-2, because of the higher boron content of Pyrex) was calculated using the height of the boron nitride shield. This calculation provided the value of r_1 . The aluminum sample holder was then modeled as filling the space between the glass cylinder and the boron nitride shield. To compensate, somewhat, for this inexact model, the air gaps of regions II and IV are introduced to indicate that thermal contact between the sample holder and the boron nitride shield is not optimal. In reality, the circular bottom of the aluminum sample holder provides the only direct contact with the boron nitride shield.

The values of r_4 , r_5 , r_8 , and r_9 were measured from the actual cylindrical boron nitride shield and aluminum rabbit. The values of r_2 , r_3 , r_6 , and r_7 were left as variables that depended on the other r_i values and the arbitrarily sized air gaps. The fixed r_i values are shown in Table D.1. Experimental values of the thermal conductivity and coefficient of thermal expansion for the materials in our model are shown in Table D.2. The boron nitride used is anisotropic, and its physical properties are different parallel and perpendicular to the direction in which it was pressed. The values used here are estimates that lie between those at the two extremes.

Finally, we present numerical results for various scenarios for our model. These

Table D.1: Values used for the r_i of Figure D-1.

r_i	Distance (mm)
r_1	0.93
r_4	7.94
r_5	9.50
r_8	13.61
r_9	14.37

Table D.2: Experimental values of thermal conductivity κ (W/m-K) and the coefficient of thermal expansion α (K^{-1}).

Material	κ	α
Aluminum	237.	2.31×10^{-5}
Pyrex	1.13	3.25×10^{-6}
Boron Nitride	100.	6.00×10^{-7}
Air	0.03	—

are summarized in Table D.3. The first flux scenario is the “best case”: thermal flux as originally quoted to us, and the boron nitride shield absorbing 99% of the incident flux. For heat generation estimates in the glass region, we used the reduced thermal neutron flux. When estimating the heat generation within the boron nitride shield itself, however, we used the average of the incident flux and the reduced (shielded) flux to account for the fact that the flux was incident from all directions, and that the boron nitride shield would self-shield. This rough estimate assumes that the boron nitride shield is a pair of parallel plates very close together, so that half the incident flux approaches from each side. In this way, each plate receives one-half the incident flux with the other half being attenuated on the other side by the other plate. We consider non-zero air gaps between regions individually for simplicity. The size of

these gaps was chosen as follows.

In the real experiment, the $3\text{ mm} \times 3\text{ mm} \times 0.78\text{ mm}$ glass samples sat in holes of about the same size, surrounded by aluminum on all sides. The real gap on any side of the sample was much smaller than 1 mm, so we adopt 1×10^{-4} as an estimate for the gap between the glass of region I and the aluminum of region III. As previously mentioned, only the base disc of the aluminum sample holder contacted the boron nitride shield directly. The equivalent air gap about our imagined infinite aluminum cylindrical shell must be consequential, therefore. We choose 1 mm as a hefty air gap between the aluminum region III and the boron nitride region V — the air gap about our sample holder was actually several mm in places, but the wide circular base of the sample holder provided a generous thermal path to the shield via direct contact. The III-V gap is not the most critical parameter for keeping temperatures low, however. This distinction belongs to the air gap between the boron nitride shield of region V and the aluminum filler region VII. The boron nitride shield was press fit to the aluminum in our experiment, so this gap should be small. Additionally, as heating occurs, the aluminum will outexpand the boron nitride, widening the gap. As the gap widens, however, the aluminum will distance itself from the heat source that is the boron nitride shield and will cool. Thus the differential thermal expansion would not actually contribute much to an air gap, as we demonstrated to ourselves with our model. Any appreciable air gap must then be the result of a poor fit. We choose 0.001 inches as the possible air gap (this was the tolerance on the machining). We don't consider the possibility of an air gap at the VII-IX interface to be very great — the press fitting of this soft pure aluminum into a rabbit of the same material

caused some of the rabbits to buckle during fabrication. The two regions will expand at the same rate during heating, keeping them in close contact. Additionally, being outside all the heat sources, it will behave much as the V-VII gap. We therefore don't consider it explicitly.

For the first flux scenario, it is seen that even a 1 mil (1 mil = 1/1000 inch = 25.4 μm) gap at the V-VII interface results in significant heating in the glass, whereas the larger estimated gaps of the other regions cause little heating of the samples. For the second scenario, we used the upper limit of 1×10^{14} n/cm²/s as the flux and allowed 10% of this amount to be incident on the glass. This latter figure is probably more realistic than 1%, according to the experience of reactor personnel at MURR.

It can be seen that the 1 mil V-VII air gap results in unacceptable heating of region I in the second scenario. Additionally, with the large flux incident on the samples, they will generate a large amount of heat themselves. Even so, it's still the heat from the boron nitride shield that is the most serious problem.

Table D.3: Scenarios for glass sample heating during the MURR irradiation. The assumed thermal neutron flux ($\text{n/cm}^2/\text{s}$) incident on the boron nitride shield and the fraction thereof that is incident on the glass are at left. Air gaps between solid regions of Figure D-1 are given in meters. ΔT represents the amount by which the glass center (r_0) is above T_o ($^{\circ}\text{C}$).

Flux	Fraction	I-III (Glass-Al)	III-V (Al-BN)	V-VII (BN-Al)	VII-IX (Al-Al)	ΔT
3×10^{13}	0.01	0.00	0.00	0.00	0.00	1.44
		1.00×10^{-4}	0.00	0.00	0.00	1.96
		0.00	1.00×10^{-3}	0.00	0.00	2.14
		0.00	0.00	2.54×10^{-5}	0.00	48.35
1×10^{14}	0.10	0.00	0.00	0.00	0.00	7.32
		1.00×10^{-4}	0.00	0.00	0.00	24.93
		0.00	1.00×10^{-3}	0.00	0.00	30.62
		0.00	0.00	2.54×10^{-5}	0.00	178.04

Appendix E

Nuclear activation estimates for glass irradiations

Detailed activation estimates were made for the glass irradiation experiments based on their chemical compositions. The following describes the method of the calculation.

Only thermal neutron activation is considered. Fast neutron reactions for the elements in our glasses were not found to be of much importance. This is fortunate, because the fast neutron energy spectrum was not well known for our experiments, and detailed prediction of activation due to fast neutron reactions would not have been possible. The probability of a thermal neutron being captured before travelling a distance x (the sample thickness) in a material is taken as

$$P_{scat}(x) = 1 - e^{-\Sigma x} \quad , \quad (E.1)$$

where Σ is equal to the product of the number density n (cm^{-3}) of the absorbing

nuclei, and their microscopic cross section σ for thermal neutron absorption.

Let a be the number of activated atoms in our sample. The rate of activation will depend on the probability of absorption P , the incident flux of thermal neutrons F , and the area A of the sample that is exposed to this flux as follows:

$$\frac{da}{dt} = FAP = FA(1 - e^{-\sigma nx}) \quad . \quad (E.2)$$

The rate of deactivation of the activated nuclei depends only on their number:

$$\frac{da}{dt} = -\alpha a \quad , \quad (E.3)$$

where α is a constant related to the half-life $t_{\frac{1}{2}}$ of the metastable nuclei by

$$\alpha = \frac{\ln 2}{t_{\frac{1}{2}}} \quad . \quad (E.4)$$

Summing the rates of activation and deactivation, we have

$$\frac{da}{dt} = FA(1 - e^{-\sigma nx}) - \alpha a \quad . \quad (E.5)$$

Once activated, a nuclei no longer is able to absorb a thermal neutron with the same cross section as before — this is known as “burn up.” Taking this into account, we have that $n = n_o - a/V$, with n_o being the initial value of n and V being the volume of the sample. Making the substitutions of $B = \sigma x/V$, $C = FA$, and $D = -FAe^{-\sigma n_o x}$,

we obtain

$$\frac{da}{dt} = De^{Ba(t)} - \alpha a(t) + C \quad . \quad (E.6)$$

Equation E.6 can be solved numerically, but for our experimental situation, the "burn up" was small. In this case, n can be approximated by the constant n_o , which allows us to solve instead Equation E.7 analytically:

$$a(t) = \frac{FA}{\alpha}(1 - e^{-\sigma n_o x})(1 - e^{-\alpha t}) \quad . \quad (E.7)$$

Equation E.7 gives the number of activated atoms present after an irradiation of time t in a flux F .

For a rectangular slab as a target (like our samples), $\sigma n_o x = \sigma N_o/A$, where N_o is the total number of target atoms (thermal neutron absorbers). For a small $\sigma N_o/A$, the first exponential term in Equation E.7 becomes $\approx (1 - \sigma N/A)$, and we have

$$a(t) = \frac{F\sigma N_o}{\alpha}(1 - e^{-\alpha t}) \quad . \quad (E.8)$$

Equation E.8 shows that for any geometry in which the absorbing nuclei can't provide significant self-shielding (*i.e.*, a small number of absorbing nuclei or a large area over which they are spread), the volume, area, and thickness of the target are not important.

Following the irradiation, the radioactive sample decays according to Equation E.3. Solving for a , we have

$$a(t) = a_o e^{-\alpha t} \quad , \quad (E.9)$$

where a_o is the initial number of activated nuclei immediately after an irradiation of time t_o :

$$a_o = \frac{FA}{\alpha}(1 - e^{-\sigma n_o x})(1 - e^{-\alpha t_o}) \quad . \quad (\text{E.10})$$

The activity of the sample at post-irradiation time t is therefore

$$\frac{da}{dt} = -FA(1 - e^{-\sigma n_o x})(1 - e^{-\alpha t_o})e^{-\alpha t} \quad . \quad (\text{E.11})$$

There are 37,000 disintegration per second per μCi . To convert activity into dose, one needs to know the probability and energy of decay products. Beta emitters were ignored (beta particles have a much shorter range in air than gamma rays). The average energy per disintegration was calculated from the probability-weighted average of the energy of the decay products. Due to the large number of isotopes in our glass samples and the many decay products for each, it was deemed necessary and acceptably accurate to ignore products of very low energy and/or frequency. Using the calculated activity of the samples, a flux F_γ of this "average-energy" E_{av} decay product was calculated at 1 cm. The dose rate was then found as

$$\dot{D} = F_\gamma E_{av} \frac{\mu_{en}}{\rho} \quad , \quad (\text{E.12})$$

where μ_{en}/ρ is the mass energy-absorption coefficient for gamma in water in cm^2/g (this coefficient holds fairly constant from 0.1–2 MeV, a range that includes most of the decay products for the radioisotopes of concern).

We illustrate an example activation calculation for an isotope present in Hoya SD-2

glass. Data for cross sections and decay products and probabilities are taken from the *Handbook of Health Physics and Radiological Health*. [111] We will consider antimony (Sb) and zinc (Zn). Twenty-nine other isotopes were considered — these three were found to be the most threatening to our experiment in terms of activation. The concentration of Zn used here was that of the original XPS measurement (see Table 1.2). The assumed antimony concentration is that calculated from the activation of a sample irradiated at the MIT reactor (see section 4.3.4.5).

It can be seen in Table E.1 that the long half lives of Sb-124 and Zn-65 are the reason they pose a problem — Sb-122 is much “hotter” than either of them at the start of the cooling period, but quickly decays.

Table E.1: Sample activation calculations for isotopes in Hoya SD-2.

<u>Parameters</u>			
Number density, Hoya SD-2	:	7.65×10^{22}	n/cm^3
Sample thickness	x	: 0.078	cm
Sample area	A	: 0.09	cm^2
Thermal neutron flux	F	: 3×10^{12}	$n/cm^2/s$
Irradiation time	t_o	: 11	hours
Mass energy absorption coefficient	μ_{en}/ρ	: 0.03	cm^2/g

Element	Sb		Zn
Hoya SD-2 atomic %	0.179	0.179	0.75
Target isotope	121	123	64
Natural abundance %	57.3	42.7	48.9
n_o, cm^{-3}	7.85×10^{19}	5.85×10^{19}	2.81×10^{20}
σ, cm^2	5.90×10^{-24}	4.15×10^{-24}	7.60×10^{-25}
Isotope created	122	124	65
$t_{1/2}$, days	2.72	60.3	265
α, s^{-1}	2.95×10^{-6}	1.33×10^{-7}	3.03×10^{-8}
$\frac{da}{dt}, s^{-1}$	1.07×10^6	2.68×10^4	5.38×10^3
γ , MeV	0.5640	0.6030	1.1155
(frequency)	(1)	(0.978)	(0.51)
	0.6930	0.7220	0.5110
	(0.05)	(0.11)	(0.0283)
	1.2000	1.6900	0.0080
	(0.01)	(0.49)	(0.2261)
E_{av} , J	9.78×10^{-14}	2.40×10^{-13}	9.38×10^{-14}
F_γ at 1 cm, $cm^{-2}s^{-1}$	8.55×10^4	2.13×10^3	4.28×10^2
Dose rate, Gy/s	2.51×10^{-7}	1.54×10^{-8}	1.20×10^{-9}
Dose rate, rad/hr	9.04×10^{-2}	5.53×10^{-3}	4.34×10^{-4}
Activity of samples			
mrem/hr, start	90.4	5.53	0.434
mrem/hr, 30 days	.0432	3.92	0.401
mrem/hr, 60 days	2.07×10^{-5}	2.77	0.371

Appendix F

Nuclear activation measurements

What follows is a listing of the activity measurements made of irradiated glass samples. The measurements were made either by MIT reactor personnel or by personnel at the MIT radiation safety office.

Table F.1: Activation of Hoya SD-2 glass. The sample was $1\text{ cm} \times 1\text{ cm} \times 0.078\text{ cm}$. The activity (μCi) was measured 7 days after a 10 minute irradiation in a thermal neutron flux of about $4 \times 10^{12}\text{ n/cm}^2/\text{s}$.

Nuclide	ID confidence	Activity	Uncertainty
Na-24	0.987	2.66×10^{-2}	9.71×10^{-4}
Zn-65	0.991	2.26×10^{-1}	6.28×10^{-3}
Sb-122	0.993	1.40	3.22×10^{-2}
I-124	0.954	2.13×10^{-2}	5.80×10^{-3}
Sb-124	0.984	1.32×10^{-1}	2.66×10^{-2}
La-140	0.943	1.65×10^{-2}	3.90×10^{-4}

Table F.2: Activation of Hoya SD-2 glass. Fifteen samples were irradiated at the Missouri reactor. Activities are in pCi.

Sample	Nuclide	Energy (keV)	Yield %	ID confidence	Activity	Uncertainty
5HA	K-42	1524.67	17.90	0.992	5.32×10^4	2.55×10^4
	Zn-65	1115.52	50.75	0.978	2.07×10^5	2.36×10^4
	Sb-124	602.71	97.87	0.976	1.43×10^6	1.04×10^5
5HB	Zn-65	1115.52	50.75	0.979	2.18×10^5	2.43×10^4
	Sb-124	602.71	97.87	0.976	1.49×10^6	1.08×10^5
5HC	Zn-65	1115.52	50.75	0.979	2.14×10^5	2.41×10^4
	Sb-124	602.71	97.87	0.974	1.50×10^6	1.09×10^5
5HD	K-42	1524.67	17.90	1.000	3.70×10^4	2.60×10^4
	Zn-65	1115.52	50.75	0.975	1.98×10^5	2.29×10^4
	Sb-124	602.71	97.87	0.975	1.39×10^6	1.01×10^5
5HE	Zn-65	1115.52	50.75	0.975	1.48×10^5	1.89×10^4
	Sb-124	602.71	97.87	0.967	1.50×10^6	1.09×10^5
	Cs-137	6661.65	85.12	1.000	3.90×10^3	2.25×10^3
4HA	Zn-65	1115.52	50.75	0.976	3.71×10^5	3.45×10^4
	Sb-124	602.71	97.87	0.974	2.19×10^6	1.57×10^5
4HB	K-42	1524.67	17.90	0.992	6.02×10^4	3.27×10^4
	Zn-65	1115.52	50.75	0.976	4.03×10^5	3.62×10^4
	Sb-124	602.71	97.87	0.975	2.27×10^6	1.63×10^5
4HC	Na-24	1368.53	100.00	0.966	7.17×10^4	1.15×10^4
	K-42	1524.67	17.90	0.989	6.92×10^4	3.33×10^4
	Zn-65	1115.52	50.75	0.976	3.84×10^5	3.51×10^4
	Kr-87	402.58	49.50	0.974	3.02×10^4	2.83×10^4
	Sb-124	602.71	97.87	0.974	2.17×10^6	1.56×10^5
4HD	K-42	1524.67	17.90	0.998	6.01×10^4	3.27×10^4
	Zn-65	1115.52	50.75	0.981	3.59×10^5	3.36×10^4
	Sb-124	602.71	97.87	0.975	2.16×10^6	1.55×10^5
	Xe-135M	526.56	81.00	0.969	9.58×10^3	4.62×10^3
	Bi-212	727.17	11.80	0.439	2.68×10^5	3.78×10^4
4HE	K-42	1524.67	17.90	0.996	4.40×10^4	2.67×10^4
	Mn-56	846.75	98.90	0.749	5.94×10^3	2.96×10^3
	Zn-65	1115.52	50.75	0.970	2.77×10^5	2.84×10^4
	Sb-124	602.71	97.87	0.970	1.66×10^6	1.20×10^5
3HA	Zn-65	1115.52	50.75	0.986	5.63×10^5	4.65×10^4
	Sb-124	602.71	97.87	0.979	3.09×10^6	2.20×10^5
3HB	K-42	1524.67	17.90	0.986	7.95×10^4	3.98×10^4
	Zn-65	1115.52	50.75	0.986	5.76×10^5	4.73×10^4
	Kr-85	513.99	0.43	0.917	1.25×10^7	1.76×10^6
	Sr-65	513.99	99.27	0.917	5.41×10^4	7.62×10^3
	Zr-89	909.10	99.04	0.988	8.09×10^3	4.84×10^3
	Sb-124	602.71	97.87	0.980	3.15×10^6	2.24×10^5

Table F.2, <i>continued</i>						
Sample	Nuclide	Energy (keV)	Yield %	ID confidence	Activity	Uncertainty
3HC	K-42	1524.67	17.90	1.000	9.23×10^4	4.24×10^4
	Zn-65	1115.52	50.75	0.985	5.63×10^5	4.65×10^4
	Sb-124	602.71	97.87	0.982	3.20×10^6	2.28×10^5
3HD	K-42	1524.67	17.90	0.981	6.11×10^4	3.90×10^4
	Zn-65	1115.52	50.75	0.986	5.25×10^5	4.43×10^4
	Sb-124	602.71	97.87	0.981	3.10×10^6	2.21×10^5
3HE	K-42	1524.67	17.90	0.999	6.80×10^4	3.64×10^4
	Zn-65	1115.52	50.75	0.983	4.56×10^5	3.98×10^4
	Sb-124	602.71	97.87	0.976	2.55×10^6	1.82×10^5

Bibliography

- [1] A. B. Van Haaften. Acute tetrabromethane (acetylene tetrabromide) intoxication in man. *American Industrial Hygiene Association Journal*, 30:251, 1969.
- [2] H. Abe, C. Kinoshita, P. R. Okamoto, and L. E. Rehn. Effect of concurrent irradiation with electrons on ion-induced amorphization in silicon. *Journal of Nuclear Materials*, 298:212, 1994.
- [3] S. Agnello, F. M. Gelardi, R. Boscaino, M. Cannas, B. Boizot, and G. Petite. Intrinsic defects induced by β -irradiation in silica. *Nuclear Instruments and Methods in Physics Research*, B191:387, 2002.
- [4] A. Alamo, M. Horsten, X. Averty, E. I. Materna-Morris, M. Rieth, and J. C. Brachet. Mechanical behavior of reduced-activation and conventional martensitic steels after neutron irradiation in the range 250–450°C. *Journal of Nuclear Materials*, 283-287:353, 2000.
- [5] A. Antonelli and J. Bernholc. Pressure effects on self-diffusion in silicon. *Physical Review B*, 40:10643, 1989.
- [6] A. Antonelli, E. Kaxiras, and D. J. Chadi. Vacancy in silicon revisited: Structure and pressure effects. *Physical Review Letters*, 81:2088, 1998.
- [7] M. G. Ashby and D. R. H. Jones. *Engineering Materials 1: An Introduction to their Properties & Applications*. Butterworth-Heinemann, Oxford, 1996.
- [8] H. Balamane, T. Halicioglu, and W. A. Tiller. Comparative study of silicon empirical interatomic potentials. *Physical Review B*, 46:2250, 1992.
- [9] J. B. Bates, R. W. Hendrick, and L. B. Shaffer. Neutron-irradiation effects and structure of noncrystalline SiO_2 . *Journal of Chemical Physics*, 61:4163, 1974.
- [10] M. Z. Bazant. *Interatomic Forces in Covalent Solids*. PhD thesis, Harvard University, 1997.
- [11] M. Z. Bazant and E. Kaxiras. On the structure of amorphous silicon and its surfaces. (unpublished).
- [12] M. Z. Bazant and E. Kaxiras. Modeling of covalent bonding in solids by inversion of cohesive energy curves. *Physical Review Letters*, 77:4370, 1996.

- [13] M. Z. Bazant, E. Kaxiras, and J. F. Justo. Environment-dependent interatomic potential for bulk silicon. *Physical Review B*, 56:8542, 1997.
- [14] P. J. Bedrossian, M.-J. Caturla, and T. Diaz de la Rubia. Damage evolution and surface defect segregation in low-energy ion-implanted silicon. *Applied Physics Letters*, 70:176, 1997.
- [15] A. Benyagoub, S. Klaumünzer, and M. Toulemonde. Radiation-induced compaction and plastic flow of vitreous silica. *Nuclear Instruments and Methods in Physics Research*, B146:449, 1998.
- [16] P. R. Bevington. *Data Reduction and Error Analysis in the Physical Sciences*. McGraw-Hill Book Company, New York, 1969.
- [17] R. Bhadra, J. Pearson, P. Okamoto, L. Rehn, and M. Grimsditch. Elastic properties of Si during amorphization. *Physical Review B*, 38:12656, 1988.
- [18] R. D. Blevins. *Formulas for Natural Frequency and Mode Shapes*. Kreiger, Melbourne, FL, 1995.
- [19] G. A. D. Briggs, O. V. Kolosov, and M. M. Puentes Heras. Materials characterization by surface acoustic waves from 200 MHz to 20 GHz. *Acoustical Imaging*, 22:657, 1996.
- [20] P. J. Burnett and G. A. D. Briggs. The elastic properties of ion-implanted silicon. *Journal of Materials Science*, 21:1828, 1986.
- [21] Carborundum corporation, Saint-Gobain advanced ceramics.
- [22] F. Cargnoni, C. Gatti, and L. Colombo. Formation and annihilation of a bond defect in silicon: An *ab initio* quantum-mechanical characterization. *Physical Review B*, 57:170, 1998.
- [23] M.-J. Caturla, T. Diaz de la Rubia, L. A. Marques, and G. H. Gilmer. Ion-beam processing of silicon at keV energies: A molecular-dynamics study. *Physical Review B*, 54:16683, 1996.
- [24] M. Chandrasekhar, H. R. Chandrasekhar, J. M. Meese, and S. L. Thaler. Effects of neutron irradiation on the Raman spectrum of silicon. In *Institute of Physics Conference Series*, number 59, page 205, Bristol, 1981. Institute of Physics.
- [25] Y.-M. Chiang, D. P. Birnie III, and W. D. Kingery. *Physical Ceramics*. John Wiley & Sons, Inc., New York, 1997.
- [26] L. A. Christel, J. F. Gibbons, and T. W. Sigmon. Displacement criterion for amorphization of silicon during ion implantation. *Journal of Applied Physics*, 52:7143, 1981.
- [27] S. J. Clark and Graeme J. Ackland. Vibrational and elastic effects of point defects in silicon. *Physical Review B*, 48:10899, 1993.

- [28] S. J. Clark and Graeme J. Ackland. Ab initio calculations of the self-interstitial in silicon. *Physical Review B*, 56:47, 1997.
- [29] L. Colombo and D. Maric. Defect-induced amorphization in silicon. *Europhysics Letters*, 29:623, 1995.
- [30] J. D. Comins, A. G. Every, P. R. Stoddart, X. Zhang, J. C. Crowhurst, and G. R. Hearne. Surface Brillouin scattering of opaque solids and thin supported films. *Ultrasonics*, 38:450, 2000.
- [31] S. L. Conners. Effects of gamma radiation on the structure and properties of borosilicate glasses. M.S. thesis, Alfred University, 1992.
- [32] Corning Specialty Lighting & Materials, Corning, New York 14831.
- [33] Material information sheet. Corning Specialty Lighting & Materials, Corning, New York 14831.
- [34] C. S. G. Cousins, L. Gerward, J. Staun Olsen, B. Selmsmark, and B. J. Sheldon. Determination of internal strain tensors by energy-dispersive x-ray-diffraction - results for si using the 006 forbidden reflection. *Journal of Applied Crystallography*, 15:154, 1982.
- [35] A. Cozma and B. Puers. Characterization of the electrostatic bonding of silicon and Pyrex glass. *Journal of Micromechanics and Microengineering*, 5:98, 1995.
- [36] J. S. Custer, M. O. Thompson, D. C. Jacobson, J. M. Poate, S. Roorda, W. C. Sinke, and F. Spaepen. Density of amorphous Si. *Applied Physics Letters*, 64:437, 1994.
- [37] T. L. Daulton, M. A. Kirk, and L. E. Rehn. In situ transmission electron microscopy study of ion-irradiated copper: comparison of the temperature dependence of cascade collapse in fcc- and bcc-metals. *Journal of Nuclear Materials*, 276:258, 2000.
- [38] M. S. Daw and M. I. Baskes. Semiempirical, quantum mechanical calculation of hydrogen embrittlement in metals. *Physical Review Letters*, 50:1285, 1983.
- [39] H. A. El-Batal. Effect of thermal neutrons on thermal expansion of some ternary borate glasses. *Nuclear Instruments and Methods in Physics Research*, B88:411, 1994.
- [40] Evans East, 104 Windsor Center, Suite 101, East Windsor, New Jersey, 08520.
- [41] F. M. Ezz-Eldin and H. A. El-Batal. Radiation effects on thermal expansion of some ternary alkali-silicate glasses. *Journal of Non-Crystalline Solids*, 152:195, 1993.
- [42] S. A. Fabritsiev and A. S. Pokrovsky. Contribution of thermal neutrons to radiation hardening of pure copper. *Journal of Nuclear Materials*, 306:78, 2002.

- [43] Far West Technology, Inc., 330 D South Kellog, Goleta, California 93117.
- [44] T. R. Forester and W. Smith. *The DL_POLY_2 Reference Manual*. CCLRC, Daresbury Laboratory, Daresbury, Warrington WA4 4AD, England, July 2001. http://www.dl.ac.uk/TCSC/Software/DL_POLY/.
- [45] J. Frantz, J. Tarus, K. Nordlund, and J. Keinonen. Mechanism of electron-irradiation-induced recrystallization in Si. *Physical Review B*, 64:125313, 2001.
- [46] G. De Sandre, L. Colombo, and C. Bottani. Calculation of elastic constants in defected and amorphous silicon by quantum simulations. *Physical Review B*, 54:11857, 1996.
- [47] S. Goedecker, T. Deutsch, and L. Billard. A fourfold coordinated point defect in silicon. *Physical Review Letters*, 88:235501, 2002.
- [48] M. L. Grossbeck, K. Ehrlich, and C. Wassilew. An assessment of tensile, irradiation creep, creep rupture, and fatigue behavior in austenitic stainless steels with emphasis on spectral effects. *Journal of Nuclear Materials*, 174:264, 1990.
- [49] Y. Hachitani and H. Sagara. Glass substrates for silicon sensors. Unpublished technical report, 1996. Hoya Corporation USA, 980 Rincon Circle, San Jose, CA 95131.
- [50] J. J. Hall. Electronic effects in the elastic constants of n-type silicon. *Physical Review*, 161:756, 1967.
- [51] W. A. Harrison. *Scattering of Electrons by Lattice Vibrations in Crystals*. PhD thesis, University of Illinois, Urbana, Illinois, 1956.
- [52] F. R. S. Hearmon. *An Introduction to Applied Anisotropic Elasticity*. Oxford University Press, London, 1961.
- [53] P. L. Higby, E. J. Friebele, C. M. Shaw, and M. Rajaram. Radiation effects on the physical properties of low-expansion-coefficient glasses and ceramics. *Journal of the American Ceramic Society*, 71:796, 1988.
- [54] L. W. Hobbs. Network topology in aperiodic networks. *Journal of Non-Crystalline Solids*, 192/193:79, 1995.
- [55] L. W. Hobbs, C. E. Jesurum, V. Pulim, and B. Berger. Local topology of silica networks. *Philosophical Magazine A*, 78:679, 1998.
- [56] L. W. Hobbs and M. Treska. Private communication.
- [57] R. L. Hollingsworth, V. K. Rowe, and F. Oyen. Toxicity of acetylene tetrabromide determined on experimental animals. *American Industrial Hygiene Association Journal*, 24:28, 1963.

- [58] J. H. Hubbell and S. M. Seltzer. Tables of x-ray mass energy-absorption coefficients. NIST Physics Laboratory online database, 2000. <http://www.physics.nist.gov/PhysRefData/XrayMassCoef/intro.html>.
- [59] A. Iwase and S. Ishino. Comparison between radiation effects in some fcc and bcc metals irradiated with energetic heavy ions — a review. *Journal of Nuclear Materials*, 276:178, 2000.
- [60] X. Jiang, M. Wang, K. Schmidt, E. Dunlop, J. Haupt, and W. Gissler. Elastic constants and hardness of ion-beam-sputtered tinx films measured by brillouin scattering and depth-sensing indentation. *Journal of Applied Physics*, 69:3053, 1991.
- [61] J. F. Justo, M. Z. Bazant, E. Kaxiras, V. V. Bulatov, and S. Yip. Interatomic potential for silicon defects and disordered phases. *Physical Review B*, 58:2539, 1998.
- [62] M. Karimi, H. Yates, J. R. Ray, T. Kaplan, and M. Mostoller. Elastic constants of silicon using monte carlo simulations. *Physical Review B*, 58:6019, 1998.
- [63] J. Keinonen, A. Kuronen, K. Nordlund, R. M. Nieminen, and A. P. Seitsonen. First-principles simulation of collision cascades in si to test pair-potential for Si-Si interaction at 10 ev - 5 kev. *Nuclear Instruments and Methods in Physics Research B*, 88:382, 1994.
- [64] P. J. Kelly and R. Car. Green's-matrix calculation of total energies of point defects in silicon. *Physical Review B*, 45:6543, 1992.
- [65] S. Klaumünzer. Ion-beam-induced plastic deformation: A universal phenomenon in glasses. *Radiation Effects and Defects in Solids*, 110:79, 1989.
- [66] S. Klaumünzer, L. Changlin, S. Löffler, M. Rammensee, and G. Schumacher. Plastic flow of vitreous silica and pyrex during bombardment with fast heavy ions. *Nuclear Instruments and Methods in Physics Research*, B39:665, 1989.
- [67] M. D. Kluge, J. R. Ray, and A. Rahman. Molecular dynamic calculation of elastic constants of silicon. *Journal of Chemical Physics*, 85:4028, 1986.
- [68] M. A. Knight. Glass densities by settling method. *Journal of the American Ceramic Society*, 28:297, 1945.
- [69] A. V. Kozlov and V. V. Kirsanov. Radiation defect formation and evolution in C0.03Cr20Ni16Mn6 steel under low-temperature neutron irradiation and their effect on physical and mechanical properties of steel. *Journal of Nuclear Materials*, 233-237:1062, 1996.
- [70] Y.-C. Lee, J. O. Kim, and J. D. Achenbach. Acoustic microscopy measurement of elastic constants and mass density. *IEEE Transactions on Ultrasonics, Ferroelectrics, and Frequency Control*, 42:253, 1995.

- [71] Chr. Lehmann. *Interaction of Radiation with Solids and Elementary Defect Production*. Elsevier North-Holland, New York, 1977.
- [72] W.-K. Leung, R. J. Needs, G. Rajagopal, S. Itoh, and S. Ihara. Calculations of silicon self-interstitial defects. *Physical Review Letters*, 83:2351, 1999.
- [73] J. Li. Atomeye: an efficient atomistic configuration viewer. *Modelling and Simulation in Materials Science and Engineering*, 11:173, 2003.
- [74] U. Lindefelt. Symmetric lattice distortions around deep-level impurities in semiconductors: Vacancy and substitutional cu in silicon. *Physical Review B*, 28:4510, 1983.
- [75] C. S. Mariani and L. W. Hobbs. Network properties of crystalline polymorphs of silica. *Journal of Non-Crystalline Solids*, 124:242, 1990.
- [76] L. A. Marques, L. Pelaz, J. Hernandez, J. Barbolla, and G. H. Gilmer. Stability of defects in crystalline silicon and their role in amorphization. *Physical Review B*, 64:045214, 2001.
- [77] V. McLane, C. L. Dunford, and P. F. Rose. *Neutron Cross Sections, Vol 2, Neutron Cross Section Curves*. Academic Press, Inc., New York, 1981. National Nuclear Data Center, Brookhaven National Laboratory.
- [78] H. J. McSkimmin. Measurement of elastic constants at low temperatures by means of ultrasonic waves - data for silicon and germanium single crystals, and for fused silica. *Journal of Applied Physics*, 24:988, 1953.
- [79] G. C. Messenger, M. S. Ash, and R. Hauserman. *The Effects of Radiation on Electronic Systems, 2nd Edition*. Van Nostrand Reinhold, New York, 1992.
- [80] T. B. Metcalfe. *Radiation Spectra of Radionuclides*. Noyes Data Corporation, Park Ridge, New Jersey, 1976.
- [81] T. Mihara and M. Obata. Elastic constant measurement by using line-focus beam acoustic microscope. *Experimental Mechanics*, 32:30, 1992.
- [82] N. R. Moody, S. L. Robinson, J. P. Lucas, J. Handrock, and R. Q. Hwang. Effects of radiation and hydrogen on the fracture resistance of borosilicate glasses. *Journal of the American Ceramic Society*, 78:114, 1995.
- [83] T. Motooka. Model for amorphization processes in ion-implanted si. *Physical Review B*, 49:16367, 1994.
- [84] N. E. Moyer and R. C. Buschert. X-ray lattice parameter studies of electron-irradiated silicon. In F. L. Vook, editor, *Radiation Effects in Semiconductors*, pages 444-451. Plenum, New York, 1968.

- [85] S. F. Mughabghab, M. Divadeenam, and N. E. Holden. *Neutron Cross Sections, Volume 1, Neutron Resonance Parameters and Thermal Cross Sections*. Academic Press, Inc., New York, 1981. National Nuclear Data Center, Brookhaven National Laboratory.
- [86] P. Nitzsche, K. Lange, B. Schmidt, S. Grigull, U. Kreissig, B. Thomas, and K. Herzog. Ion drift processes in pyrex-type alkali-borosilicate glass during anodic bonding. *Journal of the Electrochemical Society*, 145:1755, 1998.
- [87] J. Nord, K. Nordlund, and J. Keinonen. Amorphization mechanism and defect structures in ion-beam-amorphized Si, Ge, and GaAs. *Physical Review B*, 65:165329, 2002.
- [88] K. Nordlund. Molecular dynamics simulation of ion ranges in the 1-100 keV energy range. *Computational Materials Science*, 3:448, 1995.
- [89] K. Nordlund and R. S. Averback. Atomic displacement processes in irradiated amorphous and crystalline silicon. *Applied Physics Letters*, 70:3103, 1997.
- [90] K. Nordlund and R. S. Averback. Point defect movement and annealing in collision cascades. *Physical Review B*, 56:2421, 1997.
- [91] K. Nordlund, M. Ghaly, R. S. Averback, M. Caturla, T. Diaz de la Rubia, and J. Tarus. Defect production in collision cascades in elemental semiconductors and fcc metals. *Physical Review B*, 57:7556, 1998.
- [92] K. Nordlund, J. Keinonen, and A. Kuronen. Effect of the interatomic Si-Si potential on vacancy production during ion implantation of Si. *Physica Scripta*, T54:34, 1994.
- [93] K. Nordlund, P. Partyka, Y. Zhong, I. K. Robinson, R. S. Averback, and P. Ehrhart. Glancing incidence diffuse x-ray scattering studies of implantation damage in Si. *Nuclear Instruments and Methods in Physics Research B*, 147:399, 1999.
- [94] J. F. Nye. *Physical Properties of Crystals*. Oxford University Press, Oxford, 1985.
- [95] J. Paymal. Quelques effets des réactions (n, alpha) dans les verres. *Verres et Réfractaires*, 6:341, 1961.
- [96] J. Paymal. Quelques effets des réactions (n, alpha) dans les verres. *Verres et Réfractaires*, 5:259, 1961.
- [97] J. Paymal. Quelques effets des réactions (n, alpha) dans les verres. *Verres et Réfractaires*, 1:20, 1962.
- [98] J. Paymal. Quelques effets des réactions (n, alpha) dans les verres. *Verres et Réfractaires*, 2:100, 1962.

- [99] W. Primak. Fast-neutron-induced changes in quartz and vitreous silica. *Physical Review*, 110:1240, 1958.
- [100] W. Primak and R. Kampwirth. The radiation compaction of vitreous silica. *Journal of Applied Physics*, 39:5651, 1968.
- [101] S. Sato. Radiation effect of simulated waste glass irradiated with ion, electron, and gamma-ray. *Nuclear Instruments and Methods in Physics Research*, B1:534, 1984.
- [102] M. Scheffler, J. P. Vigneron, and G. B. Bachelet. Total-energy gradients and lattice distortions at point defects in semiconductors. *Physical Review B*, 31:6541, 1985.
- [103] H. R. Schober and R. Zeller. Structure and dynamics of multiple interstitials in fcc metals. *Journal of Nuclear Materials*, 69/70:341, 1978.
- [104] Schott Corporation, Technical Glass Division, 3 Odell Plaza, Yonkers, New York 10701.
- [105] R. J. Schreutelkamp, J. S. Custer, J. R. Liefting, W. X. Luand, and F. W. Saris. Pre-amorphization damage in ion-implanted silicon. *Materials science reports*, 6:275, 1991.
- [106] N. Sekimura, T. Kamada, Y. Wakasugi, T. Okita, and Y. Arai. Evaluation of radiation hardening in fe alloys under heavy ion irradiation by micro-indentation technique. *Journal of Nuclear Materials*, 307-311:308, 2002.
- [107] H. Seong and L. J. Lewis. First-principles study of the structure and energetics of neutral divacancies in silicon. *Physical Review B*, 53:9791, 1996.
- [108] G. Servalli and L. Colombo. as discussed in De Sandre *et al.*[46].
- [109] J. E. Shelby. Radiation effects in hydrogen-impregnated vitreous silica. *Journal of Applied Physics*, 50:3702, 1979.
- [110] J. E. Shelby. Effect of radiation on the physical properties of borosilicate glasses. *Journal of Applied Physics*, 51:2561, 1980.
- [111] B. Shleien, L. A. Slaback, Jr., and B. Birky. *Handbook of Health Physics and Radiological Health*. Lippincott, Williams & Wilkins, Baltimore, Maryland, 1998.
- [112] J. K. Shultis and R. E. Faw. *Radiation Shielding*. Prentice-Hall, Upper Saddle River, NJ, 1996.
- [113] E. Snoeks and A. Polman. Densification, anisotropic deformation, and plastic flow of SiO₂ during MeV heavy ion irradiation. *Applied Physics Letters*, 65:2487, 1994.

- [114] T. Soma and H.-M. Kagaya. Thermal expansion coefficient of Si. In *Properties of Silicon, EMIS Datareviews Series No. 4*. INSPEC, The Institution of Electrical Engineers, London, 1988.
- [115] M. R. Spiegel. *Schaum's Outline of Theory and Problems of Statistics*. Schaum Publishing Company, New York, 1961.
- [116] F. H. Stillinger and T. A. Weber. Computer simulation of local order in condensed phases of silicon. *Physical Review B*, 31:5262, 1985.
- [117] D. M. Stock, B. Weber, and K. Gartner. Role of the bond defect for structural transformations between crystalline and amorphous silicon: A molecular-dynamics study. *Physical Review B*, 61:8150, 2000.
- [118] S. Sung, J. G. Lee, B. Lee, and T. Kang. Design and performance test of an oscillation loop for a mems resonant accelerometer. *Journal of Micromechanics and Microengineering*, 13:246, 2003.
- [119] M. L. Swanson, J. R. Parsons, and C. W. Hoelke. Damaged regions in neutron-irradiated and ion-bombarded Ge and Si. In J. W. Corbett and G. D. Watkins, editors, *Radiation Effects in Semiconductors*. Gordon and Breach Science, London, 1971.
- [120] M. Szabadi, P. Hess, A. J. Kellock, H. Coufal, and J. E. E. Baglin. Elastic and mechanical properties of ion-implanted silicon determined by surface-acoustic-wave spectrometry. *Physical Review B*, 58:8941, 1998.
- [121] T. Diaz de la Rubia and G. H. Gilmer. Structural transformations and defect production in ion implanted silicon: A molecular dynamics simulation study. *Physical Review Letters*, 74:2507, 1995.
- [122] S. I. Tan, B. S. Berry, and B. L. Crowder. Elastic and anelastic behavior of ion-implanted silicon. *Applied Physics Letters*, 20:88, 1972.
- [123] M. Tang, L. Colombo, J. Zhu, and T. Diaz de la Rubia. Intrinsic point defects in crystalline silicon: Tight-binding molecular dynamics studies of self-diffusion, interstitial-vacancy recombination, and formation volumes. *Physical Review B*, 55:14279, 1997.
- [124] J. Tarus, K. Nordlund, A. Kuronen, and J. Keinonen. Effect of surface on defect creation by self-ion bombardment of Si (001). *Physical Review B*, 58:9907, 1998.
- [125] Y. Tatsumi and H. Ohsaki. Density of crystalline and amorphous Si. In *Properties of Silicon, EMIS Datareviews Series No. 4*. INSPEC, The Institution of Electrical Engineers, London, 1988.
- [126] J. Tersoff. Empirical interatomic potential for silicon with improved elastic properties. *Physical Review B*, 38:9902, 1988.

- [127] M. Treska. private communication.
- [128] R. L. C. Vink, G. T. Barkema, W. F. van der Weg, and N. Mousseau. Fitting the stillinger-weber potential to amorphous silicon. *Journal of Non-Crystalline Solids*, 282:248, 2001.
- [129] C. A. Volkert. Stress and plastic flow in silicon during amorphization by ion bombardment. *Journal of Applied Physics*, 70:3521, 1991.
- [130] F. L. Vook. Low-temperature length change measurements of electron-irradiated germanium and silicon. *Physical Review*, 125:855, 1962.
- [131] K. Wada. Si melt growth: concentrations and diffusivities of vacancies and interstitials. In R. Hull, editor, *Properties of Crystalline Silicon*, pages 35–37. INSPEC, London, 1999.
- [132] S. X. Wang, L. M. Wang, and R. C. Ewing. Irradiation-induced amorphization: Effects of temperature, ion mass, cascade size, and dose rate. *Physical Review B*, 63:024105, 2000.
- [133] W. J. Weber, R. C. Ewing, C. A. Angell, G. W. Arnold, A. N. Cormack, J. M. Delaye, D. L. Griscom, L. W. Hobbs, A. Navrotsky, D. L. Price, A. M. Stoneham, and M. C. Weinberg. Radiation effects in glasses used for immobilization of high-level waste and plutonium disposition. *Journal of Materials Research*, 12:1946, 1997.
- [134] M. C. Wittels. Expansions in reactor irradiated germanium and silicon. *Journal of Applied Physics*, 28:921, 1957.
- [135] A. Witvrouw and F. Spaepen. Viscosity and elastic constants of amorphous Si and Ge. *Journal of Applied Physics*, 74:7154, 1993.
- [136] C. H. Woo and F. A. Garner. Displacement rate dependence of irradiation creep as predicted by the production bias model. *Journal of Nuclear Materials*, 233-237:974, 1996.
- [137] F. Wooten, K. Winer, and D. Weaire. Computer generation of structural models of amorphous Si and Ge. *Physical Review Letters*, 54:1392, 1985.
- [138] J. J. Wortman and R. A. Evans. Young's modulus, shear modulus, and Poisson's ratio in silicon and germanium. *Journal of Applied Physics*, 36:153, 1965.
- [139] X. Yuan and A. N. Cormack. Efficient algorithm for primitive ring statistics in topological networks. *Computational Materials Science*, 24:327, 2002.
- [140] X. Yuan and L.W. Hobbs. Modeling chemical and topological disorder in irradiation-amorphized silicon carbide. *Nuclear instruments & methods in physics research B*, 191:74, 2002.

- [141] W. H. Zachariasen. The atomic arrangement in glass. *Journal of the American Chemical Society*, 54:3841, 1932.
- [142] W. A. Zdaniewski, T. E. Easler, and R.C. Bradt. Gamma radiation effects of the strength of a borosilicate glass. *Journal of the American Ceramic Society*, 66:311, 1983.
- [143] X. Zhang, J. D. Comins, A. G. Every, P. R. Stoddart, W. Pang, and T. E. Derry. Surface brillouin scattering study of the surface excitations in amorphous silicon layers produced by ion bombardment. *Physical Review B*, 58:13677, 1998.
- [144] J. F. Ziegler. *SRIM-2003 computer code*. 1201 Dixona Drive, Edgewater, MD, 21037, 2003. <http://www.srim.org>.
- [145] J. F. Ziegler and J. M. Manoyan. The stopping of ions in compounds. *Nuclear Instruments and Methods in Physics Research*, 35B:215, 1988.
- [146] H. Zillgen and P. Ehrhart. Bound vacancy pairs in irradiated silicon. *Nuclear Instruments and Methods in Physics Research B*, 127/128:27, 1997.
- [147] J. Zuk, H. Kiefte, and M. J. Clouter. Investigation of ion-implanted GaP layers by brillouin scattering. *Journal of Applied Physics*, 73:4951, 1993.